THE UNIVERSITY *of* LIVERPOOL

Perturbation Estimation Based Control of Electric Energy Conversion Systems

Thesis submitted in accordance with the
requirements of the University of Liverpool
for the degree of Doctor of Philosophy

in

Electrical Engineering and Electronics

by

Yaxing Ren, B.Eng.

August 2016

Perturbation Estimation Based Control of Electric Energy Conversion Systems

by

Yaxing Ren

Acknowledgements

I would like to give my heartfelt thanks to my supervisor, Dr. Lin Jiang, whose encouragement, guidance and support enabled me to develop a deep understanding of my work. Without his consistent and illuminating instruction, my research work could not proceed to this stage. The research skill, writing skill and presenting skill he taught me will benefit me throughout my life.

I would like to show my gratitude to my second supervisors, Prof. Q.H. Wu and Dr. John Counsell, for their kind guidance with their knowledge of control systems.

I offer my regards and blessings to all of the members of Smart grid control and renewable energy sub-group, the University of Liverpool. Special thanks to Dr. Chuan-Ke Zhang, Dr. Jian Chen, Ms. Liuying Li and Mr. Sheng Yuan, for their support and friendship. My thanks also go to the Department of Electrical Engineering and Electronics at the University of Liverpool, for providing the funding of departmental postgraduate research studentship that covered all my tuition fees and maintenance, and the research facilities that made it possible for me to carry out this research.

Last but not least, I am deeply grateful to my parents, for their support and love, during the period of my postgraduate life.

Abstract

The traditional power system includes the centralised power generation, high voltage AC power transmission and three phase energy consumption. Electric energy conversion systems (ECSs) have been applied to the power generation, energy storage and power consumption to convert energy between the electric form and other forms. In the future power system, the ratio of distributed power generation and storage will have a rapid increment with the development of power electronics technology. Thus, the robustness and stability are significant to the ECSs in the future power electronics enabled power system. This thesis deals with the design and analysis with theoretical contribution, and the implementation of a perturbation estimation based nonlinear adaptive control (NAC) on ECSs, i.e. the wind turbine (WT), the energy storage system (ESS) in converter based microgrid (MG), and the induction motor (IM), respectively, in simulation and experimental validation.

The wind turbine is one of the most promising distributed power generation resources. The challenge in controlling a wind turbine is its nonlinear behaviour of aerodynamics under random wind speed. This makes it difficult to obtain the optimal control performance operating under the time-varying wind speed via conventional linear control method. In addition, as the future power system including plenty of distributed generation and consumption, typically in MG application, the ESS is necessary to balance the power difference between power generation and consumption. Due to the low stiffness and inertia of an islanded MG, the challenge is the stability problem and power quality of MG under unknown disturbance and unbalanced power demand. Moreover, other than the disturbance from power generation side, plenty of unknown disturbance also appears on the power consumption. The most popular workhorse for industrial application is the induction motor

(IM), which is affected by the disturbance of unknown load torque under operation. The IM has highly coupled states and nonlinear interactions between states. The conventional vector control depending on the flux position is sensitive to parameter changes. And the use of a speed encoder increases the risk in the IM speed drive in the electric vehicle application.

To cope with these challenges in the ECS applications, the perturbation estimation based control method is studied and applied to improve the robustness of the ECSs for power generation, storage and consumption of the future power system. In the control method, a state and perturbation observer is used to estimate the perturbation term, which includes the nonlinear interactions between states, external disturbance, parameter changes and unmodeled dynamics. In the WT pitch angle control, a nonlinear PI-based controller is designed with a perturbation observer to estimate and compensate the system nonlinearities and disturbance of WT system. In the ESS voltage control of islanded MG, a voltage controller is designed for the ESS in MG via estimating and compensating the unknown disturbance to reduce the voltage unbalance rate. In the IM speed drive, an NAC based speed controller is investigated to control the IM directly under the stationary frame to improve its robustness under disturbance and parameter uncertainty. Another contribution is to propose a speed sensorless NAC controller with a combined SPO to control the IM without the dependency of a speed sensor. The proposed control methods are compared with the conventional methods regarding their control performance.

The results show that the perturbation estimation based method can improve the robustness of ECS under disturbance and parameter uncertainty in the renewable power generation, MG bus voltage regulation, and IM speed drive. However, the great observer bandwidth can amplify the sensor noise and reduce the robustness and stability of the closed loop system. In the study, the observer and controller bandwidth is set greater than the controller bandwidth and lower than the sensor noise bandwidth, with optimised bandwidth tuned via pole placement method and the closed loop stability of the ECS systems is analysed using Lyapunov theory.

Declaration

The author hereby declares that this thesis is a record of work carried out in the Department of Electrical Engineering and Electronics at the University of Liverpool during the period from October 2012 to August 2016. The thesis is original in content except where otherwise indicated.

Contents

List of Figures

List of Abbreviations and Notations

Abbreviations

ECS	Energy Conversion System
WT	Wind Turbine
ESS	Energy Storage System
RES	Renewable Energy System
SCIG	Squirrel-Cage Induction Generator
DFIG	Double Fed Induction Generator
FPC	Full-capacity power converter
PMSG	Permanent Magnet Synchronous Generator
WRSG	Wound Rotor Synchronous Generator
WPGS	Wind Power Generation System
DRs	Distributed Resources
PV	Photovoltaic
HVDC	High-voltage Direct Current
MG	Microgrid
LV	Low-voltage
IM	Induction Motor
EV	Electric Vehicle
HEV	Hybrid Electric Vehicle
MIMO	Multi-Input Multi-Output
ADRC	Active Disturbance Rejection Control
SMSPO	Sliding Mode State and Perturbation Observer
IAE	Integrated of Absolute Error
ITAE	Integrated of Time Absolute Error
FAST	Fatigue, Aerodynamics, Structures, and Turbulence
FLC	Feedback Linearization Control

IOL	Input-output Linearization
AFLC	Adaptive Feedback Linearization Control
NAC	Nonlinear Adaptive Control
SPO	State and Perturbation Observer
VSC	Voltage Source Converter
PI	Proportional-Integral
GSPI	Gain Scheduling Proportional-Integral
N-PI	Nonlinear PI
Vf	Voltage and frequency
VC	Vector Control
SC	Super-capacitor
PWM	Pules Width Modulation
SVM	Space Vector Modulation
DSP	Digital Signal Processor
SRF	Synchronous Reference Frames
FNS	Fundamental Negative Sequence
UCR	Unbalance Compensation Reference
UCG	Unbalance Compensation Gain
LPF	Low Pass Filter
RMS	Root Mean Square
GUUB	Globally Uniformly Ultimately Bounded
PEEPS	Power Electronics Enabled Power System
DOD	Depth of Discharge
OCV	Open Circuit Voltage
SOC	State of Charge
ESR	Equivalent Series Resistance
SSNAC	Speed Sensorless Nonlinear Adaptive Control
MRAS	Model Reference Adaptive System

Notations

x	system states vector
y	system outputs vector
u	system inputs vector
d	external disturbance
$F(x)$	system nonlinear dynamic matrix

$g(x)$ or $B(x)$	system inputs gain vector
$h(x)$	outputs function
L_f^n	the n^{th}-order Lie derivative symbol
$\Psi(x)$	lumped perturbation
v	control inputs of linearized system
P_{r}	kinetic power captured by wind turbine
ρ	air density
R	rotor radius of WT
V	wind speed
C_{p}	power coefficient
ω_{r}	rotor speed
ω_{g}	generator speed
β	pitch angle
β_{r}	pitch angle control
δ	drive train shaft twist angle
τ_β	time constant of pitch actuator
λ	tip speed ratio
T_{g}	generator torque
J_{r}	rotor inertia
J_{g}	generator inertia
N_{g}	gear ratio
D_{s}	drive-train damping constant
K_{s}	drive-train spring constant
i_{Ld}	d-axis inductor current
i_{Lq}	q-axis inductor current
v_{od}	d-axis output voltage
v_{oq}	q-axis output voltage
v_{bd}	d-axis bus voltage
v_{bq}	q-axis bus voltage
V_{dc}	DC-link capacitor voltage
ω	synchronized angular speed or grid voltage
R_{S}	equivalent resistance of LC filter
L_{S}	equivalent inductance of LC filter
C_{S}	equivalent capacitance of LC filter
R_{z}	output resistance of transformer and bus cable

L_{z}	output inductance of transformer and bus cable
ω^*	reference angular frequency of output voltage
E^*	reference magnitude of output voltage
ω_0	nominal value of voltage frequency
E_0	nominal value of voltage magnitude
P	active power
Q	reactive power
m	droop gain of frequency to active power
n	droop gain of magnitude to reactive power
ε	perturbation estimation error
e	close loop error
ω_{m}	IM rotor mechanical speed
θ	IM flux position angle
$i_{\mathrm{s}\alpha}/i_{\mathrm{s}\beta}$	IM stator currents in stationary frame
$\psi_{\mathrm{r}\alpha}/\psi_{\mathrm{r}\beta}$	IM rotor flux linkage in stationary frame
$v_{\mathrm{s}\alpha}/v_{\mathrm{s}\beta}$	IM stator voltage as system input in stationary frame
R_{s}	IM stator resistance
R_{r}	IM rotor resistance
L_{s}	IM stator inductance
L_{r}	IM rotor inductance
L_{m}	IM mutual inductance
τ_r	IM rotor time constant
σ	IM leakage coefficient
T_{L}	IM load torque
J	IM rotor inertia
n_p	IM pole pairs

Chapter 1

Introduction

1.1 Background

An energy conversion system (ECS) is to transform the energy from one form to another. Examples include the turbine, electric machine, and chemical cell, etc. In the power system, the energy conversion process covers the power generation, storage and consumption in the power system. The following sections introduce three kinds of ECSs: the wind power generation system (WPGS), the energy storage system (ESS) in microgrid application, and induction motor.

1.1.1 Wind Power Generation System

Due to the energy shortage and environmental concern, renewable energy has a great attention of researchers and industry in recent decades. The total power generation of renewable energy systems (RES) is continuously booming [6]. The main advantages of using renewable sources are reducing the harmful emissions and the inexhaustible resources of the conventional energy; while the main disadvantage is the uncontrollability of renewable energy sources' availability, which exhibits strong daily and seasonal patterns [7].

As one of the most promising renewable energy sources, wind power has received tremendous progress in the past decades, as shown by the global installation capacity in Figure 1.1. Wind turbine is an energy conversion system, converting the

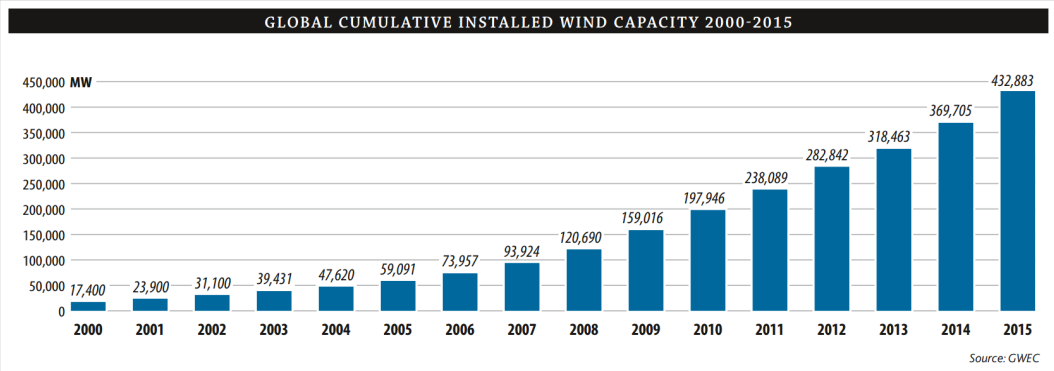

Figure 1.1: Global wind energy installation capacity [1].

kinetic energy of wind to the mechanical energy of the rotor of wind turbine, and finally the mechanical energy in wind turbine to electric energy.

Most wind power generation systems use variable speed wind turbines (WTs) with variable pitch to achieve an efficient and reliable conversion of wind power to electrical power.

Wind turbine architectures

There are a large number of choices of architecture available to the designer of a wind turbine, and most of these have been explored over the years [2, 8–10]. Machines of large size and capacity tend to operate at variable speed to accept a wider wind range, whereas smaller, simpler turbines are of fixed speed.

- Fixed-speed wind turbine

Fixed-speed wind turbines are electrically fairly simple devices without a power converter interface. It consists an aerodynamic rotor driving a low-speed shaft, a gearbox, a high-speed shaft and a squirrel cage induction generator (SCIG), as shown in Figure 1.2(a), which is coupled to the grid through a transformer. The rotational speed of the generator is determined by the grid frequency and the number of poles of the stator winding. Thus, at different wind speeds, the generator operating slip variation is generally less than 1%, this type of wind turbines is normally referred to as fixed speed [2, 11, 12].

- Variable-speed wind turbine

Comparing with the fixed-speed wind turbine, the variable-speed operation increases the energy conversion efficiency and reduces mechanical stress caused by wind gusts. The main drawback of variable-speed wind turbine is the need for a power converter interface to control the generator speed [2, 9, 13, 14]. Currently the most common variable-speed wind turbine configurations are as follows:

Doubly fed induction generator (DFIG) wind turbine. The DFIG wind turbine uses a wound-rotor induction generator whose stator winding connected to grid through a transformer and rotor winding fed through a variable-frequency power converter, as shown in Figure 1.2(b). A DFIG system can deliver power to the grid through the stator and rotor, while the rotor can also absorb power depend on the rotational speed of the generator [9].

Full-capacity power converter (FPC) wind turbine based on a synchronous or induction generator. The generator is connected to the grid via a FPC whose power rating is normally the same as that of the generator. Squirrel cage induction generators, wound rotor synchronous generators (WRSG), and permanent magnet synchronous generators (PMSGs) are all applied in this type of configuration [2], as shown in Figure 1.2(c). The power converter splits the AC connection of generator and grid by a DC link, which enables the independent control of generator-side and grid-side converters.

Control objectives of wind turbine

According to the wind speed range, a wind turbine has three operation modes, as shown in Figure 1.3 [3]. In each region, for a variable-speed variable-pitch wind turbine, the controller has different control objectives. Region I starts the wind turbine from the cut-in wind speed to the wind speed when the rotor speed reaches its rated value. In this region, the control objective is to capture the maximum available power from the wind flow [15]. The controller is to control the rotor or generator speed of the wind turbine to catch the optimized speed, meanwhile, the pitch angle of blades is kept at 0 degree to have the best wind power capture capability. Region II is the buffer region between the wind speed when the rotor speed reaches its rated value and the wind speed when the output power reaches its rated value [16].

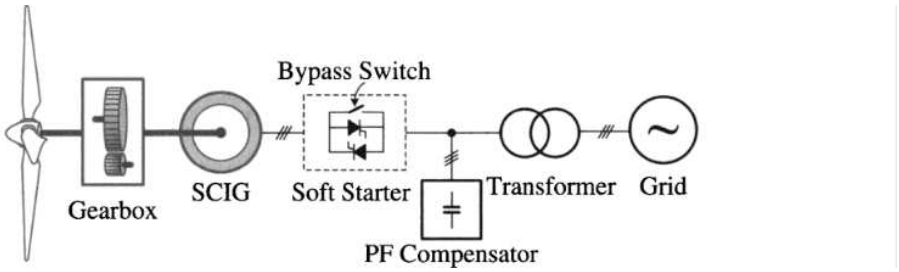

(a)

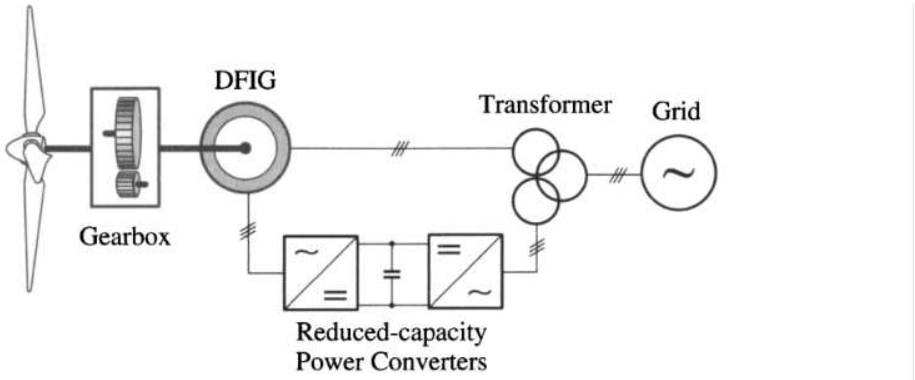

(b)

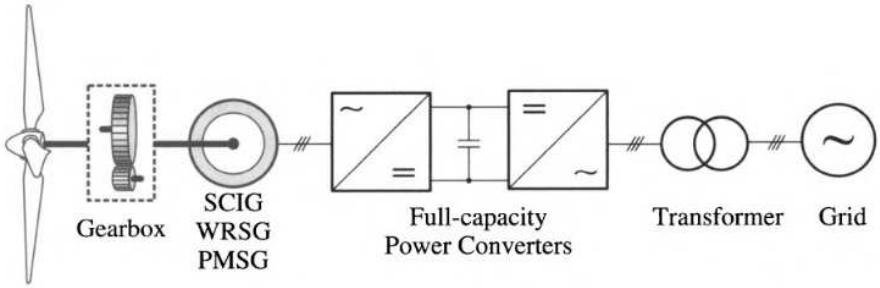

(c)

Figure 1.2: Different types of wind turbine. (a) SCIG based fixed-speed wind turbine, (b) DFIG based variable-speed wind turbien, (c) FPC based variable speed wind turbine [2].

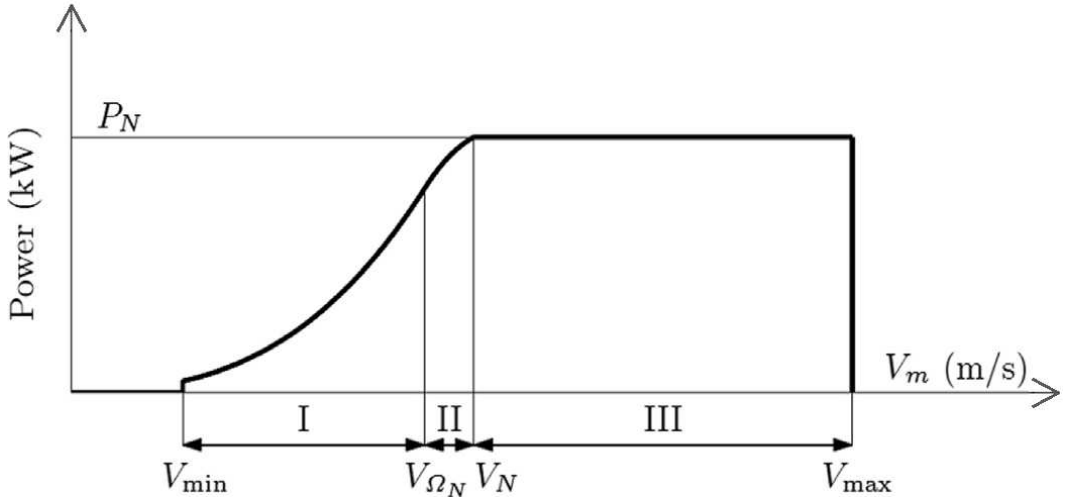

Figure 1.3: Wind turbine operation modes versus wind speed [3]

Region III ranges from the rated wind speed and to the cut-out wind speed, in which the wind power forced on the blade is larger than the nominal generated power of the wind turbine. The control objective in this region is to limit the pitch angle and, meanwhile, to minimize the load stress on drive-train shaft by a pitch angle controller [15, 16]. Under the pitch angle control, the rotor or generator speed of wind turbine is normally kept as a constant. When the wind speed is lower than the cut-in speed and higher than the cut-out speed, the wind turbine is stopped by mechanical brake and the pitch angle is adjusted to 90 degree.

Efficient and reliable operation of a wind power generation system (WPGS) heavily relies on the control systems applied on the WT operating at different regions. This thesis only considered the high speed region (Region III) in which the pitch angle control is applied to limit the wind power captured by the wind turbine.

1.1.2 Power System with More Power Electronics - Microgrid Application

In traditional power systems, the power is produced by synchronous generator based power plants of traditional energy sources, such as coal, petroleum and natural gas, and the generated power is transferred toward long distance transmission lines. However, the power system is changing, a large number of distributed resources

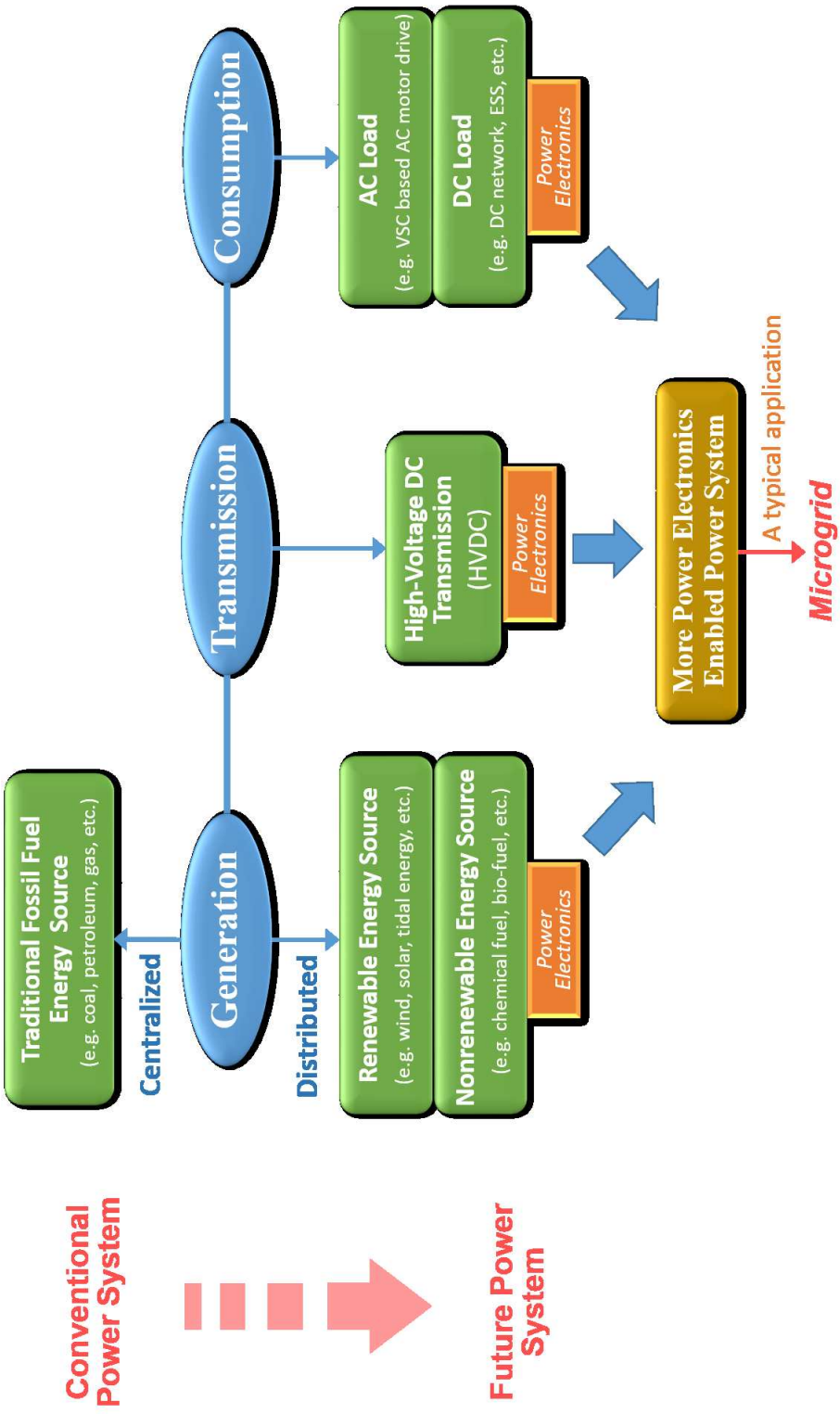

Figure 1.4: Power-electronics for the future power system.

(DRs) are being developed [7]. This leads the wide-scale use of power electronics in the power generation, the power transmission/distribution and the end-user application [6], as shown in Figure 1.4.

In the power generation of DR, the power electronic technology plays a significant role to match the characteristics of the DR units and the requirements of the grid connections, including voltage, frequency, phase, active and reactive power, harmonics minimization, etc [7]. The DRs include both the renewable energies, such as the wind energy, solar energy and tidal energy, and nonrenewable energies, such as the chemical fuel, and bio-fuel, etc. Power electronics bring in significant performance improvements for the DRs to let them act like completely controllable generation units being able to much better integrate the DRs into the power grid [17]. In the power transmission, the latest resurgence of developments is the high-voltage dc (HVDC) transmission. And the performance, reliability, and affordability of the power converters over 10 MW power levels still need further improvements [18]. In the power consumption, the converter based AC motor drive, and the typical DC load, such as the DC network, energy storage system and plug-in electric vehicle, act as the modern power demand.

Therefore, the power electronic technology plays an important role in the field of modern electrical engineering in the future power systems [7, 19, 20]. The power-electronics-enabled power systems are applied in the more electric aircraft [21–23], the ship board power system [19], and the low-voltage (LV) AC microgrid (MG) [24–27]. In this thesis, a LV-MG is studied in facing the challenge of the future more power-electronics based power systems.

The Energy Storage System in Microgrid

The MG can be defined as a LV network, including a cluster modular generations and loads, operated in both the grid-connected mode or island mode. In the grid-connected mode, the bus voltage is maintained by the utility grid, and all devices in the grid-connected AC MG stay synchronized with the voltage and frequency of the utility grid. But in the island mode, the AC MG is isolated from the utility grid and no external voltage reference to be synchronized. This makes the islanded MG has

much lower stiffness and inertia than the transmission grids [25–27]. It requires the DRs in the AC MG to have the capability of maintaining the voltage amplitude and frequency of the electric network.

In addition, as the renewable energy is unpredictable, alternative resources are needed when the renewable energy DRs cannot supply enough power to the load. The controllable micro-sources, such as micro-turbines and fuel-cells, are good alternative resources, but their response speed are not fast enough to face the fast-changing disturbance. They can be used as the auxiliary voltage sources to balance the power demands in steady states. The energy storage system (ESS), such as battery, flywheel and supercapacitor, are commonly used for the transient power response in MG due to their particular features of fast response speed, bi-direction power flow, and weather independency [28–36].

The voltage source converters (VSCs) are commonly used to rebuild the output voltage from the RES and ESS to be synchronized with the bus voltage of AC MG before connecting to the grid. The VSC based ESS are used to maintain the voltage and frequency of the AC MG when it faces the sudden disturbances, including load and generated power changes and short-circuit faults [25, 27].

In an islanded MG, all parallel connected DRs are expected to share the active and reactive power demand without centralized control or critical communication among them [37]. Thus, the power droop control for the VSC of DRs is often applied to reach this target and avoid the circulating currents between converter based DRs [27, 37–39].

In the MG, both the three-phase devices and single-phase devices could be connected due to different requirements. The single-phase loads and power generations are the major causes of voltage unbalance, which not only incurs more power loses and instability to the MG but also results in damaging the three-phase equipments installed in the MG. Therefore, the objectives of ESS controller is to recover the transient power difference between power generation and demand, meanwhile, to absorb the three-phase unbalanced power flow in the MG.

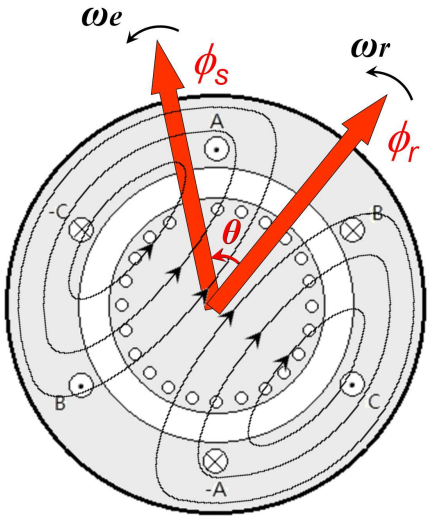

Figure 1.5: Induction motor structure.

1.1.3 Induction Motor

The electric machine is a significant energy conversion equipment that converts between the electric energy and mechanical energy. Induction motor (IM) is one of the most commonly used electric machine that not only the widely used workhorse in industrial processes and transportation applications [40] but also one of the most appropriate electric motor candidates and widely accepted choice for most of the EVs and HEVs manufacturing companies [41,42], such as Tesla Motors. The reason is its features of ruggedness, simple structure, small volume and lightweight, low cost, high efficiency and operational reliability [43]. Electric propulsion system is an integral part of electric vehicle (EVs) and hybrid electric vehicles (HEVs) [44]. Performance of the traction motor drive plays an important role in the evolution of alternative energy vehicle and electrified transport industry. Comparing with other motor candidates, the IM can easily operate in the speed higher than the rated via field weakening [45].

The main difficulties in controlling of an IM are its nonlinear dynamics, motor parameter variations during operation, and unmeasured states (rotor currents and fluxes) [46], as shown in Figure 1.5. The IM traction drive requires high performance control in order to get the fast transient response and energy optimiza-

tion [47, 48].

1.2 Control Methods for ECSs

In the conventional control systems of ECSs, linear controllers, such as the PI based control, are commonly designed based on the model of linearized systems. However, the real ECS systems are normally nonlinear systems in practical world. To control a nonlinear system, the most commonly used method is to linearize the nonlinear system based on a chosen operating point, and then design a linear controller based on the linearized system. However, the method design via linearization approach is valid only in a neighborhood of a single operating point. When the real operating points deviate the designed point, the linearized system cannot well present the dynamic response of the nonlinear system, and the designed linear controller cannot acquire the desired performance [49–51].

The nonlinearities for a nonlinear system can be classified into the continuous nonlinearities and the discontinuous nonlinearities. In a continuous nonlinear system, its input-output characteristics can be described by analytic functions and are continuously differentiable. In a discontinuous nonlinear system, its input-output characteristics cannot be modeled by analytic functions and the derivatives of output with respect to input contain singularities. The discontinuous nonlinearities are commonly produced by elements with their saturation, deadzone (or deadspace), absolute value detector, ideal relay, relay with deadzone, quantization, hysteresis, backlash, friction, etc [49].

Therefore, the real challenge is to maintain the control performance in the presence of system nonlinearity and uncertainty, including the dynamical uncertainty and parametric uncertainty.

To maintain the performance of controlling a nonlinear system when its operating points are changed, two most commonly used methods are presented to solve the nonlinear problem. One method is using the gain-scheduling method to provide an uniform performance via adjusting the controller gains based on measurable operating conditions. The other method is calculating the nonlinear changes from

the system input-output relationship and states feedback, and compensate the effect caused by the operating points changing, which is called the feedback linearization control method. These two methods are reviewed and analyzed in the following sections, and then a developed perturbation estimation based control method will be discussed.

The ECSs used in this thesis are the IM, WT, and VSC based DR in microgrid. The induction motor is developed from the 1880s, and the speed and torque control of IM still attracts researchers' attention even today. The control of wind turbine is studied from the 1980s. With the improvement of the wind turbine installation in the past decades, the control of wind turbine attracts increasing more attention of researchers. In recent years, with the development of renewable energy and power electronics technology, the microgrid techniques obtain growing concerns from researchers, especially the control of DR for sharing the power demand in a microgrid.

In this thesis, the conventional PI-based control approach, the feedback linearization control and the perturbation estimation based control with different kinds of observers that applied on the WT, VSC based DR in microgrid, and IM and are reviewed in the following parts.

1.2.1 PI and Gain Scheduling PI Control

In the wind turbine pitch angle control, the PI-type controller is the most basic method that controls the pitch angle based on the regulation error of output power, or rotor speed, with its reference value as in [3, 52].

In the microgrid application, the energy storage system (ESS) is used to maintain the bus voltage and frequency via balancing the power flow between generation and demand. The control of the ESS-VSC is implemented using the basic Vf control method, which is with a cascade-PI based control loop: an inner current control loop cascaded in an outer voltage control loop, with using PI controllers to regulate the voltages and currents [26, 53].

In the IM speed control, the most commonly used technique is the field-oriented control or vector control (VC). The VC method uses the Park transform to decouple the torque and flux and make them related to the d- and q-axis currents separately

[54], and controlled by two independent PI controllers. Thus, the VC control method achieves a good dynamic response of the controlled IM comparable to those of the dc motors [55, 56].

However, the linear PI controller with fixed gains cannot provide consistently satisfactory performance in the whole operating region, such as the wind turbine with strong aerodynamic nonlinearities operating under time-varying wind speed [57, 58]. To tackle this problem, the gain scheduling PI (GSPI) control method is presented to use the pre-scheduled control gains for the optimized performance in the whole operating region.

The 'gain-scheduling' means that the gain or other parameters of a controller can be self-adjusted to suitable or optimized values from measurable operating condition changes [51]. The gain scheduling method can be employed using powerful linear design tools based on linear parameter-varying plant models on solving difficult nonlinear problems [59]. For general nonlinear tracking problems, a family of linear dynamic controllers can be designed as a gain scheduling based on linearization of the system on operating points [60].

The purpose of the gain scheduled controller is to provide an uniform performance for the nonlinear design when the gain scheduling is possible to parameterize. Linear controllers can be designed for operating conditions in their neighborhood regions indexed by the scheduling parameters. The gain scheduling method has many different design notions, such as switching gain values according to operating conditions, controller switching, and controller blending [51].

The procedure of gain scheduling design is as follows [50]:

- The first step is to obtain a linear model of the nonlinear plant based on linearization approach about a family of operating points.
- The second step is to design a family of linear controllers for the linearized system model at each operating points or region.
- The third step is to involve implementing the family of linear controllers, such that the controller gains are scheduled according to the current condition of the scheduling variables.

- The fourth step is performance assessment, such as the capability of rapid response to changing operating conditions and the close-loop stability and robustness during gain switching.

The whole operating region is divided into some small regions, and a family of linear controllers are designed for each operating region. Thus the control system in whole operating region can be seen as a nonlinear controller. Application studies of the GSPI used in WT pitch angle control are presented in [3, 52]

1.2.2 Feedback Linearization Control

Feedback linearization theory provides methods that cancels the nonlinearities of the system through feedback. The basic idea is to transform a nonlinear system into a fully or partially linearized system, and then a controller can then be designed for the system using the powerful linear design techniques [49].

As mentioned in the previous sections, the feedback linearization control (FLC) can linearize the system by canceling the nonlinearities through feedback, it can eliminate the nonlinear problems that the linear PI-type controller cannot achieved. In the wind turbine application, the FLC is used in [61] and [58] to control pitch angle of wind turbine with optimized performance in the whole wind speed region. In the microgrid application, the FLC method is used to convert the secondary voltage control to a linear second-order tracker synchronization problem [62]. And in the IM speed drive, the nonlinear control methods to decouple the coupling nonlinearities such as the adaptive input-output linearizing control (IOLC) with parameter estimation [63], and the exact feedback linearization method with rotor flux angle estimation [64] are used to solve the effect of nonlinearity and uncertainty in the IM system. In the recent researches, the FL approaches is studied in direct-torque-controlled IM to improve the robust stability [65], theoretical framework and consequent application of FLC technique to IM [66], and considering magnetic saturation effects of using FLC on IM [67], etc.

Although feedback linearization has been used to solve a number of practical nonlinear problems, it still has an obvious drawback that it is vulnerable to handle

the presence of parameter uncertainty or external disturbances [49]. The inaccuracy of the model and parameters will lead to an unacceptable tracking error in the previous energy conversion systems. Because of which, some researchers use the observers to estimate the unavailable parts of the system, or to estimate and compensate the inaccurate parameters to the controllers.

To eliminate the problem of parameter uncertainties in the feedback linearization control, the adaptive feedback linearization control (AFLC) was studied under global Lipschitz condition on the nonlinearities multiplying unknown parameters [63, 68–71]. The AFLC method use the on-line parameter estimation to estimate the unknown parameters, or compensate the effect of parameter variations in the conventional feedback linearization control. The AFLC achieves the fully decoupling in system states and estimate the true parameter values for a better control performance. However, the AFLC can only estimate the constant or slowly changing parameters. If the system parameters are fast changing, the AFLC will have a poor estimation performance, and that will finally lead to a worse control result than before. Thus, the AFLC is an imperfect solution to reach the target of controlling a nonlinear system as simple as that of a linear system.

1.2.3 Perturbation Estimation based Control

In recent years, the problem of controlling uncertain nonlinear dynamical systems has been a topic of considerable interest. Many works in this field have been undertaken by employing robust and adaptive control method, i.e., an observation mechanism is designed to estimate disturbances or uncertainties, or both, and then use the estimate to compensate the corresponding system [72]. In the perturbation estimation based control approaches, a number of observation techniques have been proposed, such as perturbation observer [73], extended state observer (ESO) [74], uncertainty and disturbance estimator (UDE) [75, 76], equivalent input disturbance based estimator [77], disturbance observer (DOB) [78], and generalized proportional integral observer (GPIO) [79]. Among those perturbation estimation approaches, DOB and ESO are the most extensively investigated method. Recently, intelligent DOBs has been developed and widely investigated, such as fuzzy DOBs [80] and

neural network DOBs [81].

In the application of VSC control, the unknown disturbance are estimated and compensated by an extended state and perturbation observer (ESPO), which can be a linear or nonlinear observer, as the active disturbance rejection control (ADRC) used in [82] and [83]. In the wind turbine control applications, the ESPO is implemented using nonlinear observer [84, 85] based on the control theory from [74, 86, 87], linear observers [88, 89], fuzzy observers based on [80], and neural-network-based observers [81]. In the IM application, the perturbation estimation and compensation, or an alternative name is disturbance rejection, method using a linear observer in [90–92] or nonlinear observer in [93–95] to get a better dynamic performance and robustness against the modeling uncertainty and external disturbance.

1.2.4 Other Nonlinear Control Methods

Other advanced control methods for the wind turbine pitch angle control have been applied with digital robust control [96], neural-network-based control [97], model predictive control [98], etc. Some advanced control methods for VSC of DRs in microgrid were presented as the robust high bandwidth predictive current control [99], and hybrid variable-structure control [100] under balanced voltage condition; and a voltage unbalance and harmonics compensation strategy [101], a distributed negative sequence current sharing method [102], robust control strategy designed with a convex linear matrix inequality condition [103], model predictive control technique to minimize the voltage unbalance [104] were presented for the unbalanced voltage condition. In the IM speed drive, previous works used some advanced control methods to improve the robustness, such as adaptive control [105], sliding mode control [106], nonlinear sliding-mode torque control strategy [107], adaptive back-stepping sliding-mode control method [108], fuzzy control methods [109, 110], and neural network based robust control schemes [111, 112].

1.3 Objectives and Motivation

The conventional control methods of ECS expose the drawbacks of the robustness against disturbance and parameter variations. The perturbation estimation based nonlinear adaptive control method used in this thesis aims to improve the robustness of ECSs. The objective of this thesis is to design a perturbation estimation based control method to improve the robustness of target systems, and implement the control method in the ECSs depending on their characteristics.

The motivation of this thesis is to cope with the challenges of the controller design for ECSs in the future power system as follows. In the WT pitch angle control, the main challenge is the aerodynamic nonlinearities of WT and the random and time-varying wind speed cause the difficulties of obtaining the optimized performance for WT in a wide operating region. In the voltage control of ESS in MG, the main challenge is the disturbance and unbalanced power demand for the MG which has low stiffness and inertia cause its weak robustness under disturbance. And in the IM speed drive, the main challenge is the nonlinear dynamics and coupled states lead the difficulties in controlling the flux and torque separately, and the parameter sensitivity and flux position dependency problem of conventional control method causes the weak robustness under parameter uncertainty. More detailed objectives for the controller design of each ECSs are given as below:

- In the wind turbine pitch angle control, as the wind speed is varying in a wide range, the conventional PI based pitch angle controller cannot provide the optimized control performance when the operating point changes. Therefore, the objective of the controller design is to use a perturbation observer to estimate and compensate the nonlinearities during the operating point changing for having an optimized control performance in the whole wind speed region.

- In the voltage and frequency maintenance of an islanded microgrid by controlling the VSC control of ESS, the objective of the proposed controller is to design a perturbation observer to estimate and compensate the unbalanced perturbation, which includes both the positive- and negative-sequence disturbance, to eliminate the unbalanced voltage in the microgrid. And in a hybrid

ESS, a coordinate controller is designed to control the supercapacitor as an energy buffer to filter the transient power and unbalanced power demand that is to reduce the unnecessary usage of the battery in the hybrid ESS and extend its longevity.

- In an IM system, the flux and torque is coupled together and cannot fully decoupled by the Park transform in the conventional vector control. The objective of the proposed speed controller is to control the IM directly under the stationary frame which aims to improve the performance of the speed response and robustness under disturbance via fully decoupling the flux and torque without the dependency on the flux position and system parameters. And in the speed sensorless control, the new controller is designed by replacing the PI regulator with a state and perturbation observer in a speed observer with the objective of estimate the speed and its perturbation simultaneously, which is to reduce the computation load and improve the robustness of the IM system.

1.4 Major Contributions

The thesis reports the research work undertaken based on nonlinear adaptive control via perturbation estimation that is applied on the control of ECSs for the future power system. The major contribution is the implementation of the perturbation estimation based control method for the application of ECSs to find the most suitable controller bandwidth depending on the characteristics of ECSs. More detailed contributions for the ECSs application are summarized as follows:

- Due to the nonlinear behaviour of aerodynamics of wind turbine under random wind speed, the conventional linear controller cannot provide the optimized control performance in a wide wind speed range. A perturbation estimation based nonlinear PI (N-PI) controller has been applied for wind turbine pitch angle control under time-varying wind speed in Region III. The proposed N-PI based pitch angle controller is investigated to use only one set of

PI parameters to provide an optimal performance under wind speed changes via the perturbation estimation and compensation without the requirement of accurate model. The simulation results on both the simplified and detailed wind turbine model have shown that, comparing with the conventional PI and gain-scheduled PI controller, the N-PI controller provides better dynamic performance of power regulation, load stress reduction and actuator usage. And the N-PI has better robustness against of model uncertainties than the feedback linearization control.

- Due to the low stiffness and inertia of an islanded MG, a more robust voltage control for the ESS is required to maintain the bus voltage and power quality if the MG under unknown disturbance and unbalance power demand. A perturbation estimation based NAC is investigated for the VSC in the microgrid application with considering the voltage unbalance problem. The SPO is developed to estimate both the positive- and negative-sequence perturbations to compensate the voltage unbalance that is caused by single-phase disturbances in an islanded MG. The simulation results have shown that the proposed control method has better performance in eliminating the disturbance and voltage unbalance in the islanded MG.

- As the energy storage devices in ESS has different properties, such as the battery has high energy capacity and the SC has high power density and more recycling times, the challenge is to optimize the controls of the ESS considering the properties of different devices. A coordinated control strategy for the VSC of a battery-supercapacitor based hybrid energy storage system (HESS) for both improving the transient performance of MG bus voltage and reducing the battery loss. In this control strategy, the battery is controlled to provide the balanced power in steady-state while the SC is controlled to generate transient power and compensate the unbalanced power demand. Simulation results have shown that the transient response of MG bus voltage under the unbalanced load disturbance has been improved. Simultaneously, with the SC acts as an energy buffer to filter the transient and unbalanced power, the battery loss is reduced with lower discharge depth and higher efficiency.

- Due to the high coupled states and nonlinear interactions between states of IM, the conventional control method is depending on the flux position, which is parameter sensitive and cannot fully decouple the dynamics of the flux and torque. A novel NAC based controller for the IM speed drive has been investigated to improve the performance of speed and flux tracking under unknown load disturbance and uncertainties under the stationary frame to reduce the dependance on rotor flux position and system parameters. The stability of the close-loop system with the proposed NAC controller is investigated via Lyapunov theory, and its dynamic performance is verified by both simulation and experimental studies in comparison with conventional control methods, such as the vector control and model-based input-output linearizing control. The results have shown that the NAC provides faster response and less regulation error in rotor flux and speed tracking, and better robustness to disturbance and parameter uncertainties.

- Due to the risk of using a speed encoder in IM speed drive, many speed sensorless method is to add an additional speed observer to the controller, which increase the complexity of the control system structure. A speed sensorless NAC (SSNAC) controller for IM speed drive in electric vehicle (EV) application has been investigated which uses a combined SPO to reduce the use of PI regulator in a MRAS speed observer for estimating both the speed and its perturbation for fully linearizing the IM system without speed sensor. The stability of the close-loop system with the SSNAC is proved via Lyapunov theory. The performance of the SSNAC are validated in both simulation study and experiment validation with the driving profiles of the speed reference and load torque are from the operation conditions of EV, and compared with that of the conventional vector control with MRAS speed observer. The results have shown that the SSNAC provides a reliable and effective solution for the high performance robust speed sensorless control of IM for EV application.

In this thesis, the NAC for the wind turbine pitch angle control and for induction motor speed control are validated in simulation using MATLAB/Simulink, while the

NAC for the voltage and frequency control of VSC in the microgrid applications are validated in simulation using PSCAD/EMDTC. The hardware implementation of NAC based speed controller for the induction motor is in the dSPACE environment.

1.4.1 Publication List

The publications produced from this research work are listed in this section as follows:

1. Yaxing Ren, Liuying Li, Joseph Brindley, and Lin Jiang, Nonlinear PI control for variable pitch wind turbine, *Control Engineering Practice*, vol. 50, pp. 84-94, May 2016.

2. Yaxing Ren, Lin Jiang, Jian Chen, Yihua Hu, Chuan-Ke Zhang, and Yong He, Perturbation Estimation Based Nonlinear Adaptive Control for Induction Motor Speed Control with Improved Robustness, *IEEE Transaction on Power Electronics*, 2016. (Under review)

3. Yaxing Ren, Lin Jiang, Saqib Jamshed, Yihua Hu, and Huiqing Wen, Speed Sensorless Nonlinear Adaptive Control of Induction Motor for Electric Vehicles via a Combined Speed and Perturbation Observer, *IEEE Transaction on Mechatronics*, 2016. (Under the 2^{nd} review)

4. Yaxing Ren, Jian Chen, Lin Jiang, and Saqib Jamshed Rind, Perturbation Estimation Based Nonlinear Adaptive Control to Compensate Voltage Unbalance and Disturbance in Islanded Microgrid, *IEEE Transaction on Sustainable Energy*, 2016. (Submitted)

5. Yaxing Ren, Shuaihu Li, Lin Jiang, and Pingliang Zeng, Coordinated Control for Battery and Supercapacitor in Hybrid Energy Storage System in Microgrid, *International Power Electronics and Motion Control Conference (IPEMC) - ECCE Asia*, 2016.

6. Jian Chen, Yaxing Ren, Lin Jiang, Wei Yao, and Chuan-Ke Zhang, Robust Maximum Power Point Tracking Control of PMSG-Based Wind Turbine via

Perturbation Observation Based Nonlinear Adaptive Controller, *International Journal of Electrical Power & Energy Systems*, 2016. (Under review)

7. Wei Zhang, Jian Chen, Yaxing Ren, Liuying Li, Wei Yao and Lin Jiang, Nonlinear adaptive control of induction motor with sliding mode flux observer, *17th International Conference on Electrical Machines and Systems (ICEMS)*, pp. 2738-2742, Oct. 2014.

1.5 Thesis outline

The thesis is organized as follows.

Chapter 2: Review of Perturbation Observer Based Nonlinear Adaptive Control

This chapter introduce the feedback linearization method and the perturbation estimation method. The perturbation estimation method can be designed using different observers, such as the linear high-gain observer, nonlinear observer, sliding-mode observer, and finite-time observer. Then the different observers are compared for estimating the perturbation of a simple second-order system as an example.

Chapter 3: Nonlinear PI Control for Variable Pitch Wind Turbine

The renewable energy, especially the wind energy, is the most promising distributed power generation in the future power system. To control the WT with nonlinear aerodynamic under random wind speed, this chapter propose a perturbation estimation based nonlinear PI (N-PI) controller for wind turbine pitch angle control. The N-PI based pitch angle controller is investigated to provide an optimal performance under wind speed changes using only one set of PI parameters and estimated perturbation without the requirement of accurate model. The simulation verification is based on a simplified two-mass wind turbine model and a detailed aero-elastic wind turbine simulator FAST. The results show that the N-PI controller can provide better dynamic performance of power regulation, load stress reduction and actuator usage, comparing with the conventional PI and gain-scheduled PI controller, and better robustness against of model uncertainties than the feedback linearization control.

Chapter 4: Autonomous Control of Power Electronics Enabled Microgrid via Nonlinear Adaptive Control

Beside the distributed generation, the ESS is another significant devices in the the future power system due to the low inertia and unbalanced disturbance in the MG. This chapter proposed a perturbation estimation based voltage controller employing an SPO to estimate both the positive- and negative-sequence perturbations to solve the voltage unbalance problem caused by single-phase disturbances in islanded MG. The proposed control scheme is validated in PSCAD/EMTDC simulation with the single-phase impedance load and distribute resource connected to the MG as the unbalanced disturbance. Simulation results demonstrate that the proposed controller eliminates the voltage unbalance and disturbance with less voltage dip and voltage unbalance rate of the bus voltage in the islanded MG.

Chapter 5: Coordinated Control for Battery and Supercapacitor in Hybrid Energy Storage System in Microgrid

To further develop the control system of ESS with considering the different properties of energy storage devices, this chapter presents a cooperative control strategy for a battery-supercapacitor based hybrid ESS (HESS) for both improving the transient performance of MG bus voltage and reducing the battery loss. The control strategy is to distribute the power generated from different devices in HESS, as battery is controlled to provide the balanced power in steady-state while supercapacitor is controlled to generate transient and unbalanced power for an unbalanced load demand. Simulations are implemented in the PSCAD/EMTDC software environment, and the results show that the transient response of MG bus voltage has been improved and the battery loss is reduced by the proposed control strategy with lower depth of discharge, less internal power loss, and higher entire efficiency than the conventional control method in MG applications.

Chapter 6: Nonlinear Adaptive Control for Induction Motor Speed Control with Improved Robustness

The disturbance of the future power system also comes from the power consumption side, such as an IM speed drive under load torque disturbance. This chapter investigates a novel NAC based speed controller for the IM to improve the

performance of speed and flux tracking under unknown and fast-changing load disturbance and uncertainties. The control method is designed directly under the stationary frame to reduce the dependance on flux position and system parameters. State and perturbation observers are designed to estimate the perturbations, and the estimates are used to adaptively compensate the real perturbations. The stability of the close-loop system with proposed NAC is investigated via Lyapunov theory, and its dynamic performance is verified by both simulation and experimental studies in comparison with that of the conventional vector control and model-based input-output linearizing control. The results show that the NAC based speed controller provides improved performance with faster response and less regulation error in rotor flux and speed tracking, and robust to load disturbance and parameter uncertainties.

Chapter 7: Speed Sensorless Nonlinear Adaptive Control of Induction Motor for Electric Vehicles via a Combined Speed and Perturbation Observer

To further develop the speed controller of IM with reducing the dependence of a speed sensor, this chapter proposes a speed sensorless NAC controller for IM speed drive in EV application. The SSNAC uses a combined SPO to replace the PI regulator in a model reference adaptive system (MRAS) speed observer for estimating both the speed and its perturbation for fully linearizing the IM system without speed sensor. The stability of the close-loop system with the SSNAC is investigated via Lyapunov theory. The performance of the SSNAC are compared with the conventional VC with MRAS speed observer in both simulation study and experiment validation, where the driving profiles of the IM speed reference and the load torque are from the operation conditions of EV. The results show that the SSNAC provides reliable and effective solution for the high performance robust speed sensorless control of IM for EV application.

Chapter 8: Conclusions and Future Work

The thesis has concluded with a summary of the results and several suggestions for future work. The suggestions for future work will highlight the unsolved problems that remained.

Chapter 2

Review of Perturbation Observer Based Nonlinear Adaptive Control

The perturbation estimation based nonlinear adaptive control is proposed in [113, 114]. A multi-input multi-output (MIMO) system is transformed as interacted subsystems via input-output linearization at first. Then for each subsystem, a perturbation term is defined to include all subsystem nonlinearities, interactions between subsystems and uncertainties. A fictitious state is introduced to represent the perturbation and a state and perturbation observer (SPO) is designed to estimate the perturbation and other system states based upon the measurement. The estimates of perturbations are used to compensate the real perturbations, then the original nonlinear system can be controlled using a linear controller, as the schematic diagram shown in Figure 2.1. The following sections present the detailed explanation by formulas in steps.

2.1 Feedback Linearization

Feedback linearization theory provides methods that cancels the nonlinearities of the system through feedback. The basic idea is to transform a nonlinear system into a fully or partially linearized system, and then a controller can then be designed for the system using the powerful linear design techniques. The feedback linearization

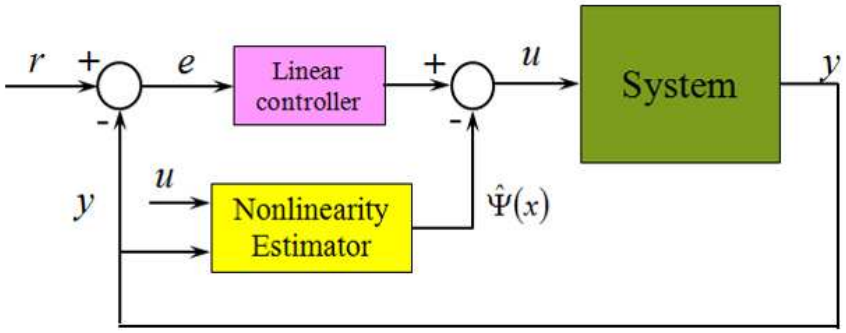

Figure 2.1: Schematic diagram of the disturbance observer based control method.

method helps to convert many intractable nonlinear problems into simpler linear problems. The theory can be divided into two kinds of approaches: the input-out linearization, and the input-state linearization [49].

- Input-output linearization (IOL) is to linearize the input-output map from system input to output even if the state equation is only partially linearized. The IOL approach is easy to obtain and requires little more number of times to differentiate the output. However, this approach may result in that some internal dynamics cannot be controlled from an input-output point of view, which is called the zero dynamic problem.

- Input-state linearization is to linearize the full state equation, which means it is not generally possible with a given system. If the solution of the partial differential equation is possible, a state transformation and a linearizing feedback can be found.

The system input-output relationship is nonlinear and the system is controlled by a linear controller based on a constant operating point, and the nonlinearity is calculated and compensate the system nonlinearity is compensated to obtain the optimized performance in the whole operating region of the nonlinear system [49].

A MIMO nonlinear system is considered as

$$\begin{cases} \dot{x} = f(x) + g(x)u \\ y = h(x) \end{cases} \tag{2.1.1}$$

where $x \in R^n$ is the state vector, $u \in R^m$ is the control input vector, $y \in R^m$ is the output vector, $f(x)$, $g(x)$ and $h(x)$ are smooth vector fields.

2.1.1 Input-State Linearization

System (2.1.1) is fully-linearizable if there exists a diffeomorphism Ψ_i: $U \to R^n$ such that $D = \Psi_i(U) \in R^n$ and the state transformation $z_i = \Psi_i(x)$ transforms the system into the form:

$$\begin{cases} \dot{z}_i = Az_i + B(\alpha_i(x) + \beta_i(x)u_i) \\ y_i = Cz_i \end{cases} \tag{2.1.2}$$

where A and B are the system parameter matrix, $\alpha_i(x)$ is the system nonlinearity and $\beta_i(x)$ is the input gain function; (A, B) is controllable and $\beta_i(z_i)$ is nonsingular $\forall z_i \in D$. With the system in form (2.1.2), we can linearize it exactly by the state feedback control

$$u_i = (-\alpha_i(z) + v_i)/\beta_i(z) \tag{2.1.3}$$

to obtain the linear system

$$\begin{cases} \dot{z}_i = Az_i + Bv_i \\ y_i = Cz_i \end{cases} \tag{2.1.4}$$

where v_i is the control of linearized system; A, B and C are given by

$$A = \begin{bmatrix} 0 & 1 & 0 & \cdots & 0 \\ 0 & 0 & 1 & & 0 \\ \vdots & \vdots & & \ddots & \vdots \\ 0 & 0 & 0 & \cdots & 1 \\ 0 & 0 & 0 & \cdots & 0 \end{bmatrix}, \quad B = \begin{bmatrix} 0 \\ 0 \\ \vdots \\ 0 \\ 1 \end{bmatrix}, \quad C = \begin{bmatrix} 1 \\ 0 \\ \vdots \\ 0 \\ 0 \end{bmatrix}^T \tag{2.1.5}$$

Consider the nonlinear system (2.1.1) having the relative degree $r = n$, i.e., exactly equal to the dimension of the state space, at the point x_0. In this case, the change of coordinates is required to construct the normal form is exactly given by

$$\Phi_i(x) = \begin{pmatrix} \Phi_{i1}(x) \\ \Phi_{i2}(x) \\ \vdots \\ \Phi_{in}(x) \end{pmatrix} = \begin{pmatrix} h_i(x) \\ L_f h_i(x) \\ \vdots \\ L_f^{n-1} h_i(x) \end{pmatrix} \tag{2.1.6}$$

where $L_f^k h_i(x)$ is the k_{th} order Lie derivative of $h_i(x)$.

i.e. by the function $h(x)$ and its first $n-1$ derivatives along $f(x)$. In the new coordinates

$$z_{ir} = \phi_r(x) = L_f^{r-1} h(x), \qquad 1 \leq r \leq n, \tag{2.1.7}$$

the system (2.1.1) will be described in the following form:

$$\begin{cases} \dot{z}_{i1} &= z_{i2} \\ &\vdots \\ \dot{z}_{i(n-1)} &= z_{in} \\ \dot{z}_{in} &= \alpha_i(z) + \beta_i(z) u_i \end{cases} \tag{2.1.8}$$

where $z = (z_{i1}, \ldots, z_{in})^T$, $\alpha_i(z) = L_f^n h_i(x)|_{x=\Psi_i^{-1}(z)}$, and $\beta_i(z) = L_g L_f^{n-1} h_i(x)|_{x=\Psi_i^{-1}(z)}$. Recall that at the point of $z^0 = \Phi_i(x_0)$, and thus for all z_i in a neighborhood of z_0, the function $\beta_i(z)$ is nonzero. Now, if we choose the state feedback control law (2.1.3) which indeed exists and is well-defined in a neighborhood of z_0.

2.1.2 Input-Output Linearization

The input-output linearization of a MIMO system is obtained via differentiating the output y_i of the system until the input u_j appears. Thus, assuming that r_i is the smallest integer such that at least one of the inputs explicitly appears in $y_i^{(r_i)}$

$$y_i^{(r_i)} = L_f^{r_i} h_i + \sum_{j=1}^{m} L_{g_j} L_f^{r_i - 1} h_i u_j \tag{2.1.9}$$

where $y_i^{(r_i)}$ is the i^{th}-order derivative of y_i, $L_{g_j} L_f^{r_i-1} h_i(x) \neq 0$ for at least one j. Performing the above procedure for each output y_i yields

$$\begin{bmatrix} y_1^{(r_1)} \\ \vdots \\ y_m^{(r_m)} \end{bmatrix} = \begin{bmatrix} L_f^{r_1} h_1 \\ \vdots \\ L_f^{r_m} h_m \end{bmatrix} + B(x) \begin{bmatrix} u_1 \\ \vdots \\ u_m \end{bmatrix} \tag{2.1.10}$$

$$B(x) = \begin{bmatrix} L_{g_1} L_f^{r_1-1} h_1 & \cdots & L_{g_m} L_f^{r_1-1} h_1 \\ \vdots & \ddots & \vdots \\ L_{g_1} L_f^{r_m-1} h_m & \cdots & L_{g_m} L_f^{r_m-1} h_m \end{bmatrix} \tag{2.1.11}$$

where $B(x)$ is a $m \times m$ control gain matrix. If $B(x)$ is invertible, the FLC of the the MIMO nonlinear system can be obtained as

$$u = B(x)^{-1} \left\{ \begin{bmatrix} -L_f^{r_1} h_1 \\ \vdots \\ -L_f^{r_m} h_m \end{bmatrix} + \begin{bmatrix} v_1 \\ \vdots \\ v_m \end{bmatrix} \right\} \tag{2.1.12}$$

where v_i are new inputs of the system. Now the input-output relations are given by

$$y_i^{(r_i)} = v_i \tag{2.1.13}$$

At this point, desired dynamics can be imposed on the system by the new system inputs.

2.1.3 Perturbation Term Definition

If the system input gain matrix $B(x)$ is unavailable or variable with states, the nominal control gain can be used and the variable part will be defined into the lumped perturbation. For system (2.1.2), assume all nonlinearities are unknown, define the system perturbation as

$$\Psi_i(x, u, t) = L_{fi}(x) + (B(x) - B_0)\, u \tag{2.1.14}$$

then the last equation of system (2.1.2) can be rewritten as

$$\dot{x}_n = \Psi(x, u, t) + B_0 u \tag{2.1.15}$$

where B_0 is the nominal constant control gain.

For the i^{th} subsystem, defining state variables as $z_{i1} = y_i, \cdots, z_{ir_i} = y_i^{(r_i-1)}$ and a virtual state to represent the perturbation $z_{i(r_i+1)} = \Psi_i$, the state equation of the i^{th} subsystem in system (2.1.1) can be represented as

$$\begin{cases} \dot{z}_{i1} &= z_{i2} \\ & \vdots \\ \dot{z}_{ir_i} &= z_{i(r_i+1)} + B_{0_i} u \\ \dot{z}_{i(r_i+1)} &= \dot{\Psi}_i \end{cases} \tag{2.1.16}$$

where B_{0_i} is the i^{th} row of the B_0, and $B_{0_{ij}}$ is the i^{th} row j^{th} column element of the B_0.

2.2 Perturbation Estimation using State and Perturbation Observers

2.2.1 Extended-Order Perturbation Observers

A MIMO system is transformed as interacted subsystems via input-output linearisation at first. A fictitious state is introduced to represent the perturbation and an perturbation observer is designed to estimate the perturbation and other system states, based upon the measurement only. The estimates of perturbations are used to compensate the real perturbations, then an adaptive linearisation and decoupled control of the original nonlinear system will be implemented. Comparing with the parameter estimation investigated in most adaptive control schemes, the technique used in the proposed control strategies can be considered as a function estimation method. For system (2.1.16), several types of perturbation observers, such as sliding mode observer, high gain observer and linear Luenberger observer, have been proposed [114].

High-Gain State and Perturbation Observer

This chapter picks up high gain observer as an example to show the design procedure, while other types observers can be designed similarly.

$$\begin{cases} \dot{\hat{z}}_{i1} &= \hat{z}_{i2} + l_{i1}(z_{i1} - \hat{z}_{i1}) \\ &\vdots \\ \dot{\hat{z}}_{ir_i} &= \hat{z}_{ir_i} + l_{ir_i}(z_{i1} - \hat{z}_{i1}) + B_{0_i}u \\ \dot{\hat{z}}_{i(r_i+1)} &= l_{i(r_i+1)}(z_{i1} - \hat{z}_{i1}), \end{cases} \tag{2.2.1}$$

where l_{i1} and l_{i2} are gains of the high gain observer. Throughout this chapter, $\hat{z}_{ir_i}$ represents the estimate of z_{ir_i}.

By choosing

$$l_{i1} = \frac{\alpha_{ij}}{\epsilon_i}, \quad l_{i2} = \frac{\alpha_{ij}}{\epsilon_i^2}, \tag{2.2.2}$$

where ϵ_i, $0 < \epsilon_i < 1$ is a positive constant to be specified and the positive constants α_{ij}, $j = 1, 2$, are chosen such that the roots of

$$s^2 + \alpha_{i1} s + \alpha_{i2} = 0 \tag{2.2.3}$$

are in the open left-half complex plane. Throughout this chapter, $\hat{z}_{ir_i}$ represents the estimate of z_{ir_i}.

The gains of the the high-gain observer can be chosen using the same method as in (2.2.2) and (2.2.3).

Nonlinear Extended State Observer

As an alternative, a nonlinear function is proposed by Han with the active disturbance rejection control (ADRC) in [74] as follows:

$$fal(e, \alpha, \delta) = \begin{cases} \frac{e}{\delta^{(1-\alpha)}}, & |e| \leq \delta \\ |e|^{\alpha} \cdot \text{sgn}(e) & |e| > \delta \end{cases} \tag{2.2.4}$$

that sometimes provides surprisingly better results in practice. In the nonlinear function, e is the tracking error, α is the precision index from 0 to 1, δ is the width of linear area of the nonlinear function.

With linear feedback, the tracking error approaches zero in infinite time with nonlinear feedback of the form

$$u = |e|^{\alpha} \cdot \text{sgn}(e) \tag{2.2.5}$$

the error can reach zero much more quickly in finite time, with $\alpha < 1$. Such α can also help reduce steady state error significantly, to the extent that an integral control, together with its downfalls, can be avoided. It is because of such efficacy and unique characteristics of nonlinear feedback that Han propose a systematic and experimental investigation [74].

Then an extended state observer with nonlinear equation can be constructed based on system (2.1.16) in the form of

$$\begin{cases} e & = & z_1 - \hat{z}_1 \\ \dot{\hat{z}}_1 & = & \hat{z}_2 + \beta_1 e \\ & \vdots & \\ \dot{\hat{z}}_{r_i} & = & \hat{z}_{r_i+1} + \beta_{r_i} fal(e, 0.5^{r_i-1}, \delta) + B_{0i}u \\ \dot{\hat{z}}_{r_i+1} & = & \beta_{r_i+1} fal(e, 0.5^{r_i}, \delta) \end{cases} \tag{2.2.6}$$

There are many ways to select the observer gains β_{r_i} for a particular problem. As an example, for a third-order system, the observer gains in (2.2.6) can be selected as [74]

$$\beta_{01} = 1 \qquad \beta_{02} = \frac{1}{2h^{0.5}} \qquad \beta_{03} = \frac{2}{5^2 h^{1.2}} \tag{2.2.7}$$

Sliding Mode State and Perturbation Observer

The sliding-mode observer potentially offers advantages of inherent robustness to parameter uncertainty and external disturbances [115,116]. It is a high-performance state estimator with a simple structure and is well suited for uncertain nonlinear systems [117–119]. The integration of the perturbation estimation into the sliding-mode observer structure can reduce substantially the amplitude of the driving term of the state-observer error dynamics and result in a sliding-mode perturbation observer, which is able to provide much better state-estimation accuracy [120]. However, the defined perturbation term is approximately estimated and its application is restricted to second-order nonlinear systems.

In this section, a sliding mode state and perturbation observer (SMSPO) is designed when only one state of the system is measurable.

Taking z_1 as the measured system output, a sliding mode observer for system (2.1.16) is designed as follows:

$$\begin{cases} \dot{\hat{z}}_1 & = & \hat{z}_2 + \alpha_1 e_1 + \beta_1 \text{sgn}(e_1) \\ & \vdots & \\ \dot{\hat{z}}_{r_i} & = & \hat{z}_{r_i+1} + \alpha_{r_i} e_1 + \beta_{r_i} \text{sgn}(e_1) + B_{0_i}u \\ \dot{\hat{z}}_{r_i+1} & = & \alpha_{r_i+1} e_1 + \beta_{r_i+1} \text{sgn}(e_1) \end{cases} \tag{2.2.8}$$

where $e_i = z_i - \hat{z}_i$ is the estimation error of the state and perturbation observer; the constants α_i are chosen as in a Luenberger observer as in (2.2.3).

From (2.1.16) and (2.2.8), the error dynamic of the observer can be obtained as:

$$\begin{cases} \dot{e}_1 &= e_2 - \alpha_1 e_1 - \beta_1 \text{sgn}(e_1) \\ &\vdots \\ \dot{e}_{r_i} &= e_{r_i+1} - \alpha_{r_i} e_1 - \beta_{r_i} \text{sgn}(e_1) \\ \dot{e}_{r_i+1} &= -\alpha_{r_i+1} e_1 - \beta_{r_i+1} \text{sgn}(e_1) + \dot{\Psi}(\cdot) \end{cases} \tag{2.2.9}$$

The sliding surface of the observer is defined as $S(e) = e_1 = 0$. Introducing the function $V = (1/2S^2)$, the sliding surface is attractive if $\dot{V} < 0$ for $e \notin S$. The condition for the existence of sliding mode is

$$\begin{cases} e_2 \leq \beta_1 + \alpha_1 e_1 & \text{if} \quad e_1 > 0 \\ e_2 \geq -\beta_1 + \alpha_1 e_1 & \text{if} \quad e_1 < 0 \end{cases} \tag{2.2.10}$$

Such a condition can be guaranteed by choosing β_1 as

$$\beta_1 \geq |e_2|_{\max} \tag{2.2.11}$$

Note that the choice of gain β_1 depends on the estimation error of e_2. Under the above condition, it is guaranteed that the system will enter into the sliding surface at $t > t_s$ and thereafter remain $S = 0$, $\forall t \geq t_s$. It follows that the switch function satisfies $S(e) = 0$, $\forall t > t_s$, which in turn implies that $\dot{S}(e) = 0$, $\forall t \geq t_s$.

Considering the designed sliding-mode observer (2.2.8), the sgn(e_1) term is a discontinuous input which enforces sliding mode to stay on sliding surface. The discontinuous input can be considered as the combination of a low-frequency control term and a high-frequency switching term. An 'equivalent control' is defined as the average value of the discontinuous control which maintains the sliding motion on sliding surface [121]. Thus, by solving the first equation of system (2.2.9), replacing $S(e)$ and $\dot{S}(\varepsilon)$ by zero, the equivalent control of the sgn(e_1) term can be obtained as follows:

$$u_{\text{eq}} = \frac{1}{\beta_1} e_2 \tag{2.2.12}$$

2.2.2 Reduced-Order Perturbation Observer

In this section, the reduced-order perturbation observer (RPO) technique is discussed. The RPO is constructed rather than ESO to enhance estimation precision and also enable easier practical implementation [122].

A reduced-order perturbation observer for estimating the disturbance $d(t)$ in system (2.1.8) is given by

$$\begin{cases} \dot{\hat{z}}_2 &= -\beta_1(\hat{z}_2+\beta_1 z_1)+\hat{z}_3+\beta_2 z_1 \\ &\vdots \\ \dot{\hat{z}}_{r_i} &= -\beta_{r_i-1}(\hat{z}_2+\beta_1 z_1)+\hat{z}_{r_i+1}+\beta_{r_i} z_1+B_{0i}u \\ \dot{\hat{z}}_{r_i+1} &= -\beta_{r_i}(\hat{z}_2+\beta_1 z_1) \\ \dot{\hat{z}}_1 &= \hat{z}_2+\beta_1 z_1,\ \ \hat{f}=\hat{z}_{r_i+1}+\beta_{r_i} z_1 \end{cases} \tag{2.2.13}$$

where $\beta_i(i=1,2,\cdots,r_i)$ is the observer gains, $\hat{z}_i(i=2,3,\cdots,r_i+1)$ are state variables of observer, $\dot{\hat{z}}_1$ and $\hat{f}$ are estimations of $\dot{z}_1$ and f, respectively.

2.2.3 Finite-time Disturbance Observer

In this section, the finite-time disturbance observer technique is discussed. This observer employs the high-order sliding mode differentiator techniques. The estimation error of observer will converge to zero in finite time, which shows a much faster convergence rate than other types of disturbance observers.

A finite-time disturbance observer for estimating disturbance $d(t)$ in system (2.1.8) has been proposed in [123], given by

$$\begin{cases} e_1 &= z_1-\hat{z}_1,\quad e_2=\dot{z}_1-\hat{z}_2,\quad \cdots \quad e_{r_i+1}=z_1^{[r_i+1]}-\hat{z}_{r_i+1}-B_{0i}u \\ \dot{\hat{z}}_1 &= \hat{z}_2+\lambda_0^{1/r_i+1}|e_1|^{r_i/r_i+1}\text{sgn}(e_1) \\ \dot{\hat{z}}_2 &= \hat{z}_3+\lambda_0^{2/r_i+1}|e_2|^{r_i-1/r_i}\text{sgn}(e_2) \\ &\vdots \\ \dot{\hat{z}}_{r_i-1} &= \hat{z}_{r_i}+\lambda_0^{r_i-1/r_i+1}|e_{r_i-1}|^{2/3}\text{sgn}(e_{r_i-1}) \\ \dot{\hat{z}}_{r_i} &= \hat{z}_{r_i+1}+\lambda_0^{r_i/r_i+1}|e_{r_i-1}|^{1/2}\text{sgn}(e_{r_i})+B_{0i}u \\ \dot{\hat{z}}_{r_i+1} &= \lambda_0\text{sgn}(e_{r_i}) \end{cases} \tag{2.2.14}$$

where $\lambda_0 > 0$ is the observer coefficients to be designed, $\hat{z}$, $\dot{\hat{z}}$, ..., $\hat{z}^{[r-1]}$ are the estimates of z, $\dot{z}$, ..., $z^{[r-1]}$, respectively.

The dynamics of observer estimation error are obtained, which are governed by

$$\begin{cases} \dot{e}_1 &= e_2 + \lambda_0^{1/r_i+1}|e_1|^{r_i/r_i+1}\text{sgn}(e_1) \\ \dot{e}_2 &= e_3 + \lambda_0^{2/r_i+1}|e_2|^{r_i-1/r_i}\text{sgn}(e_2) \\ &\vdots \\ \dot{e}_{r_i} &= e_{r_i+1} + \lambda_0^{r_i/r_i+1}|e_{r_i}|^{1/2}\text{sgn}(e_{r_i}) \\ \dot{e}_{r_i+1} &= \lambda_0\text{sgn}(e_{r_i+1}) \end{cases} \tag{2.2.15}$$

It follows that observer error system (2.2.15) is finite-time stable, that is, there exists a time constant $t_f > t_0$ such that $e_i(t) = 0$ ($i = 0, 1, \ldots, l$) (or equivalently $\hat{x}(t) = x(t)$ for $t \geq t_f$) [78].

2.3 Nonlinear Adaptive Control

Using the estimated perturbation $\hat{z}_{r_i+1} = \Psi_i$ from any observer as in (2.2.1), (2.2.6), and (2.2.8) to compensate the real system perturbation, the original nonlinear system can be linearized to a simple linear system. Then the control input, v_i, for the linearized system is designed using the linear control method

$$\begin{bmatrix} v_1 \\ \vdots \\ v_{\text{m}} \end{bmatrix} = \begin{bmatrix} k_{11}(z_{11}^* - \hat{z}_1) & \cdots & k_{1\text{r}}(z_1^{[\text{r}-1]^*} - \hat{z}_{1\text{r}_1}) \\ \vdots & \vdots & \vdots \\ k_{\text{m}1}(z_{\text{m}}^* - \hat{z}_{\text{m}1}) & \cdots & k_{\text{mr}}(z_m^{[\text{r}-1]^*} - \hat{z}_{\text{mr}}) \end{bmatrix} \tag{2.3.1}$$

where $[k_{i1}, \cdots, k_{i(r_i)}]$ are the linear feedback control gains, $z_{i1}^{[\text{r}-1]^*}$ are the references of the $n-1^{\text{th}}$ derivative of states z_i.

The final control law of the NAC can be obtained as

$$u = B_0^{-1}\left\{ \begin{bmatrix} -\hat{\Psi}_1 \\ \vdots \\ -\hat{\Psi}_{\text{m}} \end{bmatrix} + \begin{bmatrix} v_1 \\ \vdots \\ v_{\text{m}} \end{bmatrix} \right\} \tag{2.3.2}$$

where u is the real system control input, while the v_i are the control input of the linearized subsystems.

The control scheme of NAC is shown in Figure 2.2.

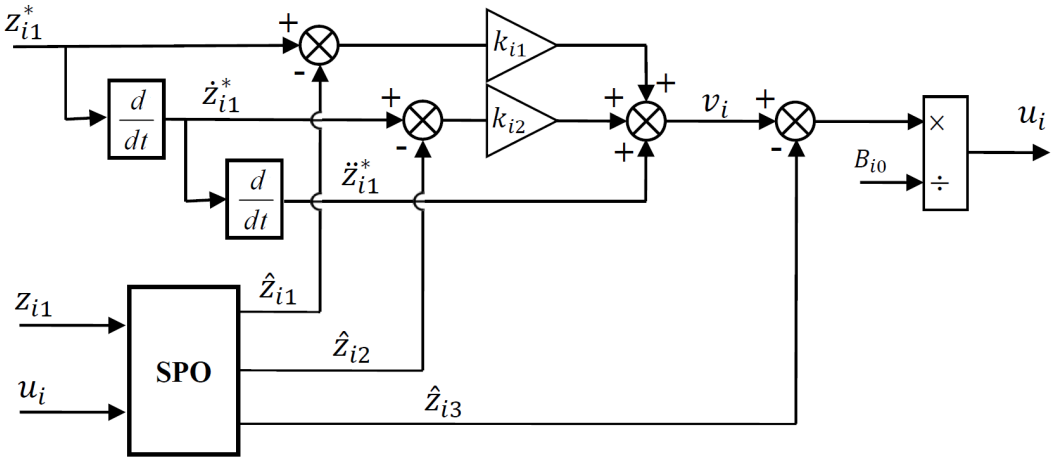

Figure 2.2: Block diagram of the nonlinear adaptive control method with linear high-gain observer.

2.4 Comparison among Different Perturbation Observer based Control Methods

As an example of a nonlinear second-order system

$$\begin{cases} \dot{x}_1(t) &= x_2(t) \\ \dot{x}_2(t) &= -(2+\sin(x_1))x_1^3 - 5(3+\cos(\pi x_1))\sin(x_2) + \\ & \quad (0.5\sin(x_1)+1)u(t) + d(t) \end{cases} \tag{2.4.1}$$

For system (2.4.1), the perturbation is defined as

$$\begin{aligned} \Psi(x,u,t) &= f(x) + d(t) + (b(x) - B_0)u \\ &= -(2+\sin(x_1))x_1^3 + d - 5(3+\cos(\pi x_1))\sin(x_2) + \\ &\quad (-1+0.5\sin(x_1))u \\ &\leq 3|x_1|^3 + 1.5|u| + |d| \end{aligned} \tag{2.4.2}$$

where $B_0 = 2$.

Assume z is the estimation of x. The perturbation observer of system 2.4.1 can be designed using the estimation methods above. The comparison among the high-gain SPO based NAC, nonlinear SPO based ADRC, sliding-mode SPO based NAC, and finite-time control are given below.

A) High-gain SPO

A linear high-gain (HG) observer can be designed based on (2.2.1) for system (2.4.1), and it is shown as

$$\begin{cases} e_1 &= x_1 - z_1 \\ \dot{z}_1 &= z_2 + 3 \times 10^2 \cdot e_1 \\ \dot{z}_2 &= z_3 + 2u + 3 \times 10^4 \cdot e_1 \\ \dot{z}_3 &= 1 \times 10^6 \cdot e_1 \end{cases} \tag{2.4.3}$$

B) Nonlinear SPO

A nonlinear observer in ADRC can be designed based on (2.2.6) for system (2.4.1), and it is shown as

$$\begin{cases} e_1 &= x_1 - z_1 \\ \dot{z}_1 &= z_2 + 2.5 \times 10^2 \cdot e_1 \\ \dot{z}_2 &= z_3 + 2u + 4 \times 10^3 \cdot fal(e_1, 0.5, 0.001) \\ \dot{z}_3 &= 2.6 \times 10^4 \cdot fal(e_1, 0.25, 0.001) \end{cases} \tag{2.4.4}$$

C) Sliding-mode SPO

A sliding-mode (SM) observer can be designed based on (2.2.8) for system (2.4.1), and it is shown as

$$\begin{cases} e_1 &= x_1 - z_1 \\ \dot{z}_1 &= z_2 + 3 \times 10^2 \cdot e_1 + 2 \times 10^{-3} \cdot \text{sgn}(e_1) \\ \dot{z}_2 &= z_3 + 2u + 3 \times 10^4 \cdot e_1 + 0.3 \cdot \text{sgn}(e_1) \\ \dot{z}_3 &= 1 \times 10^6 \cdot e_1 + 20 \cdot \text{sgn}(e_1) \end{cases} \tag{2.4.5}$$

D) Reduced-order SPO

A reduced-order perturbation observer (RPO) can be designed based on (2.2.13) for system (2.4.1), and it is shown as

$$\begin{cases} \dot{\hat{z}}_2 &= -2 \times 10^2 \cdot (\hat{z}_2 + 2 \times 10^2 \cdot z_1) + \hat{z}_3 + 1 \times 10^4 \cdot z_1 + 2u \\ \dot{\hat{z}}_3 &= -1 \times 10^4 \cdot (\hat{z}_2 + 2 \times 10^2 \cdot z_1) \end{cases} \tag{2.4.6}$$

E) Finite-time SPO

A finite-time observer can be designed based on (2.2.14) for system (2.4.1), and

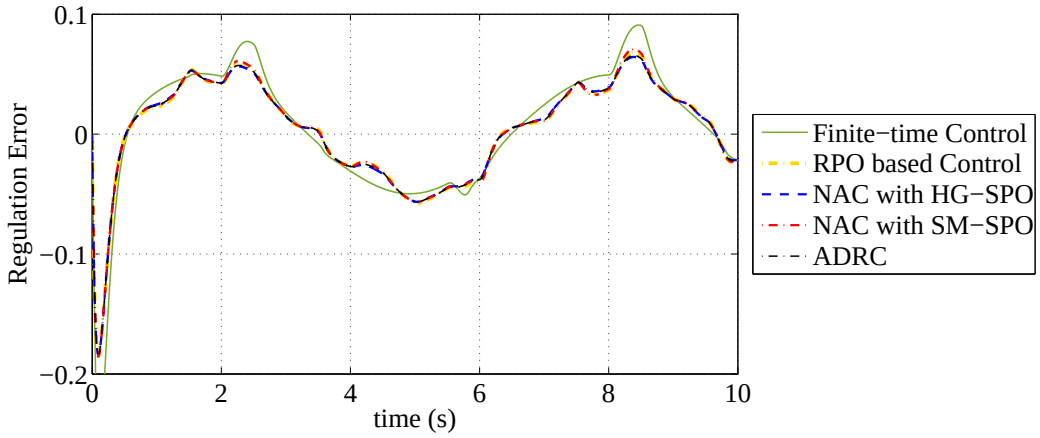

Figure 2.3: Regulation error of system output controlled by different controllers.

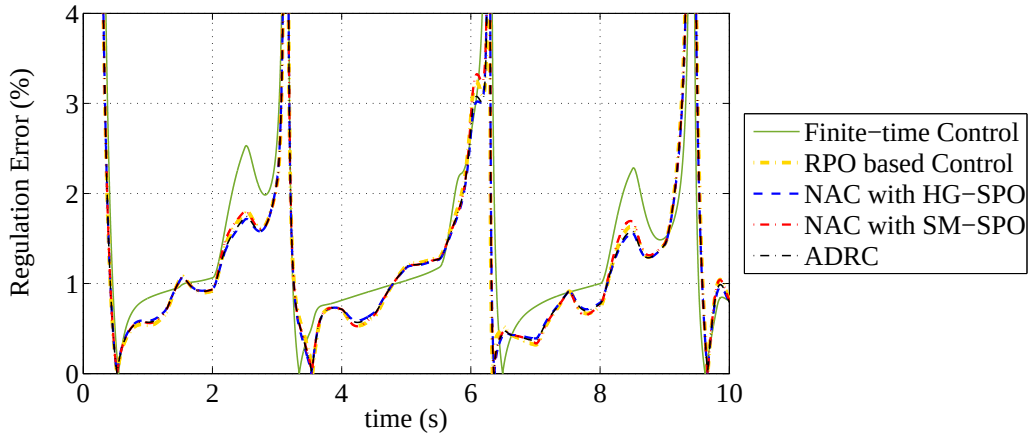

Figure 2.4: Regulation error in % of system output controlled by different controllers.

it is shown as

$$\begin{cases} e_1 &= x_1 - z_1, \quad e_2 = \dot{x}_1 - z_2, \quad e_3 = \ddot{x}_1 - z_3 - 2u \\ \dot{z}_1 &= z_2 + 30^{1/3} \cdot |e_1|^{2/3} \cdot \text{sgn}(e_1) \\ \dot{z}_2 &= z_3 + 30^{2/3} \cdot |e_1|^{1/2} \cdot \text{sgn}(e_2) + 2u \\ \dot{z}_3 &= 30 \cdot \text{sgn}(e_3) \end{cases} \tag{2.4.7}$$

The different SPOs are used for comparison to estimate the perturbation of system (2.4.1) under disturbance. The regulation errors of system outputs and absolute percentage error are compared in Figure 2.3 and 2.4. The estimation error and absolute percentage estimation error of different SPOs under constant disturbance are compare in Figure 2.5 and 2.6. The results show that the control performance of

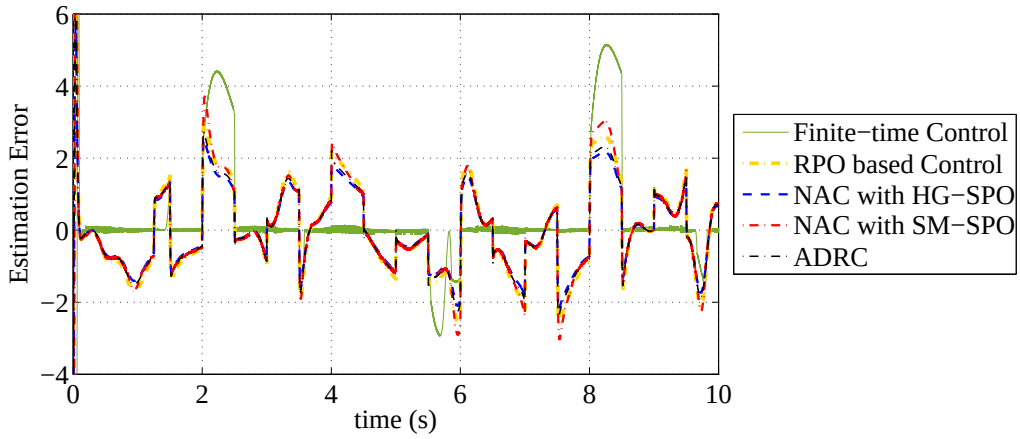

Figure 2.5: Perturbation estimation error of different observers.

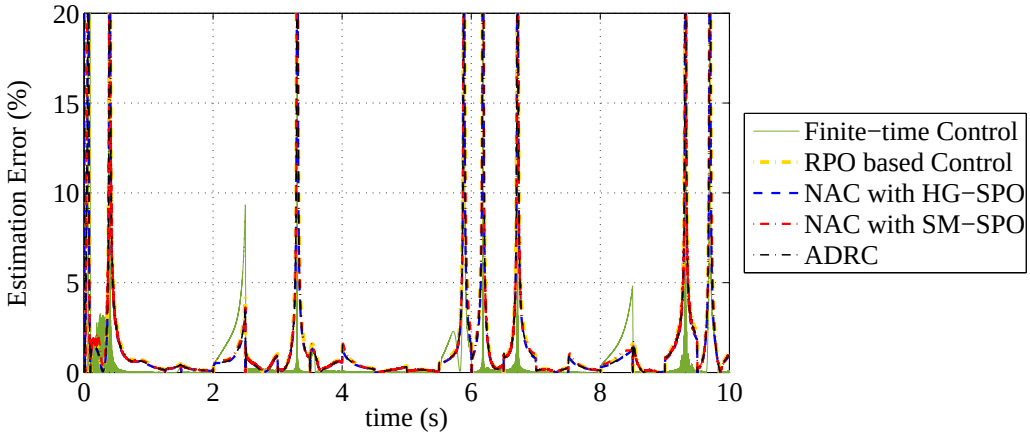

Figure 2.6: Perturbation estimation error in % of different observers.

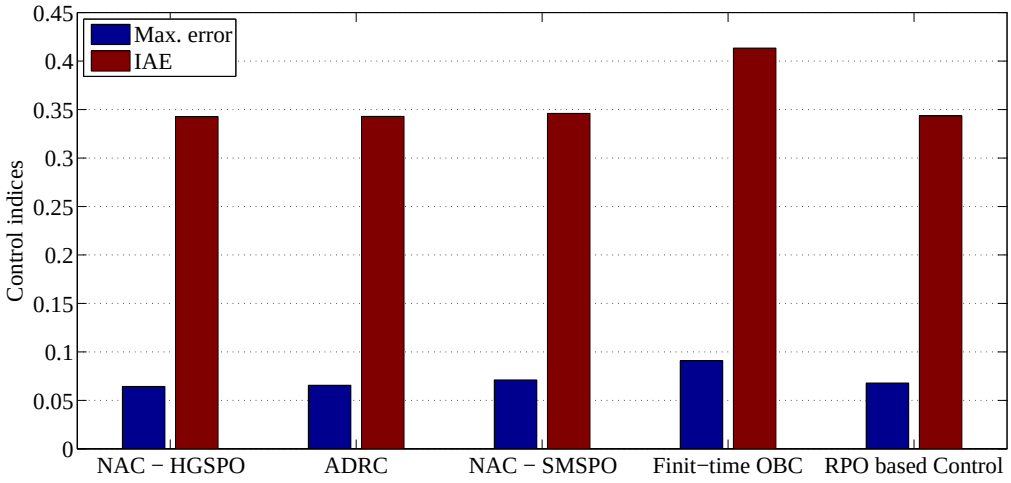

Figure 2.7: Control performance indices comparison in maximum error and IAE.

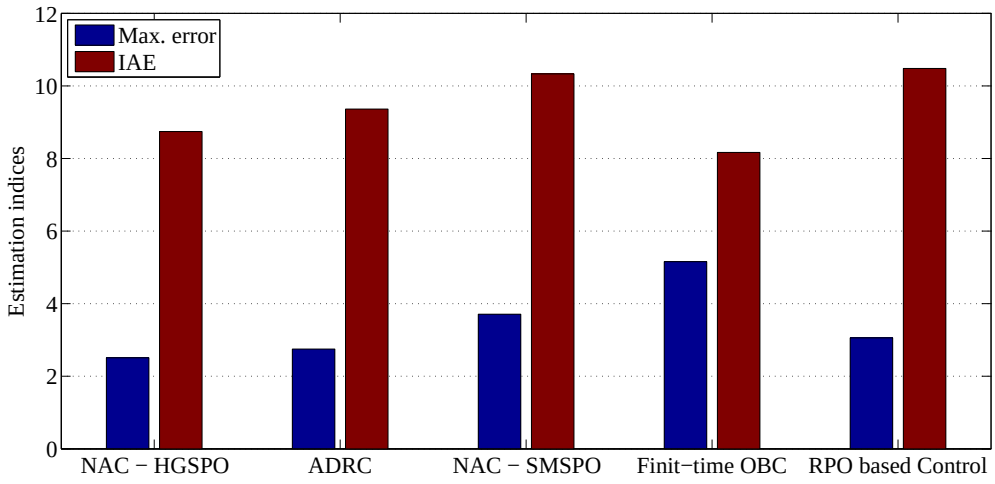

Figure 2.8: Perturbation estimation comparison in maximum error and IAE.

Table 2.1: Performance indices of different disturbance observer based controls

Indices \ Method	NAC with HG-SPO	ADRC	NAC with SM-SPO	Finite-time Control	RPO based Control
Control performance					
Maximum error	0.0644	0.0656	0.0711	0.0909	0.0679
IAE	0.343	0.343	0.346	0.413	0.344
Perturbation estimation performance					
Maximum error	2.509	2.749	3.71	5.156	3.059
IAE	8.741	9.363	10.33	8.167	10.48

different disturbance observer based control methods are similar in the maximum regulation error and IAE (integrated of absolute error). All the controller regulation error is less than 2%, and the perturbation estimation error is less than 10%.

To further compare the control and perturbation estimation performance in indices, Table 2.1 shows the maximum error and IAE in numerical, and Figure 2.7 and 2.8 shows the bar chart to compare the indices. From the comparison results, the control and estimation performance of different disturbance observer based control methods have not huge difference. As the SH-SPO is simple in structure and easy in the gain turning for stability analysis, it has the potential to be popularized in industrial application and thus used in this thesis.

2.5 Conclusion

Among the four SPOs, the performance of different SPOs has the similar performance. The HG-SPO is simple in structure. However, its observer gain is very high and its performance is easy to be disturbed by noise. The ADRC uses the nonlinear extended-order observer, which is complex in design. Other extended-order observers also can be used in this control method. The reduced-order observer require less calculation, but they are complex in design and gain turning. The HG-SPO is simple in structure and easy in the gain turning process but gets the similar performance comparing with other types of disturbance observers. Considering the simplification in observer design and stability analysis, the high-gain observer is used in the following chapters.

Chapter 3

Nonlinear PI Control for Variable Pitch Wind Turbine

3.1 Introduction

Wind power is one of the most promising renewable energy sources and has received tremendous progress in the past decades. Most wind power generation system uses variable speed wind turbine with variable pitch to achieve an efficient and reliable conversion of wind power to electrical power.

Efficient and reliable operation of a WPGS heavily relies on the control systems applied on the WT operating at different regions. At the high speed region, pitch angle control is applied to limit the wind power captured by the wind turbine. Numerous control methods have been applied to design pitch angle controllers, such as PI-type controller [3, 52]. The wind turbine is a highly non-linear system due to its nonlinear aerodynamics [57, 58]. As the wind turbine contains strong aerodynamic nonlinearities and operates under time-varying wind power disturbance, the linear PI with fixed gains cannot provide consistently satisfactory performance in the whole wind speed region. Advanced control methods have been applied to tackle this problem, such as the gain scheduling PI (GSPI) [3, 52], digital robust control [96], neural-network-based control [97], model predictive control [98], and feedback linearization control [58, 61]. However, some control methods, such as the feedback

linearization control, are designed based on the accurate wind turbine model, which is difficult to be obtained accurately in practical.

Extended-order state and perturbation (or disturbance) observer (ESPO) has been proposed to estimate system state and perturbation term, which can be represented as nonlinearities and disturbances of nonlinear system. By defining perturbation as a lumped term to include all unknown nonlinearities, parameter uncertainties and external disturbance [124], ESPO can be implemented using nonlinear observer [74, 86, 87], linear observers [113, 125], sliding mode observers [126], fuzzy observers [80], and neural-network-based observers [81]. ESPO-based controller use the estimation of perturbation to compensate its real perturbation and achieve the adaptive feedback linearizing control, without requiring a detailed and accurate system model in conventional feedback linearization (FL) control [58, 61]. They have been applied in robotic systems [127], power systems [88, 113], PMSM systems [124], induction motor [94], doubly-fed induction generator wind turbine [84].

This chapter designs a Nonlinear PI (N-PI) controller for wind turbine pitch angle control. It consists of an ESPO and a classic PI controller. The ESPO is used to estimate the unknown time-varying nonlinearities and disturbance, which are defined in a lumped perturbation term. The N-PI uses the estimated perturbation to compensate the real one for linearizing the nonlinear system. The procedure is similar to the feedback linearization (FL) method, which requires a detailed and accurate system model to calculate the nonlinearities [58, 61]. The N-PI is proposed to provide wide range and consistent optimal performance across the whole operation range only based on one set of PI gains tuned around the mean wind speed, and avoid the rapid switching of gains of the GSPI type controllers. Two types of gain scheduled PI controllers, wind speed switching and pitch-angle switching ones are compared using simulation tests based on a simplified two mass model and a detailed aero-elastic wind turbine simulator, FAST [128].

The remainder of this chapter is organized as follows. Section 3.2 presents a simplified two-mass model of wind turbine. Section 3.3 recalls a conventional PI and GSPI for comparison, respectively. The extended-order state and perturbation observer based Nonlinear PI (N-PI) controller is designed in Section 3.4. Simula-

tion test results are given in Section 3.5 based on the simplified model and a more detailed FAST model. This chapter is finally concluded in Section 3.6.

3.2 Nonlinear Wind Turbine Modeling

The configuration of a simplified two-mass model of wind turbine and its nonlinear power coefficient C_p is shown in Figure 3.1. The model is presented in a generalized nonlinear form as follows [129]:

$$\dot{\mathbf{x}} = \mathbf{F}(\mathbf{x}) + \mathbf{B}u = \begin{bmatrix} f_1 \\ f_2 \\ f_3 \\ f_4 \end{bmatrix} + \begin{bmatrix} 0 \\ 0 \\ 0 \\ g_4 \end{bmatrix} u \tag{3.2.1}$$

The state vector $\mathbf{x}$, control input u and nonlinear vector $\mathbf{F}(\mathbf{x})$ are defined as:

$$\begin{aligned} \mathbf{x} &= [\omega_r \quad \omega_g \quad \delta \quad \beta]^T \\ u &= \beta_r \end{aligned} \tag{3.2.2}$$

$$\mathbf{F}(\mathbf{x}) = \begin{bmatrix} f_1 \\ f_2 \\ f_3 \\ f_4 \end{bmatrix} = \begin{bmatrix} \frac{P_r(x_1,x_4,V)}{x_1 J_r} - \frac{x_1 D_s}{J_r} + \frac{x_2 D_s}{N_g J_r} - \frac{x_3 K_s}{J_r} \\ \frac{x_1 D_s}{N_g J_g} - \frac{x_2 D_s}{N_g^2 J_g} + \frac{x_3 K_s}{N_g J_g} - \frac{T_g}{J_g} \\ x_1 - \frac{x_2}{N_g} \\ -\frac{1}{\tau_\beta} x_4 \end{bmatrix} \tag{3.2.3}$$

$$\mathbf{B} = \begin{bmatrix} 0 & 0 & 0 & g_4 \end{bmatrix}^T$$

$$g_4 = \frac{1}{\tau_\beta}$$

where ω_r is rotor speed, ω_g is generator speed, δ is twist angle, and β is pitch angle; x_1 to x_4 are the state variables of vector $\mathbf{x}$, τ_β is time constants of pitch actuator, and β_r is the pitch angle control. T_g is generator torque, J_r and J_g are rotor and generator inertia, N_g is gear ratio, D_s and K_s are drive-train damping and spring constant, respectively.

The mechanical power P_r captured by the wind turbine is:

$$P_r = \frac{1}{2}\pi\rho R^2 V^3 C_p(x_1, x_4, V) \tag{3.2.4}$$

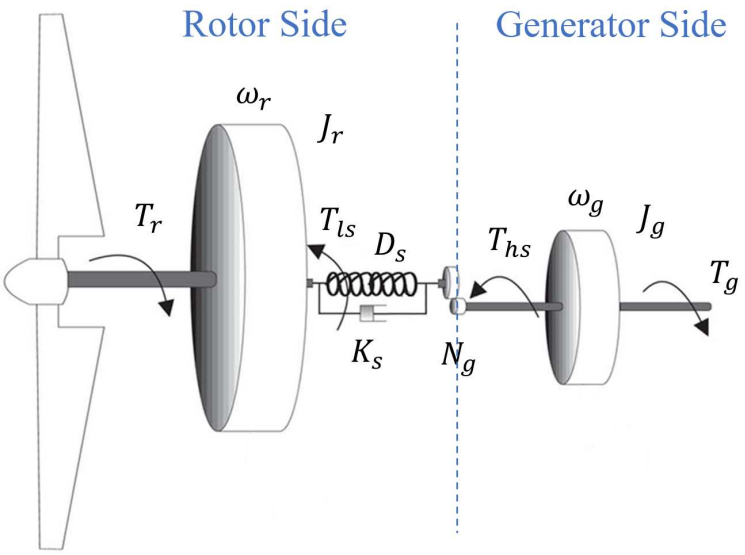

(a)

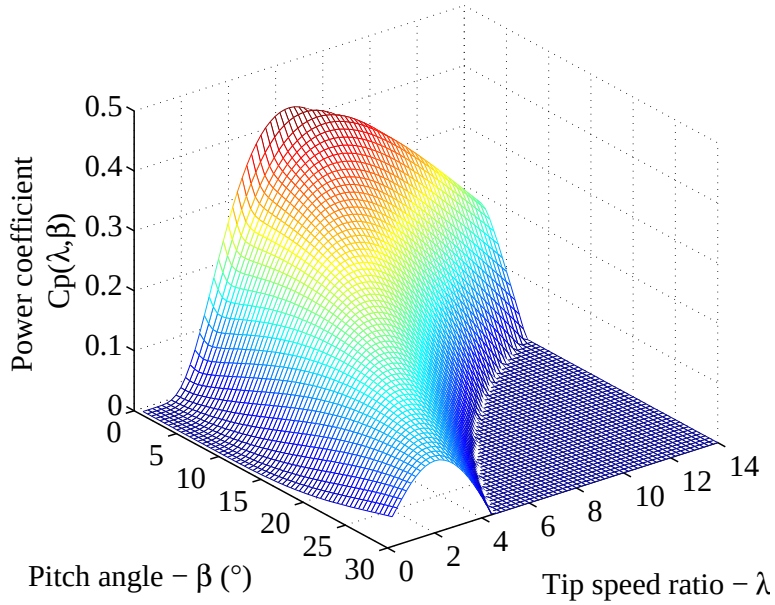

(b)

Figure 3.1: Two-mass variable speed wind turbine model and nonlinear power coefficient Cp.

where R is the rotor radius, ρ is the air density, V is the wind speed. C_p is the power conversion coefficient of wind turbine and is a nonlinear function of β and λ. This chapter uses Controls Advanced Research Turbine (CART) located at National Renewable Energy Laboratory USA and its function is given as [57]:

$$C_p = 0.22(116\lambda_t - 0.4x_4 - 5)e^{-12.5\lambda_t} \tag{3.2.5}$$

where

$$\lambda_t = \frac{1}{\lambda + 0.08\beta} - \frac{0.035}{\beta^3 + 1}$$
$$\lambda = \frac{\omega_r R}{V}$$

where λ is tip-speed ratio and λ_t is an intermediate variable.

Control objective of this chapter is to design a nonlinear pitch angle control for wind turbine operating at Region III, to maintain the rotor rotation speed ω_r, or the system output power P_e, at its rated value by limiting the power captured by the wind turbine.

3.3 Conventional PI and Gain-scheduled PI Controller

3.3.1 PI Controller

The conventional PI(D) based pitch angle controller is used to regulate the rotor speed or the output power of wind turbine [52]. To get the optimal control gain under the rated operating point, particle swarm optimization (PSO) method is used [130, 131]. The integral time absolute error (ITAE) of rotor speed is used as the optimization objective and defined as

$$ITAE = \int_0^\infty t|e(t)|dt \tag{3.3.1}$$

The PSO method is implemented following the reference [130, 131]. The the velocity for searching a new best position of each swarm in PSO is given as:

$$\begin{aligned} v = \quad & w \cdot v + c_1 \cdot \text{rand}(2, N) \times (P_{\text{l,best}} - P_{\text{current}}) \\ & + c_2 \cdot \text{rand}(2, N) \times (P_{\text{g,best}} - P_{\text{current}}) \end{aligned} \tag{3.3.2}$$

where N is the number of units, w is the momentum or inertia of PSO, $P_{\mathrm{l,best}}$ is the local best position, $P_{\mathrm{g,best}}$ is the global best position, and P_{current} is the current position; rand$(2, N)$ is to generate a $2 \times N$ matrix with random values, c_1 and c_2 are the coefficient for random values. The special parameters of PSO used in this chapter are given as N = 50, w = 0.9, c_1 = 0.12 and c_2 = 1.2.

Control gains of the PI controller is optimized at the nominal operation point under mean wind speed, where V_0 = 18 m/s, ω_{r0} = 2.1428 rad/s, and $\beta_0 = 25^\circ$. The optimized gains of the PI pitch controller are k_p = 140 and k_i = 52, respectively.

3.3.2 Gain Scheduled PI Controller

Due to the high aerodynamic nonlinearities of wind turbine and time-varying wind speed, the PI controller using one set of gains optimized based on one operation point cannot provide consistent optimal performance when operation points shifts from that normal point. To tackle this problem, gain scheduled PI pitch control has been proposed [3].

Wind-speed Based Switching

A GSPI controller requires the wind speed measuremeasent to schedule the controller gains [129]. An anemometer can be used but it can only measure the wind speed at a special point, which is not accurate for representing the effective wind speed in large wind turbines. To achieve a more accurate estimation of the effective wind speed, the wind turbine itself can be used as a sensor and the estimation can be solved by Newton-Raphson method [58].

The wind speed estimator is realized by minimizing the cost function $J(t, V)$

$$J(t, V) = \left(P_r(t) - f_r(V)\right)^2 \tag{3.3.3}$$

$$f_r(V) = \frac{1}{2}\pi\rho R^2 V^3 C_p(\beta, \lambda) \tag{3.3.4}$$

where $P_r(t)$ is a measurement of rotor power at time t, which is assumed known; $f_r(V)$ is the aerodynamic power function of wind speed V.

The problem is equivalent to find the solution of

$$I(t,V) = P_r(t) - \frac{1}{2}\pi\rho R^2 V^3 C_p(\beta,\lambda) = 0 \tag{3.3.5}$$

From the partial derivative equation

$$\Delta P_r = \frac{\partial P_r}{\partial V}\Delta V \tag{3.3.6}$$

the iteration form of the estimator can be written as:

$$\hat{\dot{V}} = \Delta P_r \left(\frac{\partial P_r}{\partial V}\right)^{-1} \tag{3.3.7}$$

where

$$\frac{\partial P_r}{\partial V} = -\frac{3}{2}\pi\rho R^2 V^2 C_p(\beta,\lambda) - \frac{1}{2}\pi\rho R^2 V^3 \frac{\partial C_p}{\partial V}$$
$$\frac{\partial C_p}{\partial V} = -\frac{0.22}{\omega_r R}\frac{178.5 - 1450\lambda_t + 5x_4}{(\lambda + 0.08x_4)^2} e^{-12.5\lambda_t}$$

At time t, using the measured rotor power $P_r(t)$, the iteration will be performed until

$$I(t,\hat{V}_t) = P_r(t) - f_r(\hat{V}_t) < \varepsilon \tag{3.3.8}$$

where ε is a small value. The estimation of wind speed at time t is then $\hat{V}_t$.

Since the rotor power P_r is unmeasurable in practice, the assumption is made that the rotor power is equal to electrical power P_e, which is measurable, divided by the wind turbine power conversion efficiency η. Then the estimated wind speed can be used in the GSPI controller to switching the scheduled gains by look-up-table for the pitch controller.

Pitch-angle Based Switching

As wind speed based switching requires a complex estimation of real-time wind speed and also may result in fast switching between gains due to the fast change of wind speed, an improved GSPI based on pitch angle switching has been proposed in [132–134]. The control block diagram of the PI and GSPI controller is shown in Figure 3.2(a), where the K_β is set to be 1 in the PI controller. Under different wind speeds, optimal gains are obtained using the PSO method with the performance

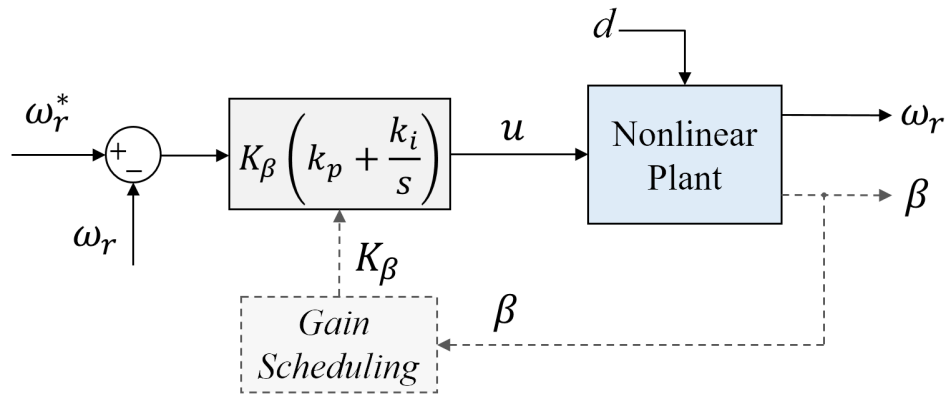

(a)

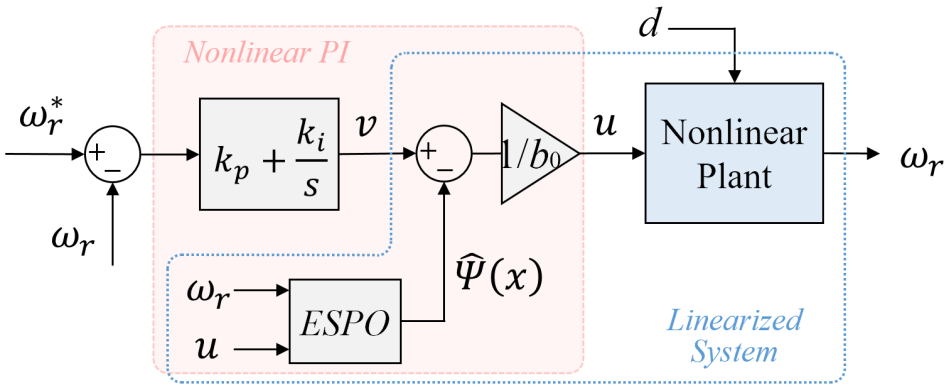

(b)

Figure 3.2: Block diagram of (a) conventional PI or GSPI controller, (b) proposed Nonlinear PI (N-PI) controller.

Table 3.1: Optimal Gains under Corresponding Wind Speed and Pitch Angle using PSO Optimization Method

V (m/s)	$\beta_{rated}(^\circ)$	$k_{\mathrm{p,opt}}(^\circ\cdot\mathrm{s/rad})$	$k_{i,opt}(^\circ\cdot\mathrm{s}^2/\mathrm{rad})$
12	3.6	186	70
14	14.1	178	66
16	20.6	160	60
18	25.1	140	52
20	28.6	124	46

index of ITAE. The optimal gains of k_p and k_i under different wind speed and the correspondent pitch angle are given in Table 3.1.

To obtain a continuous pitch angle based switching, the scheduled gain pairs are obtained as the product of a constant PI gain pair multiplied by a scheduled gain $K(\beta)$ which is a function of pitch angle [133]. The scheduled gain $K(\beta)$ is proposed to compensate the variation of the aerodynamic sensitivity, $\partial P_r/\partial\beta$, and is obtained using the trend line of the optimal gains versus pitch angle is given as [133]

$$u = K(\beta)\left(k_p + \frac{k_i}{s}\right)(x_1 - \omega_r^*) \tag{3.3.9}$$

where

$$K(\beta) = \begin{cases} 1.6, & \text{for} \quad -1^\circ < \beta \leq 0^\circ \\ -0.001\beta^2 + 0.01\beta + 1.6, & \text{for} \quad 0^\circ < \beta \leq 30^\circ \\ 1, & \text{for} \quad \beta > 30^\circ \end{cases} \tag{3.3.10}$$

and the constant proportional and integral gains, $k_p = 116$, and $k_i = 42$.

3.4 Nonlinear PI based Pitch Angle Controller

3.4.1 Input-output Linearization

The input-output relationship between the system output, the rotor speed as $y = x_1$, and the system input, the pitch angle control as $u = \beta_r$, can be obtained using differentiating the output till the control input appears. From system (3.2.1)-(3.2.3),

the rotor speed dynamic is given as:

$$\dot{x}_1 = \frac{P_r(x_1, x_4, V)}{x_1 J_r} - \frac{x_1 D_s}{J_r} + \frac{x_2 D_s}{N_g J_r} - \frac{x_3 K_s}{J_r} \tag{3.4.1}$$

Its second-order derivative can be obtained as

$$\frac{d^2 x_1}{dt^2} = L_f(x) + L_g(x)u \tag{3.4.2}$$

where

$$L_f(x) = \sum_{i=1}^{4} \left(\frac{\partial f_1}{\partial x_i} \cdot f_i \right) + \frac{\partial f_1}{\partial V} \cdot \dot{V}$$

$$\frac{\partial f_1}{\partial x_1} = -\frac{1}{J_r x_1} \left[\frac{P_r}{x_1} + 0.11\pi\rho R^3 V^2 \frac{178.5 - 1450\lambda_t + 5x_4}{(\lambda + 0.08x_4)^2} e^{-12.5\lambda_t} \right] - \frac{D_s}{J_r}$$

$$\frac{\partial f_1}{\partial x_2} = \frac{D_s}{N_g J_r}$$

$$\frac{\partial f_1}{\partial x_3} = -\frac{K_s}{J_r}$$

$$\frac{\partial f_1}{\partial x_4} =$$

$$\frac{0.11\pi\rho R^2 V^3}{x_1 J_r} \left\{ (178.5 - 1450\lambda_t + 5x_4) \left[\frac{-0.08}{(\lambda + 0.08x_4)^2} + \frac{0.105x_4^2}{(x_4^3 + 1)^2} \right] - 0.4 \right\} e^{-12.5\lambda_t}$$

$$\frac{\partial f_1}{\partial V} = \frac{0.11\pi\rho R^3 V}{J_r(\lambda + 0.08x_4)^2}(178.5 - 1450\lambda_t + 5x_4)e^{-12.5\lambda_t}$$

$$L_g(x) = \frac{\partial f_1}{\partial x_4} g_4$$

$$= \frac{0.11\pi\rho R^2 V^3}{x_1 J_r \tau_\beta} \left\{ (178.5 - 1450\lambda_t + 5x_4) \left[\frac{-0.08}{(\lambda + 0.08x_4)^2} + \frac{0.105x_4^2}{(x_4^3 + 1)^2} \right] - 0.4 \right\} e^{-12.5\lambda_t}$$

where $\dot{V}$ is the derivative of wind speed.

When nonlinearities $L_f(x)$ and system input gain $L_g(x)$, and wind speed dynamic $\dot{V}$ are known, a feedback linearized control (FLC) can be obtained as

$$u = \frac{1}{L_g(x)} \left(v - L_f(x) \right) \tag{3.4.3}$$

where $L_g(x) \neq 0$ for all operation points and v is the control of the linearized second-order system

$$\frac{d^2 x_1}{dt^2} = v \tag{3.4.4}$$

and is designed as PI-type controller in this chapter, for the convenience of comparison with PI-type controller and GSPI controller.

3.4.2 Perturbation Definition and Extended-order State Space Model

Assume all nonlinearities represented as $L_f(x)$ and $L_g(x)$ in system (3.4.2) are unknown, define a perturbation term $\Psi(x)$ to include all system nonlinearities, time-varying dynamics, and external disturbance as:

$$\Psi(x) = L_f(x) + (L_g(x) - b_0)\, u \tag{3.4.5}$$

where $b_0 = L_g(x_0)$ is the nominal constant gain of system input which can be chosen as the mean value of $L_g(x)$. Then system (3.4.2) becomes

$$\frac{d^2 x_1}{dt^2} = \Psi(x) + b_0 u \tag{3.4.6}$$

3.4.3 Extended-order States and Perturbation Observer

Define $z_1 = x_1$, $z_2 = \dot{x}_1$ and an additional state variable $z_3 = \Psi(x, z)$, an extended-order model is obtained as:

$$\begin{cases} \dot{z}_1 = z_2 \\ \dot{z}_2 = z_3 + b_0 u \\ \dot{z}_3 = \dot{\Psi}(x, t) \end{cases} \tag{3.4.7}$$

Define $\tilde{z}_1 = z_1 - \hat{z}_1$, a linear ESPO is designed as:

$$\begin{cases} \dot{\hat{z}}_1 = \hat{z}_2 + k_{01}\tilde{z}_1 \\ \dot{\hat{z}}_2 = \hat{z}_3 + b_0 u + k_{02}\tilde{z}_1 \\ \dot{\hat{z}}_3 = k_{03}\tilde{z}_1 \end{cases} \tag{3.4.8}$$

where $\hat{z}_i$, $i = 1, 2, 3$, is the estimate of z_i; and $\tilde{z}_1$ is the estimation error of z_1. k_{0i} are observer gains that can be parameterized as [94]:

$$[k_{01} \quad k_{02} \quad k_{03}] = \begin{bmatrix} 3\alpha_0 & 3\alpha_0^2 & \alpha_0^3 \end{bmatrix} \tag{3.4.9}$$

where α_0 is the observer bandwidth and the only parameter to be tuned.

Similarly, to improve the estimation performance, a nonlinear ESPO (NESPO) can also be designed based on [74] as follows:

$$\begin{cases} \dot{\hat{z}}_1 = \hat{z}_2 + k_{01}\tilde{z}_1 \\ \dot{\hat{z}}_2 = \hat{z}_3 + b_0 u + k_{02} fal(\tilde{z}_1, 0.5, h) \\ \dot{\hat{z}}_3 = k_{03} fal(\tilde{z}_1, 0.25, h) \end{cases} \tag{3.4.10}$$

$$fal(\chi, \sigma, h) = \begin{cases} \frac{\sigma^2}{h^{(1-\sigma)}}\chi & |\chi| \leq h \\ \text{sgn}(\chi) \cdot \sigma^2 |\chi|^\sigma & |\chi| > h \end{cases} \tag{3.4.11}$$

where χ is the input error of the nonlinear function, σ is the precision index from 0 to 1, h is the width of linear area of the nonlinear function.

Comparing with the linear ESPO, the NESPO can accelerate the estimation speed, with the cost of a complex nonlinear observer, which increases the difficulties of stability analysis of the closed-loop system. Note that other types of ESPO, such as sliding mode observer, can also been applied, though they all provide similar performance [113].

3.4.4 N-PI based Pitch Angle Controller

By using real-time estimate of perturbation $\hat{\Psi}(x)$ from the third-order ESPO to compensate the real perturbation, the control input u can be obtained as

$$u = \frac{1}{b_0}\left(v - \hat{\Psi}(x)\right) \tag{3.4.12}$$

where v is the control of the linearized second-order system and is designed as a classic PI controller with error between rotor speed reference ω_r^* and the system output x_1:

$$v = \left(k_p + \frac{k_i}{s}\right)(\omega_r^* - x_1) \tag{3.4.13}$$

Finally, the N-PI pitch angle control can be expressed as

$$u = \frac{1}{b_0}\left(k_p + \frac{k_i}{s}\right)(\omega_r^* - x_1) - \frac{1}{b_0}\hat{\Psi}(x) \tag{3.4.14}$$

The N-PI control diagram is given in Figure 3.2(b), and the block diagram of N-PI based pitch angle controller for WT is given in Figure 3.3. Note the N-PI

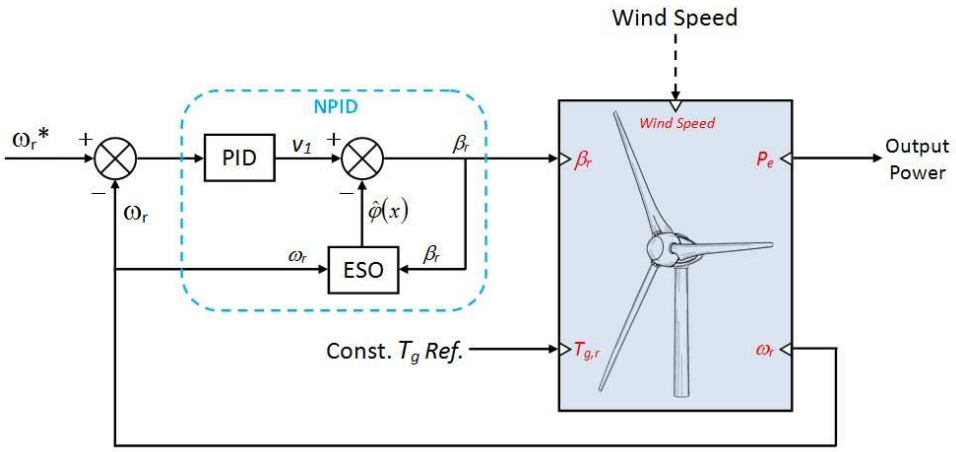

Figure 3.3: Block diagram of N-PI based controller for WT pitch angle control.

controller uses only one pair of gains rather than several scheduled gain pairs like GSPI, due to the compensation of all system nonlinearities and disturbances. The control gains can be chosen using the same optimization method as in PI and GSPI in previous sections.

3.4.5 Stability Analysis

Stability analysis of the observer (3.4.8) and the closed-loop system including controller and observer can be investigated by using Lyapunov stability similarly to [126]. Thus only stability results are summarized in this chapter and detailed steps can follow [126]. Error dynamics of the observer can be obtained from system (3.4.7) and (3.4.8) as:

$$\begin{bmatrix} \dot{\tilde{z}}_1 \\ \dot{\tilde{z}}_2 \\ \dot{\tilde{z}}_3 \end{bmatrix} = \begin{bmatrix} -k_{01} & 1 & 0 \\ -k_{02} & 0 & 1 \\ -k_{03} & 0 & 0 \end{bmatrix} \begin{bmatrix} \tilde{z}_1 \\ \tilde{z}_2 \\ \tilde{z}_3 \end{bmatrix} + \begin{bmatrix} 0 \\ 0 \\ \dot{\Psi}(\cdot) \end{bmatrix} \tag{3.4.15}$$

Define tracking error of rotor speed as $e_2 = \omega_r^* - x_1$, its integration as $e_1 = \int_0^t (\omega_r^* - x_1)dt$, and its differentiation as $e_3 = \dot{\omega}_r^* - \dot{x}_1$. From (3.4.6) and (3.4.14),

the dynamics of the closed-loop system is represented by the tracking errors as

$$\begin{bmatrix} \dot{e}_1 \\ \dot{e}_2 \\ \dot{e}_3 \end{bmatrix} = \begin{bmatrix} 0 & 1 & 0 \\ 0 & 0 & 1 \\ k_i & k_p & 0 \end{bmatrix} \begin{bmatrix} e_1 \\ e_2 \\ e_3 \end{bmatrix} + \begin{bmatrix} 0 \\ 0 \\ \tilde{z}_3 \end{bmatrix} \tag{3.4.16}$$

where $\tilde{z}_3 = \Psi(\cdot) - \hat{\Psi}(\cdot)$ is the estimation error of the perturbation.

Based on [126], assume perturbation functions $\Psi(\cdot)$ and $\dot{\Psi}(\cdot)$ are bounded over the domain of interest as:

$$|\Psi(\cdot)| \leq \gamma_1 \qquad |\dot{\Psi}(\cdot)| \leq \gamma_2 \tag{3.4.17}$$

where γ_1 and γ_2 are positive constants; then the error dynamic of ESPO (3.4.15) and the closed-loop system (3.4.16) are ultimately bounded. Furthermore, if perturbations $\Psi(\cdot)$ and $\dot{\Psi}(\cdot)$ are locally Lipschitz in their arguments, the observer error and the closed-loop tracking error can be obtained exponential converged as well.

The internal dynamic of the nonlinear system is analysed using zero-dynamic technique. When the rotor speed and its time derivative are well controlled, i.e. $e_2 = 0$ and $e_3 = 0$, then the corresponding states are controlled to their reference values, such as $\beta = \beta^*$, $\omega_r = \omega_r^*$, $\dot{\omega}_r = 0$ and $P_r(\omega_r^*, \beta^*) = P_r^* = P_e^*/\eta$, where η is the entire output power efficiency. A relation expression can be obtained as

$$\frac{P_r^*}{\omega_r^*} - \omega_r^* D_s + \frac{\omega_g D_s}{N_g} - \delta K_s = 0 \tag{3.4.18}$$

then the other two dynamics can be obtained as

$$\dot{\omega}_g \equiv 0 \tag{3.4.19}$$

$$\lim_{t \to \infty} \delta(t) = \frac{P_e^*/\eta}{\omega_r^* K_s} \tag{3.4.20}$$

The zero-dynamic of the internal system is stable, and therefore, the closed-loop system error dynamic is stable.

3.5 Simulation Results

The simulation tests were performed based on a real experimental wind turbine, CART, located at National Renewable Energy Laboratory USA and whose param-

eters are given in Table 3.2. The CART is a flexible, variable speed and pitch controlled wind turbine with 1.5 MW nominal power rating. This turbine was modeled using a two-mass model and a validated aeroelastic simulator called FAST: fatigue, aerodynamics, structures, and turbulence [128]. As discussed in Chapter 1, in different wind speed region, the controller are designed with different control objectives. This thesis only considered one region that wind speed above the rated. The wind speed is chosen in the range from 12 m/s to 24 m/s with different mean value and turbulence intensity in Region III. The wind parameters are generated from TurbSim, which is a stochastic, full-field, turbulent-wind simulator and numerically simulates 3-dimensional wind velocity vectors by time series at points in a vertical rectangular grid [135]. The proposed N-PI, a conventional PI and a GSPI are tested based on the

Table 3.2: Two-mass model parameters of the 1.5 MW experimental wind turbine.

Wind Turbine Parameters:	Value:
Rotor radius (R_{b})	35 m
Air density (ρ)	1.225 kg/m^3
Rotor inertia (J_{r})	2.96$\times 10^6$ kg·m^2
Generator inertia (J_{g})	53.0 kg·m^2
Drive-train spring factor (K_{s})	5.6$\times 10^9$ N·m/rad
Drive-train damping factor (D_{s})	1.0$\times 10^7$ N·m·s/rad
Gearbox ratio (N_{g})	87.965
Pitch actuator time constant (τ_β)	1 s
Nominal power output (P_{e})	1.5 MW
Rated rotor speed ($\omega_{\mathrm{r,rated}}$)	2.1428 rad/s
Rated generator torque ($T_{\mathrm{g,rated}}$)	8376.6 N·m
Pitch angle limit ($\beta_{\min}$ to $\beta_{\max}$)	-1° to 90°
Pitch rate limit ($\dot{\beta}_{\lim}$)	$\pm 10^\circ$/s
Wind turbine efficiency (η)	0.95

simplified two-mass model of the CART at first. Due to the N-PI is using a high-gain SPO, the large observer gains will enlarge the sensor noise and wind disturbance. Thus, the observer bandwidth is set greater than the controller bandwidth and low-

er than the sensor bandwidth, with potimised bandwidth tuned via pole placement method. The parameters of the N-PI controller are given in Table 3.3.

Table 3.3: Parameters of controllers.

Parameters:	Value:
PI Proportional gain (1/s^2): k_p	140
PI Integral gain (1/s): k_i	52
GSPI constant Proportional gain (1/s^2): k_p	116
GSPI constant Integral gain (1/s): k_i	42
FLC/N-PI Proportional gain (1/s^2): k_p	6.3
FLC/N-PI Integral gain (1/s): k_i	0.26
ESPO equivalent input gain ($^\circ$·s^3/rad): b_0	-0.04
ESPO nonlinear coefficient (rad/s): h	0.001
ESPO observer bandwidth: α_0	40
ESPO estimation gain (1/s): k_{01}	1.2×10^2
ESPO estimation gain (1/s^2): k_{02}	4.8×10^3
ESPO estimation gain (1/s^3): k_{03}	6.4×10^4

3.5.1 Simplified Two-mass Wind Turbine Model

Step Wind Speed Test

The pitch angle controller is designed to maintain the rotor speed under wind disturbance. The performance of the three controllers obtained under step wind disturbance is shown in Figure 3.4, which is simulated on the simplified two-mass model. When wind speed is increased in steps, it is clear that the PI controller (dotted line) cannot provide consistently optimal dynamic performance when wind speed changes. The GSPI controller (dashed line) with the entire-region optimal gains can eliminate the effect of the shift of operating points caused by the change of wind speed. The N-PI (solid line) provides better transient response with smaller overshoot and faster settling time, over the whole operation range.

Furthermore, dynamic response under step wind speed change from 12 m/s to

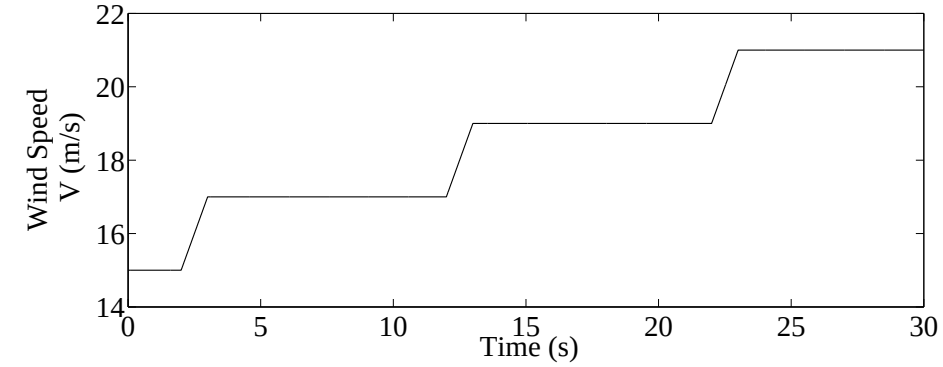

(a)

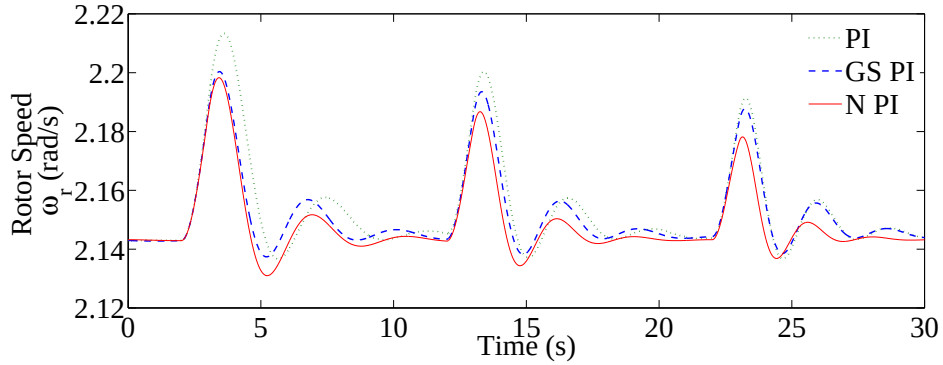

(b)

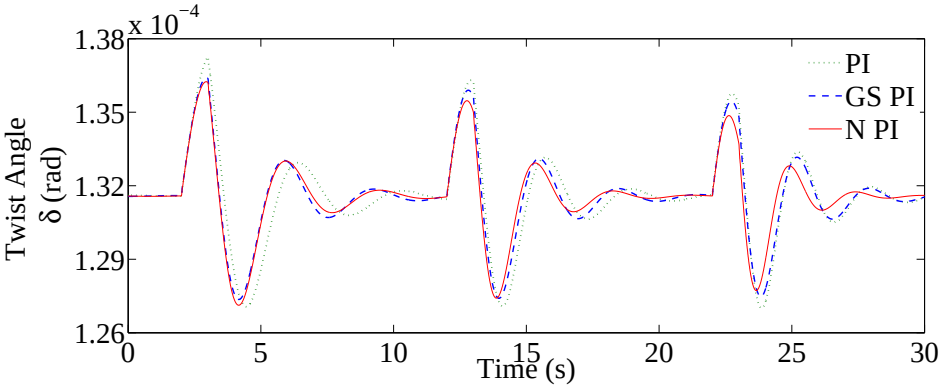

(c)

Figure 3.4: Response of PI, GSPI and N-PI under step wind test. (a) wind speed, (b) rotor speed, (c) drive train shaft twist angle.

24 m/s are compared in terms of settling time, overshoot and ITAE for different controllers. As shown in Figure 3.5, it can be found that the N-PI has about 18% less settling time, 15% less overshoot, and 20% less ITAE value than the other two when the wind speed above 16 m/s. At lower wind speed, the N-PI performs better than the PI but no obvious improvement than the GSPI. Overall, the N-PI has the best performance with the least ITAE value among the three controllers.

The performance of the ESPO in N-PI is given in Figure 3.6. Note that the observer needs a short period to track the variation of the operating point depending on the bandwidth of the observer. It will have transient error under step wind, but will eliminate to zero in a short time period. There is no steady-state error between the real perturbation and the estimated value.

Random Wind Speed Test

The simulation results under random wind with 18 m/s mean speed and 15% turbulence intensity are presented in Figure 3.7, which contains wind speed, response of rotor speed, and drive train shaft twist angle. All controllers control the pitch angle and the generator torque is held as a constant in its rated value. The control performances are compared under cases with combination of different mean wind speed and turbulence intensity, based on the RMS value of the regulation error of the following four dynamic variables: the rotor speed ω_r for the control performance, the changes of twist angle δ as the second control objective, the actuator usage in terms of the pitch acceleration $\dot{\beta}$, and the controller output change rate $\dot{\beta}_r$. Their performances are presented using bar chart in Figure 3.8. The PI controller performs worst under the random wind speed as shown in the comparison bar charts. This is because that the PI controller is a linear controller with its control gain is optimized at one operation point, while the other three controllers are nonlinear controllers whose control gains are suitable for the whole wind speed region, based on the cancellation of nonlinearities or gain scheduled technique.

On the other hand, the GSPI gain pairs are switching rapidly under the random wind speed. Its entire control performance is not as good as the FLC and the N-PI. Due to the system model and parameters are known accurately in simulation, the

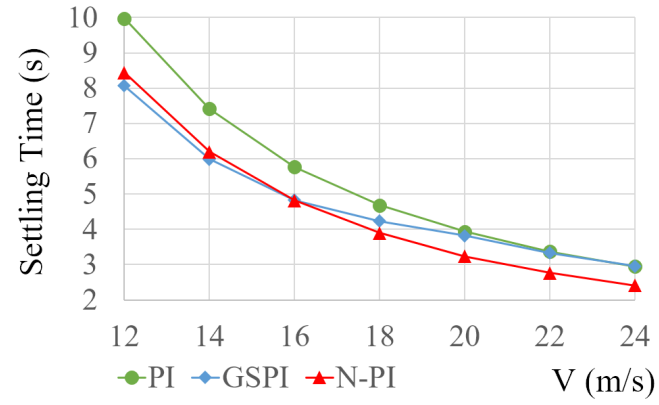

(a)

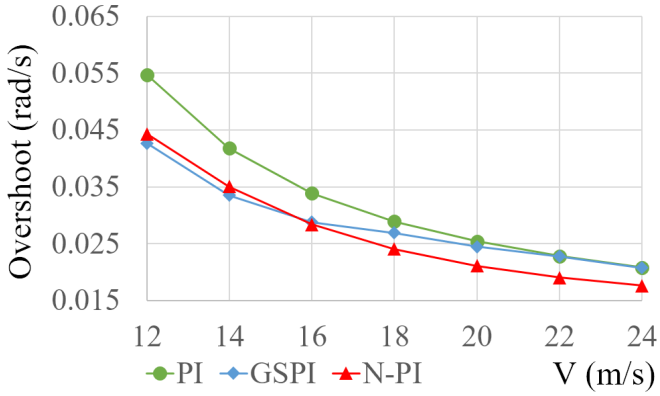

(b)

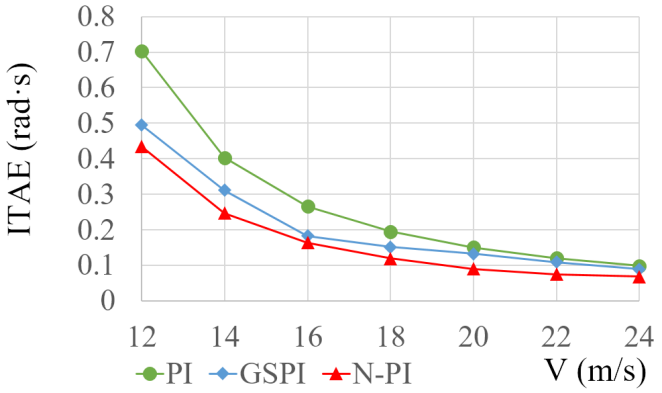

(c)

Figure 3.5: Performance comparison in metrics of: (a) settling time (s), (b) overshoot (rad/s), and (c) ITAE (rad·s) under step change wind speed.

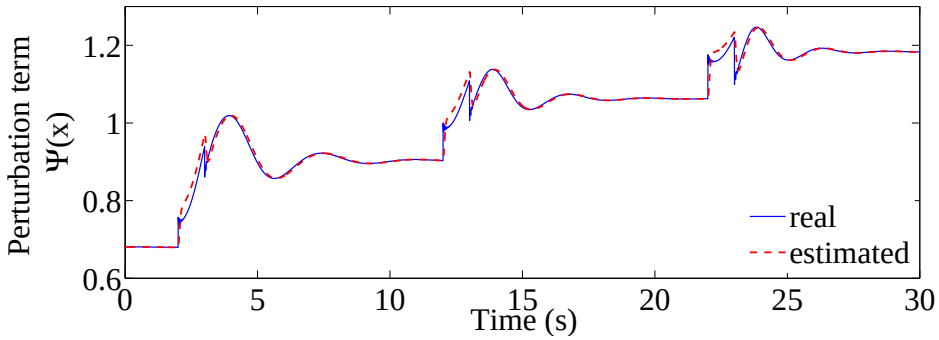

(a)

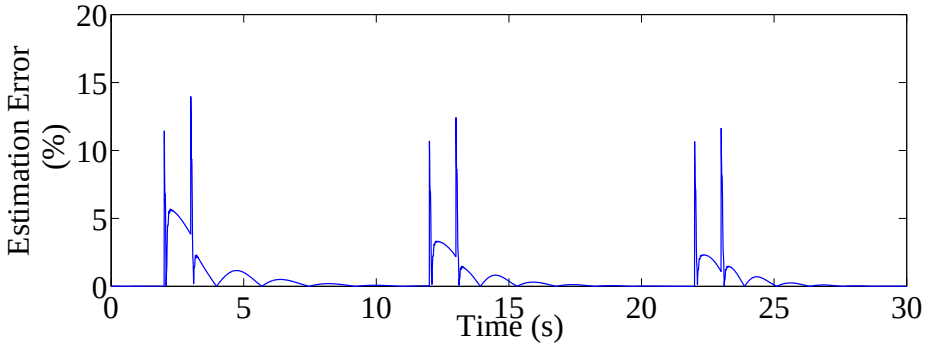

(b)

Figure 3.6: Perturbation estimation result under step wind speed. a) Real and estimated perturbation comparison; b) Estimation error in percentage.

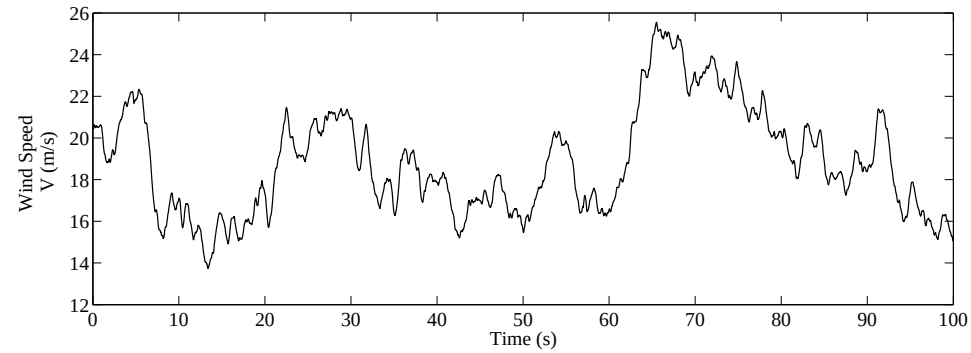

(a)

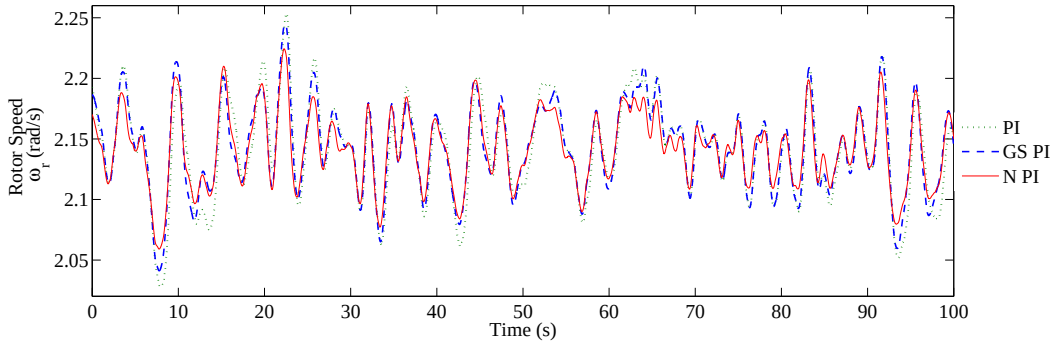

(b)

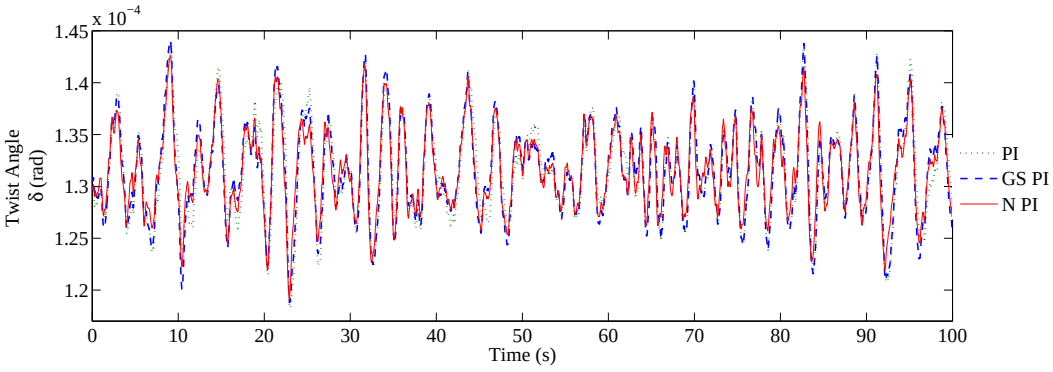

(c)

Figure 3.7: Response of N-PI compared with PI and GSPI under random wind speed. (a) Random wind speed, (b) rotor speed, (c) drive train shaft twist angle.

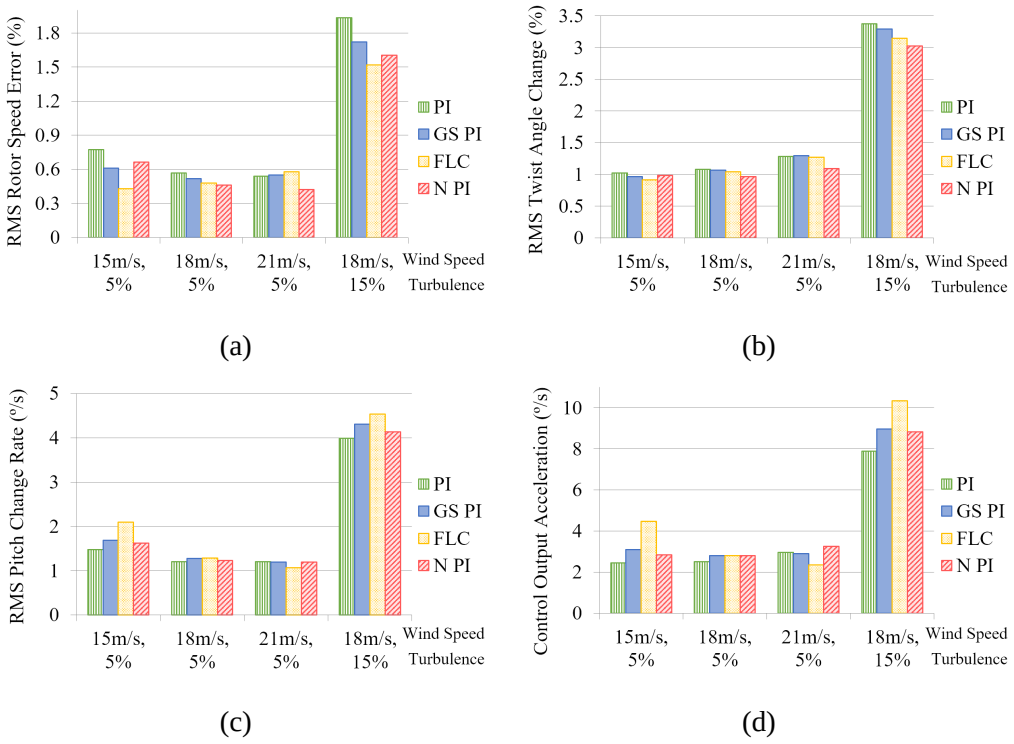

Figure 3.8: Performance comparison for PI, GSPI, FLC and N-PI under random wind speed with different mean value (m/s) and turbulence intensity (%). (a) RMS Rotor Speed Error; (b) RMS Twist Angle Change; (c) RMS Pitch Actuator Usage; (d) RMS Controller Output Acceleration.

FLC has absolutely the best performance among the four controllers. N-PI performs as good as FLC, but the perturbation observer has a small time delay and estimation error by the ESPO estimation before compensating the real ones. The rotor speed regulation error of N-PI is 20% less than the PI controller and 10% less than the GSPI. The reduction of twist angle change is 12% better than the PI and GSPI. In addition, the actuator usage of N-PI is 4% less than that of GSPI and 9% less than that of FLC, in terms of the pitch change rate and control output acceleration.

The estimation performance of the linear ESPO in the N-PI controller is shown in Figure 3.9, whose average estimation error is around 7.5%.

Due to the high change rate of the random wind speed with high turbulence, the estimated perturbation from ESPO should be filtered before used to compensate the real perturbation. Moreover, the N-PI controller using a nonlinear ESPO is compared a N-PI with a linear ESPO. As the observer gains of both ESPOs are chosen to be far greater than the upper bound of the time derivative of perturbation, there is no obvious improvement obtained by the nonlinear ESPO. Thus this chapter uses a high-gain linear ESPO for perturbation estimation [126].

The proposed N-PI pitch controller has better control performance in the whole wind speed region, especially at high turbulence intensity. Moreover, to extend the service life of equipment, high actuator usage should be avoided in practise. The GSPI requires to tune several set of gains around several operating points, while the N-PI only needs to tune one pair of gains of PI the whole wind speed region, which make it be much easier to comprise the control performance and the actuator usage.

Robustness of Model Uncertainties

When the accurate system model is available, the FLC provides the best results. However, in practical application, there are many model uncertainties, such as air density change caused by different weather condition, dust effect [136], and ice accretion [137] [138], which will affect the aerodynamic power coefficient of the wind turbine. Figure 3.10 shows the dynamic response when the power coefficient is reduced to 70% of its rated value. As the FLC requires an accurate model and parameters, it cannot maintain the rated rotor speed. As the N-PI based controller

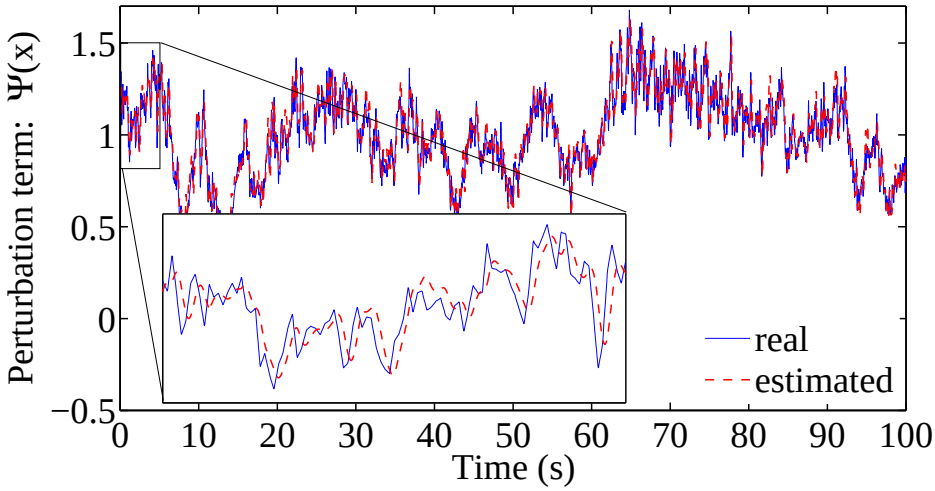

(a)

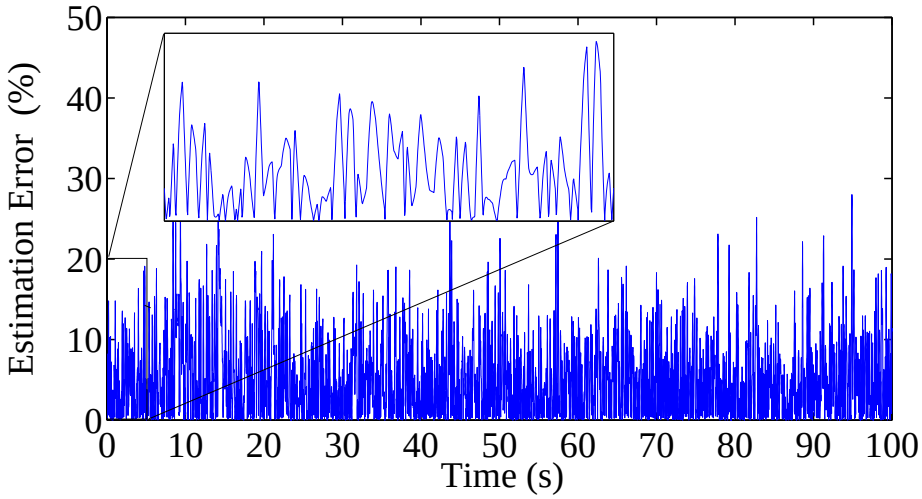

(b)

Figure 3.9: Perturbation estimation result under random wind speed. a) Real and estimated perturbation comparison; b) Estimation error in percentage.

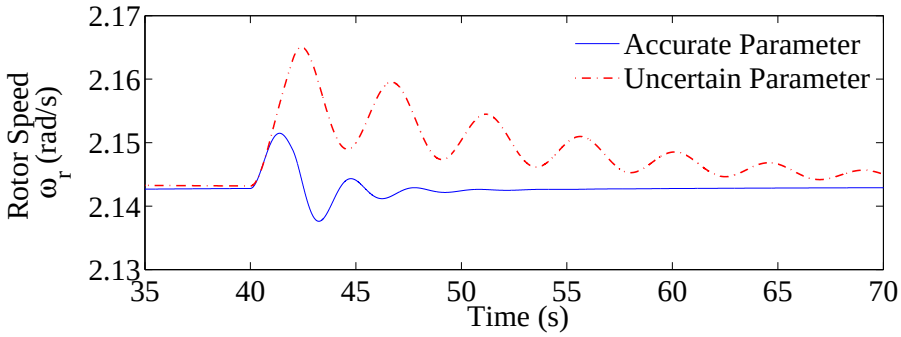

(a) FLC

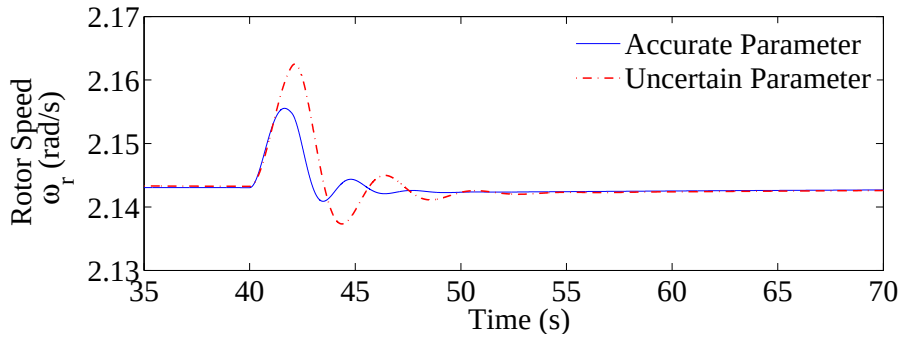

(b) N-PI

Figure 3.10: Dynamic response comparison under the power coefficient change to 70% its rated value. (a) Dynamic response of FLC; (b) Dynamic response of N-PI.

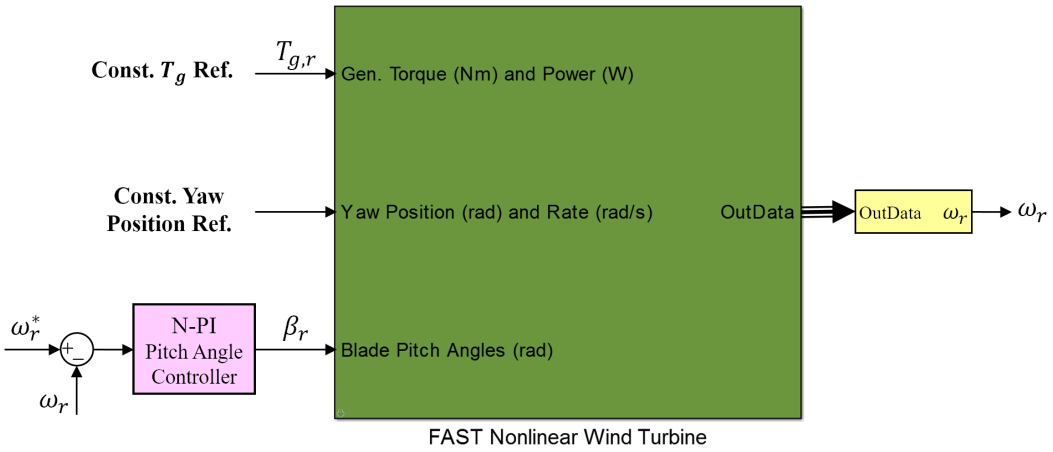

Figure 3.11: Configuration of test N-PI pitch angle controller using FAST.

do not need the accurate system model and can compensate the perturbation caused by the variation of system model uncertainties, it can provide much better and robust response. The PI and GSPI can also provide similar robust performance than the N-PI and their results are not presented.

3.5.2 Validation on FAST Simulator

As the two-mass model is a simplified wind turbine model that neglects many dynamic behavior, the N-PI controller is also validated on a more detailed model, the FAST model, which is capable of predicting both the extreme and fatigue loads of two and three-bladed horizontal-axis wind turbines and suitable for verification and testing of wind turbine control. Figure 3.11 shows the configuration of the N-PI and the FAST in Simulink.

As suggested in the FAST user manual, the FAST model does not include the pitch angle actuator dynamics and the blade base can rotate to the reference angle without delays. An additional actuator dynamic block is added to regulate the pitch angle. Furthermore, the FAST model has no direct output of the twist angle value like in the two-mass model, as it uses a full flexible dynamic model with segmented elastic model in the entire drive train shaft. The low speed shaft damage equivalent load (LSS DEL) is used to display the equivalent performance of the twist angle of the drive train shaft.

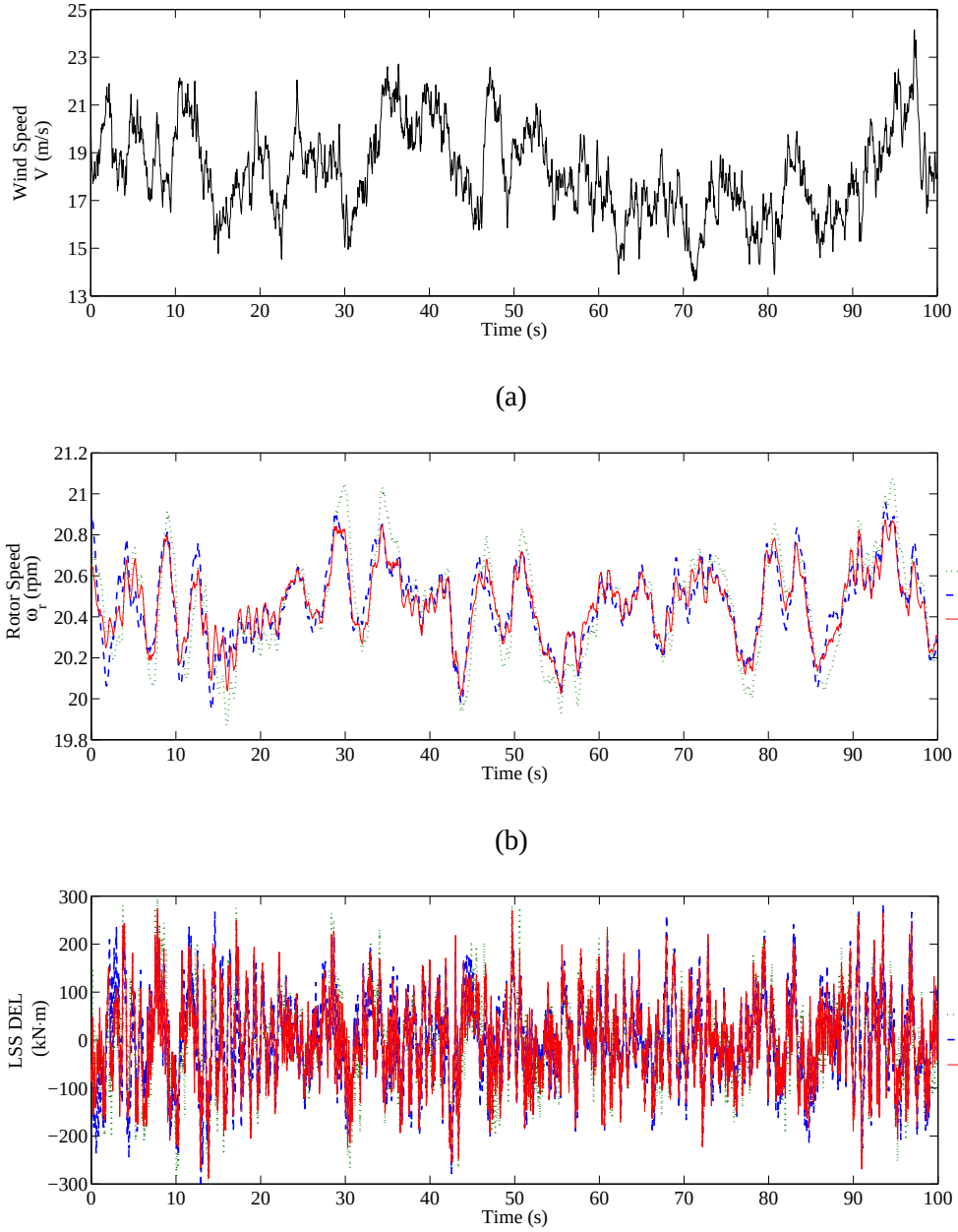

Figure 3.12: Simulation verification result on FAST model. (a) wind speed, (b) rotor speed, (c) LSS DEL.

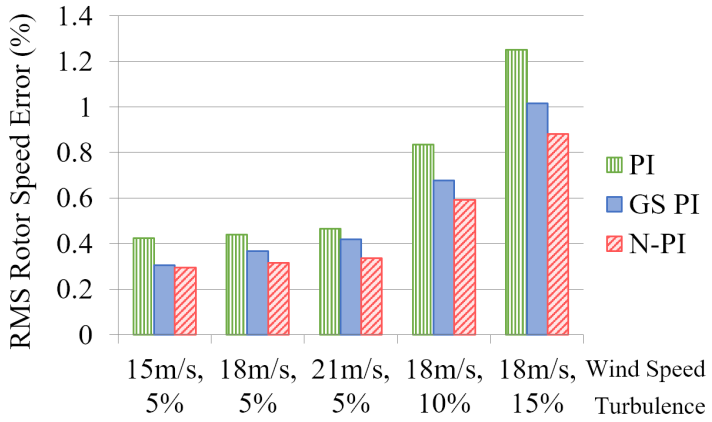

(a)

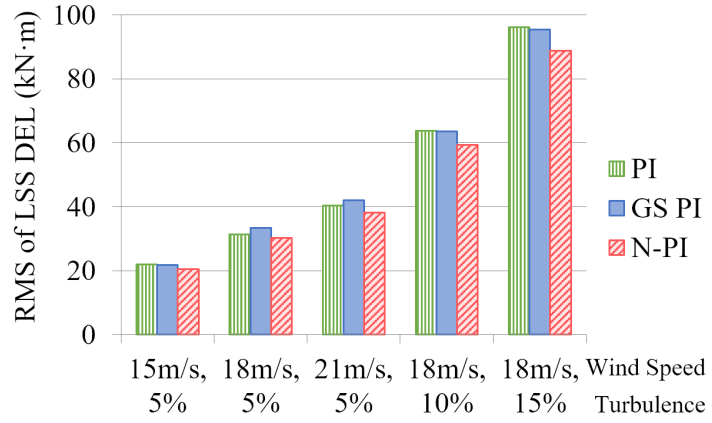

(b)

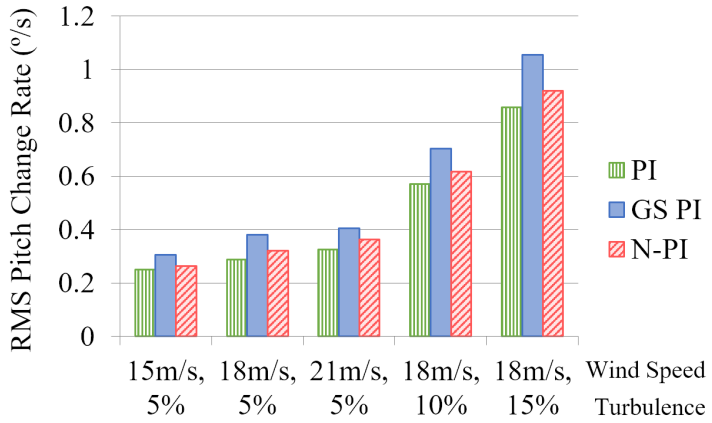

(c)

Figure 3.13: Performance comparisons of PI, GSPI and N-PI controllers using FAST simulator under different wind input: (a) RMS rotor speed error; (b) RMS LSS DEL; (c) RMS pitch change rate.

In the simulation on the FAST model, the RMS value of the following two variables are used to compare the controller performance: the rotor speed regulation error, and the pitch acceleration of the pitch angle (in °/s). The dynamic responses under random wind input with 18 m/s mean speed and 15% turbulence intensity is presented in Figure 3.12.

Comparing with the response of two mass model, the FAST simulation result includes many authentic dynamics and high frequency noise. Due to the observer bandwidth is chosen less than the noise bandwidth, the observer performance will not be affected by the noise. In addition, the wind turbine system has large inertia to damp the impact from noise, the N-PI controller is not sensitive to noise in the wind turbine application. The comparison performance in the bar chart shows that the N-PI has the rotor speed regulation error 25% to 30% less than the PI and 5% to 15% less than the GSPI as shown in Figure 3.13(a). And in the RMS of LSS DEL, the N-PI has approximate 7% less than both the PI and the GSPI as shown in Figure 3.13(b).

In the FAST simulation, the pitch angle response time constant depends on many conditions, such as wind speed at different height, yaw angle, and tower shadow, etc. Therefore, the pitch angle control response in FAST simulation is worse under higher wind speed and greater turbulence intensity as shown in Figure 3.13(c).

Nevertheless, the results under both low and high turbulence wind show that the N-PI controller has approximate 13% less actuator usage than the GSPI and gets about 10% better performance, and it has approximate 6% more actuator usage to get a 28% improvements comparing with PI controller in wind turbine pitch control.

3.6 Conclusion

A Nonlinear PI (N-PI) pitch angle controller has been designed to regulate the wind turbine to capture the rated wind power when the wind speed exceeds the rated value. Based on the two-mass nonlinear wind turbine model, an extended-order state and perturbation observer is designed to estimate the unknown and time-varying nonlinearities and external disturbances. The estimated perturbation dy-

namic is used to compensate the real unknown dynamics and a PI type controller is designed for the linearized system. Only one set of PI parameters need to be tuned for covering the whole operation region. The N-PI avoids the requirement of tuning and switching of controller gains in GSPI and the requirement of accurate system model in the feedback linearization control (FLC). The proposed N-PI pitch angle controller is verified on the two-mass simplified model and the detailed FAST simulator under step and random wind speed tests. Simulation results show that the N-PI based pitch angle controller performs better in constant power regulation and drive-train stress minimization, with less actuator usage comparing with the conventional PI and gain-scheduled PI controllers, and better robustness than FLC in the model uncertainties.

Chapter 4

Autonomous Control of Power Electronic Enabled Microgrid via Nonlinear Adaptive Control

4.1 Introduction

Growing interests of connecting the small generation units to local LV networks make the proposition of the MG concept to provide a new paradigm of distributed generation [24]. The MG can be defined as a LV network, including a cluster modular generations and loads, operated in both the grid-connected mode or island mode. In the grid-connected mode, the bus voltage is maintained by the utility grid, and all devices in the grid-connected MG stay synchronized with the voltage and frequency of the utility grid. In the island mode, the MG is isolated from the utility grid and no external voltage reference to be synchronized. This makes the islanded MG has much lower stiffness and inertia than the transmission grids [25–27]. It requires the DRs in the MG to have the capability of maintaining the voltage amplitude and frequency of the electric network. Under the impact that large amount of DRs and loads are connected to the LV networks, a fast-response voltage controller is required to enhance the robustness of the islanded MG.

In an islanded MG, all parallel connected DRs are expected to share the active

and reactive power demand without centralized control or critical communication among them. Thus, the power droop control is often applied to achieve this target and avoid the circulating currents between converter based DRs [27, 37]. The main idea of the droop control is to emulate the behaviour of synchronous generators operated parallelly in large power system: active power versus frequency and reactive power versus voltage magnitude.

The DRs use droop control to distribute the power demand to all parallelly connected DRs without centralized control or critical communication among them [37]. The droop control is implemented using the basic voltage and frequency (Vf) control method with a cascade-PI based control loop: an inner current control loop cascaded in an outer voltage control loop, with using PI controllers to regulate the voltages and currents [26, 53]. Moreover, advanced control methods have been proposed to control the converters in MG under balanced voltage condition, such as the feedback linearization control [62], robust high bandwidth predictive current control [99], and hybrid variable-structure control [100].

On the other hand, both the three-phase devices and single-phase device could be connected due to different requirements in the MG. The single-phase loads and power generations are the major causes of voltage unbalance, which not only incurs more power loses and instability to the MG but also results in damaging the three-phase equipments installed in the MG. The voltage unbalance problem has been addressed with different methods, such as filtering the negative-sequence voltage via the power filter device in series with distribution line [139], dual synchronous reference frames (SRF) based on the positive- and negative-sequences currents control to eliminate the negative-sequence currents [140], imbalance compensation droop control to compensate the voltage unbalance in the control input [141], direct voltage reference change method which is to compensate voltage unbalance in the reference of voltage control loop for a droop-controlled MG [142], a voltage unbalance and harmonics compensation strategy [101], a distributed negative sequence current sharing method [102], robust control strategy designed with a convex linear matrix inequality condition [103], model predictive control technique to minimize the voltage unbalance [104]. However, the previous unbalance compensation method

cannot fully linearize the system to completely eliminate the effect of voltage unbalance and disturbance.

This chapter designs a nonlinear adaptive control (NAC) method with using a state and perturbation observer (SPO) to estimate the perturbation in both the positive- and negative-sequence frames, and use the estimated perturbation to compensate the disturbance and voltage unbalance to improve the robustness of the MG system against all kinds of disturbances. As the lumped perturbation term is defined to include both the balanced and unbalanced disturbance, nonlinearities and parameter uncertainties, all disturbances can be compensated and the original system is fully linearized without the dependence of an accurate system model and fast changing disturbance.

This chapter is organized as follows. Section 4.2 presents the structure of MG and the dynamic model of converter based DR. Section 4.3 reviews the standard droop control for the DRs used in islanded MG and a unbalance compensate reference method. Section 4.4 presents the design of NAC-based droop controller for energy storage system and PV system. The cases analysis with simulation results are presented in Section 4.5 and the whole chapter is concluded finally.

4.2 Dynamic Model of Voltage Source Converter based Distributed Resources

The scheme of VSC based distributed resources in a microgrid is shown in Figure 4.1

The current and output voltage dynamics of the VSC with LC filter, transformed in Park's d-q frame which synchronized with angular speed ω, can be represented as follows [62, 143]:

$$\begin{cases} \frac{di_{\mathrm{Ld}}}{dt} = -\frac{R_{\mathrm{s}}}{L_{\mathrm{s}}} i_{\mathrm{Ld}} + \omega i_{\mathrm{Lq}} - \frac{1}{L_{\mathrm{s}}} v_{\mathrm{od}} + \frac{1}{L_{\mathrm{s}}} v_{\mathrm{d}} \\ \frac{di_{\mathrm{Lq}}}{dt} = -\frac{R_{\mathrm{s}}}{L_{\mathrm{s}}} i_{\mathrm{Lq}} - \omega i_{\mathrm{Ld}} - \frac{1}{L_{\mathrm{s}}} v_{\mathrm{oq}} + \frac{1}{L_{\mathrm{s}}} v_{\mathrm{q}} \\ \frac{dv_{\mathrm{od}}}{dt} = \frac{1}{C_{\mathrm{s}}} i_{\mathrm{Ld}} + \omega v_{\mathrm{oq}} - \frac{1}{C_{\mathrm{s}}} i_{\mathrm{od}} \\ \frac{dv_{\mathrm{oq}}}{dt} = \frac{1}{C_{\mathrm{s}}} i_{\mathrm{Lq}} - \omega v_{\mathrm{od}} - \frac{1}{C_{\mathrm{s}}} i_{\mathrm{oq}} \end{cases} \tag{4.2.1}$$

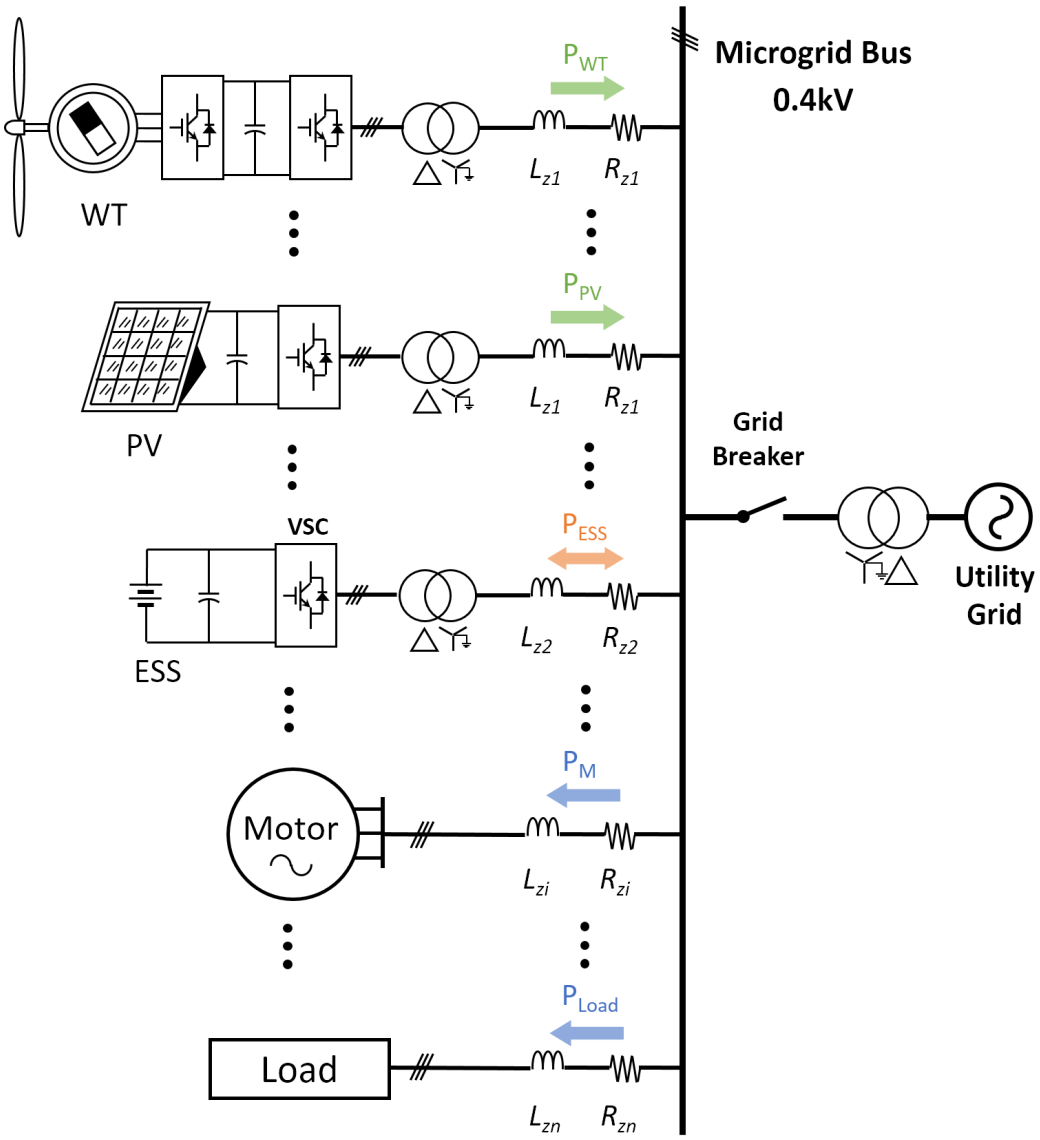

Figure 4.1: More power electronics converter based microgrid

where v_{od}, v_{oq}, i_{od} and i_{oq} are the d- and q-axis output voltages and currents; i_{Ld}, i_{Lq} are the currents flowing into the inductor of LC filter; v_{d} and v_{q} are the d-q voltage control input; R_{s}, L_{s} and C_{s} are the equivalent resistance, inductance and capacitance of the LC filter.

The output current dynamic is represented as

$$\begin{cases} \frac{di_{\mathrm{od}}}{dt} = -\frac{R_{\mathrm{z}}}{L_{\mathrm{z}}} i_{\mathrm{od}} + \omega i_{\mathrm{oq}} + \frac{1}{L_{\mathrm{z}}}(v_{\mathrm{od}} - v_{\mathrm{bd}}) \\ \frac{di_{\mathrm{oq}}}{dt} = -\frac{R_{\mathrm{z}}}{L_{\mathrm{z}}} i_{\mathrm{oq}} - \omega i_{\mathrm{od}} + \frac{1}{L_{\mathrm{z}}}(v_{\mathrm{oq}} - v_{\mathrm{bq}}) \end{cases} \tag{4.2.2}$$

where v_{bd} and v_{bq} are the d- and q-axis bus voltage of MG; R_{z} and L_{z} are the resistance and inductance of the output impedance

4.2.1 Distributed Power Sources in Microgrid

The photovoltaic (PV) system is one of the most promising renewable energy sources in MG, due to its features of low cost, low voltage, high reliability, and environmental friendly operation [25]. Only the grid-connected PV converter model is used in this chapter to test the penetration of renewable energy for DR [144]. The PV power generation model used in this chapter is a single-phase circuit presented in [145]. The nonlinear model of PV cell and array are not considered and replaced by an adjustable dc voltage source. Assuming the PV generator array is always working at its maximum power level, and its grid-connect converter operates the PV system as a current source that tracks the bus voltage to inject available active power into the grid [25, 144].

4.3 Conventional Control Structure for Converter-based Distributed Resources with Unbalance Compensation

The control structure of a DR system includes an outer loop to generate the references of voltage amplitude and phase, and an inner loop to regulate the voltage and frequency of output voltage. The outer loop is using the well-known droop control,

which depends on the output active and reactive power. In addition, a compensation loop is added to compensate the fundamental negative sequence reactive power to eliminate the voltage unbalance.

4.3.1 Outer Loop: Power Droop Control

In an islanded MG, all parallel connected DRs are expected to share the active and reactive power demand without centralized control or critical communication among them. Thus, the power droop control is often applied to reach this target and avoid the circulating currents between converter based DRs [27, 37]. The main idea of the droop control is to emulate the behaviour of a single synchronous generator in large power system: active power versus frequency and reactive power versus voltage magnitude.

To regulate the active and reactive power outputs, the DRs need to provide the frequency (or phase) and amplitude of voltage references [37]. The references are based on two sets of droops as

$$\begin{cases} \omega^* = \omega_0 - m \cdot P(t) \\ E^* = E_0 - n \cdot Q(t) \end{cases} \tag{4.3.1}$$

where ω^* and E^* are the angular frequency and magnitude of the output voltage reference, ω_0 and E_0 are their rated values, respectively; P and Q are the active and reactive power; m and n are the proportional droop gains. The gains are to maintain the system synchronization, and below the voltage stability limits [27]. The droop gains can be designed as follows:

$$\begin{cases} m = \Delta\omega / P_{\max} \\ n = \Delta E / Q_{\max} \end{cases} \tag{4.3.2}$$

$P_{\max}$ and $Q_{\max}$ are the maximum active and reactive power delivered by the inverter; $\Delta\omega$ and ΔE are the maximum deviations of frequency and amplitude, which are mostly designed at 2% and 5%, respectively, as acceptable values [53]. The outer loop power droop control adjusts the frequency and amplitude references of output voltage, and provides the references to the inner voltage and frequency control loops.

4.3.2 Output Impedance Compensation

In MG, the distributed voltage sources are commonly connected to the bus by transmission lines and sometimes with a transformer, which can be seen as the coupling output impedance of the converter. As the output current dynamic in (4.2.2), the output impedance will cause voltage drop on the output impedance when current flowing from DRs to the MG bus. Thus, the voltage drop caused by output impedance can be compensated in the voltage control loop of VSC-based DRs. As the differential block is not commonly used in practical for its high sensitivity to noise, the compensation only considered the steady-state voltage drop on output impedance. The compensated voltage reference can be represented as:

$$\begin{cases} v_{\mathrm{zd}}^{*} = R_{\mathrm{z}} i_{\mathrm{od}} - \omega^{*} L_{\mathrm{z}} i_{\mathrm{oq}} \\ v_{\mathrm{zq}}^{*} = R_{\mathrm{z}} i_{\mathrm{oq}} + \omega^{*} L_{\mathrm{z}} i_{\mathrm{od}} \end{cases} \tag{4.3.3}$$

where v_{zd}^{*} and v_{zq}^{*} are the compensation voltage references.

The inverter output voltage references in d-q axis are designed as the sum of two components: the voltage droop references E^{*} from (4.3.1), and output impedance compensation as follows

$$\begin{cases} v_{\mathrm{od}}^{*} = E^{*} + v_{\mathrm{zd}}^{*} \\ v_{\mathrm{oq}}^{*} = v_{\mathrm{zq}}^{*} \end{cases} \tag{4.3.4}$$

where v_{od}^{*} and v_{oq}^{*} are the reference voltages for the inner voltage control loop.

4.3.3 Inner Loop: Conventional Voltage and Frequency Control and Unbalance Compensation

The control objective of the inner loop is to regulate the output voltage produced by the VSC to track the voltage reference given by the outer loop. The most commonly used method is the cascaded-PI based voltage and frequency control, which uses two control loops: a voltage controller to regulate the output voltage via adjusting the current reference, and a current controller to regulate the current of converter via generating the command voltage vector synthesized by PWM or SVM modulation [26, 53, 99, 142].

To eliminate the voltage unbalance, the fundamental negative sequence (FNS) reactive power can be used for unbalance compensation [142]. The instantaneous FNS reactive power can be calculated as

$$Q^{-} = v_{\mathrm{od}}^{n} i_{\mathrm{oq}}^{n} - v_{\mathrm{oq}}^{n} i_{\mathrm{od}}^{n} \tag{4.3.5}$$

where v_{od}^{n}, v_{oq}^{n}, i_{od}^{n} and i_{oq}^{n} represent negative-sequence voltage and current in d-q axis, respectively.

Then the unbalance compensation reference (UCR) can be designed as [142]

$$\mathbf{UCR} = LPF(s) \cdot Q^{-} \cdot \mathbf{V}_{\mathrm{o}}^{-} \cdot UCG \tag{4.3.6}$$

where $\mathbf{V}_{\mathrm{o}}^{-}$ represents the vector of the FNS output voltage, UCG is the unbalance compensation gain which is a constant that should be selected, $LPF(s)$ represents the low-pass filter to apply virtual inertia of microgrid to the disturbance [37].

4.4 Nonlinear Adaptive Controller Design

The proposed NAC controller is based on perturbation estimation, which is used to adaptively compensate the total perturbation, including interactions between subsystems, parameter uncertainties, disturbances and the voltage unbalance. The input-output linearization of the system is to help designing a perturbation observer. The system dynamics can be fully decoupled to two subsystems $(i = 1, 2)$ depending on outputs in d-q axis, each of which includes both the positive- and negative-sequence components. The linearized subsystems can be linearly controlled by a simple linear control law [88, 146]. The inner current control loop is unnecessary in this control method as shown in the final control output expression.

4.4.1 Model of Converter-based DR in Dual Synchronous Reference Frames

The original model (4.2.1) can be generically understood as a summation of balanced positive-, negative- and zero-sequence components. The positive- and

negative-sequence components are considered under two rotating reference frames: dq^+ rotating with positive synchronous speed ω and angular position θ; and dq^- rotating with negative synchronous speed $-\omega$ and angular position $-\theta$ [147]. The rotating speed of positive-sequence voltage components can be obtained by the detector proposed in [148]. The DR model can be rewritten in dq^+ and dq^- reference frame, which are presented with superscript p and n for positive- and negative-sequence, as:

$$\begin{cases} \dot{\mathbf{x}}(t) = \begin{bmatrix} \mathbf{A}^p & \mathbf{0} \\ \mathbf{0} & \mathbf{A}^n \end{bmatrix} \mathbf{x}(t) + \begin{bmatrix} \mathbf{B}^p & \mathbf{0} \\ \mathbf{0} & \mathbf{B}^n \end{bmatrix} \mathbf{u}(t) + \mathbf{d} \\ \mathbf{y}(t) = \begin{bmatrix} \mathbf{C} & \mathbf{0} \\ \mathbf{0} & \mathbf{C} \end{bmatrix} \mathbf{x}(t) \end{cases} \tag{4.4.1}$$

where

$$\mathbf{A}^p = \begin{bmatrix} -\frac{R_\mathrm{s}}{L_\mathrm{s}} & \omega & -\frac{1}{L_\mathrm{s}} & 0 \\ -\omega & -\frac{R_\mathrm{s}}{L_\mathrm{s}} & 0 & -\frac{1}{L_\mathrm{s}} \\ \frac{1}{C_\mathrm{s}} & 0 & 0 & \omega \\ 0 & \frac{1}{C_\mathrm{s}} & -\omega & 0 \end{bmatrix}, \mathbf{A}^n = \begin{bmatrix} -\frac{R_\mathrm{s}}{L_\mathrm{s}} & -\omega & -\frac{1}{L_\mathrm{s}} & 0 \\ \omega & -\frac{R_\mathrm{s}}{L_\mathrm{s}} & 0 & -\frac{1}{L_\mathrm{s}} \\ \frac{1}{C_\mathrm{s}} & 0 & 0 & -\omega \\ 0 & \frac{1}{C_\mathrm{s}} & \omega & 0 \end{bmatrix}$$

$$\mathbf{B}^p = \mathbf{B}^n = \begin{bmatrix} \frac{1}{L_\mathrm{s}} & 0 & 0 & 0 \\ 0 & \frac{1}{L_\mathrm{s}} & 0 & 0 \end{bmatrix}^T, \mathbf{C} = \begin{bmatrix} 0 & 0 & 1 & 0 \\ 0 & 0 & 0 & 1 \end{bmatrix}$$

$$\mathbf{x} = \begin{bmatrix} i^p_{\mathrm{Ld}} & i^p_{\mathrm{Lq}} & v^p_{\mathrm{od}} & v^p_{\mathrm{oq}} & i^n_{\mathrm{Ld}} & i^n_{\mathrm{Lq}} & v^n_{\mathrm{od}} & v^n_{\mathrm{oq}} \end{bmatrix}^T$$

$$\mathbf{y} = \begin{bmatrix} v^p_{\mathrm{od}} & v^p_{\mathrm{oq}} & v^n_{\mathrm{od}} & v^n_{\mathrm{oq}} \end{bmatrix}^T, \mathbf{u} = \begin{bmatrix} v^p_{\mathrm{d}} & v^p_{\mathrm{q}} & v^n_{\mathrm{d}} & v^n_{\mathrm{q}} \end{bmatrix}^T$$

$$\mathbf{d} = \begin{bmatrix} 0 & 0 & -\frac{i^p_{\mathrm{od}}}{C_\mathrm{s}} & -\frac{i^p_{\mathrm{oq}}}{C_\mathrm{s}} & 0 & 0 & -\frac{i^n_{\mathrm{od}}}{C_\mathrm{s}} & -\frac{i^n_{\mathrm{oq}}}{C_\mathrm{s}} \end{bmatrix}^T$$

where $\mathbf{A}^p$, $\mathbf{A}^n$, $\mathbf{B}^p$ and $\mathbf{B}^n$ are the gain matrices of states and system inputs for positive- and negative-sequence variables, respectively; $\mathbf{C}$ is the output gain matrix of states; $\mathbf{x}, \mathbf{y}, \mathbf{u}$ are the system states, outputs, and inputs vectors; $\mathbf{d}$ is the system disturbance, which is depending on the load.

4.4.2 Input-output Linearization

Consider a MIMO system, differentiates the system output y_i until the system input u_j first decoupled with other states in the differential order of y_i. From system (4.4.1), the input-output relationship between the system outputs y_i and inputs u_i is obtained in its second-order derivatives, which are represented as:

$$\begin{bmatrix} \ddot{y}_1^p \\ \ddot{y}_2^p \\ \ddot{y}_1^n \\ \ddot{y}_2^n \end{bmatrix} = \begin{bmatrix} L_{f1}^p(x) \\ L_{f2}^p(x) \\ L_{f1}^n(x) \\ L_{f2}^n(x) \end{bmatrix} + \begin{bmatrix} L_g & 0 & 0 & 0 \\ 0 & L_g & 0 & 0 \\ 0 & 0 & L_g & 0 \\ 0 & 0 & 0 & L_g \end{bmatrix} \begin{bmatrix} u_1^p \\ u_2^p \\ u_1^n \\ u_2^n \end{bmatrix} \tag{4.4.2}$$

where

$$\begin{aligned} L_{f1}^p(x) = &-\frac{R_\mathrm{s}}{L_\mathrm{s}C_\mathrm{s}} i_{\mathrm{Ld}}^p + \frac{2\omega}{C_\mathrm{s}} i_{\mathrm{Lq}}^p - \left(\frac{1}{L_\mathrm{s}C_\mathrm{s}} + \omega^2\right) v_{\mathrm{od}}^p \\ &- \frac{\omega}{C_\mathrm{s}} i_{\mathrm{oq}}^p + v_{\mathrm{oq}}^p \frac{d\omega}{dt} - \frac{1}{C_\mathrm{s}} \frac{di_{\mathrm{od}}^p}{dt} \end{aligned}$$

$$\begin{aligned} L_{f2}^p(x) = &-\frac{R_\mathrm{s}}{L_\mathrm{s}C_\mathrm{s}} i_{\mathrm{Lq}}^p - \frac{2\omega}{C_\mathrm{s}} i_{\mathrm{Ld}}^p - \left(\frac{1}{L_\mathrm{s}C_\mathrm{s}} + \omega^2\right) v_{\mathrm{oq}}^p \\ &+ \frac{\omega}{C_\mathrm{s}} i_{\mathrm{od}}^p + v_{\mathrm{od}}^p \frac{d\omega}{dt} - \frac{1}{C_\mathrm{s}} \frac{di_{\mathrm{oq}}^p}{dt} \end{aligned}$$

$$\begin{aligned} L_{f1}^n(x) = &-\frac{R_\mathrm{s}}{L_\mathrm{s}C_\mathrm{s}} i_{\mathrm{Ld}}^n - \frac{2\omega}{C_\mathrm{s}} i_{\mathrm{Lq}}^n - \left(\frac{1}{L_\mathrm{s}C_\mathrm{s}} + \omega^2\right) v_{\mathrm{od}}^n \\ &+ \frac{\omega}{C_\mathrm{s}} i_{\mathrm{oq}}^n + v_{\mathrm{oq}}^n \frac{d\omega}{dt} - \frac{1}{C_\mathrm{s}} \frac{di_{\mathrm{od}}^n}{dt} \end{aligned}$$

$$\begin{aligned} L_{f2}^n(x) = &-\frac{R_\mathrm{s}}{L_\mathrm{s}C_\mathrm{s}} i_{\mathrm{Lq}}^n + \frac{2\omega}{C_\mathrm{s}} i_{\mathrm{Ld}}^n - \left(\frac{1}{L_\mathrm{s}C_\mathrm{s}} + \omega^2\right) v_{\mathrm{oq}}^n \\ &- \frac{\omega}{C_\mathrm{s}} i_{\mathrm{od}}^n + v_{\mathrm{od}}^n \frac{d\omega}{dt} - \frac{1}{C_\mathrm{s}} \frac{di_{\mathrm{oq}}^n}{dt} \end{aligned}$$

$$L_g = \frac{1}{L_\mathrm{s}C_\mathrm{s}}$$

$L_{fi}(x)$ are the nonlinearities, interactions between states, and external disturbance, which can be defined as the perturbation of the linearized subsystems. The

lumped perturbation that is presented by the positive- and negative-sequence perturbation is as follows

$$\begin{cases} L_{f1}(x) = L_{f1}^{p}(x) + L_{f1}^{n}(x) \cdot e^{-j2\omega t} \\ L_{f2}(x) = L_{f2}^{p}(x) + L_{f2}^{n}(x) \cdot e^{-j2\omega t} \end{cases} \tag{4.4.3}$$

The perturbation terms can be obtained using the state and perturbation observers (SPOs).

4.4.3 State and Perturbation Observer

As both the positive- and negative-sequence perturbations can be estimated independently, only the positive-sequence perturbations estimations are given here, and the negative-sequence perturbations are estimated in the same way.

Define $z_{i1}^{p} = x_i^{p}$, $z_{i2}^{p} = \dot{x}_i^{p}$ and an additional state variable $z_{i3}^{p} = L_{fi}^{p}(x)$ $(i = 1, 2)$, an extended-order model of one subsystem is obtain as:

$$\begin{cases} y_i^{p} = z_{i1}^{p} \\ \dot{z}_{i1}^{p} = z_{i2}^{p} \\ \dot{z}_{i2}^{p} = z_{i3}^{p} + L_g u_i^{p} \\ \dot{z}_{i3}^{p} = \dot{L}_{fi}^{p}(\cdot) \end{cases} \tag{4.4.4}$$

The SPOs can be designed on the basis of derived input-output linearization function (4.4.4). There are several types of perturbation observers, such as sliding mode observer and linear Luenberger observer etc. In this chapter, high-gain observers are used in the SPOs design.

Define $\hat{z}_{i1}^{p}$ is the estimated value of z_{i1}^{p}, the observer function can be expressed as:

$$\begin{cases} \dot{\hat{z}}_{i1}^{p} = \hat{z}_{i2}^{p} + l_{i1}(y_i^{p} - \hat{z}_{i1}^{p}) \\ \dot{\hat{z}}_{i2}^{p} = \hat{z}_{i3}^{p} + l_{i2}(y_i^{p} - \hat{z}_{i1}^{p}) + L_g u_i^{p} \\ \dot{\hat{z}}_{i3}^{p} = l_{i3}(y_i^{p} - \hat{z}_{i1}^{p}) \end{cases} \tag{4.4.5}$$

The estimation gain l_{ij} of the high-gain SPOs can be expressed as [88]:

$$l_{ij} = \frac{\alpha_{ij}}{\epsilon_i^{j}}, \quad j = 1, 2, 3 \tag{4.4.6}$$

where ϵ_i is a small positive parameter specifies to represent the time-dynamics between the observer and the real system. The parameters α_{ij} are chosen such that the roots of

$$S^{r_i+1} + \alpha_{i1}S^{r_i} + \cdots + \alpha_{ir_i}S + \alpha_{i(r_i+1)} = 0 \tag{4.4.7}$$

To simplify the tuning process, the observer gains can be parameterized for a third-order SPO as:

$$\begin{bmatrix} \alpha_{i1} & \alpha_{i2} & \alpha_{i3} \end{bmatrix} = \begin{bmatrix} 3\alpha_0 & 3\alpha_0^2 & \alpha_0^3 \end{bmatrix}^T \tag{4.4.8}$$

where α_0 is the observer bandwidth and is the only parameter that needs to be tuned.

From (4.4.3), the lumped perturbation estimations that include both positive- and negative-sequence components are presented as

$$\begin{cases} \hat{z}_{i2} = \hat{z}_{i2}^p + \hat{z}_{i2}^n \cdot e^{-j2\omega t} \\ \hat{z}_{i3} = \hat{z}_{i3}^p + \hat{z}_{i3}^n \cdot e^{-j2\omega t} \end{cases} \tag{4.4.9}$$

4.4.4 Design of NAC

After the perturbation terms of subsystems are compensated by the estimated ones, the control v_i of the linearized second-order subsystems can be designed as

$$\frac{d^2 y_i}{dt^2} = v_i \tag{4.4.10}$$

Each subsystem can be controlled independently. To simplify the controller design, all subsystems are designed to have the same dynamic response in this chapter. The linear control law can be designed as:

$$v_i = k_1(y_{i,\text{ref}} - y_i) + k_2(\dot{y}_{i,\text{ref}} - \hat{z}_{i2}) + \ddot{y}_{i,\text{ref}} \tag{4.4.11}$$

where $y_{1,\text{ref}}$ and $y_{2,\text{ref}}$ are from the outer loop droop control.

By using the real-time estimated perturbation terms from the SPOs to compensate the real perturbations, the control inputs in positive- and negative-sequence can be obtained as:

$$u_i = L_g^{-1}\left(v_i - \hat{z}_{i3}^{p,n}\right) \tag{4.4.12}$$

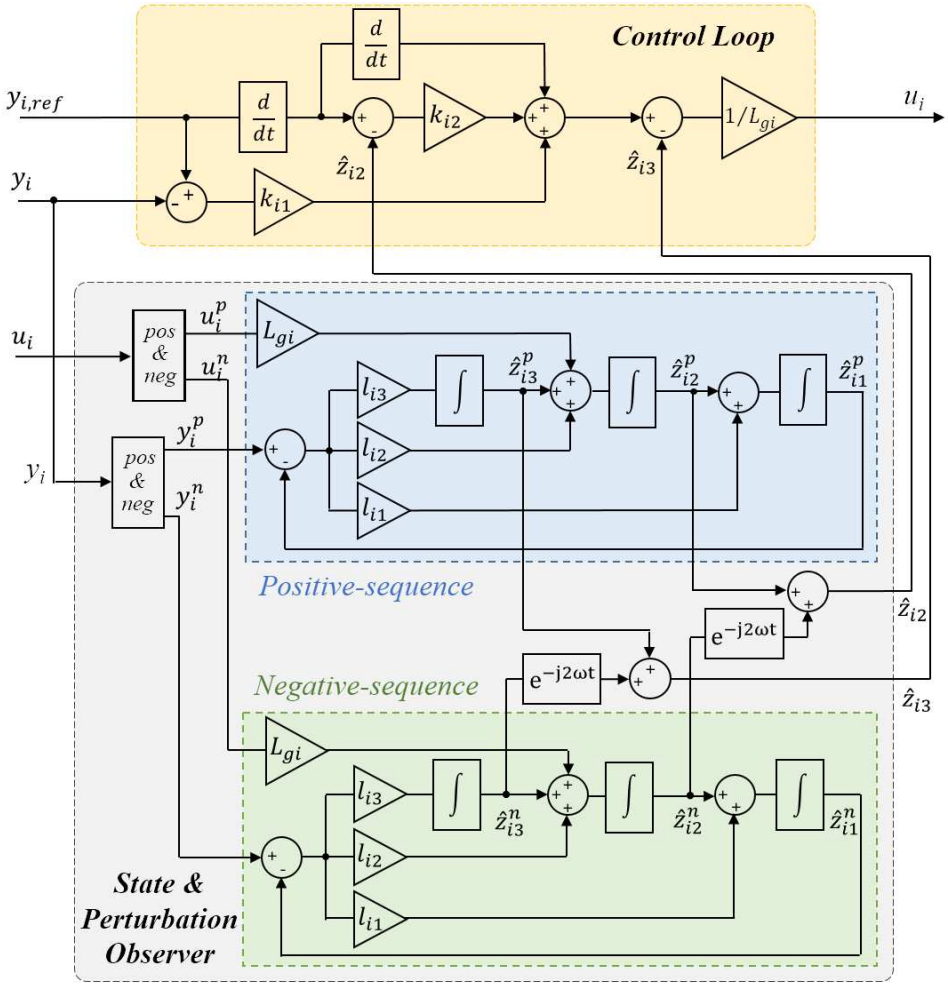

Figure 4.2: Block diagram of the nonlinear adaptive controller

Combining (4.4.9) and (4.4.11) into (4.4.12), the lumped control input that include both the positive- and negative-sequence components is obtained as:

$$u_i = L_g^{-1}\left[k_1(y_{i,\mathrm{ref}} - y_i) + k_2(\dot{y}_{i,\mathrm{ref}} - \hat{z}_{i2}) + \ddot{y}_{i,\mathrm{ref}} - \hat{z}_{i3}\right] \tag{4.4.13}$$

The schematic block diagram of the proposed NAC is shown in Figure 4.2. The final control outputs from the NAC controller represented by physical variables are

given as:

$$\begin{cases} v_{\mathrm{d}} = & L_{\mathrm{s}}C_{\mathrm{s}}[-\hat{z}_{13} + k_1(E^* + v^*_{\mathrm{zd}} - v_{\mathrm{od}}) + \\ & k_2(\dot{E}^* + \dot{v}^*_{\mathrm{zd}} - \hat{z}_{12}) + \ddot{E}^* + \ddot{v}^*_{\mathrm{zd}}] \\ v_{\mathrm{q}} = & L_{\mathrm{s}}C_{\mathrm{s}}[-\hat{z}_{23} + k_1(v^*_{\mathrm{zq}} - v_{\mathrm{oq}}) + \\ & k_2(\dot{v}^*_{\mathrm{zq}} - \hat{z}_{22}) + \ddot{v}^*_{\mathrm{zq}}] \end{cases} \tag{4.4.14}$$

NAC only requires the nominal value of L_{s} and C_{s}, and measurements of v_{od} and v_{oq}, all other states and parameter changes, including the $\Delta\omega$ adjusted by the outer loop power droop control, are included in the estimated perturbation terms.

4.4.5 Stability Analysis

The closed-loop system has been investigated via Lyapunove stability theory. Firstly, define the estimation error $\varepsilon^p_{i1} = z^p_{i1} - \hat{z}^p_{i1}$, $\varepsilon^p_{i2} = z^p_{i2} - \hat{z}^p_{i2}$, and $\varepsilon^p_{i3} = \Psi^p_i(\cdot) - \hat{z}^p_{i3}$. The positive-sequence error function of the SPOs in (4.4.5) can be rewritten in

$$\dot{[\varepsilon^p_i]} = [A^p_i][\varepsilon^p_i] + [W^p_i] \tag{4.4.15}$$

where $[A^p_i]$ is non-singular in both SPOs $(i = 1, 2)$.

For the estimation error system (4.4.15), consider the Lyapunov function $V_{i1} = [\varepsilon^p_i]^{\mathrm{T}} P_1 [\varepsilon^p_i]$. The high gains of SPOs (4.4.5) are determined by requiring (4.4.8) holds, which means A^p_i is Hurwitz. One can find a feasible positive definite solution, P_1, of Riccai equation $[A^p_i]^{\mathrm{T}} P_1 + P_1[A^p_i] = -I$. Similarly, define the Lyapunov function of negative-sequence error function as $V_{i2} = [\varepsilon^n_i]^{\mathrm{T}} P_2 [\varepsilon^n_i]$.

Secondly, define the tracking error of the subsystems as $e^p_{i1} = y^p_{i,\mathrm{ref}} - z^p_{i1}$ and $e^p_{i2} = \dot{y}^p_{i,\mathrm{ref}} - z^p_{i2}$. The linear control algorithm in (4.4.11) can be presented as:

$$v_i = k_{i1}(y_{i,\mathrm{ref}} - z_{i1}) + k_{i2}(\dot{y}_{i,\mathrm{ref}} - z_{i2}) = k_{i1}e_{i1} + k_{i2}e_{i2} \tag{4.4.16}$$

From (4.4.10), (4.4.12) and (4.4.16), the dynamics of the closed-loop error equation is obtained as

$$\begin{bmatrix} \dot{e}_{i1} \\ \dot{e}_{i2} \end{bmatrix} = \begin{bmatrix} 0 & 1 \\ -k_{i1} & -k_{i2} \end{bmatrix} \begin{bmatrix} e_{i1} \\ e_{i2} \end{bmatrix} + \begin{bmatrix} 0 \\ -\xi_i \end{bmatrix} \tag{4.4.17}$$

where $\xi_i = \varepsilon_{i3}^p + \varepsilon_{i3}^n \cdot e^{-j2\omega t}$ $(i = 1, 2)$, which includes the positive- and negative-sequence estimation error of the lumped perturbation.

Rewrite system (4.4.17) in

$$[\dot{e_i}] = [M_i][e_i] + [\Lambda_i] \tag{4.4.18}$$

and define its Lyapunov function as $V_{i3} = e_i^{\mathrm{T}} P_3 e_i$, where P_3 is the positive definite solution of the Lyapunov equation $M_i^{\mathrm{T}} P_3 + P_3 M_i = -I$.

Calculating the derivative of V_i along the solution of closed-loop system, and if $\|\varepsilon_i^p\| \geq \gamma_1$, $\|\varepsilon_i^n\| \geq \gamma_n$ and $\|e_i\| \geq \gamma_3$, it yields

$$\begin{aligned}
\dot{V}_i &= \varepsilon_i^{pT}\left(A_{i1}^T P_1 + P_1 A_{i1}\right)\varepsilon_i^p + W_i^{pT} P_1 \varepsilon_i^p + \varepsilon_i^{pT} P_1 W_i^p \\
&\quad + \varepsilon_i^{nT}\left(A_{i2}^T P_2 + P_2 A_{i2}\right)\varepsilon_i^n + W_i^{nT} P_2 \varepsilon_i^n + \varepsilon_i^{nT} P_1 W_i^n \\
&\quad + {e_i}^T\left(M_i^T P_3 + P_3 M_i\right) e_i + \Lambda_i^{pT} P_3 e_i + {e_i}^T P_3 \Lambda_i \\
&\leq -\|\varepsilon_i^p\|^2 + 2\|\varepsilon_i^p\| \cdot \|W_i^p\| \cdot \|P_1\| - \|\varepsilon_i^n\|^2 + \\
&\quad + 2\|\varepsilon_i^n\| \cdot \|W_i^n\| \cdot \|P_2\| - \|e_i\|^2 + 2\|e_i\| \cdot \|\Lambda_i\| \cdot \|P_3\| \\
&\leq -\|\varepsilon_i^p\|\left(\|\varepsilon_i^p\| - 2\gamma_1\|P_1\|\right) - \|\varepsilon_i^n\|\left(\|\varepsilon_i^n\| - 2\gamma_2\|P_2\|\right) \\
&\quad - \|e_i\|\left(\|e_i\| - 2\gamma_3\|P_3\|\right)
\end{aligned} \tag{4.4.19}$$

Then $V_i \leq 0$ when $\|\varepsilon_i^p\| \geq 2\gamma_1\|P_1\|$ and $\|\varepsilon_i^n\| \geq 2\gamma_2\|P_2\|$. One can find that $\|\vartheta_i\| \leq \|K_i\|\gamma_3$ with $\|K_i\|$ based on $\|\varepsilon_i^{p,n}(t)\| \leq \zeta_{1,2}$. Thus there exists T_1, T_2, and T_3 such that

$$\begin{cases}
\|\varepsilon_i^p(t)\| \leq \zeta_1 = 2\gamma_1\|P_1\|, & \forall t \geq T_1 \\
\|\varepsilon_i^n(t)\| \leq \zeta_2 = 2\gamma_2\|P_2\|, & \forall t \geq T_2 \\
\|e_i(t)\| \leq 2\gamma_3\|P_3\| \leq 4\gamma_1\|K_i\|\|P_{1,2}\|\|P_3\|, & \forall t \geq T_3
\end{cases} \tag{4.4.20}$$

Setting $T = \max\{T_1, T_2, T_3\}$, it lead to that the error system is globally uniformly ultimately bounded (GUUB) within the time period of T.

Moreover, if $W_i^{p,n}$ are locally Lipschitz in their arguments, it will guarantee the exponential convergence of the observation error and closed-loop tracking error into [126]

$$\lim_{t\to\infty} \varepsilon_i^{p,n}(t) = 0 \quad \text{and} \quad \lim_{t\to\infty} e_i(t) = 0$$

Then it proved that the closed-loop system is stable with using the nonlinear adaptive controller. The power stage and control system of the NAC-based droop control the the DR is shown in Figure 4.3.

4.5 Simulation Results

The LV MG operating in island mode is simulated in PSCAD/EMTDC software environment with detailed switch model of VSCs. The proposed control method is validated in an islanded MG system which includes ESS, single-phase PV resources, and impedance load. The bus voltage and frequency of the MG are maintained by the converter-based ESS, which is controlled by the proposed NAC-based droop controller. To validate the dynamic response and stability, the MG system operates under unbalanced impedance load disturbance, and single-phase time-varying PV power generation disturbance. The performance comparison is among three control method: the cascade-PI based droop control without unbalance compensation, the cascade-PI based droop control with the FNS reactive power based UCR method, and the proposed NAC based droop control method. The parameters of the MG system are given in Table 4.1 and the controller parameters of NAC, whose parameters are tuned using the pole placement method to get the optimized performance, are given in Table 4.2.

4.5.1 Three-phase Motor Load

During the induction motor (IM) start-up, it influences the stability of MG via absorbing large currents. The transient procedure needs both reactive power for flux excitation and active power to overcome its rotational inertia. The motor load is a 3-phase induction motor that is chosen from the PSCAD library with its nominal power around 20kVA. Its start-up power is nearly four times its nominal power.

The simulation results of the cascade PI based controller and NAC controller under motor load disturbance are compared in Fig. 4.4. The transient response of the bus voltage controlled by NAC has about 7% voltage dip and no overshoot, as shown in Fig. 4.4(a). The entire transient response time last about 0.03s. As a comparison,

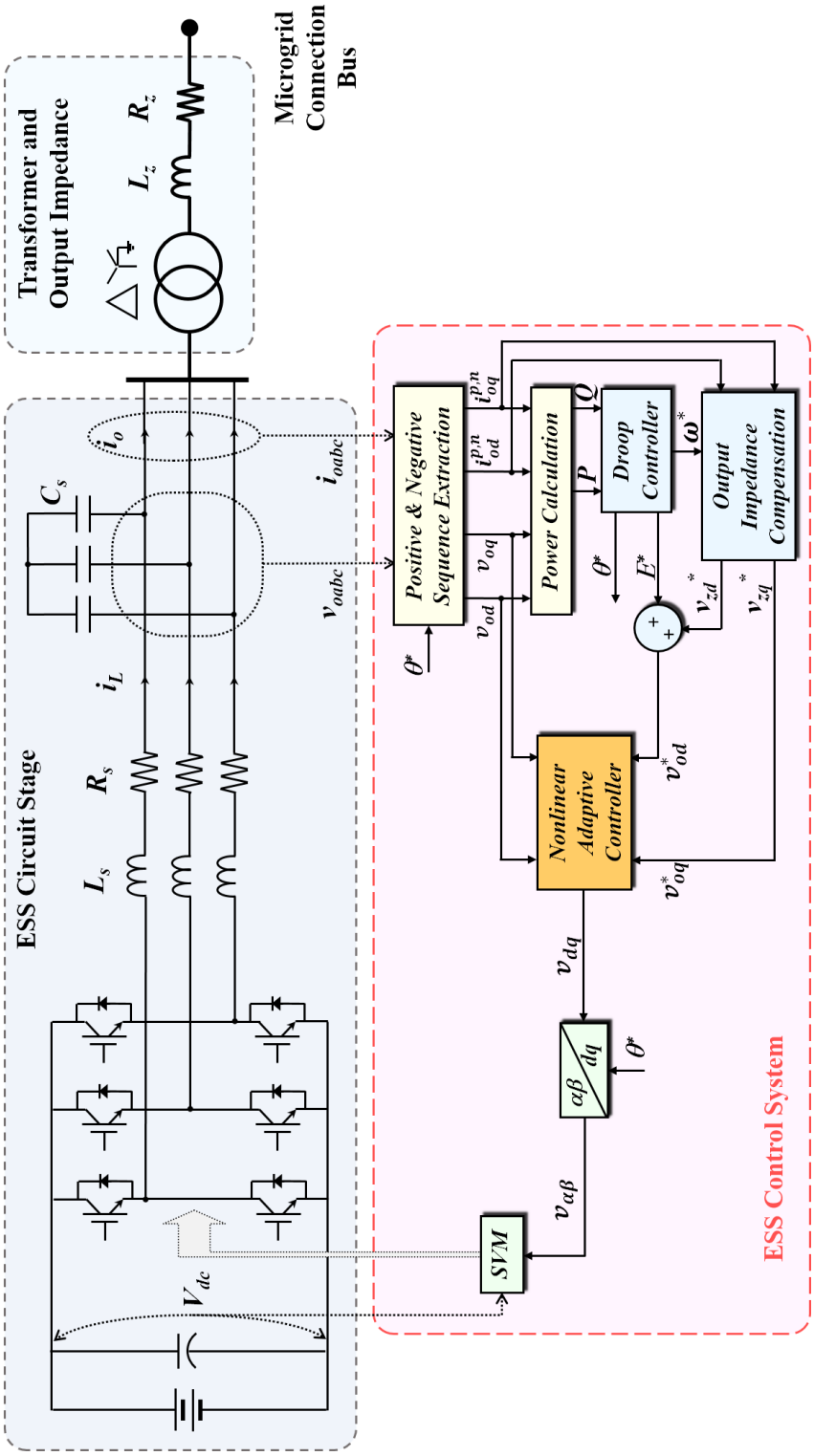

Figure 4.3: The power stage of an inverter based DR and its control system.

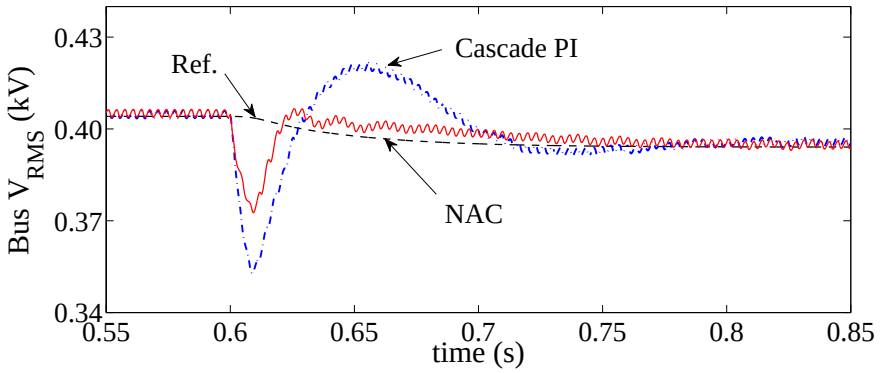

(a)

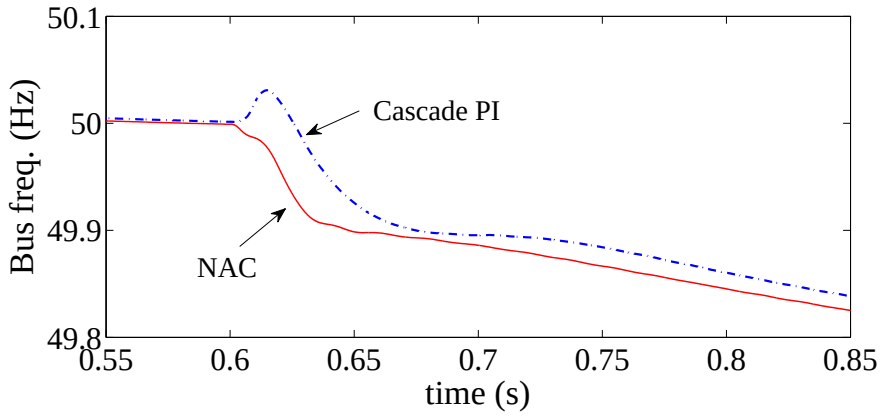

(b)

Figure 4.4: Comparison of (a) RMS bus voltage (kV) and (b) bus frequency (Hz) under induction motor startup.

Table 4.1: Parameters of MG System

Parameters	Values
MG rated bus voltage (rms/line-to-line)	v_{b} = 0.4 kV
MG rated bus frequency	f_{b} = 50 Hz
DC link voltage of DR	v_{dc} = 650 V
PWM frequency of DR	f_{PWM} = 2 kHz
Converter filter inductance (per phase)	L_{s} = 2.4 mH
Converter filter resistance (per phase)	R_{s} = 0.01 Ω
Converter filter capacitance (per phase)	C_{s} = 290 μF
Output transformer voltage ratio	n_{tr} = 1.5/4
Output transformer impedance (p.u.)	x_{tr} = 0.04
Output Inductance	L_{z} = 0.53 mH
Output resistance	R_{z} = 0.1 Ω
P-ω Droop gain	m = 0.126 rad/kW·s
Q-V Droop gain	n = 0.14 V/kVar

the cascaded PI controlled MG system has about 12% dip and 5% overshoot in bus voltage. The response time last about 0.15s, five times the result of using NAC-based droop controller. In Fig. 4.4(b), the steady-state frequency change is controlled by the P-ω droop. Comparing with the cascade PI based controller, the performance of the NAC based droop control has less influence under the transient impact of motor load. The negative-sequence perturbation terms L_{f3} and L_{f4} are both zero under the balanced 3-phase motor load. The positive-sequence perturbations L_{f1} and L_{f2} that estimated by the SPOs in the NAC controller are shown in Fig. 4.5. The estimated perturbations have a transient error under sudden disturbance and track the real perturbation in steady states.

To further comparing the control performance numerically, the indices of maximum voltage dip and the IAE of voltage regulation is given in the Table 4.3.

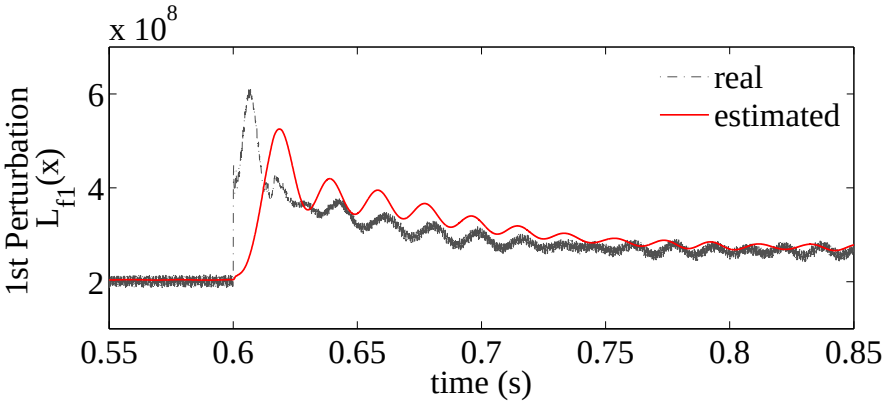

(a)

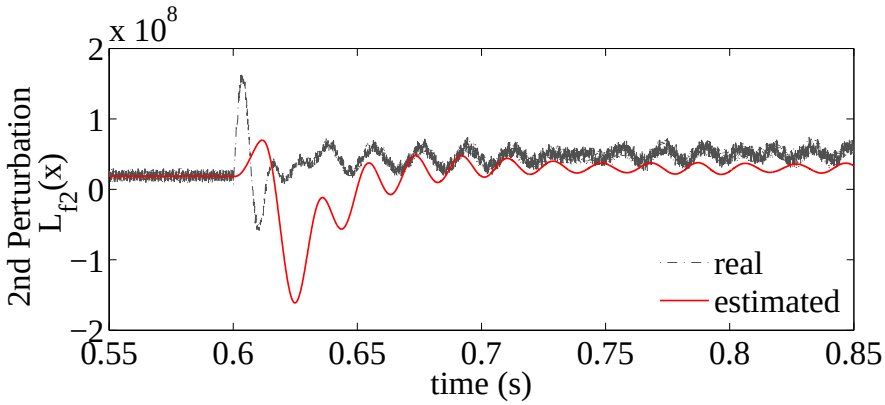

(b)

Figure 4.5: Comparison of the real and estimated perturbation terms. (a) the first perturbation term, (b) the second perturbation term.

Table 4.2: Parameters of NAC

Item	Symbol (i=1,2)	Values
SPOs	l_{i1}	6×10^5
	l_{i2}	1.2×10^9
	l_{i3}	8×10^{10}
Controller	k_{i1}	1000
	k_{i2}	5.7

Table 4.3: Performance indices comparison under three phase motor load

Indices \ Method	Cascade PI	NAC
Maximum voltage dip (kV)	0.04899	0.02987
Voltage IAE (kV·s)	2.366×10^{-3}	1.105×10^{-3}

4.5.2 Unbalanced Impedance Load

The unbalanced network conditions are significant in a practical scenario of MG as unbalanced generators and loads might be included. The controller of the converter-based DR have to eliminate the voltage unbalance in islanded MG when the unbalanced disturbances occurred. The impedance load, which is the most commonly used equivalent load, can be seen as a transient disturbance to the MG system. The droop control is to reduce the reference of the frequency and voltage amplitude when active power and reactive power is absorbed by the load, respectively. In this case, a single-phase impedance load, which includes both resistive and inductive elements, is connected to the MG bus.

Figure 4.6 shows the RMS value of bus voltage in kV that is comparing among the cascade-PI based droop control without and with the UCR method, and the NAC method. The frequency tracking performance and instantaneous three-phase bus voltage are shown in Figure 4.7 and 4.8, respectively. From the bus voltage waveform, it is obviously to find the difference of the unbalanced three-phase voltage among the three control methods. In addition, the voltage unbalance factor (VUF) of the MG bus voltage is compared as the index of power quality. The VUF is

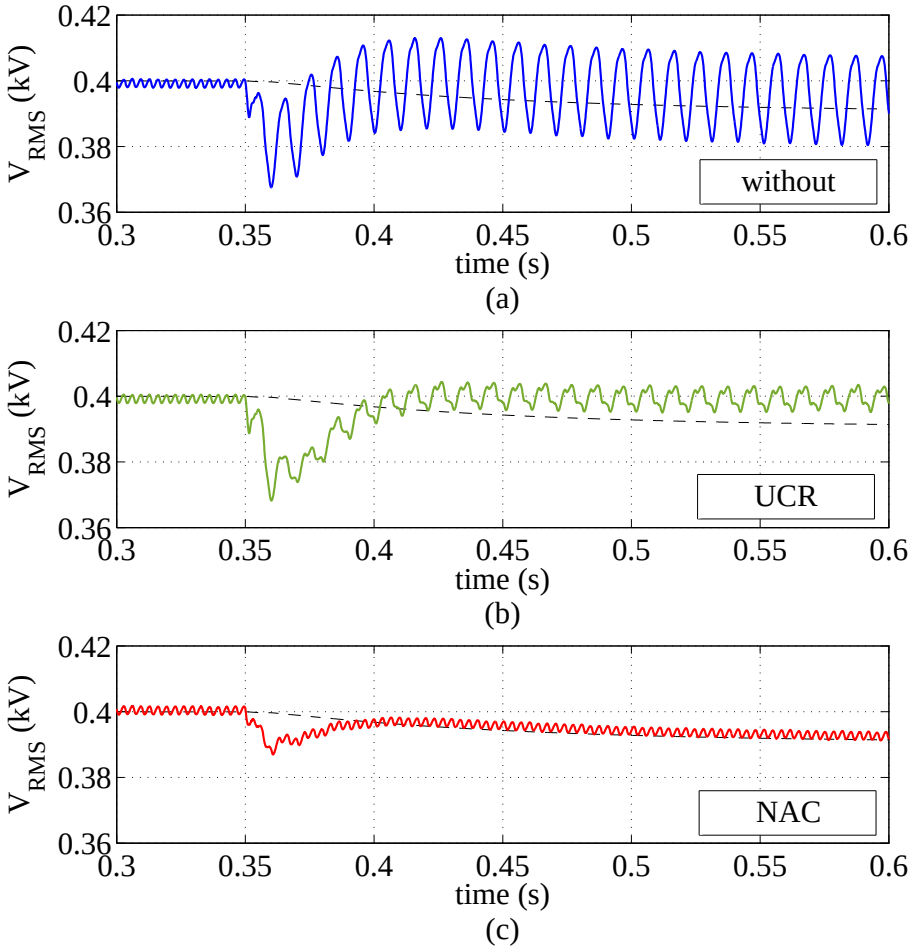

Figure 4.6: Comparison of RMS bus voltage amplitude under unbalanced load among (a) the conventional control method without unbalance compensation, (b) the conventional method with UCR, and (c) the proposed NAC.

defined as follows [142, 149]:

$$VUF = \frac{v^n_{\mathrm{b(rms)}}}{v^p_{\mathrm{b(rms)}}} \times 100\% \tag{4.5.1}$$

where $v^p_{\mathrm{b(rms)}}$ and $v^n_{\mathrm{b(rms)}}$ are the positive- and negative-sequences of bus voltage in RMS value. The VUF comparison are shown in Figure 4.9 among the three control methods.

The comparison results are summarized in Table 4.4 in terms of six performance indices: the maximum voltage dip, voltage IAE, the maximum frequency regulation error, frequency IAE, the maximum VUF, and average VUF in steady-state. The

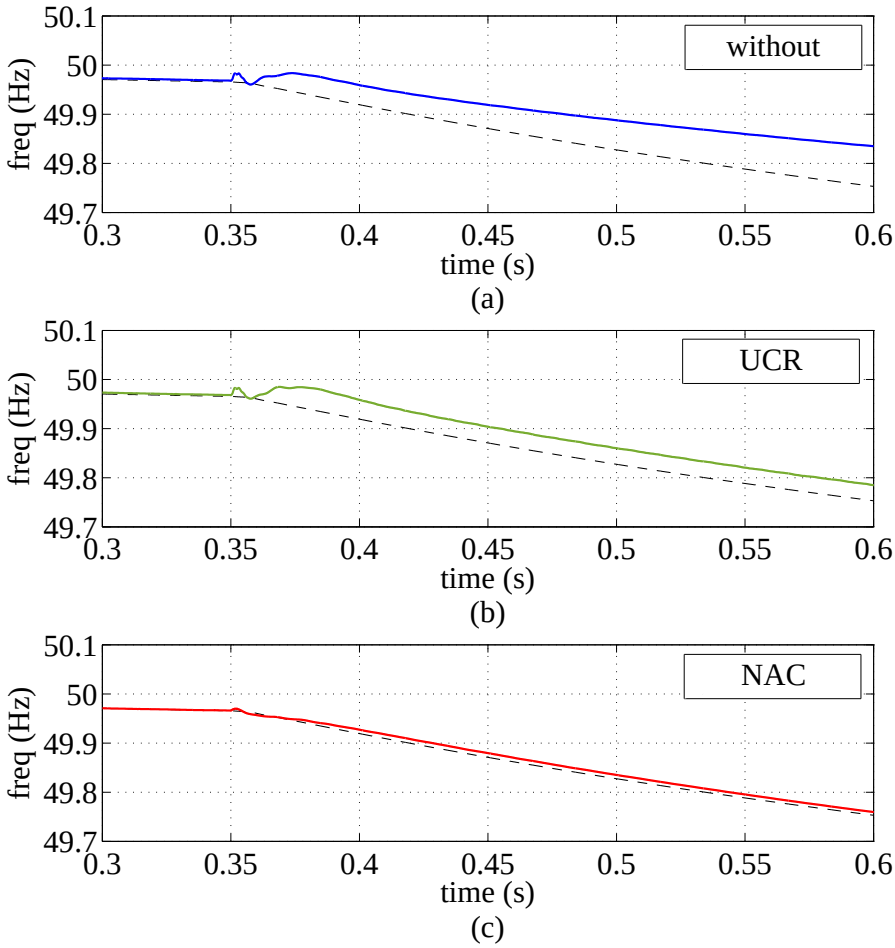

Figure 4.7: Comparison of bus frequency under unbalanced load among (a) the conventional control method without unbalance compensation, (b) the conventional method with UCR, and (c) the proposed NAC.

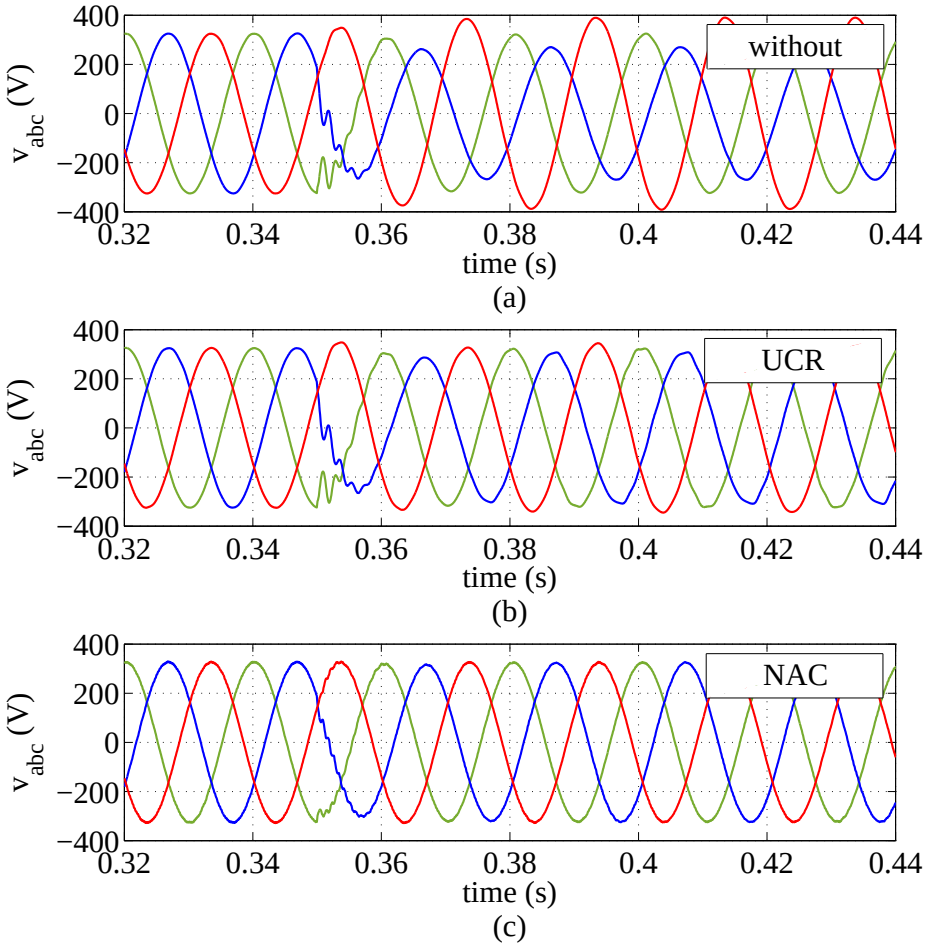

Figure 4.8: Comparison of bus voltage waveform under unbalanced load among (a) the conventional control method without unbalance compensation, (b) the conventional method with UCR, and (c) the proposed NAC.

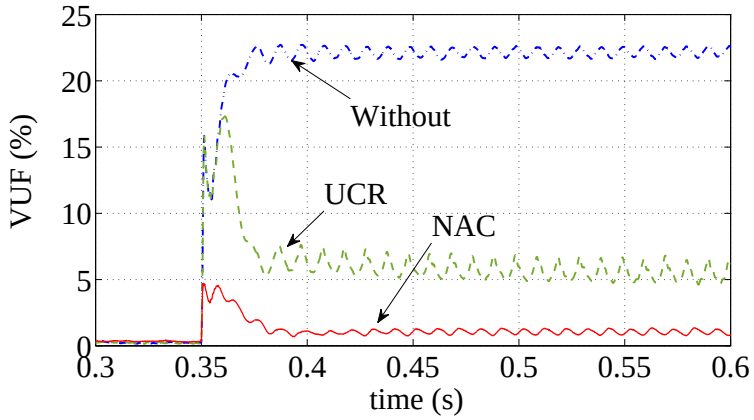

Figure 4.9: Voltage unbalance factor comparison under unbalanced load.

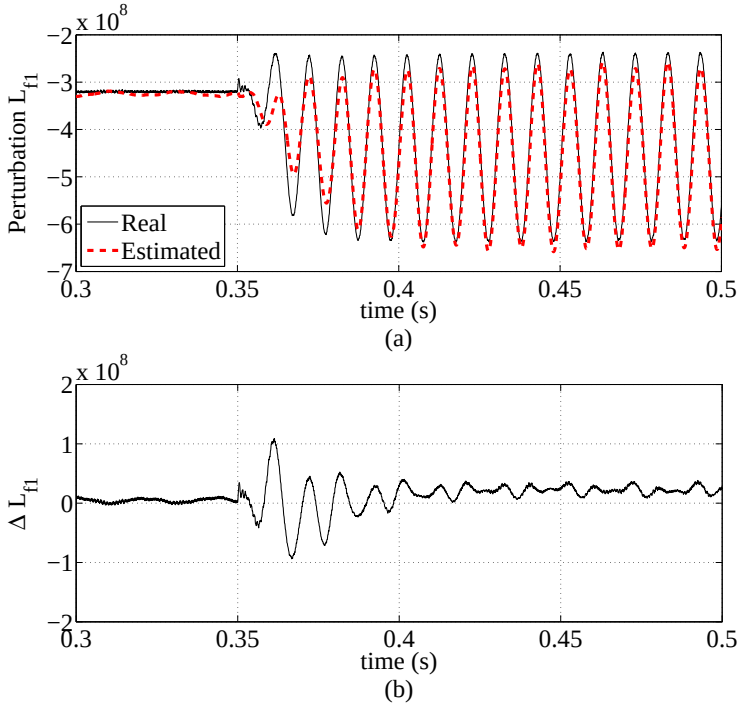

Figure 4.10: Comparison of real and estimated perturbation terms L_{f1} and its estimation error ΔL_{f1} under unbalance impedance load.

RMS bus voltage comparison result shows that the NAC has 59.6% less voltage dip and 62.5% less IAE than the cascade-PI based control method under sudden unbalanced impedance load disturbance, the maximum frequency error and IAE are 80.3% and 79.5% less, respectively. The index of VUF shows that the cascade-PI based droop control without unbalance compensation has significant impact by the unbalanced load and cannot eliminate the unbalanced voltage, which has about 22% VUF in steady state. The UCR method compensates the voltage unbalance obviously, whose maximum VUF is 17.3% when the unbalanced load connected and then eliminated to 5.3% at steady state. The NAC has faster response speed and better performance in eliminating the VUF. The maximum and steady state VUF are 4.7% and 1.0%, respectively.

The estimation results of the two perturbation terms from SPOs in NAC are shown in Figure 4.10 and 4.11. At 0.35s, the unbalance impedance load is connected to the MG bus, and the SPOs estimate the perturbations with negative-sequence components, which are the ac terms in twice the foundational frequency seen from

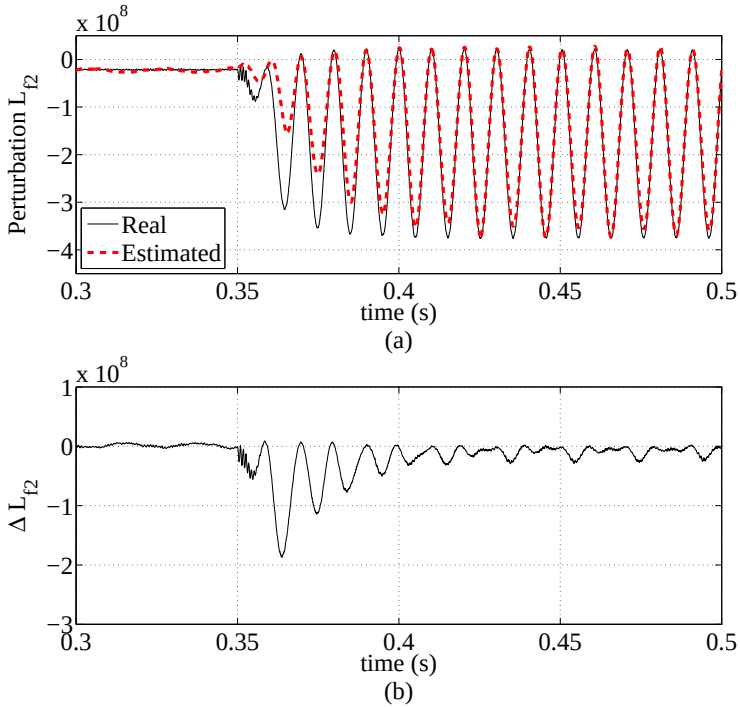

Figure 4.11: Comparison of real and estimated perturbation terms L_{f2} and its estimation error ΔL_{f2} under unbalance impedance load.

the positive-sequence frame. The estimated perturbations catch up the real perturbation terms with the estimation error less than 10%. The estimated L_{f1} and L_{f2} are used to compensate the real perturbation terms to eliminates the voltage unbalance and disturbance in the bus voltage of MG system.

4.5.3 Single-phase PV Power Generation to the Microgrid

In this case, the controller is validated under the single-phase power generation from a PV resource in the MG. The solar power input is given as a time-varying dc current source in the grid-connected PV system, and the time-varying power disturbance is injected by the single-phase PV to the MG.

The performance of RMS value of bus voltage, frequency tracking, and instantaneous three-phase bus voltage comparing among the three control method are shown in Figure 4.12, 4.13 and 4.14, respectively. The harmonics in the bus voltage is higher than that in the load disturbance due to the power electronic devices in the PV power generation system bring more harmonics in its output power to the MG.

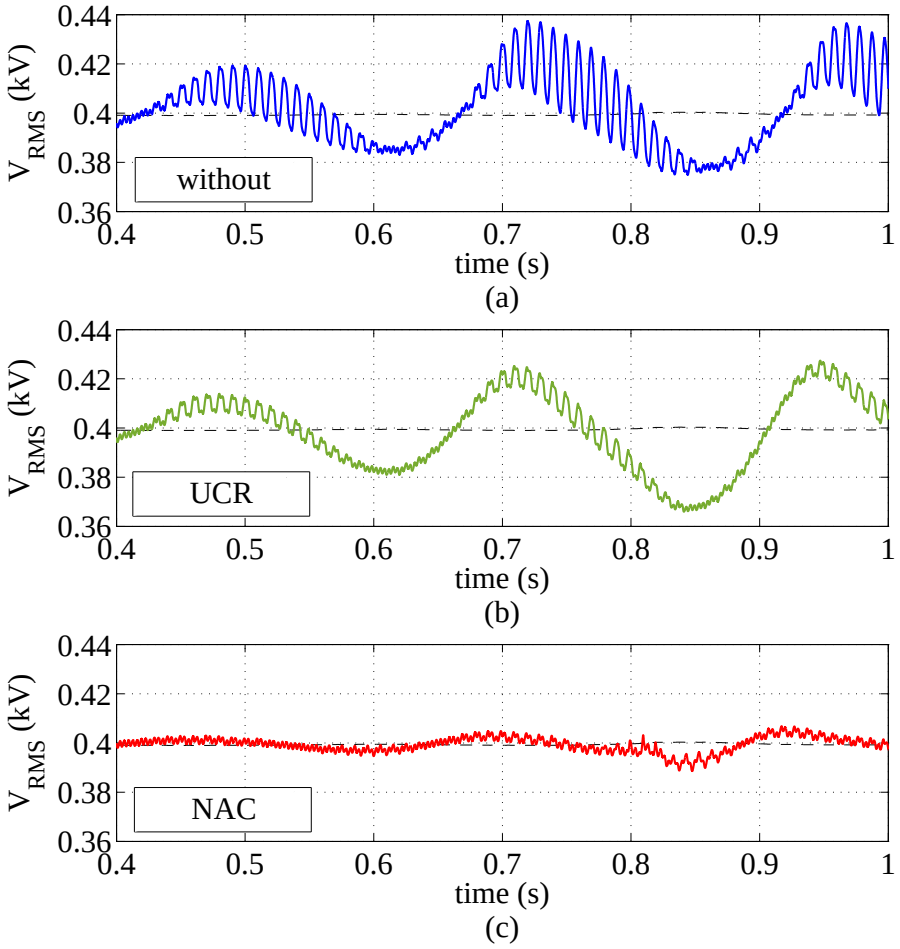

Figure 4.12: Comparison of RMS bus voltage amplitude under single-phase power generation among (a) the conventional control method without unbalance compensation, (b) the conventional method with UCR, and (c) the proposed NAC.

The performance indices are chosen the same with that in the first case and given in Table 4.4. Comparing between the NAC and the method of cascade-PI with UCR, the RMS voltage of using NAC has 69.1% less maximum voltage error and 79.6% less IAE under single-phase power generation, the maximum frequency error and IAE of NAC are 63.4% and 65.8%, respectively, less than the cascade-PI with UCR method.

The VUF comparison result in Figure 4.15 shows that the NAC performs the best in eliminating the unbalanced voltage. Both the UCR and NAC has obvious effectiveness in eliminating the unbalance voltage under single-phase power gener-

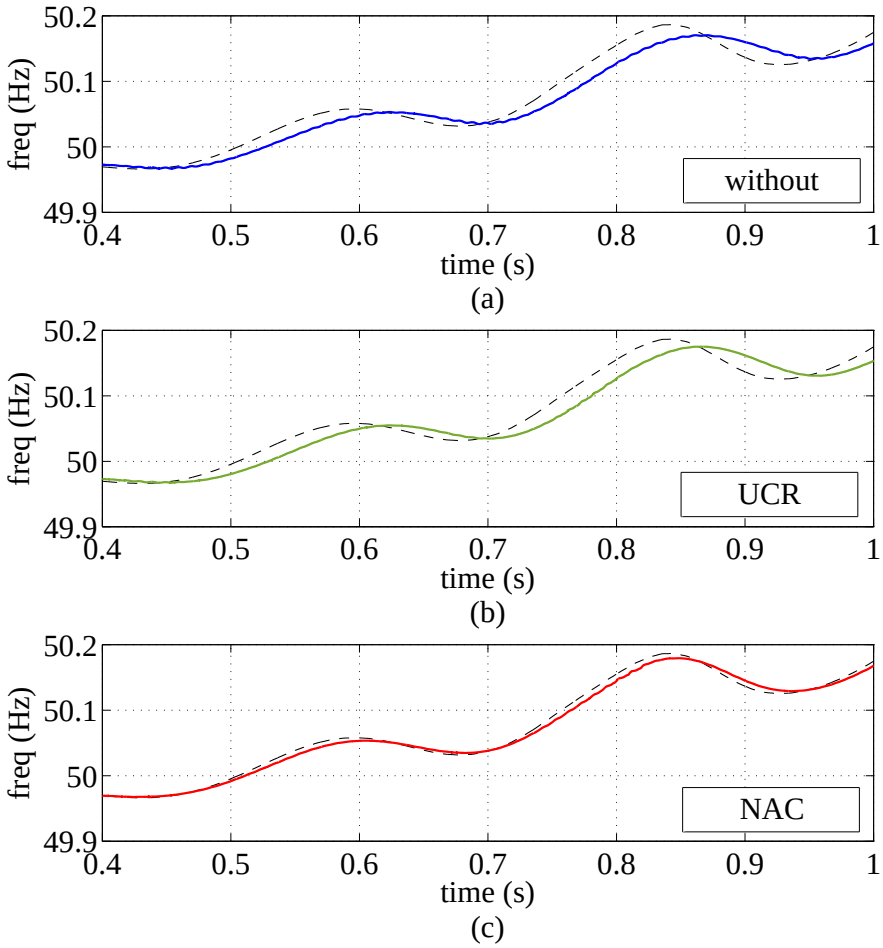

Figure 4.13: Comparison of bus frequency under single-phase power generation among (a) the conventional control method without unbalance compensation, (b) the conventional method with UCR, and (c) the proposed NAC.

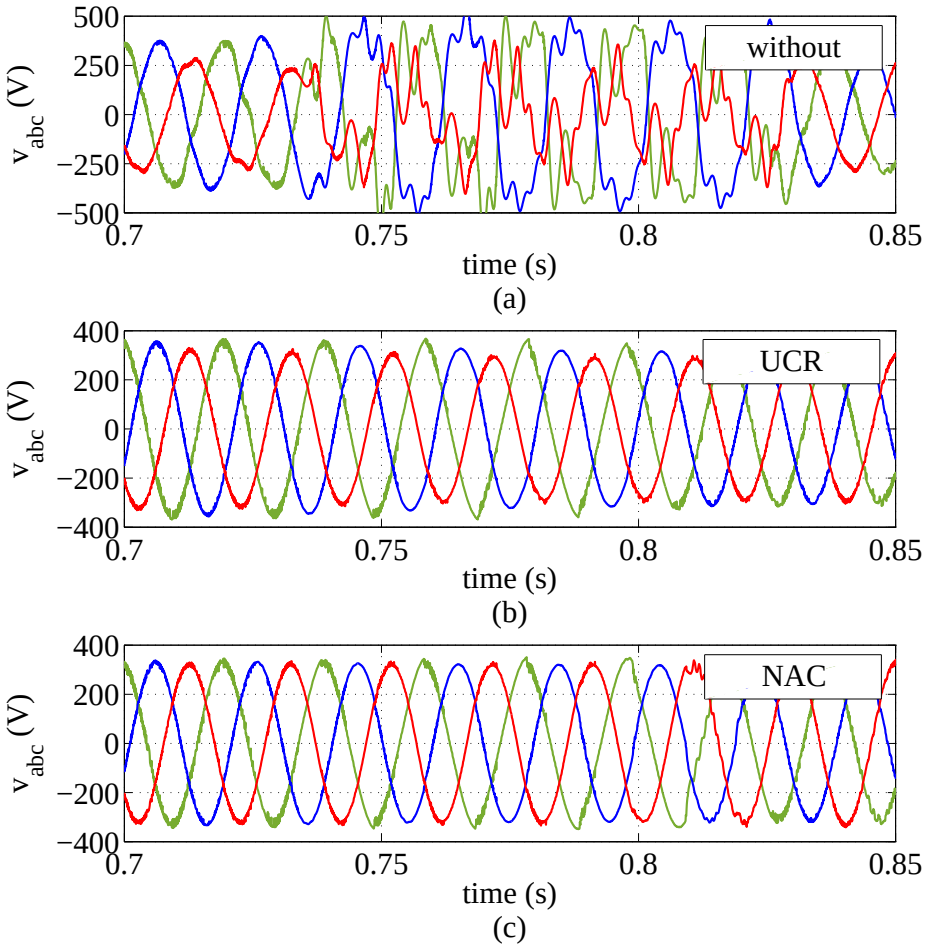

Figure 4.14: Comparison of bus voltage waveform under single-phase power generation among (a) the conventional control method without unbalance compensation, (b) the conventional method with UCR, and (c) the proposed NAC.

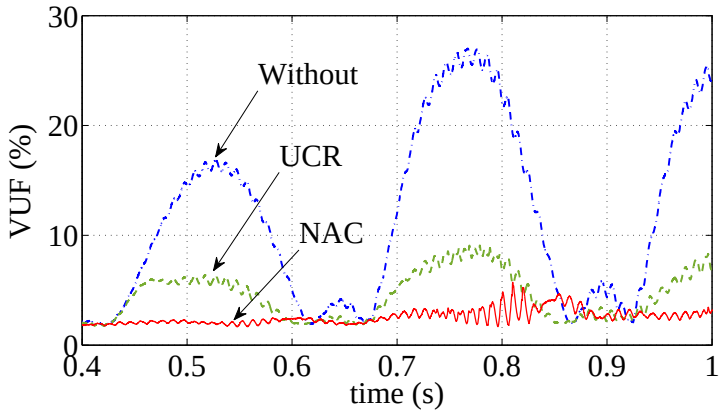

Figure 4.15: Voltage unbalance factor comparison under single-phase power generation.

Table 4.4: Performance indices comparison under unbalance load disturbance

Indices \ Method	without	UCR	NAC
Case: Unbalance load disturbance			
Maximum voltage dip (kV)	0.0321	0.0314	0.0127
Voltage IAE (kV·s)	1.64×10^{-3}	1.32×10^{-3}	0.495×10^{-3}
Maximum frequency error (Hz)	0.164	0.0450	0.00884
Frequency IAE (Hz·s)	6.78×10^{-3}	5.37×10^{-3}	1.10×10^{-3}
Maximum VUF (%)	22.7	17.3	4.73
Average VUF (%)	22.1	5.25	1.03
Case: Single-phase power generation			
Maximum voltage error (kV)	0.0384	0.0385	0.0119
Voltage IAE (kV·s)	1.55×10^{-2}	1.77×10^{-2}	0.361×10^{-2}
Maximum frequency error (Hz)	0.0338	0.0325	0.0119
Frequency IAE (Hz·s)	1.63×10^{-2}	1.73×10^{-2}	0.592×10^{-2}
Maximum VUF (%)	27.4	9.37	5.81
Average VUF (%)	11.2	4.45	2.76

ation. And the bus voltage controlled by NAC has about 38% less VUF than that of the UCR unbalance compensation method. The PI based control method is using the cascaded loop to regulate the current in the inner loop and voltage in the outer loop. While the NAC is estimating the lumped perturbation which includes the dynamic of input and output and disturbance and compensate the perturbation to the system input. This makes the control performance of NAC far better than that of the cascaded PI control. However, at 0.81 s in Figure 4.14 (c) and 4.15, the NAC has affected by the harmonics because of the high-gain perturbation observer is sensitive to the noise, which is the main drawback of using a high-gain observer. Thus, the observer bandwidth needs to be turned to filter the sensor noise for an optimal performance.

The estimation results of the perturbations as shown in Figure 4.16 and 4.17. The ac components is from the negative-sequence voltage, which increases with the rising of generated power from the single-phase PV resource. The unbalance

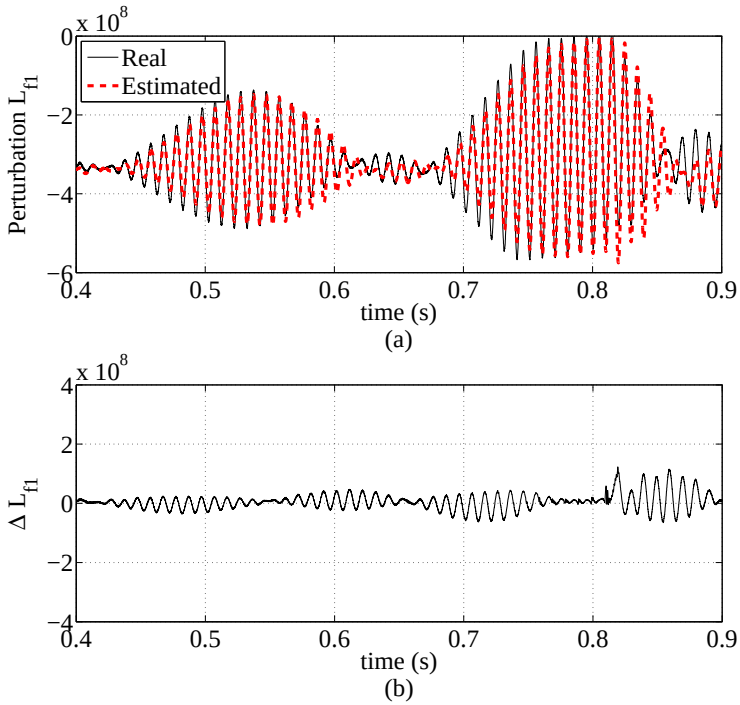

Figure 4.16: Comparison of real and estimated perturbation terms L_{f1} and its estimation error ΔL_{f1} under single-phase power generation condition.

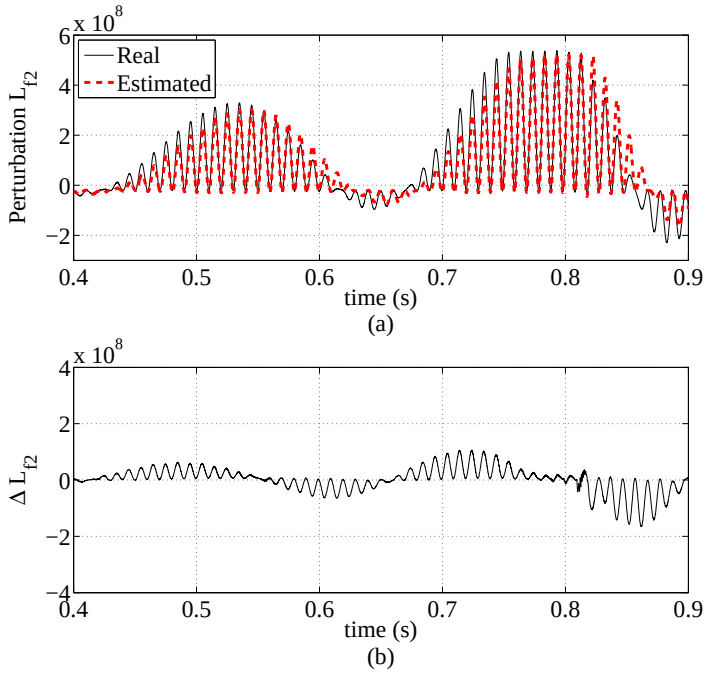

Figure 4.17: Comparison of real and estimated perturbation terms L_{f2} and its estimation error ΔL_{f2} under single-phase power generation condition.

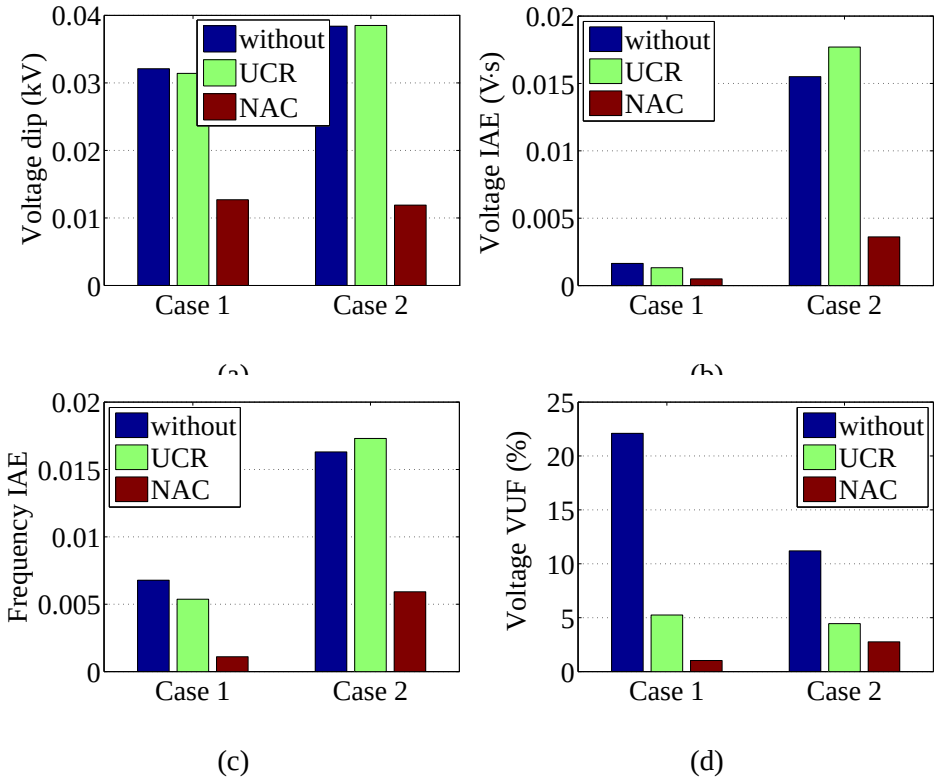

Figure 4.18: Indices comparison between BESS and HESS in the bus voltage (a) IAE, (b) VUF, and battery performance (c) accumulate DOD, (d) average efficiency.

power generation disturbance is time-varying which makes the estimated perturbation terms has time-varying estimation error. Nevertheless, the effectiveness of the compensation is demonstrated that the estimated perturbation terms from SPOs compensates the real perturbations and eliminate the disturbance and voltage unbalance.

4.6 Conclusion

In this chapter, a nonlinear adaptive controller for the voltage source converter-based distributed resource has been designed to improve the robustness of an islanded microgrid by compensating the voltage unbalance and disturbances. Based on the dynamic model of converter-based DR in dual synchronous reference frames, the state and perturbation observers have been designed to estimate the unknown and time-varying nonlinearities, external disturbances and voltage unbalance, which are

defined in the lumped perturbation terms. The estimated perturbation dynamics are used to compensate the real perturbations for linearizing the system, and the linearized system is controlled by a linear control law. The NAC controller has been validated in an islanded MG under unbalanced impedance load and single-phase PV generation in PSCAD/EMTDC simulation environment. Simulation results show that, comparing with the cascaded PI based controller, the NAC maintains the bus voltage with less voltage dip and faster voltage unbalance compensation under single-phase disturbance in the MG. The parameter uncertainty, such as the change of resistance, inductance and capacitance of system, will be considered in the future work.

Chapter 5

Coordinated Control of a Hybrid Energy Storage System with Battery and Supercapacitor for Microgrid

5.1 Introduction

Modern power system is developed with a large number of DRs, including both the renewable energy generations, such as wind turbine, PV and wave generation, and nonrenewable generations, such as fuel cell and micro-turbine [7]. This leads the increased use of power electronics in the power generation, transmission/distribution and end-user stage [6]. Those power-electronics-enabled power systems (PEEPS) have been applied in the more electric aircraft [21–23], ship board power system [19], and the LV-MG [24–27]. The MG is a typical LV PEEPS with more renewable energy resources, which makes the MG weak in both its stiffness and inertia comparing with the utility power grids [25–27].

Due to the renewable energy is unpredictable, alternative resources are needed when the renewable energy DRs cannot supply enough power to the MG. The controllable micro-sources, such as micro-turbines and fuel-cells, are good alternative resources. But their response speed are not fast enough to handle the fast-changing disturbances, and they are uni-directional power source which can only output pow-

er to the grid. Thus, the micro-sources can be only used as the auxiliary sources. The energy storage system (ESS), such as battery, flywheel and supercapacitor (SC), are used for balancing the power difference between generation side and demand side due to their particular features of fast response speed, bi-direction power flow, and weather independency [28–36], as shown in Figure 5.1. Consider that the battery has a high energy capacity while low in power density, and the SC has much higher power densities and extremely high cycling capability with less maintenance, a hybrid energy storage system (HESS) combining battery and SC together can provide both high power density and energy capacities [150, 151]. Due to time-varying and unpredictable renewable power generation, large amount of DRs in the MG cause the frequent charging-discharging cycles of ESS, which increases the accumulate depth of discharge (DOD) and reduces the lifetime of battery [150], and thus it is not economical to use battery for energy storage in a MG.

The battery-supercapacitor based HESSs have been applied in electric vehicle [28, 29, 152], wind power generation system [30], PV generation system [31], other renewable energy sources [34], and DC microgrid [32, 153]. Some coordinated control strategies for the HESS in an AC microgrid are presented, such as using fast fourier transfer to decompose the low-frequency and high-frequency power of fluctuant loads [154]; using the SC to compensate the harmonic and unbalance of current outputs from battery to enhance the power quality [155], etc. The previous coordinated control strategies have not been designed to control the battery and SC individually with different purposes for optimizing their usage efficiency based on their features.

This chapter proposes a coordinated control strategy for the HESS that controls the battery and SC with different objectives based on their features in order to improve the transient response of the MG bus voltage and reduce the accumulate DOD of battery. The battery and SC are interfaced with individual VSCs connecting to the MG. The proposed control strategy controls the SC to balance the fast unbalanced power whereas the battery to produce the balanced active power in steady state for less unnecessary loss.

The remainder of this chapter is organized as follows. Section 5.2 presents the

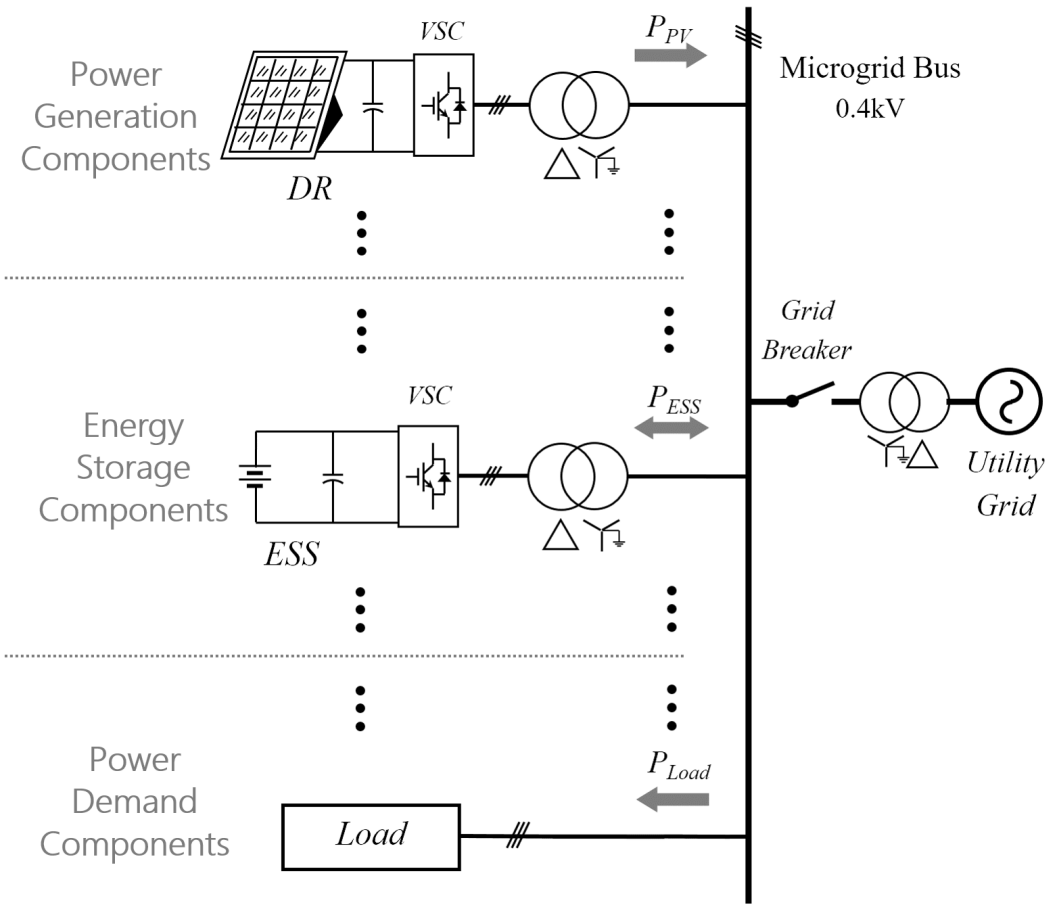

Figure 5.1: Scheme of microgrid including renewable power resource, customer load, and energy storage system.

dynamic model of battery, supercapacitor, and VSC. Section 5.3 presents the design of coordinated control strategy for battery-SC based HESS. The simulation validation result of the proposed control strategy is presented in Section 5.4. The chapter is finally concluded in Section 5.5.

5.2 Model of Energy Storage System

5.2.1 Battery model and state of charge

The electrical models of battery used in literatures can be divided into two categories: the low-power application that neglects the thermal effect, and high-power application that includes the impact of temperature in battery performance [156]. This chapter use the electrical model of battery without the temperature impact as the temperature is not a direct control objective that considered in this chapter. The terminal voltage of a battery is presented from the Thevenin battery model depending on the open circuit voltage (OCV) V_{ocv}, the internal resistance R_{i}, and the paralleled RC circuit as shown in Figure 5.2(a). The battery transient behaviour corresponding to the load change is represented by the transient contact resistance R_{T} with a paralleled capacitor C_{T}. The battery OCV is depending on its actual state of charge (SOC) with a non-linear equation. This term represents a non-linear voltage that changes with the amplitude of the current and the actual charge of the battery [4].

The dynamic model of battery is presented as [157]

$$V_{\mathrm{t}} = V_{\mathrm{OCV}} - R_{\mathrm{i}} \cdot I - V_{\mathrm{T}} \tag{5.2.1}$$

where

$$V_{\mathrm{OCV}} = E_0 - K\frac{Q_0}{Q_0 - \int idt} + Ae^{\left(-B\cdot\int Idt\right)} \tag{5.2.2}$$

$$V_{\mathrm{T}} = \frac{1}{C_{\mathrm{T}}}\int\left(I - \frac{V_{\mathrm{CT}}}{R_{\mathrm{T}}}dt\right) \tag{5.2.3}$$

where V_{T} is the voltage over the parallel transient resistor and capacitor, E_0 is the nominal battery voltage, Q_0 is the rated charge capacity, K is the polarization volt-

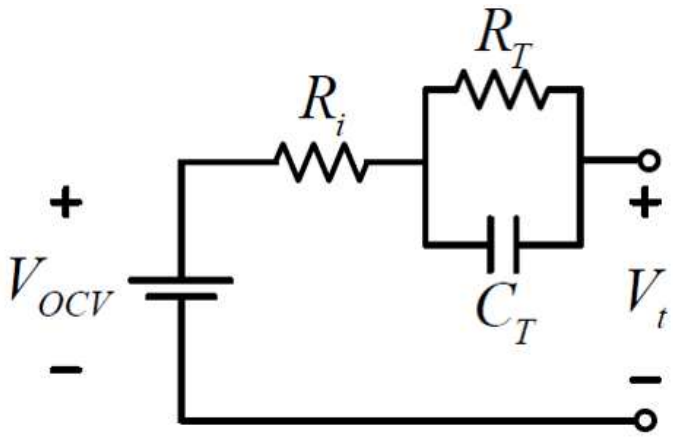

(a)

(b)

Figure 5.2: Equivalent circuit of (a) battery [4], and (b) supercapacitor [5].

age, A and B are the exponential zone amplitude and time constant inverse, respectively. In different types of batteries, the battery parameters are variable [157]. This chapter is not considering the battery aging, which decreases the battery fully charged capacity.

The SOC is defined as the ratio between the charge left in a battery and its rated capacity, and the DOD equals to the change of SOC in one discharge cycle. The SOC and DOD are presented as [151]

$$SOC = \frac{Q}{Q_0} \tag{5.2.4}$$

$$DOD = \Delta SOC = \frac{1}{Q_0} \int I(t)dt \tag{5.2.5}$$

where Q is the amount of charge at a given moment, I is the discharge current, and Q_0 is the nominal capacity of the battery, which is a fixed value.

5.2.2 Supercapacitor Model

The SC is a high power density energy storage device with good efficiency and much higher recharging cycles than batteries. The SC has a very fast dynamic response in charging and discharging operations. Its output voltage simultaneously reaches its steady state when it switches from maximum charging current to the maximum discharging current [158]. Thus, it is one of the most commonly used energy storage device for short-term power exchange.

Within the linear working region, the SC can be model by a fixed value capacitance and equivalent series resistance (ESR) accurately without considering the effect by temperature and other operation conditions [5]. The Thevenin equivalence circuit of SC is shown in Figure 5.2(b), whose dynamic model is presented as

$$V_{sc} = V_{co} - \frac{1}{C_s}\int idt - R_{ES} \cdot i \tag{5.2.6}$$

where V_{sc} is the terminal voltage of SC, V_{co} is its initial open circuit voltage, i is the discharging current, C_s and R_{ES} are the capacitance and equivalent series resistor of SC.

5.2.3 Model of voltage source converter

The VSCs are used to rebuild the output voltage from the ESS to be synchronized with the bus voltage of MG before connecting to the grid. The VSC based ESS are used to maintain the voltage and frequency of the AC MG when it faces the sudden disturbances, including load and generated power changes and short-circuit faults [25, 27]. The model of VSC with a LC filter considering the current and voltage dynamics in d-q axis is the same with that given in the previous chapter in (4.2.1). The d-q frame bus voltage references are defined as v^*_{od} and v^*_{oq}, and their tracking error are defined as $e_{\mathrm{d}}(t) = v_{\mathrm{od}}(t) - v^*_{\mathrm{od}}(t)$, $e_{\mathrm{q}}(t) = v_{\mathrm{oq}}(t) - v^*_{\mathrm{oq}}(t)$. Then it gives the control objective that is to obtain $e_{\mathrm{d}} = 0$ and $e_{\mathrm{q}} = 0$ as t approaching to infinite under sudden unbalanced load disturbance.

5.3 Control Strategy for HESS

The proposed coordinated control method is designed to use the supercapacitor as an energy buffer for the battery which filters the transient power and/or unbalanced power demand to reduce the overuse of battery. The controller for VSC base HESS is aiming at both improving the transient performance of MG bus voltage and reducing the battery loss. In this control strategy, the battery is controlled to provide the balanced power in steady-state while the supercapacitor (SC) is controlled to generate transient power and compensate the unbalanced power demand. Under unbalanced voltage condition, the steady state operation of SC is to provide the oscillated power with the mean value of zero. The battery generates the balanced power while the SC compensates the unbalanced power to minimize the recharging operation in the battery.

5.3.1 Controller for Battery VSC

In the HESS, the battery is to generate balanced power under unbalanced voltage condition in MG. The controller only focuses on the positive components of grid voltage to generate the reference of output current for cascaded inner loop current controller that are presented as

$$i_{\mathrm{d+}}^{*} = \left(k_p + \frac{k_i}{s}\right)\left(v_{\mathrm{dref}} - v_{\mathrm{od+}}\right) - \omega C v_{\mathrm{oq+}} \tag{5.3.1}$$

$$i_{\mathrm{q+}}^{*} = \left(k_p + \frac{k_i}{s}\right)\left(v_{\mathrm{qref}} - v_{\mathrm{oq+}}\right) + \omega C v_{\mathrm{od+}} \tag{5.3.2}$$

If the output current of battery VSC is controlled following the positive current reference above, the effect of the negative-sequence voltage will make the output power with oscillation components that injected into the MG. Under the unbalanced voltage condition, the most common way for decoupling the sequence components is to synchronize them in the same frequency with opposite different direction, i.e. the positive-sequence frame rotates with the frequency of ω, while the negative-sequence frame rotates with the frequency of $-\omega$. Due to that the controller is designed under the rotating frame that is synchronized to the positive-sequence

voltage, the negative-sequence components also need to be transferred to the same coordinate. Then the negative-sequence components of voltages and currents are presented in periodical sine-wave signals with the frequency of 2ω, twice the bus voltage fundamental frequency of MG.

The instantaneous active power function has been studied in previous literatures for power quality analysis of transmission power grid [159], and this chapter uses the similar method for the controller design. The instantaneous active power function is represented as

$$\begin{aligned} p =& v_{\mathrm{od}} i_{\mathrm{d}} + v_{\mathrm{oq}} i_{\mathrm{q}} \\ =& (v_{\mathrm{od}+} + v_{\mathrm{od}-})(i_{\mathrm{d}+} + i_{\mathrm{d}-}) + (v_{\mathrm{oq}+} + v_{\mathrm{oq}-})(i_{\mathrm{q}+} + i_{\mathrm{q}-}) \\ =& \underbrace{v_{\mathrm{od}+} i_{\mathrm{d}+} + v_{\mathrm{oq}+} i_{\mathrm{q}+} + v_{\mathrm{od}-} i_{\mathrm{d}-} + v_{\mathrm{oq}-} i_{\mathrm{q}-}}_{P} + \\ & \underbrace{v_{\mathrm{od}+} i_{\mathrm{d}-} + v_{\mathrm{od}-} i_{\mathrm{d}+} + v_{\mathrm{oq}+} i_{\mathrm{q}-} + v_{\mathrm{oq}-} i_{\mathrm{q}+}}_{\widetilde{p}} \end{aligned} \tag{5.3.3}$$

where P and $\widetilde{p}$ present the average power and oscillation power components respectively; $v_{\mathrm{od}+}$, $v_{\mathrm{oq}+}$, $i_{\mathrm{d}+}$ and $i_{\mathrm{q}+}$ are the positive-sequence components of output voltage and current in d-q axis; $v_{\mathrm{od}-}$, $v_{\mathrm{oq}-}$, $i_{\mathrm{d}-}$ and $i_{\mathrm{q}-}$ are the negative-sequence components of output voltage and current in the reference frame of positive-sequence d-axis.

To eliminate the power oscillation, let $\widetilde{p} = 0$, and assume $v_{\mathrm{oq}+} = 0$ in steady state, the d-axis negative-sequence current can be presented as

$$i_{d-} = -\frac{v_{\mathrm{od}-}}{v_{\mathrm{od}+}} i_{\mathrm{d}+} - \frac{v_{\mathrm{oq}-}}{v_{\mathrm{od}+}} i_{\mathrm{q}+} \tag{5.3.4}$$

Then the reference d-axis current reference can be designed as

$$i_{\mathrm{d}}^{*} = i_{\mathrm{d}+}^{*} + i_{\mathrm{d}-}^{*} = \left(1 - \frac{v_{\mathrm{od}-}}{v_{\mathrm{od}+}}\right) i_{\mathrm{d}+}^{*} - \frac{v_{\mathrm{oq}-}}{v_{\mathrm{od}+}} i_{\mathrm{q}+}^{*} \tag{5.3.5}$$

Similarly, the instantaneous reactive power can be obtained as

$$\begin{aligned} q =& \underbrace{v_{\mathrm{oq}+} i_{\mathrm{d}+} - v_{\mathrm{od}+} i_{\mathrm{q}+} + v_{\mathrm{oq}-} i_{\mathrm{d}-} + v_{\mathrm{od}-} i_{\mathrm{q}-}}_{Q} + \\ & \underbrace{v_{\mathrm{oq}-} i_{\mathrm{d}+} - v_{\mathrm{od}-} i_{\mathrm{q}+} + v_{\mathrm{oq}+} i_{\mathrm{d}-} - v_{\mathrm{od}+} i_{\mathrm{q}-}}_{\widetilde{q}} \end{aligned} \tag{5.3.6}$$

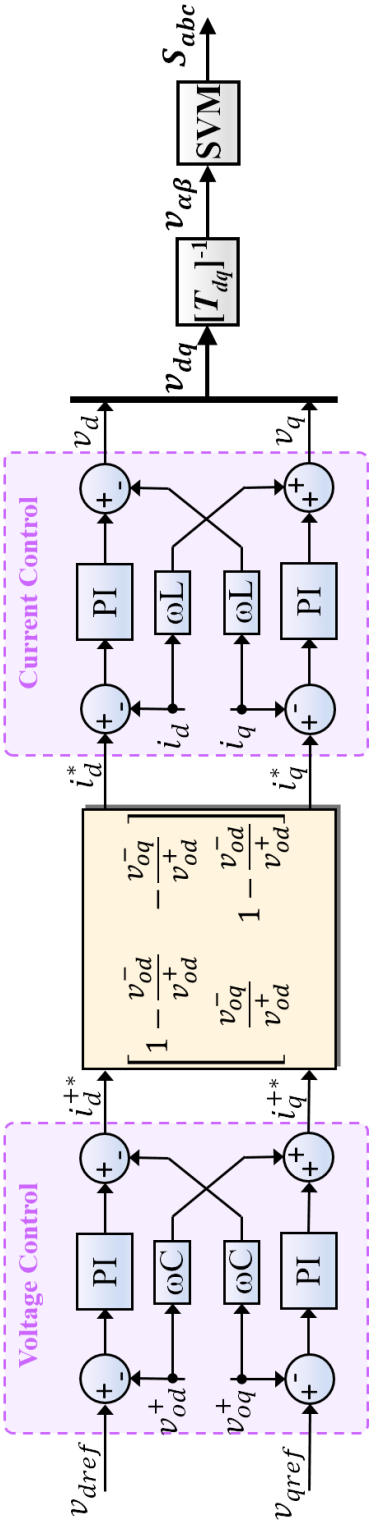

Figure 5.3: Block diagram of the controller for the VSC of battery.

and the reference q-axis current can be designed as

$$i_{\mathrm{q}}^{*} = i_{\mathrm{q}+}^{*} + i_{\mathrm{q}-}^{*} = \left(1 - \frac{v_{\mathrm{od}-}}{v_{\mathrm{od}+}}\right) i_{\mathrm{q}+}^{*} + \frac{v_{\mathrm{oq}-}}{v_{\mathrm{od}+}} i_{\mathrm{d}+}^{*} \tag{5.3.7}$$

The reference current of the battery VSC is presented as

$$\begin{bmatrix} i_{\mathrm{d}}^{*} \\ i_{\mathrm{q}}^{*} \end{bmatrix} = \begin{bmatrix} 1 - \dfrac{v_{\mathrm{od}-}}{v_{\mathrm{od}+}} & -\dfrac{v_{\mathrm{oq}-}}{v_{\mathrm{od}+}} \\ \dfrac{v_{\mathrm{oq}-}}{v_{\mathrm{od}+}} & 1 - \dfrac{v_{\mathrm{od}-}}{v_{\mathrm{od}+}} \end{bmatrix} \times \begin{bmatrix} i_{\mathrm{d}+}^{*} \\ i_{\mathrm{q}+}^{*} \end{bmatrix} \tag{5.3.8}$$

The controller block diagram of VSC based battery is shown in Figure 5.3.

5.3.2 Controller for VSC of Supercapacitor

Due to the SC is a high power density devices with less energy capacity than battery, it cannot be used for long-term (tens of minutes or hours) power supply. Therefore, no integral part is used in the positive-sequence voltage controller design of SC. Only the proportional gain is used for a rapid dynamic response in eliminating the transient regulation error.

However, due to its characteristic of low energy capacity, the SC needs to be recharged to its nominal DC voltage level for the next transient power response. An additional control loop is added to the whole control strategy for charging the SC. The control algorithm of output current from the SC is designed under dual synchronous reference frames (SRF) considering both the positive- and negative-sequence components, and is presented as

$$i_{\mathrm{d,sc}}^{+*} = k_{\mathrm{m}}(v_{\mathrm{dref}} - v_{\mathrm{od}+}) - \omega C v_{\mathrm{oq}+} + k_{\mathrm{dc}}(V_{\mathrm{dc}} - V_{\mathrm{dc}}^{*}) \tag{5.3.9}$$

$$i_{\mathrm{q,sc}}^{+*} = k_{\mathrm{m}}(v_{\mathrm{qref}} - v_{\mathrm{oq}+}) + \omega C v_{\mathrm{od}+} \tag{5.3.10}$$

$$i_{\mathrm{d,sc}}^{-*} = -k_{\mathrm{n}} v_{\mathrm{od}-} + \omega C v_{\mathrm{oq}-} \tag{5.3.11}$$

$$i_{\mathrm{q,sc}}^{-*} = -k_{\mathrm{n}} v_{\mathrm{oq}-} - \omega C v_{\mathrm{od}-} \tag{5.3.12}$$

where $i_{\mathrm{d_sc}+}^{*}$ and $i_{\mathrm{q_sc}+}^{*}$ are the positive-sequence reference current with synchronizing frequency ω; $i_{\mathrm{d_sc}-}^{*}$ and $i_{\mathrm{q_sc}-}^{*}$ are the negative-sequence reference current of supercapacitor VSC with synchronizing frequency $-\omega$; k_{m} and k_{n} are the proportional control gain for positive- and negative-sequence voltages, respectively; k_{dc} is the recharging control gain of SC DC voltage V_{dc}.

The current references calculated from the previous control algorithm are feeding the cascaded inner loop current controller, which uses PI controllers, for the regulation of output current. The final control output is the reference voltage in d-q axis, which is transformed back to the stationary frame by the inverse Park's transformation. The final control output of the reference voltage are presented as

$$\begin{aligned}\begin{bmatrix} v_\alpha \\ v_\beta \end{bmatrix} =& T_{\mathrm{dq^+}}^{-1} \begin{bmatrix} v_{\mathrm{d+}} \\ v_{\mathrm{q+}} \end{bmatrix} + T_{\mathrm{dq^-}}^{-1} \begin{bmatrix} v_{\mathrm{d-}} \\ v_{\mathrm{q-}} \end{bmatrix} \\ =& \begin{bmatrix} \cos(\theta) & -\sin(\theta) \\ \sin(\theta) & \cos(\theta) \end{bmatrix} \begin{bmatrix} v_{\mathrm{d+}} \\ v_{\mathrm{q+}} \end{bmatrix} \\ &+ \begin{bmatrix} \cos(\theta) & \sin(\theta) \\ -\sin(\theta) & \cos(\theta) \end{bmatrix} \begin{bmatrix} v_{\mathrm{d-}} \\ v_{\mathrm{q-}} \end{bmatrix}\end{aligned} \tag{5.3.13}$$

where v_α, v_β are the reference voltage control signal in stationary frame, $v_{\mathrm{d+}}$, $v_{\mathrm{q+}}$, $v_{\mathrm{d-}}$ and $v_{\mathrm{q-}}$ are the reference voltage from the output of current controller in positive- and negative-sequence control loop, respectively; $T_{\mathrm{dq+}}^{-1}$ and $T_{\mathrm{dq-}}^{-1}$ are the positive- and negative-sequence inverse Park transform matrix.

The space vector modulation (SVM) is used to produce duty cycle based on the voltage reference that drives the VSC. The control scheme of the SC VSC is given in Figure 5.4.

5.4 Simulation Results

The HESS in an island MG under unbalanced condition is simulated in PSCAD/EMTDC software environment. The simulation validation of the proposed coordinated control method is in PSCAD/EMTDC software environment. A battery-SC based HESS system is used to balance the power generation and demand in an island MG, as the power stage shown in Figure 5.5. As the control system of the HESS is designed to use battery and SC for different objectives, the simulation cases are to test their performance of cooperative operation performance and the whole effectiveness under unbalanced disturbance, including the single-phase impedance load and variable power generation. The method has compared with the battery only method to validate the improvement of using supercapacitor to extend the battery longevity. The

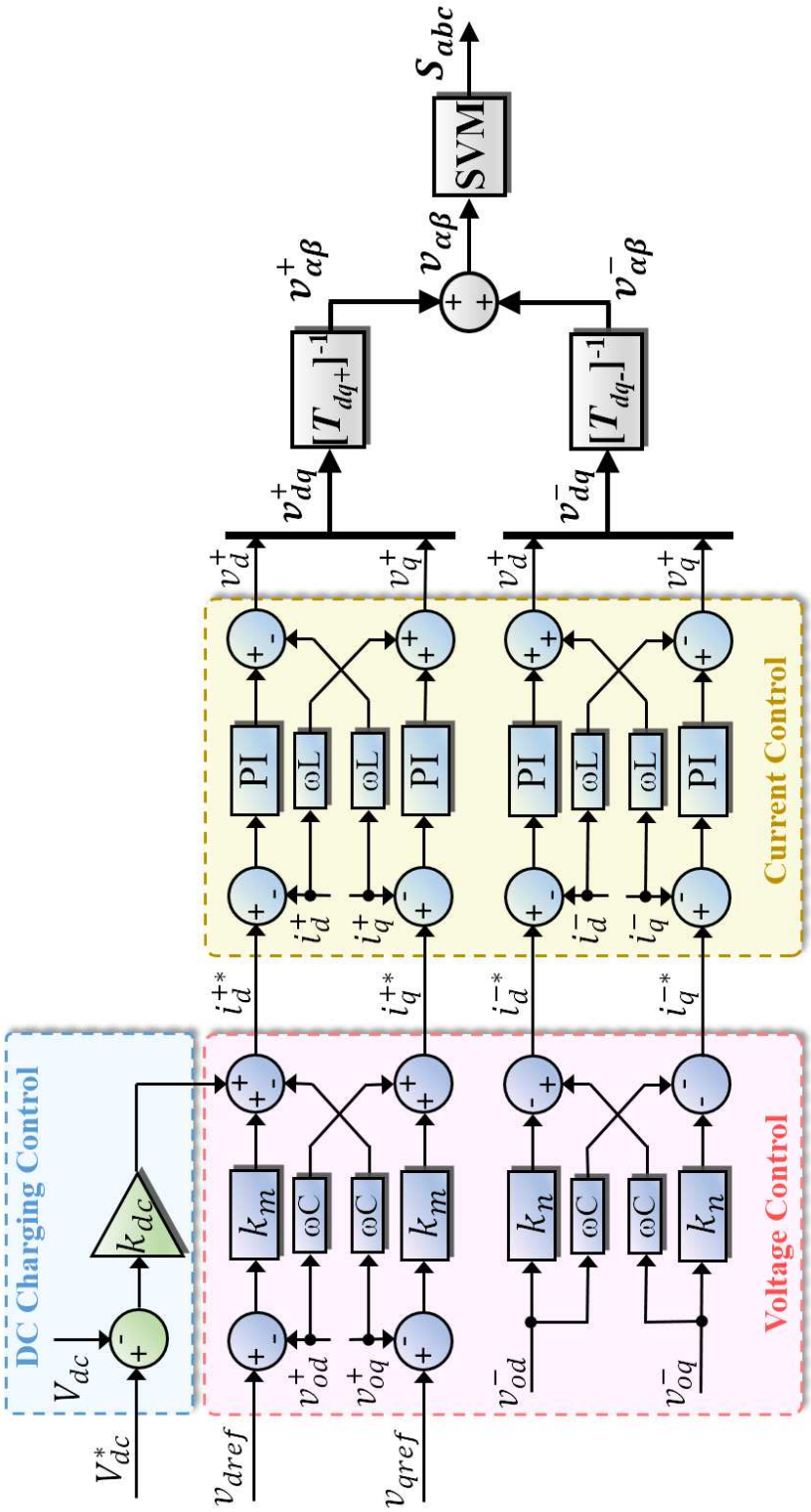

Figure 5.4: Block diagram of the controller for the VSC of supercapacitor.

MG parameters used in simulation are given in Table 5.1, and the controller parameters are given in Table 5.2.

Table 5.1: Parameters of MG and HESS.

Parameters:	Value:
MG rated bus voltage (RMS/line-to-line) ($v_{\mathrm{b(RMS)}}$)	0.4 kV
MG rated bus frequency (f_{b})	50 Hz
Battery nominal DC link voltage (E_0)	480 V
Battery internal resistance (R_{i})	0.005 Ω
Battery thermal resistance (R_{T})	0.0052 Ω
Battery thermal capacitance (C_{T})	0.52 F
Battery polarization voltage (K)	0.00876 V
Battery exponential zone amplitude (A)	0.468 V
Battery exponential zone time constant inverse (B)	3.529 A·h^{-1}
Battery rated charge capacity (Q_0)	2800 Ah
Battery initial SOC	50 %
SC nominal DC link voltage (V_{dc0})	0.4 kV
SC equivalent series resistance (R_{ES})	0.6 Ω
SC capacitance (C_{S})	0.58 F
VSC PWM frequency (f_{PWM})	2 kHz
VSC filter inductance - per phase (L_{s})	2.4 mH
VSC filter resistance - per phase (R_{s})	1 mΩ
VSC filter capacitance - per phase (C_{s})	290 μF

5.4.1 Single-phase impedance load

The unbalanced disturbance will lead more power loss due to the negative-sequence voltage components. To reduce the accumulated DOD and enhance the average efficiency of battery, the unbalance power is designed to be absorbed by the SC. When the single-phase load is connected to the MG, the bus voltage drops immediately. The SC responds rapidly to produce transient power output and compensate the unbalanced power demand, and the battery has a slower response speed

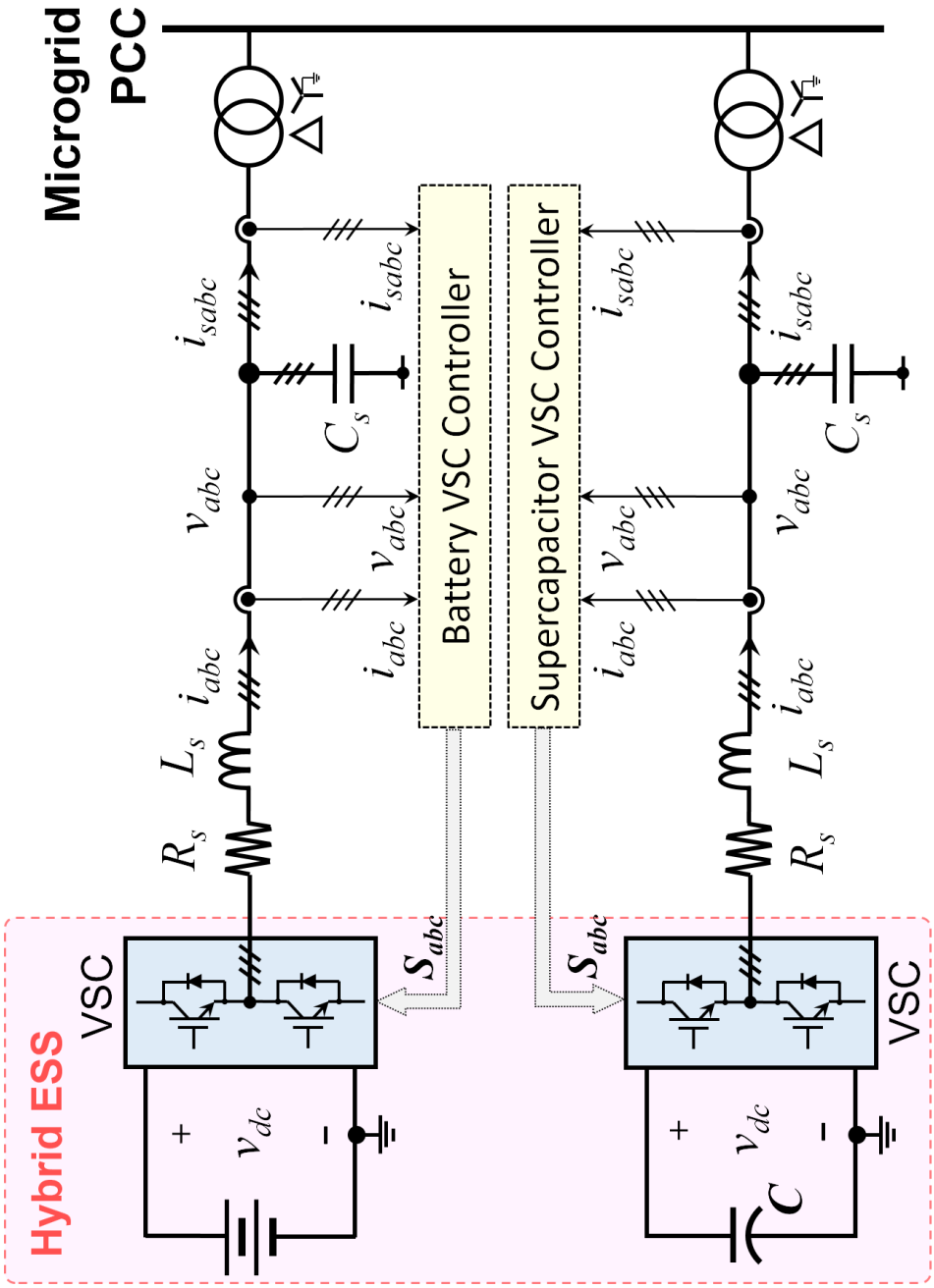

Figure 5.5: The power stage of a VSC based HESS and its control system.

Table 5.2: Controller parameters of HESS

	Voltage Controller			Current Controller	
Battery	k_{p}	k_{i}		k_{p}	k_{i}
	0.5	50		5	1000
SC	k_{m}	k_{n}	k_{dc}	k_{p}	k_{i}
	20	50	5	5	1000

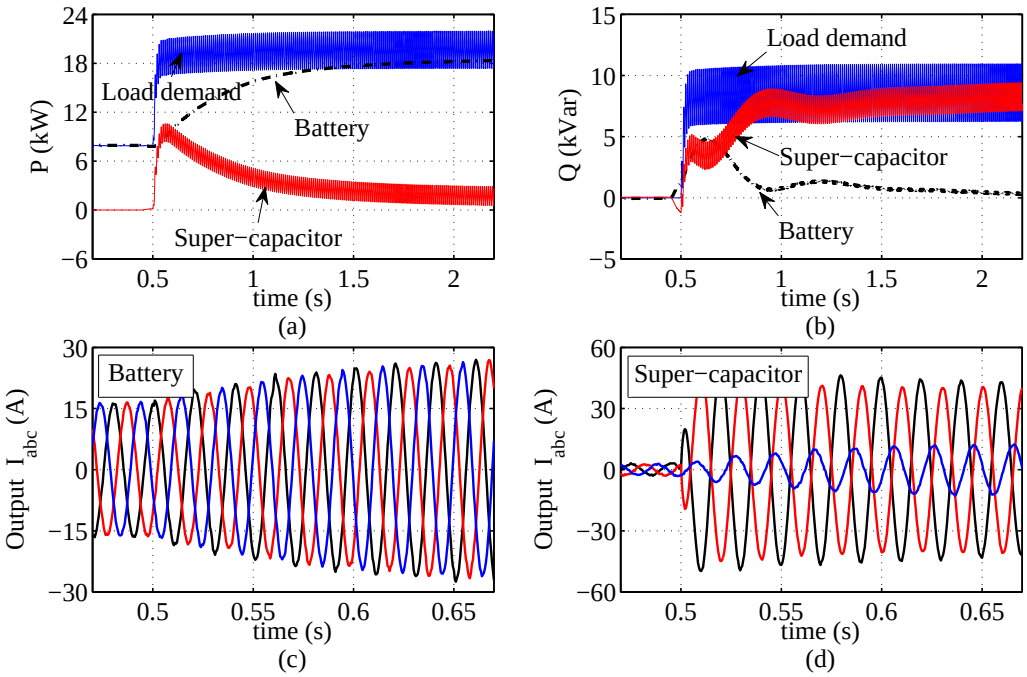

Figure 5.6: Simulation results of the HESS with its power flow and current outputs under single phase load. (a) Active power flow in kW; (b) reactive power flow in kVar; (c) output current from the battery; and (d) output current from the SC.

on producing balanced power to eliminate the steady state error on bus voltage, as shown in Figure 5.6 (a) and (b). The steady state operation of the SC is to produce the oscillated active and reactive power with its average power output equals to zero under unbalance load condition. That is to use the SC for frequent discharging usage to reduce the discharging cycles of battery, and thus to improve its longevity. The three-phase output current from the battery and SC are shown in Figure 5.6 (c) and (d). From which it is clear to find that the output current from the battery is balanced, while that from the SC is to satisfy the unbalanced current demand from the single-phase load.

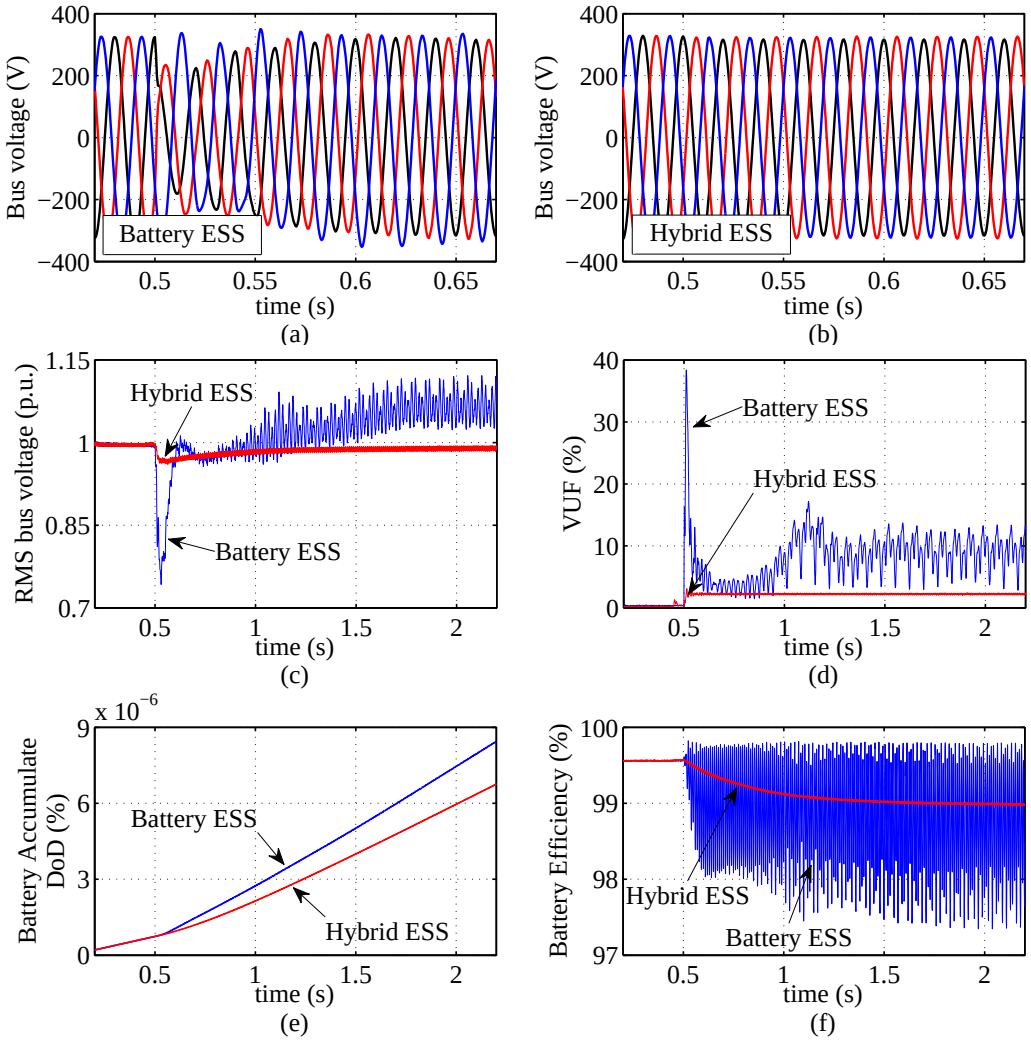

Figure 5.7: Comparison results between the BESS and HESS in bus voltage transient response and battery performance under single phase load. (a) Bus voltage with using the battery ESS; (b) bus voltage with using the hybrid ESS; (c) RMS bus voltage comparison in p.u.; (d) bus voltage unbalance factor; (e) battery accumulate DOD; and (f) battery instantaneous efficiency.

Figure 5.7 (a) and (b) show the bus voltage waveform of the conventional battery based ESS (BESS) and the HESS with proposed control method under unbalanced load disturbance. To have a more distinct comparison of the bus voltage, the RMS voltage in p.u. and the voltage unbalance factor (VUF) are used in the comparison, as shown in Figure 5.7 (c) and (d). The VUF is defined as the ratio of the negative-sequence voltage over the positive-sequence voltage as an index [142]:

$$VUF = \frac{v^{-}_{\mathrm{b(RMS)}}}{v^{+}_{\mathrm{b(RMS)}}} \times 100\% \tag{5.4.1}$$

where $v^{+}_{\mathrm{b(RMS)}}$ and $v^{-}_{\mathrm{b(RMS)}}$ are the positive- and negative-sequences of bus voltage in root-mean-square (RMS) value.

Under the single-phase load, the bus voltage is maintained by the VSC of ESS to balance the power demand and generation. Beside to improve the transient response of bus voltage, another objective of using the SC in the HESS is to extend the longevity of the battery. As discussed in previous sections, the battery longevity is affected by the ambient temperature and equivalent full cycles, which is represented as the accumulate DOD. In addition, the power dissipation on the internal resistance of battery will not only decrease the efficiency but also increase the ambient temperature. The higher the battery efficiency, the less the power dissipation and the longer the life cycle of battery. The efficiencies during charge and discharge are defined as

$$\eta_{\mathrm{charge}} = \frac{P_{\mathrm{stored}}}{P_{\mathrm{input}}} \tag{5.4.2}$$

$$\eta_{\mathrm{discharge}} = \frac{P_{\mathrm{output}}}{P_{\mathrm{generated}}} \tag{5.4.3}$$

which can be combined into a formula to the ratio between the minimum value and the maximum value of battery terminal power and the cell power

$$\eta_{\mathrm{battery}} = \frac{\min\left(|\mathrm{P_{term}}|, |\mathrm{P_{cell}}|\right)}{\max\left(|\mathrm{P_{term}}|, |\mathrm{P_{cell}}|\right)} \tag{5.4.4}$$

To validate the performance, the accumulated DOD and power efficiency is used to represent the usage of battery, as shown in Figure 5.7 (e) and (f). To further validate the performance improvement of using a SC in a HESS than a BESS, the indices are compared in Figure 5.10 and Table 5.3.

From the bar chart in Figure 5.10, it is obviously to find that the HESS with the proposed control strategy performs better than the conventional BESS in bus voltage IAE and VUF in both cases. The battery accumulate DOD of using the HESS is less than that of using the BESS, and the battery efficiency of HESS is higher than that of the BESS under both the single-phase impedance load and power generation disturbance.

From the simulation results, the maximum voltage dip in a BESS based MG is 0.258, while using a HESS the maximum voltage dip is 0.0394, 84.7% less than the former. The regulation IAE of the MG bus voltage maintained by the HESS is about 72.7% less than the BESS based MG. The maximum VUF and average VUF of the bus voltage that controlled by a HESS are 91.9% and 74.0% less than the BESS, respectively.

In addition, the battery usage is compared with three indices, the internal power loss, the accumulate DOD, and the battery average efficiency. Comparing with the BESS, the HESS with SC improve the effective usage of battery with 48.2% less internal power loss, 18.5% less accumulated DOD, and 0.22% higher battery efficiency in average.

5.4.2 Single-phase power generation

As the renewable energy is unpredictable, its generated power cannot always be equal to the power demand load from customer side. In this case, the ESS, which is used to balance the power difference, can both be used to generate power to the grid or absorb power from the grid depending on the power condition. The output power in both active and reactive power of the battery and SC in the HESS are shown in the Figure 5.8 (a) and (b). And the output current from the battery and SC in the HESS are given separately in the Figure 5.8 (c) and (d).

The comparison between the battery ESS and hybrid ESS in terms of the RMS bus voltage, VUF, battery accumulated DOD, battery efficiency, and the instant bus voltage, which are shown in Figure 5.9, and the numerical indices are compared in Figure 5.10 and Table 5.3. The maximum voltage regulation error and voltage IAE with using the HESS are 83.7% and 66.3% less than that of using the BESS,

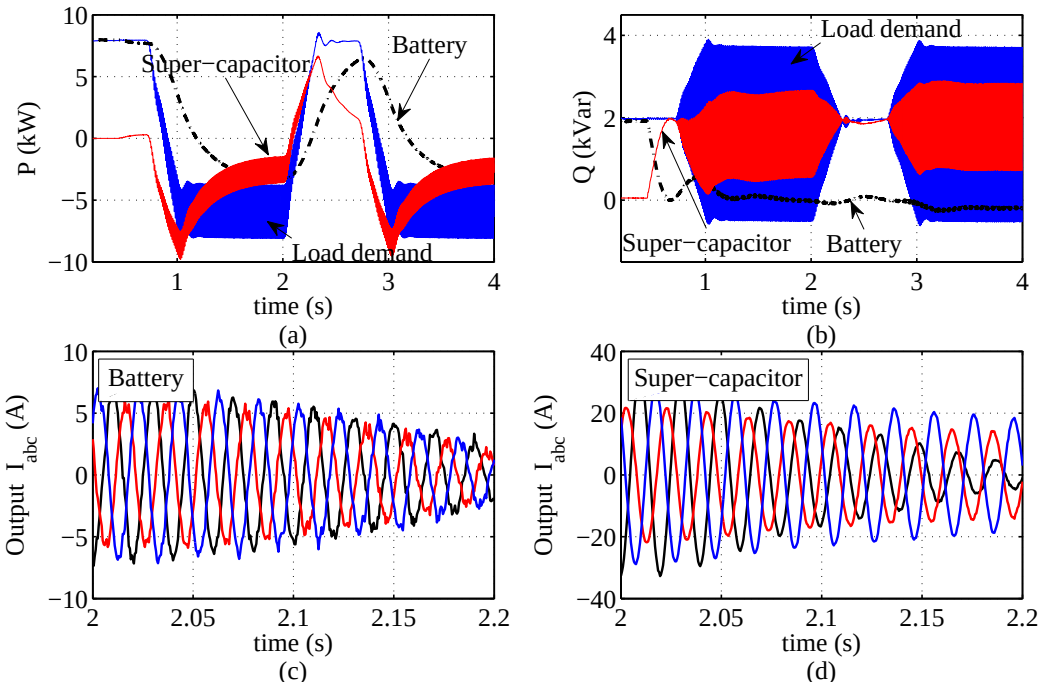

Figure 5.8: Simulation results of the HESS with its power flow and current outputs under single-phase power generation. (a) Active power flow in kW; (b) reactive power flow in kVar; (c) output current from the battery; and (d) output current from the SC.

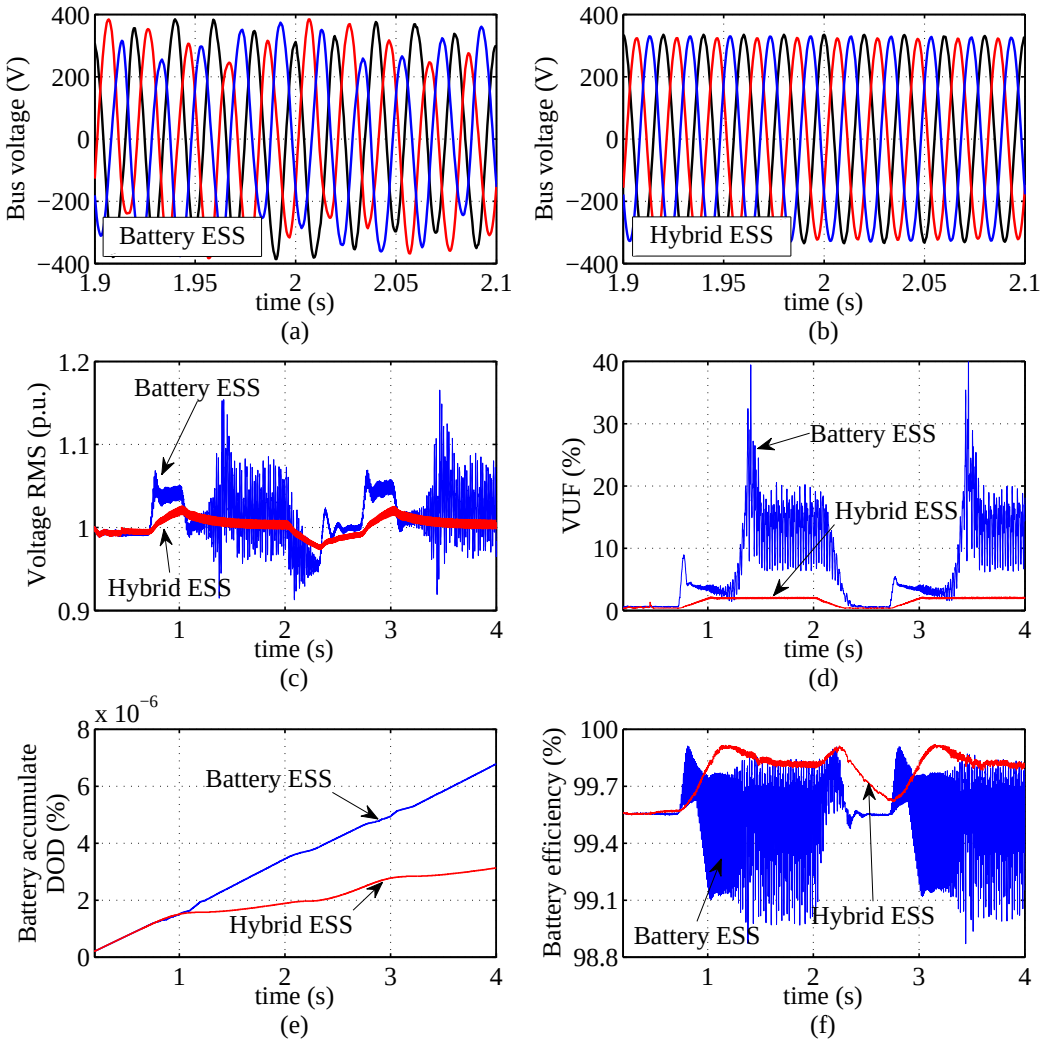

Figure 5.9: Comparison results between the BESS and HESS in bus voltage transient response and battery performance under single-phase power generation. (a) Bus voltage with using the battery ESS; (b) bus voltage with using the hybrid ESS; (c) RMS bus voltage comparison in p.u.; (d) bus voltage unbalance factor; (e) battery accumulate DOD; and (f) battery instantaneous efficiency.

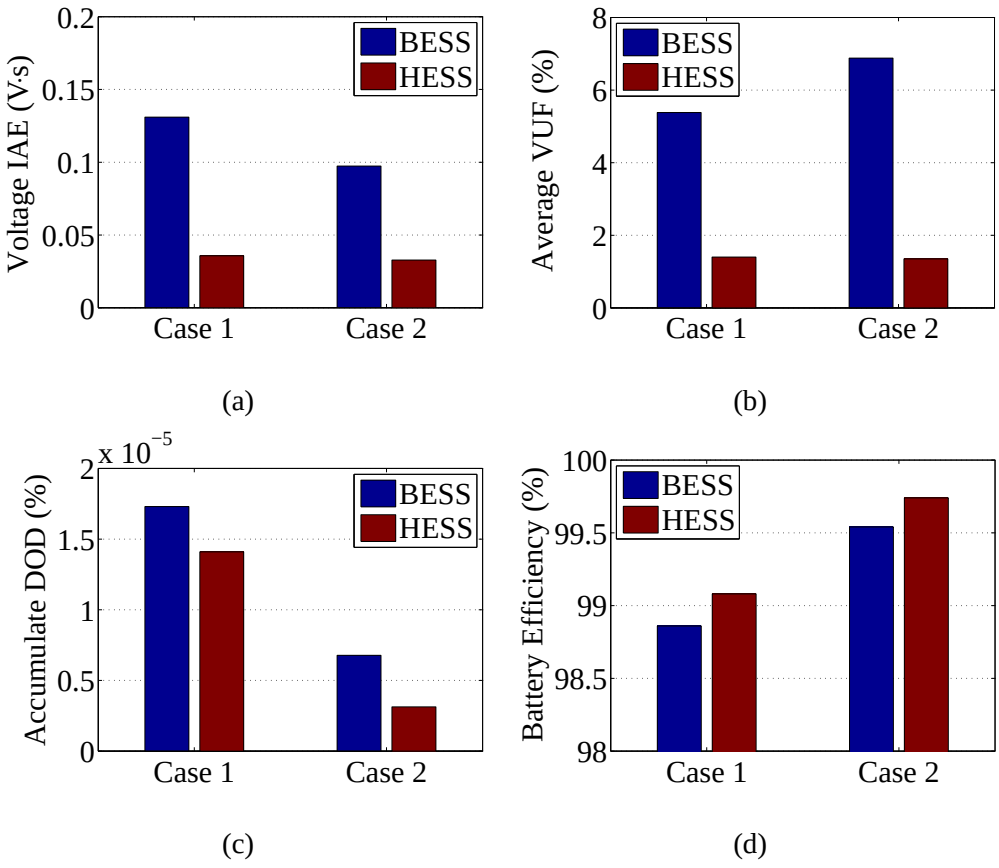

Figure 5.10: Indices comparison between BESS and HESS in the bus voltage (a) IAE, (b) VUF, and battery performance (c) accumulate DOD, (d) average efficiency.

Table 5.3: Performance indices of Battery ESS and Hybrid ESS in simulation

Indices \ Method	Battery ESS	Hybrid ESS	Improvements
Case 1: Single-phase impedance load			
Maximum voltage error (p.u.)	0.258	0.0394	84.7% less
Voltage IAE	0.131	0.0357	72.7% less
Maximum VUF (%)	38.39	3.09	91.9% less
Average VUF (%)	5.38	1.40	74.0% less
Internal power loss (W)	514.5	266.3	48.2% less
Accumulate DOD ($\times 10^{-5}$)	1.73	1.41	18.5% less
Battery Average Efficiency (%)	98.86	99.08	0.22% higher
Case 2: Single-phase power generation			
Maximum voltage error (p.u.)	0.165	0.0269	83.7% less
Voltage IAE	0.0974	0.0328	66.3% less
Maximum VUF (%)	42.73	2.21	94.8% less
Average VUF (%)	6.88	1.35	80.4% less
Internal power loss (W)	62.4	22.5	63.9% less
Accumulate DOD ($\times 10^{-5}$)	0.678	0.313	53.8% less
Battery Average Efficiency (%)	99.54	99.74	0.2% higher

respectively. The maximum and average VUF of bus voltage by using the HESS are 94.8% and 80.4% less than that of using the BESS.

With the use of the SC in a HESS, the SC is designed to compensate all the

oscillation power flow, which can be used as a power buffer to smooth the output power from battery, and then reduce the unnecessary usage of battery. Thus, during the frequent discharging cycles, the battery in a HESS with the proposed control strategy has less accumulate DOD and higher efficiency than in a BESS as shown in Figure 5.9 (e) and (f). The internal power loss and accumulate DOD of the battery in a HESS are 63.9% and 53.8% less than that in a BESS, respectively. And the battery average efficiency in a HESS is 0.2% higher than that in a BESS. These results show that the SC used in a HESS with the proposed method improves the performance of bus voltage maintaining, and reduce the battery usage frequency to extend the longevity of a battery.

5.5 Conclusion

In this chapter, a coordinated control strategy has been presented for a battery and supercapacitor (SC) based hybrid energy storage system (HESS) to improve the transient response of bus voltage in an island microgrid (MG) and reduce the accumulate depth of discharge (DOD) of the battery. As a SC has much more recharging cycles than a battery, the SC is controlled to generate power for the transient and unbalanced power demand, while the battery is controlled to provide the balanced active power in steady state. The coordinated control method has been verified on a HESS in an island MG in simulation using PSCAD/EMTDC. The results show that the transient response of MG bus voltage has been improved and the battery loss has been reduced with lower accumulate DOD and higher average efficiency.

Chapter 6

Nonlinear Adaptive Control for Induction Motor Speed Control with Improved Robustness

6.1 Introduction

IMs are widely used in industrial processes, transportation application, and electric vehicles, such as Tesla Motors, due to their ruggedness, simple structure, small volume and lightweight, low cost, high efficiency and operational reliability [43]. The main difficulties in controlling of an IM are its nonlinear dynamics, parameter variations during operation, and unmeasured states (rotor currents and fluxes) [46]. The most commonly used technique in IM speed control is the field-oriented control or vector control (VC), as shown in Figure 6.1(a), which decouples the torque and flux to achieve a good dynamic response of the controlled IM comparable to those of the dc motors [55, 56]. The VC transforms the IM system from stationary frame to rotating frame with the requirement of accurate parameters to decouple the flux and the torque and control them separately [54]. However, in real-time implementation, the VC is sensitive to the system uncertainties, which include external load disturbances, inaccuracy and changes of motor equivalent circuit parameters, and unmodeled system dynamics [93, 160–162]. The deterioration in current dis-

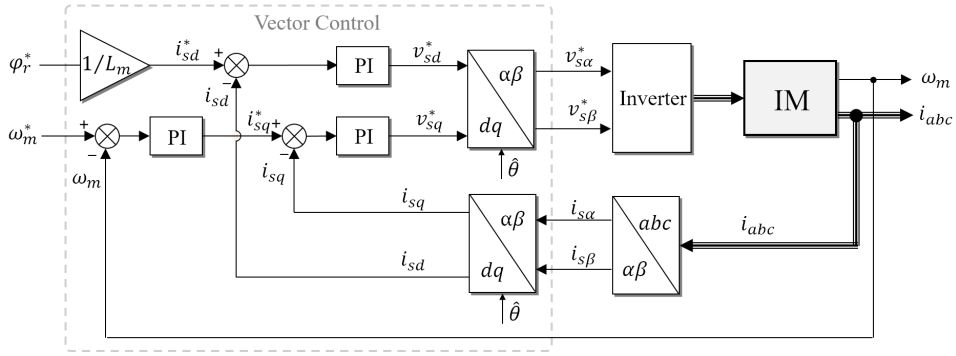

(a)

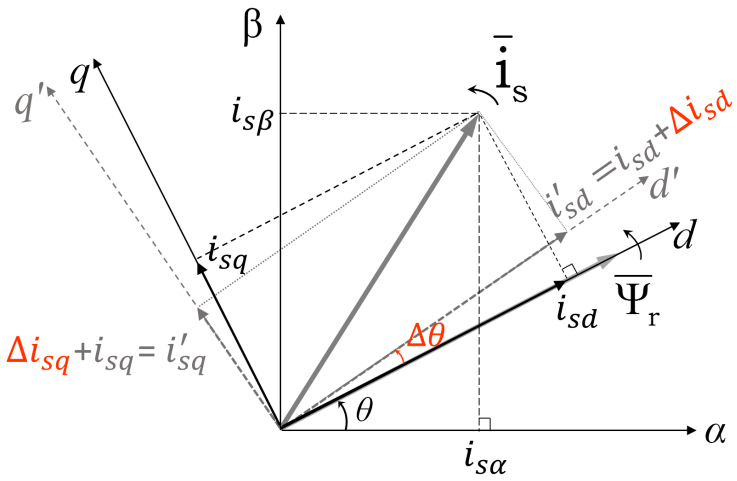

(b)

Figure 6.1: (a) Scheme of conventional vector control for IM speed drive; (b) Vector control under inaccurate flux position.

tribution (i_{sd} and i_{sq}) reduces the torque capability, which is a significant impact especially in the field-weakening region and efficiency optimization [48, 163, 164]. In addition, when the load disturbances are present, the proportional-integral (PI) regulators based VC scheme may have a longer recovery period [95].

In the past few decades, many previous works aimed to solve these problems. One method is to on-line estimate the parameters as reviewed in [165], such as the stator resistance adaptation law [166]; adaptive input-output linearizing control (I-OLC) with parameter estimation [63]; on-line stator and rotor resistances estimation using artificial neural networks [167]. But the parameter estimation methods are d-

ifficult to estimate the rotor resistance under constant rotor flux [168], and complex to identify the inherent dependency with other parameters [95]. Another method is to design the robust controller, which is independent with system parameters, such as a nonlinear sliding-mode torque control strategy [107]; an adaptive back-stepping sliding-mode control method [108]; exact feedback linearization method with rotor flux angle estimation [64]; fuzzy control methods [109, 110]; neural network based robust control schemes [111, 112], and perturbation rejection characteristics based analysis scheme [169]. In the robust control methods, several disturbance observer based approaches have been proposed to estimate system uncertainties, including nonlinear observer based active disturbance rejection control (ADRC) [93, 95, 170] to estimate disturbances, and extended state observer (ESO) based controller [91] to estimate the mismatched uncertainties, etc. On the other hand, most control methods for IM speed drive were designed to decouple the flux and the torque (or speed) dynamics by Park transformation, which requires to obtain the angular position of rotor flux by using a phase lock loop (PLL). However, if the parameters were changed or the unbalanced disturbance occurred, the conventional PLL cannot obtain the accurate flux position, and that will bring new disturbance to the distributed currents and reduce the robustness of the system, as the Δi_{sd} and Δi_{sq} are caused by $\Delta\theta$ shown in Figure 6.1(b).

In order to decouple the flux and torque with less dependency on flux position and system parameters, this chapter designs a nonlinear adaptive controller (NAC) for IM speed control in stationary frame, with estimating the perturbation terms to fully decouple flux and speed dynamics and to linearize the original nonlinear system, without acquiring the rotor flux position and the accurate system model. The NAC employs a linear high-gain observer to estimate the perturbation terms and the estimated perturbation is applied to cancel its real value and thus improve the robustness in the presence of parameter uncertainties and disturbances, and to remove the dependence of an accurate system model required by the model based IOLC. Moreover, due to the NAC has fully decoupled the flux and speed dynamics and controlled them independently, the NAC has improved the efficiency through a better flux control under time-varying load disturbance.

The remainder of this chapter is organized as follows. Section 6.2 presents the dynamic model of IM system in stationary frame. Section 6.4 presents the design of the proposed NAC with SPOs. Sections 6.6 and 6.7 provide the simulation and experimental results, respectively. And the chapter is finally concluded in Section 6.8. The stability of the closed-loop system is proved using Lyapunov theory as given in Appendix.

6.2 Induction Motor System

The dynamic model of a three-phase induction motor in stationary stator α-β reference frame, with neglecting the iron losses and magnetic saturation, can be described as [107] [171]:

$$\dot{x} = f(x) + Bu \tag{6.2.1}$$

where

$$x = \begin{bmatrix} i_{\mathrm{s}\alpha} & i_{\mathrm{s}\beta} & \psi_{\mathrm{r}\alpha} & \psi_{\mathrm{r}\beta} & \omega_{\mathrm{m}} \end{bmatrix}^{\mathrm{T}}$$

$$u = \begin{bmatrix} u_1 \; u_2 \end{bmatrix}^{\mathrm{T}} = \begin{bmatrix} v_{\mathrm{s}\alpha} \; v_{\mathrm{s}\beta} \end{bmatrix}^{\mathrm{T}}$$

$$f(x) = \begin{bmatrix} -\left(\frac{R_{\mathrm{s}}}{\sigma L_{\mathrm{s}}} + \frac{L_{\mathrm{m}}^2}{\sigma L_{\mathrm{s}} L_{\mathrm{r}} \tau_{\mathrm{r}}}\right) i_{\mathrm{s}\alpha} + \frac{L_{\mathrm{m}}}{\sigma L_{\mathrm{s}} L_{\mathrm{r}} \tau_{\mathrm{r}}} \psi_{\mathrm{r}\alpha} + \frac{n_{\mathrm{p}} \omega_{\mathrm{m}} L_{\mathrm{m}}}{\sigma L_{\mathrm{s}} L_{\mathrm{r}}} \psi_{\mathrm{r}\beta} \\ -\left(\frac{R_{\mathrm{s}}}{\sigma L_{\mathrm{s}}} + \frac{L_{\mathrm{m}}^2}{\sigma L_{\mathrm{s}} L_{\mathrm{r}} \tau_{\mathrm{r}}}\right) i_{\mathrm{s}\beta} + \frac{L_{\mathrm{m}}}{\sigma L_{\mathrm{s}} L_{\mathrm{r}} \tau_{\mathrm{r}}} \psi_{\mathrm{r}\beta} - \frac{n_{\mathrm{p}} \omega_{\mathrm{m}} L_{\mathrm{m}}}{\sigma L_{\mathrm{s}} L_{\mathrm{r}}} \psi_{\mathrm{r}\alpha} \\ \frac{L_{\mathrm{m}}}{\tau_{\mathrm{r}}} i_{\mathrm{s}\alpha} - \frac{1}{\tau_{\mathrm{r}}} \psi_{\mathrm{r}\alpha} - n_{\mathrm{p}} \omega_{\mathrm{m}} \psi_{\mathrm{r}\beta} \\ \frac{L_{\mathrm{m}}}{\tau_{\mathrm{r}}} i_{\mathrm{s}\beta} - \frac{1}{\tau_{\mathrm{r}}} \psi_{\mathrm{r}\beta} + n_{\mathrm{p}} \omega_{\mathrm{m}} \psi_{\mathrm{r}\alpha} \\ \frac{3 n_{\mathrm{p}} L_{\mathrm{m}}}{2 J L_{\mathrm{r}}} \left(\psi_{\mathrm{r}\alpha} i_{\mathrm{s}\beta} - \psi_{\mathrm{r}\beta} i_{\mathrm{s}\alpha}\right) - \frac{T_{\mathrm{L}}}{J} \end{bmatrix}$$

$$B = \begin{bmatrix} \frac{1}{\sigma L_{\mathrm{s}}} & 0 & 0\,0\,0 \\ 0 & \frac{1}{\sigma L_{\mathrm{s}}} & 0\,0\,0 \end{bmatrix}^{\mathrm{T}}$$

and the system output vector y is

$$y = \begin{bmatrix} y_1 \; y_2 \end{bmatrix}^{\mathrm{T}} = \begin{bmatrix} \psi_{\mathrm{r}}^2 \; \omega_{\mathrm{m}} \end{bmatrix}^{\mathrm{T}} \tag{6.2.2}$$

where $i_{s\alpha}$, $i_{s\beta}$ and $\psi_{r\alpha}$, $\psi_{r\beta}$ are the stator currents and the rotor flux linkages in fixed stationary frame, respectively; $v_{s\alpha}$ and $v_{s\beta}$ are the stator voltages as system control inputs; ω_r and ω_m are the rotor electrical and mechanical speed, where $\omega_r = n_p\omega_m$; n_p, J and T_L are the number of pole pairs, rotor inertia and load torque disturbance; R_s, R_r and L_s, L_r are the resistances and the inductances of stator and rotor, respectively; and L_m is the mutual inductance. $\tau_r = L_r/R_r$ represents the rotor time constant, and $\sigma = 1 - L_m^2/L_sL_r$ is the leakage coefficient. The rotor flux square ψ_r^2 is obtained as $\psi_r^2 = \psi_{r\alpha}^2 + \psi_{r\beta}^2$.

The rotor current can be expressed by the states shown as

$$\begin{cases} i_{r\alpha} = \frac{1}{L_s}\psi_{r\alpha} - \frac{L_m}{L_r}i_{s\alpha} \\ i_{r\beta} = \frac{1}{L_s}\psi_{r\beta} - \frac{L_m}{L_r}i_{s\beta} \end{cases} \tag{6.2.3}$$

Moreover, the reference rotor flux square and mechanical speed are defined as ψ_r^{*2} and ω_m^*, respectively, and their tracking error are defined as $e_1 = \psi_r^2 - \psi_r^{*2}$, $e_2 = \omega_m - \omega_m^*$.

The objective of work presented in this chapter is to design a NAC speed control algorithm to achieve the tracking (i.e., e_1 and e_2 tend to 0) in the presence of various uncertainties such as variable speed reference, step and time-varying load disturbances, system parameter uncertainties and other unknown external disturbances.

6.3 Rotor Flux Optimization to Minimize Power Loss

6.3.1 Rotor Flux Estimation

In the real-time implementation, the rotor flux of IM is not always available due to it requires the installation of external hall sensor and that will increase the total cost. One alternative way is to estimate the rotor flux using the current model of IM. The model is based on rotor circuit equation, in order to estimate the rotor flux with the stator current feedback as follows:

$$\begin{cases} \frac{d\hat{\psi}_{r\alpha}}{dt} = \frac{L_m}{\tau_r}i_{s\alpha} - \frac{1}{\tau_r}\hat{\psi}_{r\alpha} - \omega_r\hat{\psi}_{r\beta} \\ \frac{d\hat{\psi}_{r\beta}}{dt} = \frac{L_m}{\tau_r}i_{s\beta} + \omega_r\hat{\psi}_{r\alpha} - \frac{1}{\tau_r}\hat{\psi}_{r\beta} \end{cases} \tag{6.3.1}$$

The rotor flux can be obtained as follows:

$$|\hat{\psi}_{\mathrm{r}}| = \sqrt{\hat{\psi}_{\mathrm{r}\alpha}^2 + \hat{\psi}_{\mathrm{r}\beta}^2} \tag{6.3.2}$$

The estimated rotor flux is used as feedback for rotor flux excitation in both the conventional vector control and the proposed nonlinear adaptive control.

6.3.2 Power Loss Minimization

IMs are normally designed to operate at its rated flux condition to provide fast response in torque. However, the industrial applications mostly drives the IMs in light loads. The rated flux will cause unnecessary core and copper losses under the light loads condition and result in poor efficiency in drives [172]. The efficiency of the IM is defined as [173].

$$\eta = \frac{P_{\mathrm{out}}}{P_{\mathrm{in}}} = \frac{T_{\mathrm{L}} \cdot \omega_{\mathrm{m}}}{p_{\mathrm{a}} + p_{\mathrm{b}} + p_{\mathrm{c}}} \tag{6.3.3}$$

where p_{a}, p_{b} and p_{c} are the average electric power consumption in phase a, b and c, and can be calculated as $p_{\mathrm{a}} = 1/T \cdot \int_0^T v_{\mathrm{a}} i_{\mathrm{a}} dt$, where T is the time period.

The loss minimization can be achieved by different methods, such as model based method to set the loss derivative to zero [174], perturb-and-observe techniques [175], etc. The loss model based method is used in this chapter. Define the P_{loss} as the total loss, where the copper and iron losses dominate the overall power loss [174]. The core loss includes the eddy currents and hysteresis loss in the rotor core, and it is presented with an equivalent core resistance R_{c}. The copper loss is due to the flow of current through stator and rotor windings. The power loss function is given by

$$P_{\mathrm{loss}} = \frac{3}{2}\left(|i_{\mathrm{s}}|^2 R_{\mathrm{s}} + |i_{\mathrm{r}}|^2 R_{\mathrm{r}}\right) + \frac{3}{2}\frac{(\omega_{\mathrm{e}}|\psi_{\mathrm{r}}|)^2}{R_{\mathrm{c}}} \tag{6.3.4}$$

In steady-state condition, since the speed and load are both unchanged, the electromagnetic torque is a constant, and the rotor flux is related with stator current, which are represented as

$$\begin{cases} T_{\mathrm{e0}} = \frac{3 n_{\mathrm{p}} L_{\mathrm{m}}}{2 L_{\mathrm{r}}} |\psi_{\mathrm{r}}||i_{\mathrm{s}}| \sin(\delta) \\ |\psi_{\mathrm{r}}| = L_{\mathrm{m}} |i_{\mathrm{s}}| \cos(\delta) \end{cases} \tag{6.3.5}$$

where δ is the position difference between the vector of stator current $\vec{i}_{\mathrm{s}}$ and rotor flux $\vec{\psi}_{\mathrm{r}}$.

Eliminate δ in (6.3.5) and the stator current can be represented as

$$|i_{\mathrm{s}}|^2 = \frac{T_{\mathrm{e0}}^2}{K^2}\frac{1}{|\psi_{\mathrm{r}}|^2} + \frac{|\psi_{\mathrm{r}}|^2}{L_{\mathrm{m}}^2} \tag{6.3.6}$$

where $K = 3n_{\mathrm{p}}L_{\mathrm{m}}/2L_{\mathrm{r}}$. Substitute (6.2.3) and (6.3.6) into (6.3.4) to eliminate the stator and rotor current states, the power loss can be represented as a function of rotor flux as

$$P_{\mathrm{loss}} = \frac{3}{2}\left(M\frac{T_{\mathrm{e0}}^2}{K^2}\frac{1}{|\psi_{\mathrm{r}}|^2} + N|\psi_{\mathrm{r}}|^2\right) \tag{6.3.7}$$

where

$$M = R_{\mathrm{s}} + \tfrac{L_{\mathrm{m}}^2}{L_{\mathrm{r}}^2}R_{\mathrm{r}}$$
$$N = \tfrac{R_{\mathrm{s}}}{L_{\mathrm{m}}^2} + \left(\tfrac{1}{L_{\mathrm{r}}} - \tfrac{1}{L_{\mathrm{s}}}\right)^2 R_{\mathrm{r}} + \tfrac{\omega_{\mathrm{e}}^2}{R_{\mathrm{c}}}$$

Differentiating the loss with respect to rotor flux and let $dP_{\mathrm{loss}}/d|\psi_{\mathrm{r}}| = 0$ to minimize the power loss. Then optimal rotor flux can be obtained as

$$\psi_{\mathrm{r,opt}}^{*} = \sqrt[4]{\frac{M}{N}(\psi_{\mathrm{r}\alpha}i_{\mathrm{s}\beta} - \psi_{\mathrm{r}\beta}i_{\mathrm{s}\alpha})^2} \tag{6.3.8}$$

6.4 Nonlinear Adaptive Controller for IM Speed Tracking

The NAC has been proposed in [126] and applied on power system [88, 89]. In the first step, a nonlinear system is transformed into interacted subsystems by input-output linearization. Both the nonlinearities and uncertainties are defined in a fictitious state and known as perturbation terms. The IOLC method can only calculate the certain perturbation terms from a detailed mathematic model and accurate parameters. In this chapter, the perturbations are estimated by the designed SPOs and used to adaptively compensate the real perturbations, which includes both the nonlinearities and the uncertainties.

6.4.1 Input-output Linearization

From the IM model given in Section 6.2, chose outputs of system (6.2.1) as

$$\begin{cases} h_1(x) = y_1 = \psi_{\mathrm{r}\alpha}^2 + \psi_{\mathrm{r}\beta}^2 \\ h_2(x) = y_2 = w_{\mathrm{m}} \end{cases} \tag{6.4.1}$$

Then the input-output linearization of system (6.2.1) can be obtained from its second-order derivative as

$$\begin{bmatrix} \ddot{y}_1(x) \\ \ddot{y}_2(x) \end{bmatrix} = \begin{bmatrix} \Psi_1(x) \\ \Psi_2(x) \end{bmatrix} + g(x) \begin{bmatrix} u_1 \\ u_2 \end{bmatrix} \tag{6.4.2}$$

where

$$\begin{aligned} \Psi_1(x) = & \frac{2L_{\mathrm{m}}^2}{\tau_{\mathrm{r}}^2}(i_{\mathrm{s}\alpha}^2 + i_{\mathrm{s}\beta}^2) - \omega_{\mathrm{r}}(i_{\mathrm{s}\alpha}\psi_{\mathrm{r}\beta} - i_{\mathrm{s}\beta}\psi_{\mathrm{r}\alpha}) \\ & -\frac{2L_{\mathrm{m}}}{\sigma\tau_{\mathrm{r}}}(\frac{R_{\mathrm{s}}}{L_{\mathrm{s}}} + \frac{1+2\sigma}{\tau_{\mathrm{r}}})(i_{\mathrm{s}\alpha}\psi_{\mathrm{r}\alpha} + i_{\mathrm{s}\beta}\psi_{\mathrm{r}\beta}) \\ & +\frac{2(1+\sigma)}{\sigma\tau_{\mathrm{r}}^2}(\psi_{\mathrm{r}\alpha}^2 + \psi_{\mathrm{r}\beta}^2) \end{aligned} \tag{6.4.3}$$

$$\begin{aligned} \Psi_2(x) = & \frac{3n_{\mathrm{p}}L_{\mathrm{m}}}{2JL_{\mathrm{r}}}\left[(\frac{R_{\mathrm{s}}}{\sigma L_{\mathrm{s}}} + \frac{1}{\sigma\tau_{\mathrm{r}}})(i_{\mathrm{s}\alpha}\psi_{\mathrm{r}\beta} - i_{\mathrm{s}\beta}\psi_{\mathrm{r}\alpha})\right. \\ & \left.-\frac{\omega_{\mathrm{r}}L_{\mathrm{m}}}{\sigma L_{\mathrm{s}}L_{\mathrm{r}}}(\psi_{\mathrm{r}\alpha}^2 + \psi_{\mathrm{r}\beta}^2) - \omega_{\mathrm{r}}(i_{\mathrm{s}\alpha}\psi_{\mathrm{r}\alpha} + i_{\mathrm{s}\beta}\psi_{\mathrm{r}\beta})\right] \\ & -\frac{\dot{T}_{\mathrm{L}}}{J} \end{aligned} \tag{6.4.4}$$

$$g(x) = \begin{bmatrix} g_{11} & g_{12} \\ g_{21} & g_{22} \end{bmatrix} = \begin{bmatrix} \frac{2L_{\mathrm{m}}\psi_{\mathrm{r}\alpha}}{\sigma L_{\mathrm{s}}\tau_{\mathrm{r}}} & \frac{2L_{\mathrm{m}}\psi_{\mathrm{r}\beta}}{\sigma L_{\mathrm{s}}\tau_{\mathrm{r}}} \\ -\frac{3n_{\mathrm{p}}L_{\mathrm{m}}\psi_{\mathrm{r}\beta}}{2J\sigma L_{\mathrm{s}}L_{\mathrm{r}}} & \frac{3n_{\mathrm{p}}L_{\mathrm{m}}\psi_{\mathrm{r}\alpha}}{2J\sigma L_{\mathrm{s}}L_{\mathrm{r}}} \end{bmatrix} \tag{6.4.5}$$

As $det[g(x)] \neq 0$ when $|\psi_{\mathrm{r}}| \neq 0$, the $g(x)$ is non-singular for all nominal operating points. Then the system input can be designed as

$$\begin{bmatrix} u_1 \\ u_2 \end{bmatrix} = g(x)^{-1}\left(\begin{bmatrix} -\Psi_1(x) \\ -\Psi_2(x) \end{bmatrix} + \begin{bmatrix} v_1 \\ v_2 \end{bmatrix}\right) \tag{6.4.6}$$

where v_1 and v_2 are the linear control inputs, which are designed using the linear control theory.

6.4.2 Definition of Perturbation and SPO Design

For the ith (i=1,2) subsystem in (6.4.2), defining state variables as $z_{i1} = y_i$, $z_{i2} = \dot{y}_i$ and a fictitious state to represent the perturbation $z_{i3} = \Psi_i$, the ith subsystem is represented as:

$$\begin{cases} \dot{z}_{i1} = z_{i2} \\ \dot{z}_{i2} = z_{i3} + g_{i1}u_1 + g_{i2}u_2 \\ \dot{z}_{i3} = \dot{\Psi}_i \end{cases} \tag{6.4.7}$$

The change of parameter R_r affects the perturbation Ψ_i and the time constant τ_r in g_i in (6.4.5). The new perturbation becomes:

$$z'_{i3} = \Psi_i + \Delta R_\mathrm{r}\left(\frac{\partial \Psi_i}{\partial R_\mathrm{r}} + \frac{\partial g_{i1}}{\partial R_\mathrm{r}}u_1 + \frac{\partial g_{i2}}{\partial R_\mathrm{r}}u_2\right) \tag{6.4.8}$$

where ΔR_r is the mismatched rotor resistance comparing with the nominal value.

For system (6.4.7), several types of state and perturbation observers (SPOs) have been proposed, such as high-gain observer [88], sliding mode observer [126], and nonlinear observer [170]. In this chapter, two high-gain observers are used to estimate the perturbations. Other types of observer can be designed similarly, and used for comparing the performance with the high-gain observer in observer based control methods in Section 6.6.

When the system outputs y_i are available, two third-order SPOs are designed to estimate the subsystem states and perturbation as:

$$\begin{cases} \dot{\hat{z}}_{i1} = \hat{z}_{i2} + l_{i1}(z_{i1} - \hat{z}_{i1}) \\ \dot{\hat{z}}_{i2} = \hat{z}_{i3} + g_{i1}u_1 + g_{i2}u_2 + l_{i2}(z_{i1} - \hat{z}_{i1}) \\ \dot{\hat{z}}_{i3} = l_{i3}(z_{i1} - \hat{z}_{i1}) \end{cases} \tag{6.4.9}$$

where $\hat{z}_{ij}$ (j=1,2,3) are the estimations of z_{ij} and l_{ij} the observer gains, which are defined as $l_{ij} = \alpha_j/\varepsilon^j$, and $0 < \varepsilon < 1$ is a small positive parameter to be specified to represent times of the time-dynamics between the observer and the real system. The parameters α_j are chosen such that the roots of

$$s^3 + \alpha_1 s^2 + \alpha_2 s + \alpha_3 = 0 \tag{6.4.10}$$

are in the open left-half complex plane.

6.4.3 Nonlinear Adaptive Controller

For subsystems, two third-order SPOs are designed to estimate the states z_{i1}, z_{i2} and perturbations z'_{i3}. By compensating the real perturbations using the estimated ones, the original nonlinear system is linearized from (6.4.2) and (6.4.12), where v_i are the fictitious inputs that are defined using the linear control algorithm as follows:

$$v_i = k_{i1}(y_i^* - \hat{z}_{i1}) + k_{i2}(\dot{y}_i^* - \hat{z}_{i2}) + \ddot{y}_i^* \tag{6.4.11}$$

The original system inputs are finally transformed back using

$$\begin{bmatrix} u_1 \\ u_2 \end{bmatrix} = g(x)^{-1} \left(\begin{bmatrix} v_1 \\ v_2 \end{bmatrix} - \begin{bmatrix} \hat{z}_{13} \\ \hat{z}_{23} \end{bmatrix} \right) \tag{6.4.12}$$

where

$$g(x)^{-1} = \begin{bmatrix} \frac{\sigma L_\mathrm{s} \tau_\mathrm{r} \psi_{\mathrm{r}\alpha}}{2L_\mathrm{m}(\psi_{\mathrm{r}\alpha}^2 + \psi_{\mathrm{r}\beta}^2)} & \frac{-2J\sigma L_\mathrm{s} L_\mathrm{r} \psi_{\mathrm{r}\beta}}{3n_\mathrm{p} L_\mathrm{m}(\psi_{\mathrm{r}\alpha}^2 + \psi_{\mathrm{r}\beta}^2)} \\ \frac{\sigma L_\mathrm{s} \tau_\mathrm{r} \psi_{\mathrm{r}\beta}}{2L_\mathrm{m}(\psi_{\mathrm{r}\alpha}^2 + \psi_{\mathrm{r}\beta}^2)} & \frac{2J\sigma L_\mathrm{s} L_\mathrm{r} \psi_{\mathrm{r}\alpha}}{3n_\mathrm{p} L_\mathrm{m}(\psi_{\mathrm{r}\alpha}^2 + \psi_{\mathrm{r}\beta}^2)} \end{bmatrix}$$

which is using the nominal values of system parameters.

The final control law to be represented by physical variables, such as inductance, inertia, rotor flux and mechanical rotation speed, is given as:

$$\begin{aligned} \begin{bmatrix} v_{\mathrm{s}\alpha} \\ v_{\mathrm{s}\beta} \end{bmatrix} = & \begin{bmatrix} \frac{\sigma L_\mathrm{s} \tau_\mathrm{r} \psi_{\mathrm{r}\alpha}}{2L_\mathrm{m}(\psi_{\mathrm{r}\alpha}^2 + \psi_{\mathrm{r}\beta}^2)} & \frac{-2J\sigma L_\mathrm{s} L_\mathrm{r} \psi_{\mathrm{r}\beta}}{3n_\mathrm{p} L_\mathrm{m}(\psi_{\mathrm{r}\alpha}^2 + \psi_{\mathrm{r}\beta}^2)} \\ \frac{\sigma L_\mathrm{s} \tau_\mathrm{r} \psi_{\mathrm{r}\beta}}{2L_\mathrm{m}(\psi_{\mathrm{r}\alpha}^2 + \psi_{\mathrm{r}\beta}^2)} & \frac{2J\sigma L_\mathrm{s} L_\mathrm{r} \psi_{\mathrm{r}\alpha}}{3n_\mathrm{p} L_\mathrm{m}(\psi_{\mathrm{r}\alpha}^2 + \psi_{\mathrm{r}\beta}^2)} \end{bmatrix} \\ & \times \begin{bmatrix} k_{11}(\psi_\mathrm{r}^{*2} - \hat{z}_{11}) - k_{12}\hat{z}_{12} - \hat{z}_{13} \\ k_{21}(\omega_\mathrm{m}^* - \hat{z}_{21}) - k_{22}\hat{z}_{22} - \hat{z}_{23} \end{bmatrix} \end{aligned} \tag{6.4.13}$$

6.5 Stability Analysis

This section analyzes the stability of the closed-loop system equipped with the perturbation estimation based NAC designed in the previous section.

At first, both the estimation error system and the tracking error system are obtained. On one hand, by defining estimation errors $\varepsilon_{i1} = z_{i1} - \hat{z}_{i1}$, $\varepsilon_{i2} = z_{i2} - \hat{z}_{i2}$, and $\varepsilon_{i3} = z'_{i3} - \hat{z}_{i3}$, and subtracting (6.4.9) from (6.4.7), the following estimation error system is yielded:

$$\dot{\varepsilon}_i = A_i \varepsilon_i + \eta_i \tag{6.5.1}$$

where

$$\varepsilon_i = \begin{bmatrix} \varepsilon_{i1} \\ \varepsilon_{i2} \\ \varepsilon_{i3} \end{bmatrix}, \quad A_i = \begin{bmatrix} -l_{i1}\ 1\ 0 \\ -l_{i2}\ 0\ 1 \\ -l_{i3}\ 0\ 0 \end{bmatrix}, \quad \eta_i = \begin{bmatrix} 0 \\ 0 \\ \dot{\bar{\Psi}}_i \end{bmatrix}$$

On the other hand, define the tracking errors be $e_{i1} = y_i^* - z_{i1}$ and $e_{i2} = \dot{y}_i^* - z_{i2}$. It follows from (6.4.7) that

$$\dot{e}_{i1} = e_{i2}$$

And, it follows from $z_{i2} = \dot{y}_i$, (6.4.2), (6.4.11), and (6.4.12) that

$$\dot{e}_{i2} = -k_{i1}e_{i1} - k_{i2}e_{i2} - k_{i1}\varepsilon_{i1} - k_{i2}\varepsilon_{i2} - \varepsilon_{i3}$$

Thus, the tracking error system can be summarized as

$$\dot{e}_i = M_i e_i + \vartheta_i \tag{6.5.2}$$

where

$$e_i = \begin{bmatrix} e_{i1} \\ e_{i2} \end{bmatrix}, \quad M_i = \begin{bmatrix} 0 & 1 \\ -k_{i1} & -k_{i2} \end{bmatrix}, \quad \vartheta_i = \begin{bmatrix} 0 \\ -\xi_i \end{bmatrix}$$

with $\xi_i = k_{i1}\varepsilon_{i1} + k_{i2}\varepsilon_{i2} + \varepsilon_{i3}$ being the lumped estimation error.

The stability analysis of the closed-loop control system is transformed into the GUUB of error systems, and the following theorem is summarized.

Theorem 1. *Consider the IM system (6.2.1) equipped the proposed NAC (6.4.13) with two SPOs (6.4.9). If the real perturbation $\bar{\Psi}_i(x,t)$ defined in (6.4.8) satisfying*

$$||\dot{\bar{\Psi}}_i(x,t)|| \leq \gamma_1 \tag{6.5.3}$$

then both the estimation error system (6.5.1) and the tracking error system (6.5.2) are GUUB, i.e.,

$$||\varepsilon_i(t)|| \leq 2\gamma_1||P_1||,\ ||e_i(t)|| \leq 4\gamma_1||K_i||||P_1||||P_2||,\ \forall t \geq T \tag{6.5.4}$$

where $P_i, i = 1, 2$ are respectively the feasible solutions of Riccati equations $A_i^{\mathrm{T}}P_1 + P_1A_i = -I$ and $M_i^{\mathrm{T}}P_2 + P_2M_i = -I$; and $||K_i||$ is a constant related to $k_{ij}, j = 1, 2$.

Proof. For the estimation error system (6.5.1), consider the following Lyapunov function:

$$V_{i1}(\varepsilon_i) = \varepsilon_i^{\mathrm{T}} P_1 \varepsilon_i \tag{6.5.5}$$

The high gains of SPOs (6.4.9) are determined by requiring (6.4.10) holds, which means A_i is Hurwitz. One can find a feasible positive definite solution, P_1, of Riccati equation $A_i^{\mathrm{T}} P_1 + P_1 A_i = -I$. Calculating the derivative of $V_{i1}(\varepsilon_i)$ along the solution of system (6.5.1) and using (6.5.3) yield

$$\begin{aligned} \dot{V}_{i1}(\varepsilon_i) &= \varepsilon_i^T (A_i^{\mathrm{T}} P_1 + P_1 A_i)\varepsilon_i + \eta_i^{\mathrm{T}} P_1 \varepsilon_i + \varepsilon_i^{\mathrm{T}} P_1 \eta_i \\ &\leq -\|\varepsilon_i\|^2 + 2||\varepsilon_i|| \cdot ||\eta_i|| \cdot ||P_1|| \\ &\leq -\|\varepsilon_i\|(\|\varepsilon_i\| - 2\gamma_1 ||P_1||) \end{aligned} \tag{6.5.6}$$

Then $\dot{V}_{i1}(\varepsilon_i) \leq 0$ when $\|\varepsilon_i\| \geq 2\gamma_1 ||P_1||$. Thus there exists $T_1 > 0$ such that

$$\|\varepsilon_i(t)\| \leq \gamma_2 = 2\gamma_1 ||P_1||, \quad \forall\, t \geq T_1 \tag{6.5.7}$$

For the tracking error system (6.5.2), one can find that $||\vartheta_i|| \leq ||K_i||\gamma_2$ with $||K_i||$ based on $\|\varepsilon_i(t)\| \leq \gamma_2$. Consider the Lyapunov function $V_{i2}(e_i) = e_i^{\mathrm{T}} P_2 e_i$. Similarly, one can prove that, there exists an instant, $\bar{T}_1$, the following holds

$$\|e_i(t)\| \leq 2||K_i||\gamma_2||P_2|| \leq 4\gamma_1||K_i||||P_1||||P_2||, \ \forall\, t \geq \bar{T}_1 \tag{6.5.8}$$

Using (6.5.7) and (6.5.8) and setting $T = \max\{T_1, \bar{T}_1\}$ lead to (6.5.4).

Moreover, if W_i is locally Lipschitz in its arguments, it will guarantee the exponential convergence of the observation error [126] and closed-loop tracking error into

$$\lim_{t\to\infty} \varepsilon_i(t) = 0 \quad \text{and} \quad \lim_{t\to\infty} e_i(t) = 0 \tag{6.5.9}$$

After the states ω_{m} and ψ_{r}^2 and their derivatives are stable that controlled by NAC, the decoupling makes one state unobservable (zero dynamic) and that is the rotation angle of the flux vector [63], which is always stable in cycles.

The parameter variation is considered in the error system in (6.5.1) and (6.5.2), and the error system is proved as converged to zero in (6.5.9). This guarantees

Table 6.1: System parameters of IM

R_{s}	R_{r}	L_{s}	L_{r}
0.1607 Ω	0.1690 Ω	6.017 mH	5.403 mH
L_{m}	J	n_{p}	
5.325 mH	0.000145 kg·m^2	2	

that the estimated perturbations track the extended states defined in (6.4.8), which includes the uncertainties affected by the parameter variations, and compensated the control input in (6.4.12). Then the linearized subsystem in (6.4.7) is independent with the parameters and disturbance.

6.6 Simulation Results

The NAC speed controller is validated in simulation using MATLAB/Simulink. The speed tracking performance of NAC is compared with the conventional VC and the IOLC. Both the VC and the NAC use the same rotor flux observer to estimate the rotor flux. The conventional VC uses the estimated flux position to transform the voltage and current from stationary frame into rotating frame. The NAC controls the IM system directly under fixed stationary frame, and its scheme diagram is shown in Figure 6.2. The parameters of IM used for the simulation purpose are given in Table 6.1. Controller parameters of NAC controllers and the SPOs are given in Table 6.2.

6.6.1 Constant speed test for loss minimization

In the simulation test, the motor was running with a constant speed of 100 rad/s (0.3 p.u.) under a constant load torque of 0.1 N·m (0.2 p.u.) and with the rated flux current with the NAC speed controller. At t = 1 s, the rotor flux smoothly switched from its rated value to the optimal value calculated from the power loss minimization algorithm. The results are shown in Figure 6.3, which includes the speed regulation, flux tracking, and input power. The results show that the loss minimization algorithm for NAC reduced the input electrical power with about 20% less than that of using rated flux under light load condition.

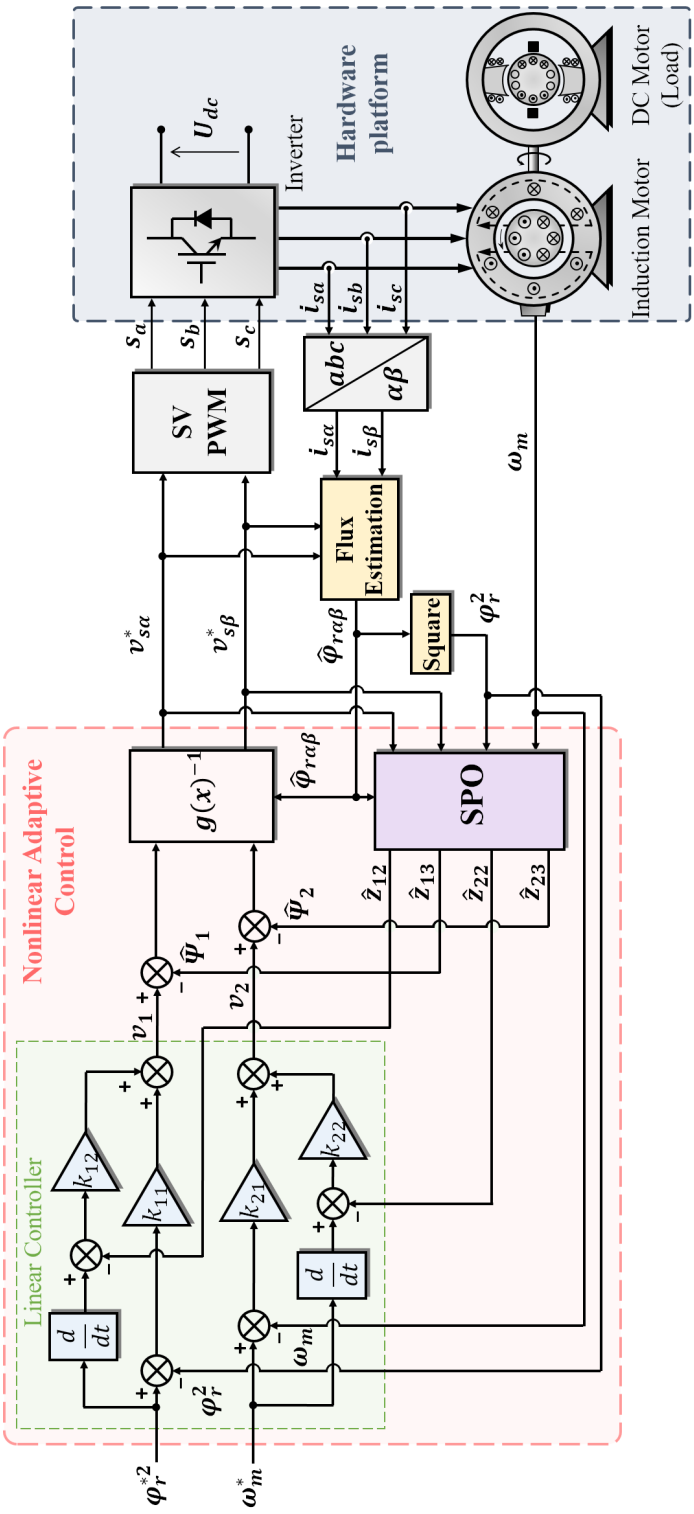

Figure 6.2: The NAC control scheme for IM speed drive.

Table 6.2: Controller parameters

Nonlinear Adaptive Controller		
Flux SPO	$l_{11} = 6 \times 10^3$	$l_{12} = 1.1 \times 10^7$
	$l_{13} = 5.6 \times 10^9$	
Speed SPO	$l_{21} = 1.8 \times 10^3$	$l_{22} = 9.7 \times 10^5$
	$l_{23} = 4.5 \times 10^8$	
Flux Controller	$k_{11} = 1 \times 10^5$	$k_{12} = 4 \times 10^3$
Speed Controller	$k_{21} = 8 \times 10^3$	$k_{22} = 4 \times 10^2$

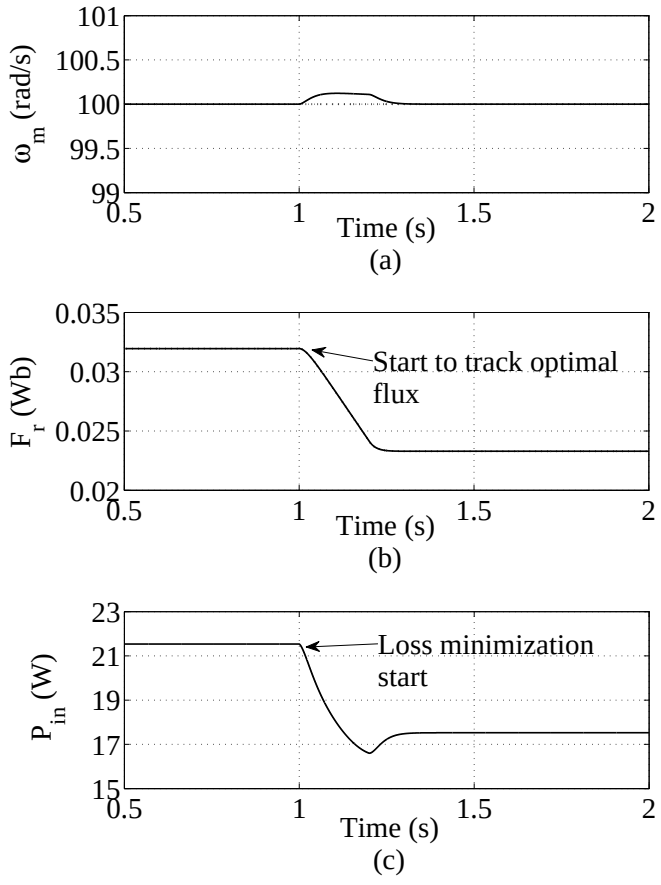

Figure 6.3: Efficiency optimization test under constant reference speed and load disturbance in simulation. (a) Mechanical rotor speed; (b) rotor flux; (c) input power.

6.6.2 Step Load Disturbance

In the simulation test, the motor starts up to a constant speed of 100 rad/s under rated rotor flux and no load. At t = 3 s, a step load disturbance of 0.4 N·m is applied to the IM system. The simulation tests compare the high-gain observer based NAC with the conventional VC and other perturbation observer based control methods, such as the nonlinear state and perturbation observer (NSPO) based ADRC, and sliding mode state and perturbation observer (SMSPO) based control. The control performance of different control methods is compared in Figure 6.4 with the tracking performance of rotor flux ϕ_{r} and mechanical rotor speed ω_{m} and their regulation errors in percentage.

The results show that the NAC has less regulation error and faster recovery speed in both flux and rotor speed. The IOLC performs the best under the assumption that all the conditions are known in simulation. To further identify the improvement of NAC numerically, the control performance of VC and NAC are compared with the following indices: the maximum flux and speed regulation error, their recovery time, and their integral-absolute-error (IAE) in regulation. The performance indices are summarized in Table 6.3, in which it is shown that the NAC has 71% and 67% less regulation error in flux and speed tracking, respectively. The flux recovery time, which is defined as the time period to eliminate the tracking error into 5% of the maximum error, of VC is 1.3 s while that of NAC is 0.2 s, and the speed recovery time of VC is 1.5 s while that of NAC is 0.2 s, which shows the NAC improved the speed of eliminating the error. In addition, the flux and speed IAE in NAC are 10% less than that in VC. The regulation performance of NAC has obvious improvement than the conventional control method.

The perturbation estimation performance of different types of observer are shown in Figure 6.5 with the performance comparison and their estimation error. The results show that the estimated perturbations track the real ones with steady state estimation error keeps zero. The HGSPO has the maximum estimation error of approximate 0.7 $\mathrm{Wb}^2/\mathrm{s}^2$ and 1×10^4 $\mathrm{rad/s}^3$, which are less than 7% of the real perturbations. Other perturbation observers got the similar results in perturbation estimation but with much more complex structure.

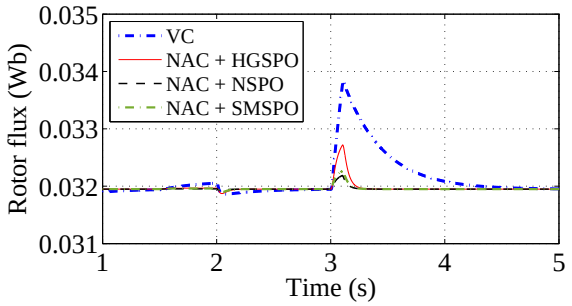

(a)

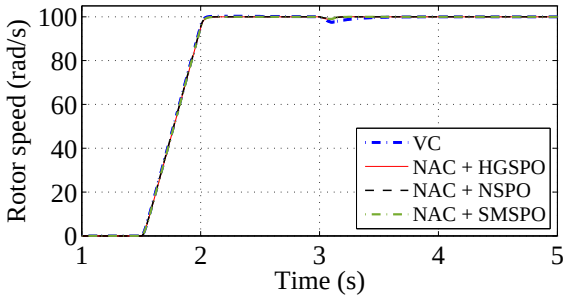

(b)

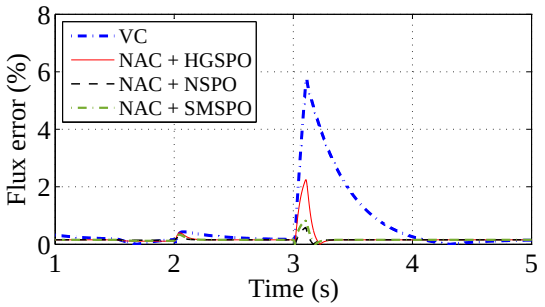

(c)

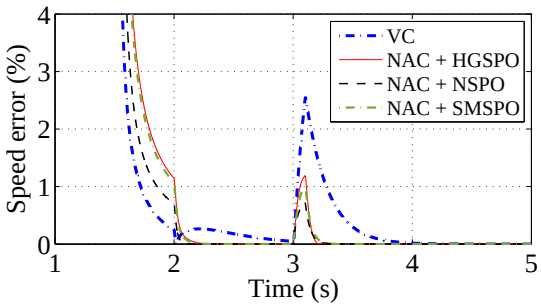

(d)

Figure 6.4: Dynamic response of rotor flux and speed, and their regulation error of different disturbance observer based control methods.

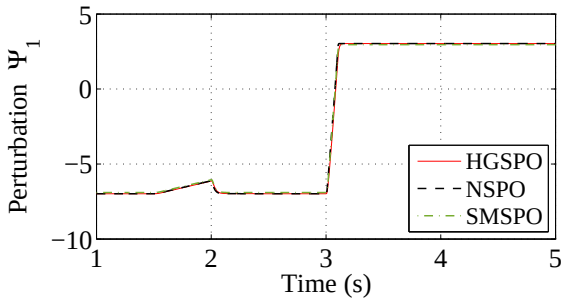

(a)

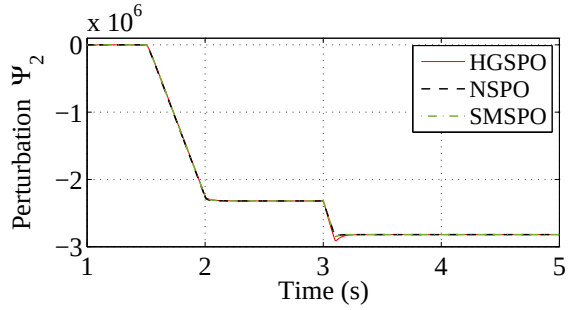

(b)

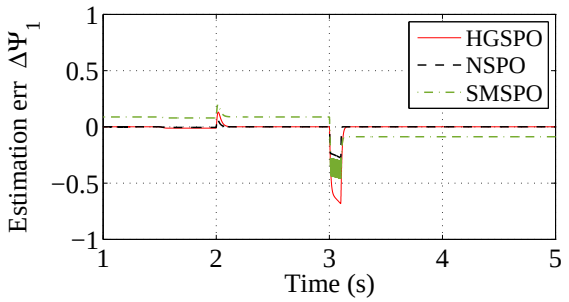

(c)

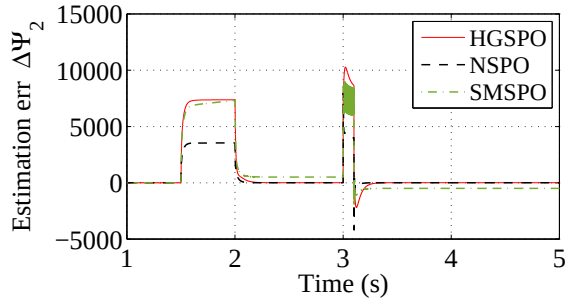

(d)

Figure 6.5: The performance of perturbation Ψ_1, Ψ_2 and their estimation error $\Delta\Psi_1$ and $\Delta\Psi_2$ under step load disturbance in simulation.

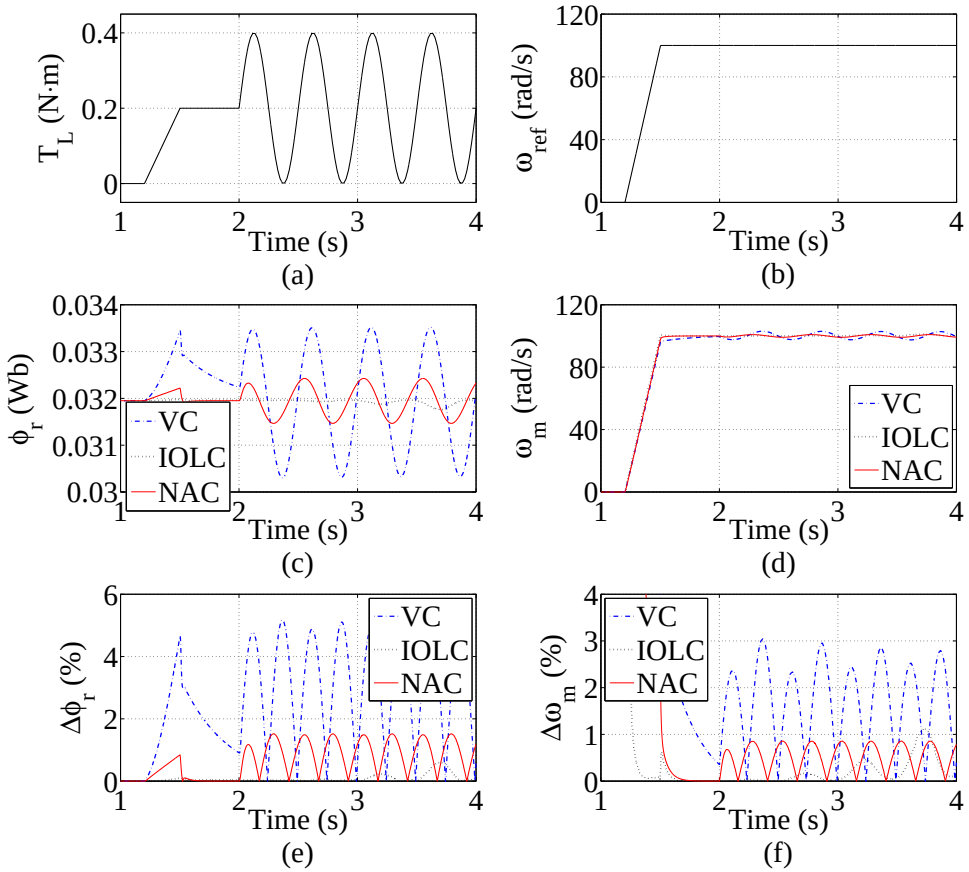

Figure 6.6: Dynamic response of rotor flux and speed as well as their regulation error under time-varying load torque in simulation.

6.6.3 Time-varying Load Disturbance

The second case is the constant speed regulation with unknown time-varying load disturbance. In this case, the induction motor starts up to 100 rad/s with a ramp load disturbance from 0 to 0.2 N·m. At t = 2.0 s, a sinusoidal load disturbance oscillated between 0 and 0.4 N·m is applied to the motor. The load disturbance and reference speed are given in Figure 6.6 (a) and (b). The rotor flux and mechanical speed tracking performance and their tracking errors of all controllers are compared in Figure 6.6 (c) to (f).

Due to the disturbance is estimated in the perturbation and compensated in the system, the time-varying disturbance has less impact to the NAC than that of the VC. In addition, the IOLC gets the best performance under the time-varying disturbance as it is assumed that all the system dynamics and disturbance are available to

the controller. The control performance indices of VC and NAC are compared in Table 6.3. The results in the table show that the NAC has obviously improvement in control performance with about 64% less flux error and 75% less IAE in flux tracking, and about 72% less speed error and 64% less IAE in speed tracking under time-varying load disturbance.

Table 6.3: Performance indices of VC and NAC in simulation

Indices \ Method	VC	NAC	Improvements
Case: Speed regulation under step load disturbance			
Maximum flux error (Wb)	2.7×10^{-3}	7.7×10^{-4}	71% less
Flux recovery time (s)	1.3	0.2	85% less
Flux IAE (Wb·s)	1.2×10^{-3}	8.5×10^{-5}	93% less
Maximum speed error (rad/s)	-4.3	-1.4	67% less
Speed recovery time (s)	1.5	0.2	87% less
Speed IAE (rad)	2.8	0.14	95% less
Case: Speed regulation under time-varying load disturbance			
Maximum flux error (Wb)	1.6×10^{-3}	5.7×10^{-4}	64% less
Flux IAE (Wb·s)	2.5×10^{-3}	6.3×10^{-4}	75% less
Maximum speed error (rad/s)	3.05	0.86	72% less
Speed IAE (rad)	5.0	1.8	64% less

The perturbation estimation performances under time-varying load disturbance are shown in Figure 6.7. The results show that the maximum estimation error is less than 8% of the real perturbations, and the estimated performance tracks the real one in a good performance. And from its profile, the load disturbance is estimated and

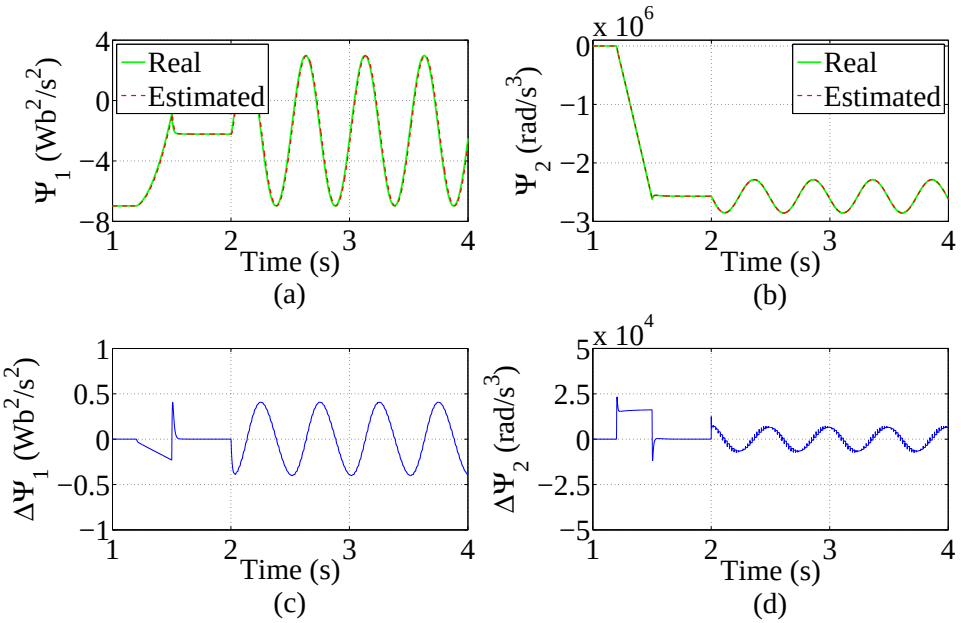

Figure 6.7: The performance of perturbation Ψ_1 and Ψ_2 as well as their estimation error $\Delta\Psi_1$ and $\Delta\Psi_2$ under time-varying load disturbance in simulation.

included in the lumped perturbation as expected in design.

The efficiency of the IM is tested versus different magnitude of the time-varying load, from 0 to 1.4 p.u., and operating speed, 50 rad/s, 100 rad/s and 150 rad/s. The comparison of efficiency is among three different control method: the NAC with flux optimization, the VC with flux optimization, and the NAC with rated constant flux. The result of efficiency comparison is shown in Figure 6.8. Comparing between the NAC with flux optimization and NAC with rated flux, it can be found that the flux optimization algorithm has obviously improvement in efficiency when IM operates with light load. Comparing between the NAC and VC both with flux optimization algorithm, it is obviously to find that the NAC always has higher efficiency than VC. That is because of the NAC has fully linearized the flux and speed to obtain a much better control performance in tracking the optimal flux command than VC.

6.6.4 Parameter Variation Performance

In the IM systems, the rotor resistance is possible varied during the operation, especially in the wound-rotor IMs [95]. The step variation of the rotor resistance is chosen to evaluate the NAC scheme under the worst operation condition. Figure 6.9

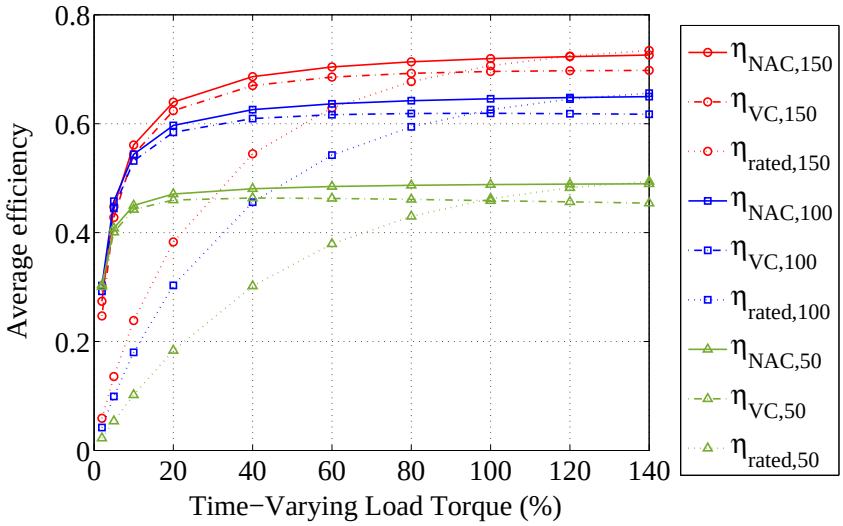

Figure 6.8: Comparison of motor efficiency among VC and NAC with loss minimization algorithm, and NAC with rated flux under different speed and time-varying load.

shows the comparison results among VC, IOLC and NAC when the rotor resistance steps up and down in simulation. At t = 4 s, the rotor resistance steps up from its nominal value to twice the nominal value, and steps down to its nominal value at the end. The result shows that the NAC is more robust than the conventional VC, and the IOLC is seriously impacted by the parameter variation, which shows that the IOLC requires the detailed system model and accurate parameters to get a good performance.

The response curves of the mechanical speed controlled by VC and NAC in the presence of different rotor resistance, which includes the mismatched R_{r} with 0.5, 0.8, 1.2, 1.5 and 2.0 p.u., are shown in Figure 6.10. The results show that the PI controller based VC is particular sensitive to rotor resistance variation. The NAC is much more robust than VC under mismatched parameters offers an almost flat response, which illustrates the adaptive capacity of the proposed control scheme.

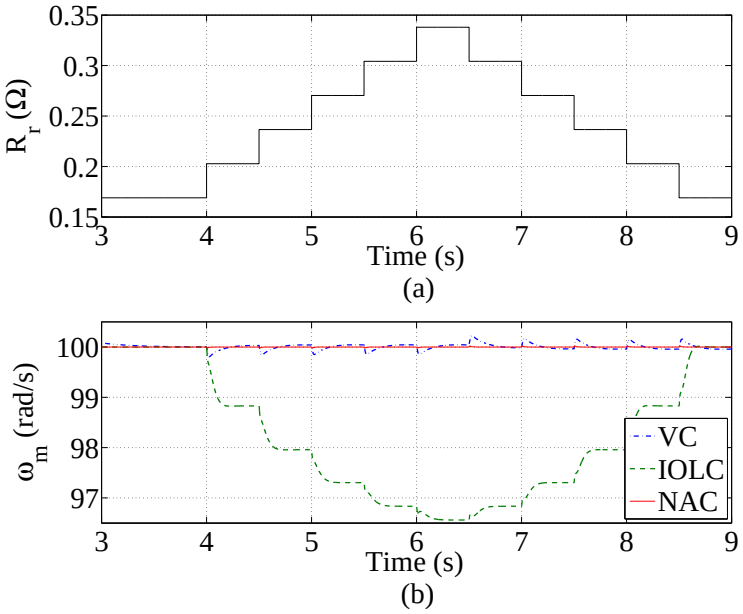

Figure 6.9: Speed response of different control methods when rotor resistance step up and down.

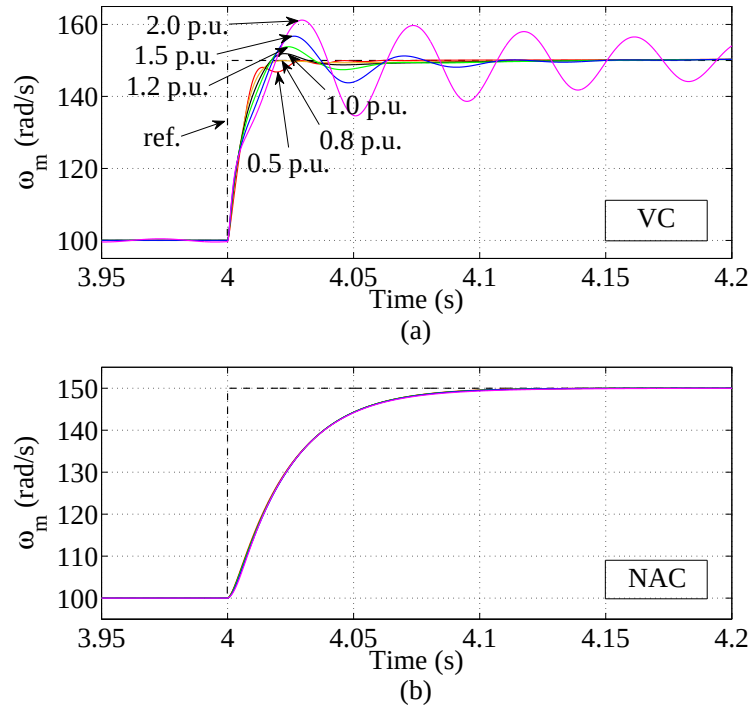

Figure 6.10: Step response of rotor speed ω_{m} under parameter uncertainty, where the rotor resistance R_{r} is mismatched.

6.7 Experiment Results

In this section, the DSP-based electric drive system in the dSPACE environment is used for hardware implementation. The dSPACE real-time simulator can transform the MATLAB/Simulink block diagrams to the C code language automatically in the embedded controller.

6.7.1 dSPACE Platform

In dSPACE, a discrete controller is used to control the continuous systems with the sampling time period of T. Figure 6.11 shows the connections between the system and its controller. To transfer between the voltage signal to digital, the analog-to-digital converters (ADC) is needed to read the information of the sensors, and the digital-to-analog converters (DAC) is also needed to apply the control commands.

In the system, the DS1104 controller board, as shown in Figure 6.12, is used to monitor the input signal, such as motor voltage, current or speed command, and produce the control signal during every sampling step. It has a real-time interface of the producing program which is embedded inside the board to translate the MATLAB/Simulink controller model to C code. The CP1104 I/O board is an input-output interface board between the Power Electronics Drive Board and DS1104 controller board. In the motor control experiment, the speed and current signals are measured from the ADC inputs of DS1104, and the command generated by the extremum seeking is the pulse duration which applied to the input of the PWM generator. And the digital PWM signals are transmitted by CP1104 from DS1104 Controller Board to the power electronic drive board [176].

The power electronic drive board is supplied by a 42V DC source and has the feature to generate two different voltage sources (A1B1C1 and A2B2C2) because there are two independent three-phase PWM inverters on this board as shown in Figure 6.13. Thus, the two machines in the coupling system can be driven respectively. In addition, the phase current provide to the machines also can be controlled with speed and torque command. The output PWM voltage is controlled by the PWM signals, which is the various digital command signals to determine the duty

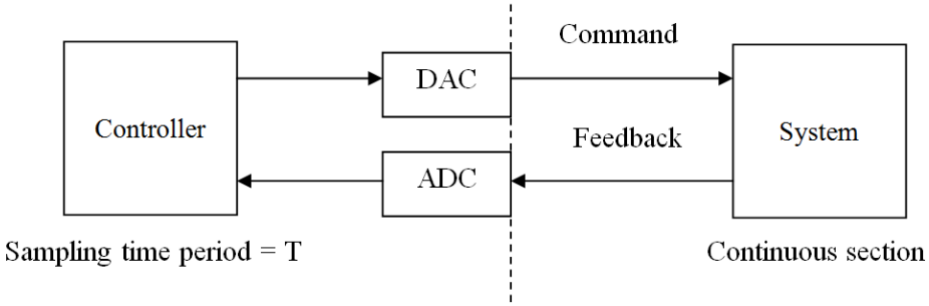

Figure 6.11: Block diagram of dSPACE control system.

Figure 6.12: The DS1104 control panel of dSPACE with ADC/DAC interface.

cycle of the switches, and then control the magnitude and phase of AC current from the source. The PWM signals are generated by the DS1104 R&D Controller board inside the computer [176].

The electric-drive experimental setup shown in Figure 6.14 consists of a 200 W, 2 pole-pairs, three-phase induction motor from Motorsolver; a power electronic converter unit; a DS1104 controller with interface board; and the dSPACE based control desk. The motor bench has a mechanical coupling arrangement, a target IM for motor driving coupled with a DC motor to produce load torque.

The interface of dSPACE is shown in Figure 6.15 as an example. The control desk is a user designed interface to monitor the signal feedbacks from ADC.

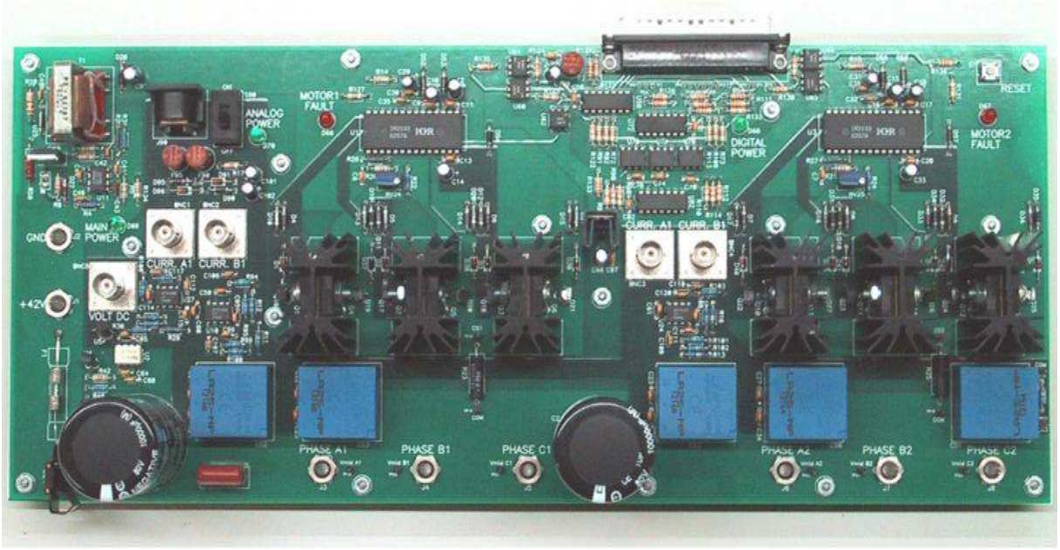

Figure 6.13: The power electronics board suitable for dSPACE DS1104.

6.7.2 Step Load Disturbance

The experimental validation for speed regulation under step load disturbance is set to be the same with that in simulation. At t = 10 s, a step load disturbance of 0.4 N·m, which is produced by the coupled DC motor via control its current in experiment, is applied to the IM when it is operating at the speed of 100 rad/s. The experimental results, as in Figure 6.16, show that the NAC has less regulation error and shorter recovery time under load disturbance. The performance indices are compared in Table 6.4, in which maximum flux error and speed dip in NAC are 69% and 76% less than that in VC, and their recovery time, which is defined the same as in the simulation section, in NAC are about 85% less than that of VC. And the flux IAE and speed IAE in NAC are only 11% and 28% of them in the VC. The stator current waveform of IM using both controllers are given in Figure 6.17, which shows that the NAC has less current magnitude in both peak and steady state value.

6.7.3 Time-varying Load Disturbance

In the experiment case of constant speed regulation under unknown time-varying load disturbance, the operating states are chosen to drive the IM under constant speed of 100 rad/s with optimal flux tracking. At t = 11.5 s, a load disturbance of

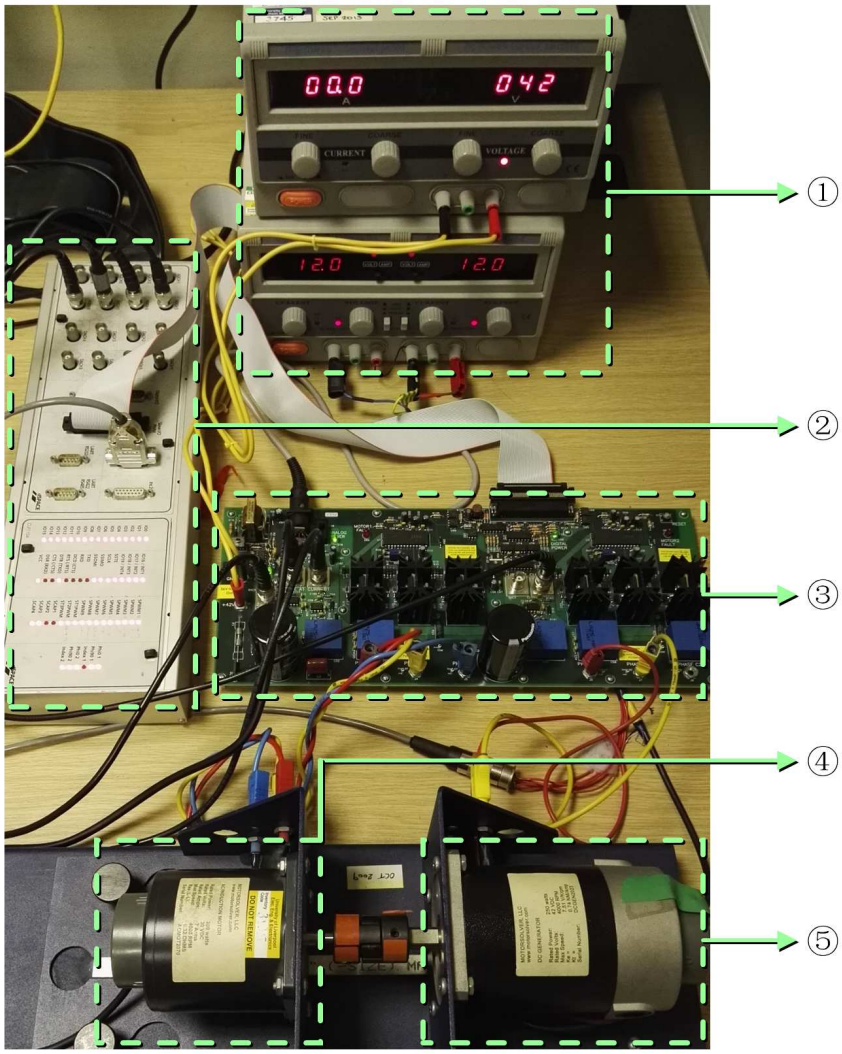

① DC power supply
② dSPACE CLP1104 control panel
③ MOSFET based power electronics board
④ Controlled target induction motor
⑤ Load DC motor

Figure 6.14: Experimental platform of NAC for IM drive.

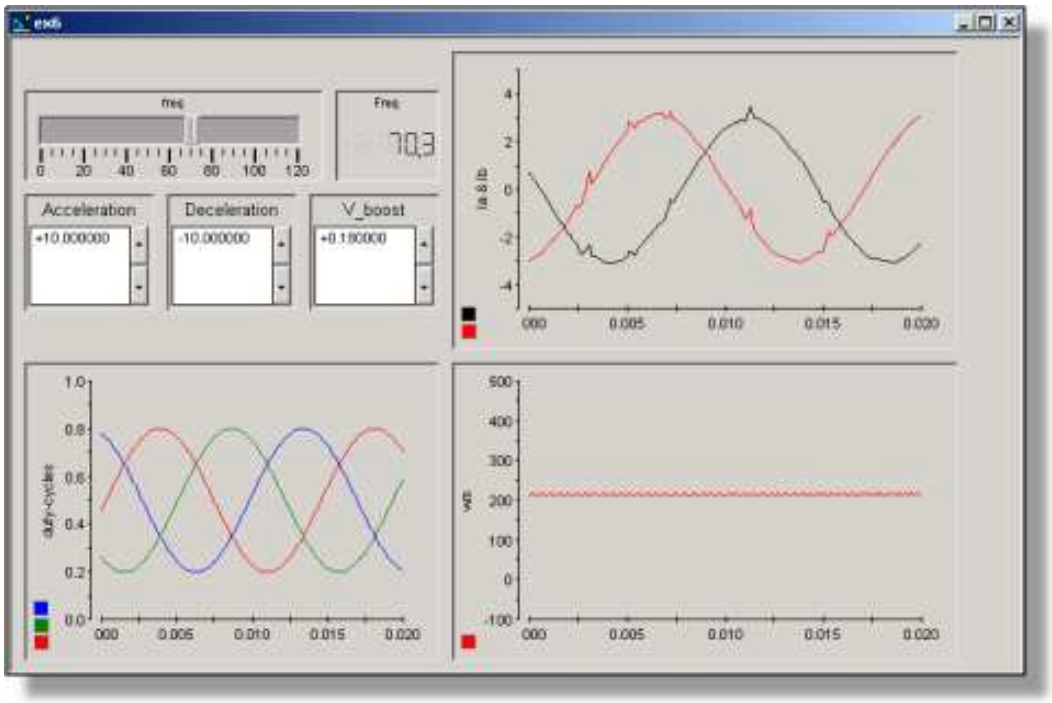

Figure 6.15: The interface of dSPACE control desk.

0.4 N·m time-varying torque is applied on the motor. The flux and speed tracking performance under load disturbance are shown in Figure 6.18. The performance indices of the two controllers compared in Table 6.4 show that in NAC the maximum flux error, maximum speed error, flux IAE and speed IAE are 68%, 70%, 74%, and 78% less than them in VC, respectively. The NAC performs better than the VC with faster response and less regulation error in speed and flux tracking in all the indices. The stator current waveforms are given in Figure 6.19. The peak current magnitude of NAC is less than that in VC, which shows that the NAC has less change of over-current than VC in practice.

In the experimental validation, the efficiency of IM is tested under different magnitude of time-varying load and speed. The comparison of efficiency results shown in Figure 6.21 is in the same performance as in simulation. The average efficiency is less than that in simulation due to the external loss in the hardware platform. The results show that the NAC improves the efficiency comparing with VC, especially under the time-varying load disturbance, in both simulation and experimental

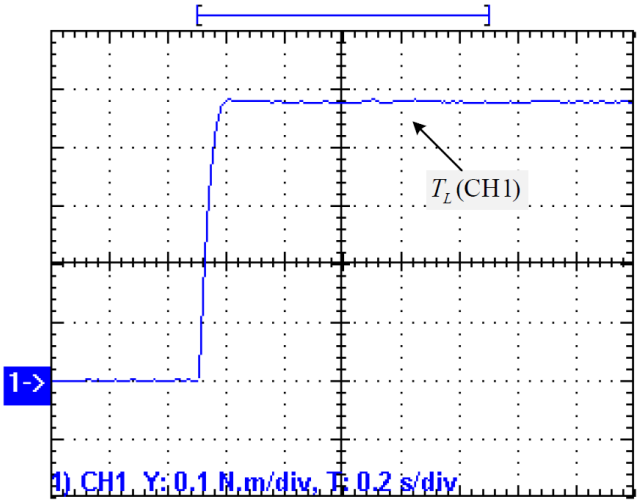

(a)

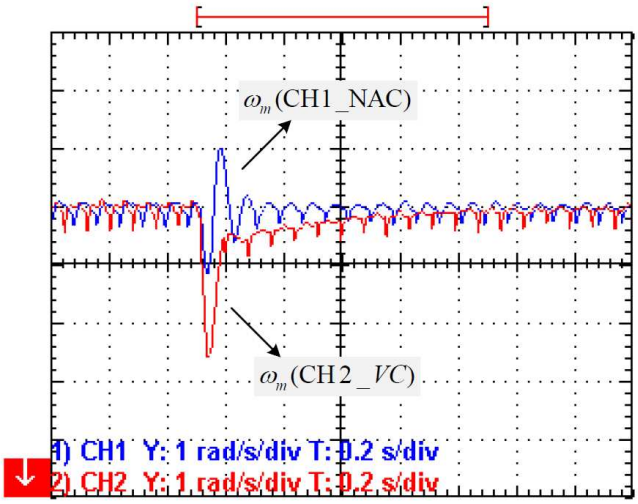

(b)

Figure 6.16: Constant speed regulation under step load disturbance in experiment. (a) Load torque, (b) rotor speed.

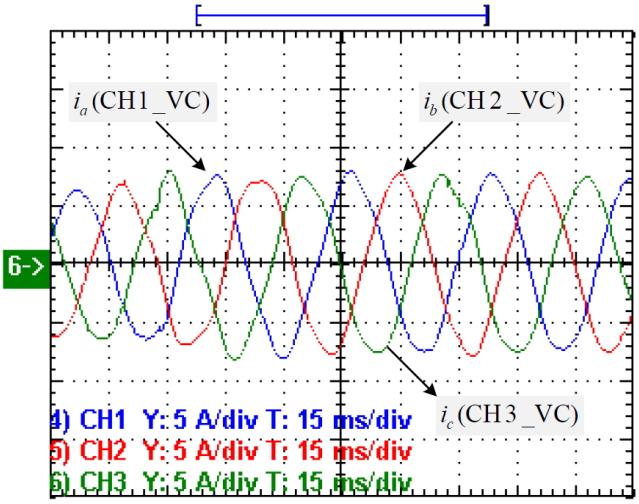

(a)

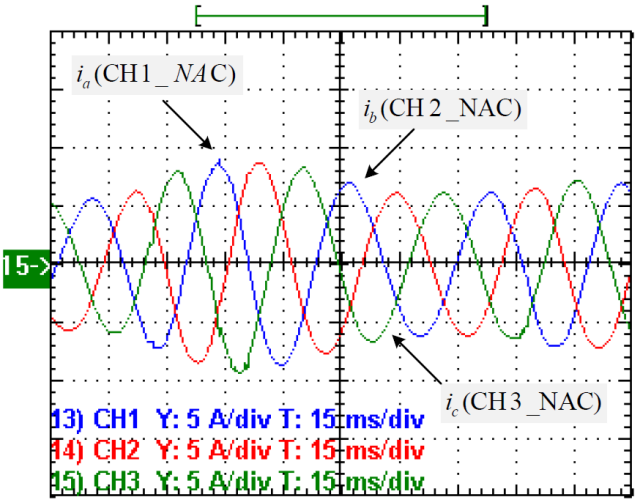

(b)

Figure 6.17: Stator current of IM controlled by (a) VC, and (b) NAC under step load disturbance in experiment.

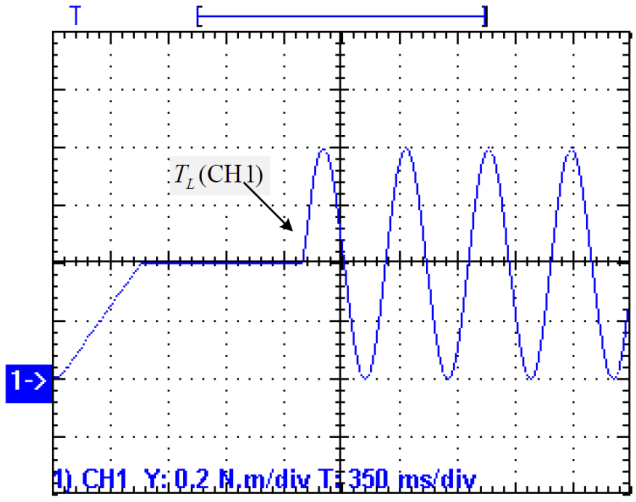

(a)

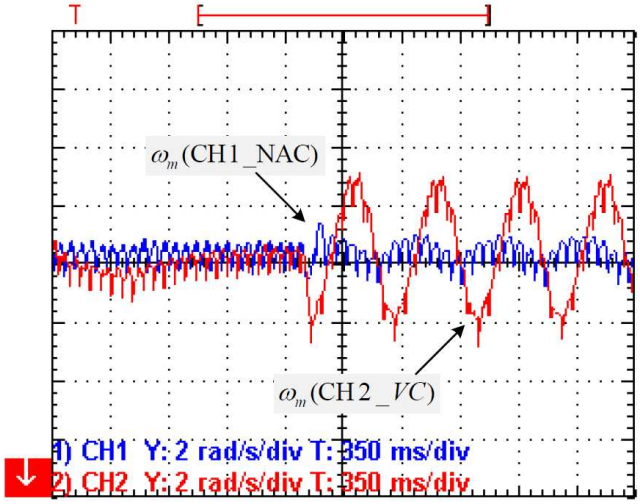

(b)

Figure 6.18: Constant speed under time-varying load disturbance in experiment. (a) Load torque, (b) rotor speed.

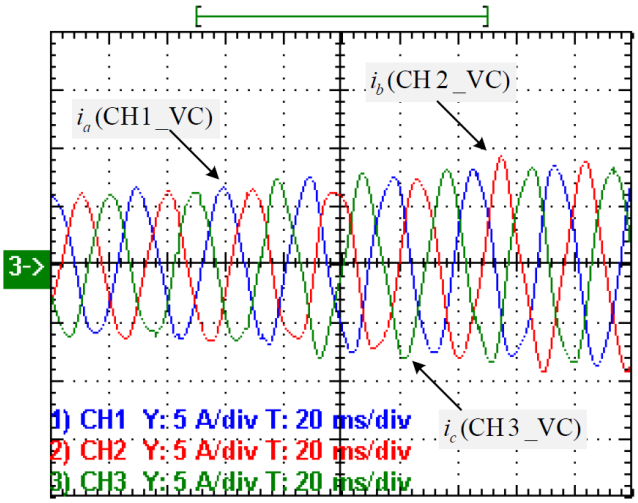

(a)

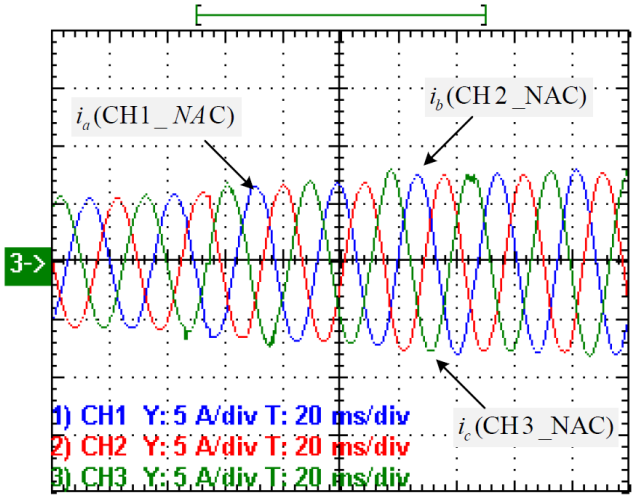

(b)

Figure 6.19: Stator current of IM controlled by (a) VC, and (b) NAC under time-varying load disturbance in experiment.

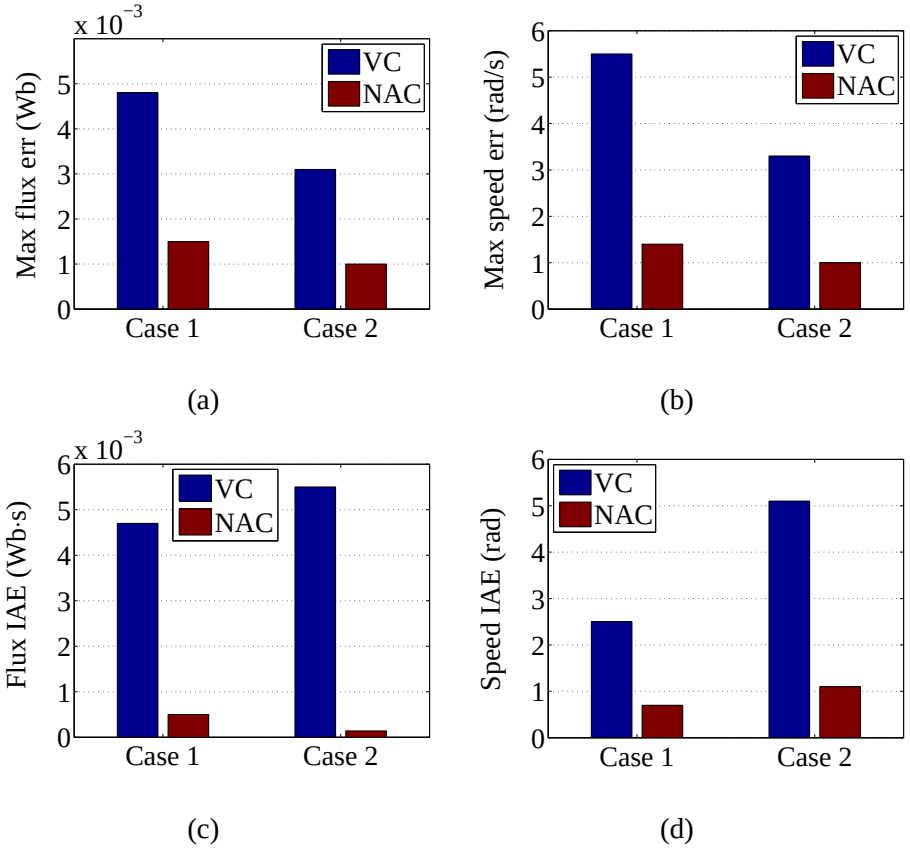

Figure 6.20: Indices comparison of VC and NAC in the (a) maximum flux error, (b) maximum speed error, (c) flux IAE, and (d) speed IAE.

Table 6.4: Experimental performance indices comparison between VC and NAC

Indices \ Method	VC	NAC	Improvements
Case: Speed regulation under step load disturbance			
Maximum flux error (Wb)	4.8×10^{-3}	1.5×10^{-3}	69% less
Flux recovery time (s)	1.3	0.2	85% less
Flux IAE (Wb·s)	4.7×10^{-3}	0.5×10^{-3}	89% less
Maximum speed error (rad/s)	-5.8	-1.4	76% less
Speed recovery time (s)	1.4	0.2	86% less
Speed IAE (rad)	2.5	0.7	72% less
Case: Speed regulation under time-varying load disturbance			
Maximum flux error (Wb)	3.1×10^{-3}	1.0×10^{-3}	68% less
Flux IAE (Wb·s)	5.5×10^{-3}	1.4×10^{-4}	74% less
Maximum speed error (rad/s)	3.3	1.0	70% less
Speed IAE (rad)	5.1	1.1	78% less

validation.

6.8 Conclusion

This chapter has proposed a nonlinear adaptive controller for flux and speed tracking of induction motors without acquiring the position of rotor flux and requiring accurate model of induction motors. The NAC controller utilizes state and perturbation observers to estimate the states and perturbations which are defined to include fast varying nonlinear dynamics, parameter uncertainties and external dis-

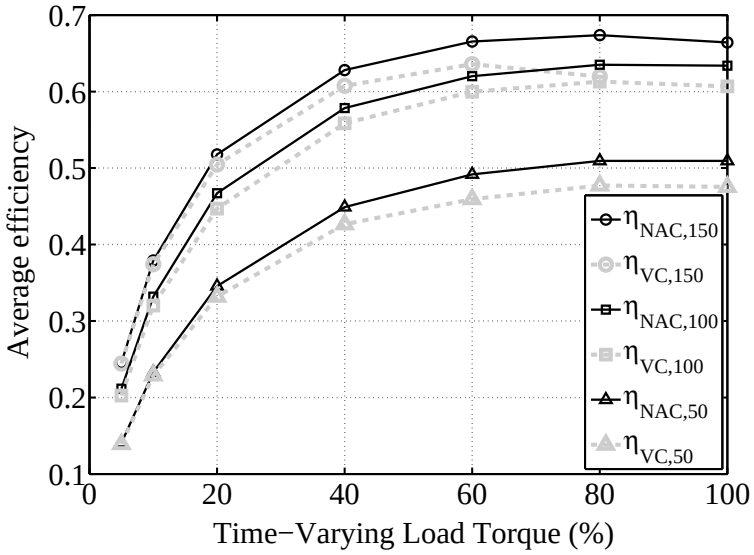

Figure 6.21: Average efficiency under different speed and time-varying load disturbance in experiment.

turbances. The estimate of perturbation is used to compensate the real perturbation for fully linearizing the induction motor system and improving robustness to parameter uncertainties and external load disturbances. The proposed controller is designed under stationary frame. Both simulation studies and experiment verifications are carried out to verify the control performance in comparison with the conventional vector control under rotating frame and model-based input-output linearizing control. The results showed that the NAC controller has better performance with faster dynamic response, less tracking error and improved robustness under step and time-varying load disturbances.

Chapter 7

Speed Sensorless Nonlinear Adaptive Control of Induction Motor for Electric Vehicles via a Combined Speed and Perturbation Observer

7.1 Introduction

Electric propulsion system is an integral part of EVs and HEVs [44, 177]. The performance of the traction motor drive plays an important role in the evolution of alternative energy vehicle and electrified transport industry. An IM is not only the workhorse of different kinds of domestic and industrial applications [40] but also one of the most appropriate electric motor candidates and widely accepted choice for most of the EVs and HEVs manufacturing companies [41, 42, 45]. However, the controlling of IM drive has difficulties because of its nonlinear dynamics, motor parameter variations during the operation and the unavailability of rotor currents and flux measurement [46]. As the conventional vector control cannot fully linearize the nonlinear IM system, for a better decoupled dynamics between the flux loop and the speed loop under nonlinearity and disturbances, a high performance controller is required for IM traction drive to achieve the fast transient response and energy

optimization [47, 48, 63]. Chapter 6 has studied the robust control method for the IM in the flux and speed tracking.

On the other side, due to the cost of the rotor speed and position sensor and the problem of sensor electrical noise, sensorless control which estimates the rotor speed instead of installing a speed encoder is preferred in high performance IM and EV applications [178]. The sensorless control methods for IM are possible after the rapid developments in the field of power electronics and digital signal processing [179–181].

The speed sensorless control has received great efforts, such as MRAS speed observer [105, 182, 183], MRAS-fuzzy logic observer [184], sliding mode observer [185], unscented Kalman filter [186], and artificial neural network speed observer [187], etc. Among them, rotor flux based MRAS speed observer is one of the most applied schemes. The currently two widely used control methods for IM are VC and direct torque control [47]. As the standard VC techniques can only achieve asymptotically decoupling of the flux and speed dynamics and also is sensitive to parameter uncertainties [93, 162], many advanced control methods are proposed to reduce the effect of parameter uncertainties and load disturbances, such as adaptive input-output linearization control [63], nonlinear exact feedback linearizing control which can fully decouple the flux and speed dynamics [64], parameter on-line estimation techniques [105, 106] and sliding mode control [188–191], fuzzy control [109, 110], and auto-disturbance rejection control [93, 95], etc. However, parameter estimation based controls can only deal with unknown constant or slow-varying parameters [63]. Moreover, most speed sensorless solution are achieved via augmenting an additional speed observer to the designed speed controller, such as the conventional VC controller with MRAS speed observer in Figure 7.1, while the combined design of the speed observer with the original control system has not been considered.

This chapter designs a speed sensorless nonlinear adaptive controller (SSNAC) which estimate and compensate the perturbation using a SPO in order to linearize the IM system, and further reduce the complexity via using a combined SPO to replace the PI regulator in the MRAS speed observer.

As the vector control can only achieve asymptotic input-output linearization of

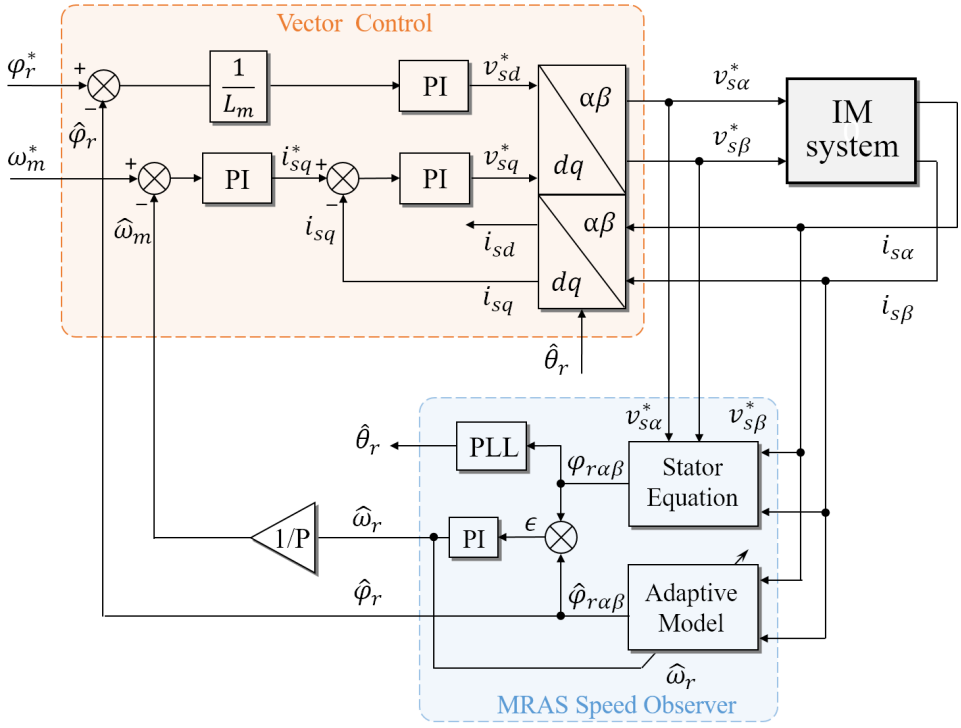

Figure 7.1: The controller scheme of conventional vector control with MRAS speed observer.

the IM system, in which the flux amplitude is regulated to the constant reference value at first and then rotor speed dynamics can be regulated independently, it can be improved via exact input-output linearization control (IOLC) [63]. The IOLC can achieve fully decoupling of the speed and the flux dynamics and thus the speed and the flux can be regulated/controlled instantaneously, which is useful for flux weakening for high speed operation and efficiency improvement via dynamically adjusting the flux level for light load and fast changing of load conditions (which is a typical for EV application). However, one main disadvantage of the IOLC is that the accurate system model and parameter is required, which results in a complex control law, weak robustness and is not practically feasible such as the time-varying of rotor/stator resistances. This stimulates the application of the proposed perturbation estimation and compensation method [88, 114] in this chapter which employs the online estimation and compensation of all nonlinear dynamics, together with the external disturbance and parameter uncertainties, and does not require the accurate system model of the induction motor.

The SSNAC employs the estimates of the rotor speed and the perturbation to replace/compensate their real values and thus improves the robustness in the presence of disturbance without the dependence of an accurate system model.

The remainder of this chapter is organized as follows. Section 7.2 presents the vehicle dynamic model and IM dynamic model in d-q frame. Section 7.3 presents the design of the proposed SSNAC controller. In Section 7.4, the stability of the closed-loop system is proved using Lyapunov theory. The effective application of NAC is validated in simulation and presented in Section 7.5 and validated experimentally in Section 7.6. Finally the chapter concludes in Section 7.7.

7.2 Model of Induction Motor Based Vehicle

7.2.1 Vehicle Dynamics of Motion

The model of vehicle dynamics and required tractive force to move the vehicle forward is discussed in [192, 193]. The acceleration dynamic equation of the vehicle

can be expressed as [193]

$$M_{\mathrm{v}}\frac{dV}{dt} = (F_{\mathrm{tf}} + F_{\mathrm{tr}}) - (F_{\mathrm{r}} + F_{\mathrm{w}} + F_{\mathrm{g}}) \tag{7.2.1}$$

where M_{v} is the vehicle mass, and V is the vehicle speed, F_{tf} and F_{tr} are the tractive force from front wheels and rear wheels; F_{r} is the rolling resistance of tires, F_{w} is the aerodynamic drag, and F_{g} is the grading resistance during hill climbing. When vehicle moves up on a sloped surface with angle α, the main load is the grading resistance caused by its weight as [193]

$$F_{\mathrm{g}} = M_{\mathrm{v}} g \sin\alpha \tag{7.2.2}$$

where g is the gravitational acceleration.

7.2.2 Induction Motor Model

A three-phase IM is transformed to the stationery $\alpha - \beta$ frame via Clark transformation and then to the rotating $d-q$ frame via Park transformation, based on the rotor flux angle θ_r obtained from the MRAS described $\alpha - \beta$ frame in section 7.3.4. Dynamic model of an induction machine is modelled in a rotating $d-q$ frame as follows [171, 194]:

$$\dot{x} = f(x) + Gu \tag{7.2.3}$$

where

$$x = \begin{bmatrix} i_{\mathrm{sd}} & i_{\mathrm{sq}} & \psi_{\mathrm{rd}} & \psi_{\mathrm{rq}} & \omega_{\mathrm{m}} \end{bmatrix}^T$$

$$f(x) = \begin{bmatrix} -\left(\frac{R_{\mathrm{s}}}{\sigma L_{\mathrm{s}}} + \frac{R_{\mathrm{r}} L_{\mathrm{m}}^2}{\sigma L_{\mathrm{s}} L_{\mathrm{r}}^2}\right) i_{\mathrm{sd}} + \omega_{\mathrm{e}} i_{\mathrm{sq}} + \frac{R_{\mathrm{r}} L_{\mathrm{m}}}{\sigma L_{\mathrm{s}} L_{\mathrm{r}}^2}\psi_{\mathrm{rd}} + \frac{\omega_{\mathrm{r}} L_{\mathrm{m}}}{\sigma L_{\mathrm{s}} L_{\mathrm{r}}}\psi_{\mathrm{rq}} \\ -\left(\frac{R_{\mathrm{s}}}{\sigma L_{\mathrm{s}}} + \frac{R_{\mathrm{r}} L_{\mathrm{m}}^2}{\sigma L_{\mathrm{s}} L_{\mathrm{r}}^2}\right) i_{\mathrm{sq}} - \omega_{\mathrm{e}} i_{\mathrm{sd}} - \frac{\omega_{\mathrm{r}} L_{\mathrm{m}}}{\sigma L_{\mathrm{s}} L_{\mathrm{r}}}\psi_{\mathrm{rd}} + \frac{R_{\mathrm{r}} L_{\mathrm{m}}}{\sigma L_{\mathrm{s}} L_{\mathrm{r}}^2}\psi_{\mathrm{rq}} \\ -\frac{R_{\mathrm{r}}}{L_{\mathrm{r}}}\psi_{\mathrm{rd}} + (\omega_{\mathrm{e}} - \omega_{\mathrm{r}})\psi_{\mathrm{rq}} + \frac{R_{\mathrm{r}} L_{\mathrm{m}}}{L_{\mathrm{r}}} i_{\mathrm{sd}} \\ -\frac{R_{\mathrm{r}}}{L_{\mathrm{r}}}\psi_{\mathrm{rq}} - (\omega_{\mathrm{e}} - \omega_{\mathrm{r}})\psi_{\mathrm{rd}} + \frac{R_{\mathrm{r}} L_{\mathrm{m}}}{L_{\mathrm{r}}} i_{\mathrm{sq}} \\ \frac{3PL_{\mathrm{m}}}{2JL_{\mathrm{r}}}\left(\psi_{\mathrm{rd}} i_{\mathrm{sq}} - \psi_{\mathrm{rq}} i_{\mathrm{sd}}\right) - \frac{T_{\mathrm{L}}}{J} \end{bmatrix}$$

$$G = \begin{bmatrix} \frac{1}{\sigma L_{\rm s}} & 0 & 0 & 0 & 0 \\ 0 & \frac{1}{\sigma L_{\rm s}} & 0 & 0 & 0 \end{bmatrix}^T$$

$$u = \begin{bmatrix} u_1 & u_2 \end{bmatrix}^T = \begin{bmatrix} v_{\rm sd} & v_{\rm sq} \end{bmatrix}^T$$

the system output vector y is as

$$y = [\,|\psi_{\rm r}| \;\; \omega_{\rm m}\,]^T \tag{7.2.4}$$

where

$$|\psi_{\rm r}| = \sqrt{\psi_{\rm rd}^2 + \psi_{\rm rq}^2}$$

and the rotor currents are expressed as

$$\begin{cases} i_{\rm rd} = \frac{1}{L_{\rm s}}\psi_{\rm rd} - \frac{L_{\rm m}}{L_{\rm r}} i_{\rm sd} \\ i_{\rm rq} = \frac{1}{L_{\rm s}}\psi_{\rm rq} - \frac{L_{\rm m}}{L_{\rm r}} i_{\rm sq} \end{cases} \tag{7.2.5}$$

where $i_{\rm sd}$, $i_{\rm sq}$ and $\psi_{\rm rd}$, $\psi_{\rm rq}$ are the stator currents and the rotor fluxes in d-q frame, respectively; $v_{\rm sd}$ and $v_{\rm sq}$ are the voltage control inputs; $\omega_{\rm e}$, $\omega_{\rm r}$ and $\omega_{\rm m}$ are the synchronous speed, rotor electrical and mechanical speed, which satisfies $\omega_{\rm r} = P\omega_{\rm m}$; P and J are the number of pole pairs and rotor inertia; $T_{\rm L}$ is the load torque disturbance; $R_{\rm s}$, $R_{\rm r}$ and $L_{\rm s}$, $L_{\rm r}$ are the stator and rotor resistances and inductances, respectively, and $L_{\rm m}$ is the mutual inductance. Parameter $\sigma = 1 - L_{\rm m}^2/L_{\rm s}L_{\rm r}$ is the leakage coefficient.

Moreover, the reference rotor flux and mechanical speed are defined as $\psi_{\rm r}^*$ and $\omega_{\rm m}^*$, respectively, and their tracking error are defined as $e_1 = \psi_{\rm r} - \psi_{\rm r}^*$, $e_2 = \omega_{\rm m} - \omega_{\rm m}^*$.

The objective of the work presented in this chapter is to design a sensorless speed controller in the presence of various uncertainties and disturbances.

7.3 Speed Sensorless Nonlinear Adaptive Controller

This section applies the perturbation observer based nonlinear adaptive control (NAC) for speed and flux regulation of induction motor [88, 89, 114], then combines

the mostly used rotor-flux based MRAS speed observer for a speed sensorless control. The nonlinear IM system is transformed into two interacted flux and speed subsystems via input-output linearization at first. Then all system unknown nonlinearities, uncertainties and interactions between two subsystems are defined as perturbation terms. A MRAS speed observer and two state and perturbation observers (SPOs) are designed to estimate unmeasured states and perturbations. A combined SPO with MRAS is designed to estimate the speed and the perturbation by replacing the conventional PI regulator in the MRAS speed observer with the SPO, which can reduce the duplicated estimation of the rotor speed. The estimated perturbations are used to compensate their real value and thus to achieve the robust and adaptive linearization of the original nonlinear IM.

7.3.1 Input-output Linearization

The controller design is based on the $d-q$ frame IM model in Eq. (7.2.3), in which the d-axis is aligned with the rotor flux direction and thus $\psi_{rd} = \psi_r$, and $\psi_{rq} = 0$ [95, 194]. This shares the similar idea as the VC because the advantage of variables in the $d-q$ frame is slow time-varying [95]. Note that ψ_r is not required to be regulated to the reference value like the VC and it is still time-varying variable.

Choose outputs of system (7.2.3) as:

$$\begin{cases} y_1 = h_1(x) = \psi_{\mathrm{r}} - \psi_{\mathrm{r0}} \\ y_2 = h_2(x) = w_{\mathrm{m}} - w_{\mathrm{m0}} \end{cases} \tag{7.3.1}$$

Differentiate the output of the system (7.2.3) until its inputs appear, then obtain the input-output relationship as [88, 89]:

$$\begin{bmatrix} \ddot{y}_1 \\ \ddot{y}_2 \end{bmatrix} = \begin{bmatrix} L_{f1}(x) \\ L_{f2}(x) \end{bmatrix} + B(x) \begin{bmatrix} u_1 \\ u_2 \end{bmatrix} \tag{7.3.2}$$

where

$$L_{f1}(x) = \left(\frac{R_{\rm r}^2}{L_{\rm r}^2} + \frac{L_{\rm m}^2 R_{\rm r}^2}{\sigma L_{\rm s} L_{\rm r}^3}\right)\psi_{\rm r} - \left(\frac{L_{\rm m} R_{\rm r}^2}{\sigma L_{\rm r}^2} + \frac{L_{\rm m} R_{\rm s} R_{\rm r}}{\sigma L_{\rm s} L_{\rm r}}\right) i_{\rm sd} + \frac{L_{\rm m} R_{\rm r}}{L_{\rm r}} \omega_{\rm e} i_{\rm sq} \tag{7.3.3}$$

$$L_{f2}(x) = \frac{3PL_{\rm m}}{2JL_{\rm r}}\left[-\left(\frac{R_{\rm s}}{\sigma L_{\rm s}} + \frac{R_{\rm r}}{\sigma L_{\rm r}}\right)\psi_{\rm r} i_{\rm sq} - \omega_{\rm e}\psi_{\rm r} i_{\rm sd} + \frac{L_{\rm m} R_{\rm r}}{L_{\rm r}} i_{\rm sd} i_{\rm sq} - \frac{\omega_{\rm r} L_{\rm m}}{\sigma L_{\rm s} L_{\rm r}}|\psi_{\rm r}|^2\right] - \frac{1}{J}\dot{T}_{\rm L} \tag{7.3.4}$$

$$B(x) = \begin{bmatrix} B_1(x) \\ B_2(x) \end{bmatrix} = \begin{bmatrix} \frac{L_{\rm m}}{\sigma L_{\rm s}\tau_{\rm r}} & 0 \\ 0 & \frac{3PL_{\rm m}\psi_{\rm r}(x)}{2J\sigma L_{\rm s} L_{\rm r}} \end{bmatrix}$$

where $\tau_{\rm r} = L_{\rm r}/R_{\rm r}$ is the time constant of rotor windings.

As $det[B(x)] \neq 0$ when $\psi_r \neq 0$, the $B(x)$ is non-singular for all nominal operating points. Then the system input can be designed as

$$\begin{bmatrix} u_1 \\ u_2 \end{bmatrix} = B^{-1}(x)\left(\begin{bmatrix} -L_{f1}(x) \\ -L_{f2}(x) \end{bmatrix} + \begin{bmatrix} v_1 \\ v_2 \end{bmatrix}\right) \tag{7.3.5}$$

where v_1 and v_2 are the linear control inputs.

7.3.2 Definition of Perturbation and Fictitious State

As $B(x)$ in (7.3.2) is a gain that related to the motor parameters, define two perturbation terms considering its parameter variations. Define $B_0 = B(x)|_{x=x(0)}$ as the nominal control gain at rated value. The defined perturbation terms to rewrite (7.3.2) as:

$$\begin{bmatrix} \ddot{y}_1 \\ \ddot{y}_2 \end{bmatrix} = \begin{bmatrix} \Psi_1(x) \\ \Psi_2(x) \end{bmatrix} + B_0 \begin{bmatrix} u_1 \\ u_2 \end{bmatrix} = \begin{bmatrix} v_1 \\ v_2 \end{bmatrix} \tag{7.3.6}$$

where

$$\begin{bmatrix} \Psi_1(x) \\ \Psi_2(x) \end{bmatrix} = \begin{bmatrix} L_{f1}(x) \\ L_{f2}(x) \end{bmatrix} + (B(x) - B_0)\begin{bmatrix} u_1 \\ u_2 \end{bmatrix}$$

$$B_0 = \begin{bmatrix} \frac{L_{\rm m}}{\sigma L_{\rm s}\tau_{\rm r}} & 0 \\ 0 & \frac{3PL_{\rm m}\psi_{\rm r0}}{2J\sigma L_{\rm s} L_{\rm r}} \end{bmatrix}$$

where ψ_{r0} is chosen as the nominal value of the rotor flux under the rated operation condition. As ψ_{r0} is usually a non-zero constant to make sure the B_0 is nonsingular, when the rotor flux $\psi_r(t)$ is regulated from a small value close to zero to its rated value, the control law (7.3.6) still works.

Defines state variables for system (7.3.6) as $z_{i1} = y_i$, $z_{i2} = \dot{y}_i$, and a fictitious state to represent the perturbation $z_{i3} = \Psi_i$, i=1, 2 for subsystem 1 and 2, system (7.3.6) can be represented as:

$$\begin{cases} z_{i1} = y_i \\ \dot{z}_{i1} = z_{i2} \qquad\qquad (i = 1, 2) \\ \dot{z}_{i2} = z_{i3} + B_{i0} u_i \end{cases} \tag{7.3.7}$$

Several types of state and perturbation observers (SPOs) have been proposed for subsystems (7.3.7), such as high-gain observers [88], sliding mode observer [126] and nonlinear observer [170]. As those observers can provide similar performance, high-gain observers are designed in this chapter [126].

7.3.3 Design of States and Perturbation Observer

When the output of the subsystems $z_{i1} = y_i$ are available, two third-order SPOs can be designed for system (7.3.7) as:

$$\begin{cases} \dot{\hat{z}}_{i1} = \hat{z}_{i2} + l_{i1}(z_{i1} - \hat{z}_{i1}) \\ \dot{\hat{z}}_{i2} = \hat{z}_{i3} + l_{i2}(z_{i1} - \hat{z}_{i1}) + B_{i0} u_i \\ \dot{\hat{z}}_{i3} = l_{i3}(z_{i1} - \hat{z}_{i1}) \end{cases} \tag{7.3.8}$$

where $\hat{z}_{ij}$ are the estimations of z_{ij} and l_{i1}, l_{i2}, l_{i3} are the observer gains, which can be parameterized as [195]

$$\begin{bmatrix} l_{i1} \; l_{i2} \; l_{i3} \end{bmatrix} = \begin{bmatrix} 3\alpha_0 \; 3\alpha_0^2 \; \alpha_0^3 \end{bmatrix} \tag{7.3.9}$$

where α_0 is the observer bandwidth and a tuning parameter which is usually designed to make observer dynamic faster than the controlled system [195]. However, a high observer bandwidth will amplify the sensor noise. On the other hand,

observer with bandwidth lower than the sensor noise will act as a filter to sensor noise [196]. Thus, it is usually to set the observer bandwidth greater than the controller bandwidth and lower than the sensor noise bandwidth.

7.3.4 Conventional Rotor-flux MRAS Speed Observer

Rotor flux based MRAS speed observer adjusts the estimated speed in an adaptive model to track the rotor flux of the reference model [182,184]. The stator circuit equation based on stator voltages and currents is given as:

$$\frac{d\psi_{\mathrm{r}\alpha}}{dt} = \frac{L_{\mathrm{r}}}{L_{\mathrm{m}}} v_{\mathrm{s}\alpha} - \frac{L_{\mathrm{r}} R_{\mathrm{s}}}{L_{\mathrm{m}}} i_{\mathrm{s}\alpha} - \frac{\sigma L_{\mathrm{s}} L_{\mathrm{r}}}{L_{\mathrm{m}}} \frac{di_{\mathrm{s}\alpha}}{dt} \tag{7.3.10}$$

$$\frac{d\psi_{\mathrm{r}\beta}}{dt} = \frac{L_{\mathrm{r}}}{L_{\mathrm{m}}} v_{\mathrm{s}\beta} - \frac{L_{\mathrm{r}} R_{\mathrm{s}}}{L_{\mathrm{m}}} i_{\mathrm{s}\beta} - \frac{\sigma L_{\mathrm{s}} L_{\mathrm{r}}}{L_{\mathrm{m}}} \frac{di_{\mathrm{s}\beta}}{dt} \tag{7.3.11}$$

The adaptive model is based on the rotor circuit equation as [182, 184]:

$$\frac{d\hat{\psi}_{\mathrm{r}\alpha}}{dt} = \frac{L_{\mathrm{m}}}{\tau_{\mathrm{r}}} i_{\mathrm{s}\alpha} - \frac{1}{\tau_{\mathrm{r}}} \hat{\psi}_{\mathrm{r}\alpha} - \hat{\omega}_{\mathrm{r}} \hat{\psi}_{\mathrm{r}\beta} \tag{7.3.12}$$

$$\frac{d\hat{\psi}_{\mathrm{r}\beta}}{dt} = \frac{L_{\mathrm{m}}}{\tau_{\mathrm{r}}} i_{\mathrm{s}\beta} + \hat{\omega}_{\mathrm{r}} \hat{\psi}_{\mathrm{r}\alpha} - \frac{1}{\tau_{\mathrm{r}}} \hat{\psi}_{\mathrm{r}\beta} \tag{7.3.13}$$

Error signal ϵ, the difference between the imaginary components of the reference and the estimated rotor fluxes, is defined as:

$$\epsilon = \psi_{\mathrm{r}\beta} \hat{\psi}_{\mathrm{r}\alpha} - \psi_{\mathrm{r}\alpha} \hat{\psi}_{\mathrm{r}\beta} \tag{7.3.14}$$

Then the adaption mechanism is using a PI regulator to estimate the rotor speed as [184]:

$$\hat{\omega}_{\mathrm{m}} = \left(k_{\mathrm{p}} + \frac{k_{\mathrm{i}}}{s} \right) \epsilon \tag{7.3.15}$$

Using the rotor speed and the rotor flux estimated from the MRAS in (7.3.10), (7.3.11) and (7.3.15), as the system outputs, two third-order SPOs in (7.3.8) are designed to estimate the two perturbations.

7.3.5 Combined MRAS Speed and Perturbation Observer

This section proposes a new combined speed and perturbation observer which uses a third-order SPO as an adaption mechanism to replace the PI regulator (7.3.15)

in the conventional MRAS speed observer. In fact, two SPOs can be designed for state and perturbation estimation, one for the speed loop and one for the flux loop; and one conventional MRAS for the speed estimation, in which the estimated speed from the MARS is used as the measurement speed for the speed SPO. To reduce the complexity of the speed loop, the speed SPOs and the MRAS have been combined by replacing the PI regulator in the MARS with the speed SPO to design a combined speed and perturbation observer. The separate and the combined design procedure are shown in Figure 7.2. The stability of the combined design is given Section 7.5.

The MRAS uses the same equations in (7.3.10)-(7.3.13), and the adaption mechanism is driving by the error signal ϵ. Define $y_2 = z_{21} = w_{\mathrm{m}}$, use ϵ as input of the rotor speed SPO, we have

$$\begin{cases} \hat{\omega}_{\mathrm{m}} = \hat{z}_{21} + l_{20}\epsilon \\ \dot{\hat{z}}_{21} = \hat{z}_{22} + l_{21}\epsilon \\ \dot{\hat{z}}_{22} = \hat{z}_{23} + B_{20}u_2 + l_{22}\epsilon \\ \dot{\hat{z}}_{23} = l_{23}\epsilon \end{cases} \tag{7.3.16}$$

The observer gains l_{21}, l_{22}, l_{23} are obtained via the same method in (7.3.9). Besides, the proportional gain l_{20} is determined via pole placement to improve the stability of the observer. The stability of the combined speed and perturbation observer can be proved using the same method as in [182], which gives the stability proof of the conventional MRAS speed observer with PI regulator. The combined speed and perturbation observer consists of equation (7.3.10)-(7.3.14) and (7.3.16), which can estimate, the rotor speed, the speed loop perturbation term and the rotor flux. After the estimation error of the rotor flux converges to zero, the estimated state $\hat{z}_{21}$ tracks the real rotor speed and can be used for the speed control. At the same time, the $\hat{z}_{23}$ tracks the rotor speed perturbation, which is used to linearize the nonlinear system in the SSNAC controller.

7.3.6 Speed Sensorless Nonlinear Adaptive Controller

A third-order SPO like (7.3.8) is designed to estimate z_{12} and perturbation z_{13} of the flux subsystem, and a combined SPO from (7.3.14) and (7.3.16) is designed

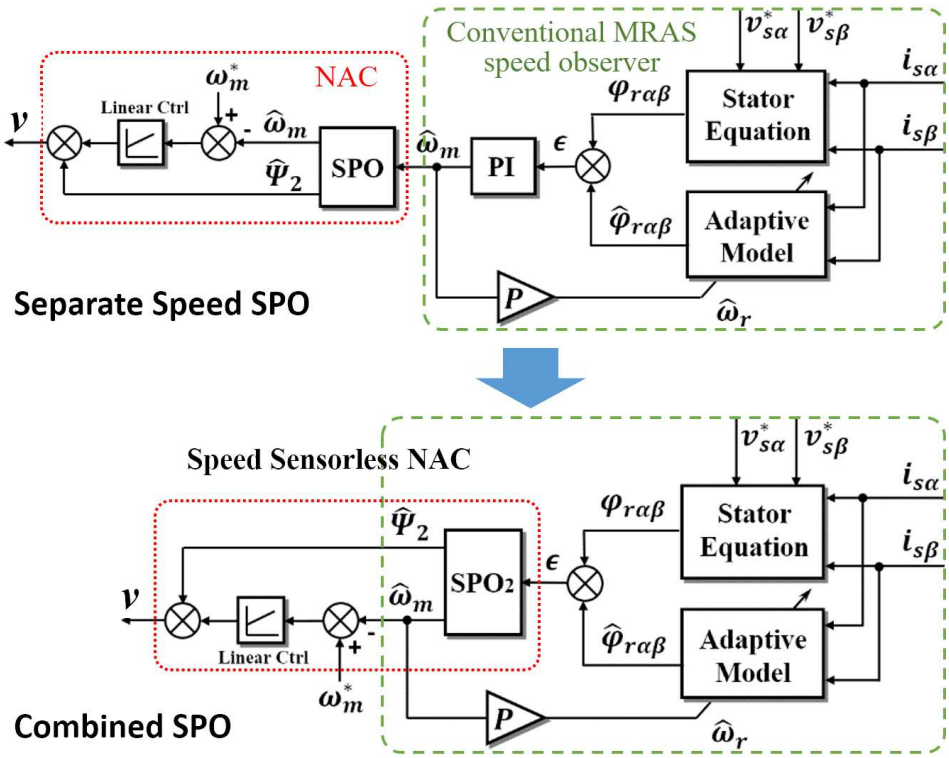

Figure 7.2: The design steps of using a combined SPO to replace the PI regulator in a MRAS speed observer.

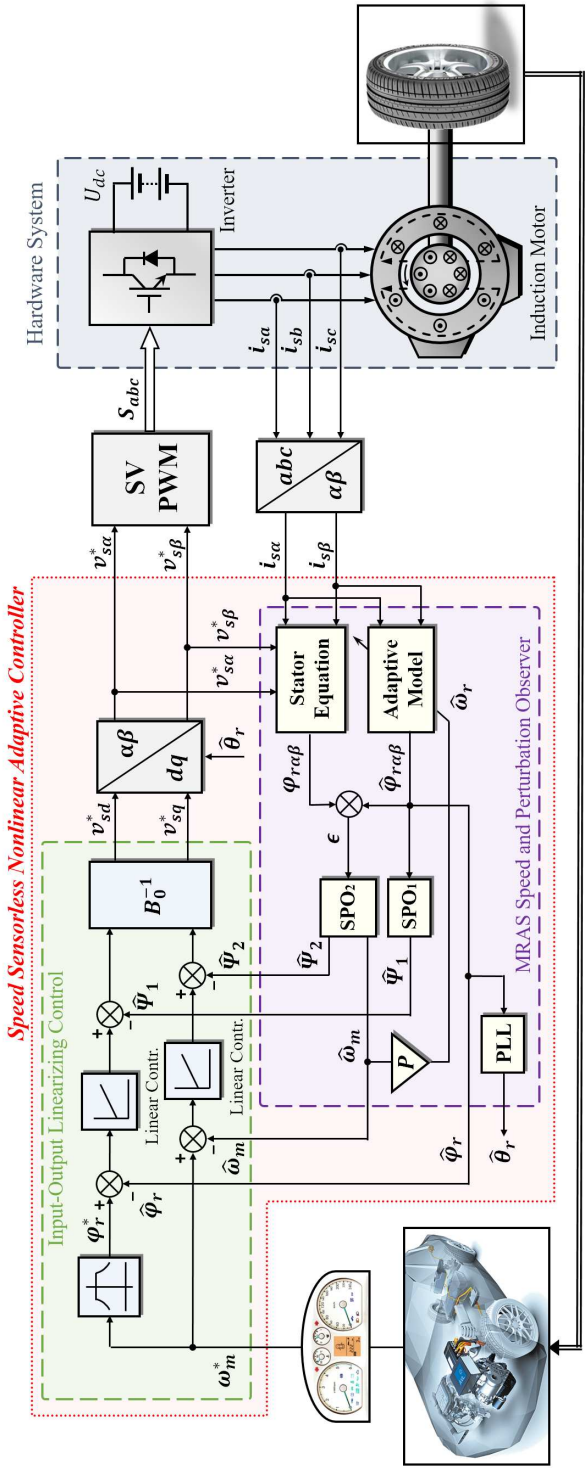

Figure 7.3: The controller scheme of the proposed speed sensorless nonlinear adaptive control for IM drive in EV application.

to estimate z_{22} and z_{23} of the speed subsystem. By compensating the real perturbation terms with their estimates, and using the estimated speed, the speed sensorless nonlinear adaptive control law can be obtained as:

$$\begin{bmatrix} u_1 \\ u_2 \end{bmatrix} = B_0^{-1} \left(\begin{bmatrix} v_1 \\ v_2 \end{bmatrix} - \begin{bmatrix} \hat{z}_{13} \\ \hat{z}_{23} \end{bmatrix} \right) \tag{7.3.17}$$

where

$$B_0^{-1} = \begin{bmatrix} \frac{\sigma L_{\mathrm{s}} \tau_{\mathrm{r}}}{L_{\mathrm{m}}} & 0 \\ 0 & \frac{2J\sigma L_{\mathrm{s}} L_{\mathrm{r}}}{3PL_{\mathrm{m}}\psi_{\mathrm{r0}}} \end{bmatrix}$$

and v_i are control of the linear systems

$$v_i = \ddot{z}_{i1r} + k_{i1}(z_{i1r} - z_{i1}) + k_{i2}(\dot{z}_{i1r} - \hat{z}_{i2}) \tag{7.3.18}$$

Control law of the linearised system can be obtained by the rich linear system methods, such as optimal control and pole placement technique. In this chapter, the pole placement technique is used to determine gains of linear controller. For a given pole location n, $k_{i1} = n^2$, $k_{i2} = 2 \cdot n$, $i = 1, 2$. Same gains are used for the flux loop and the speed loop controller. For a given transient dynamic requirement, i.e. settling time and rise time, the pole location of the second-order linear system can be directly obtained. Figure 7.3.5 shows the power stage and control scheme of the SSNAC for IM in EV applications.

7.4 Stability of the Closed-loop System

The closed-loop system includes a flux SPO, a flux controller, a combined speed and perturbation observer, and a speed controller. Define estimation error of the flux SPO as $\varepsilon_{i1} = z_{i1} - \hat{z}_{i1}$, $\varepsilon_{i2} = z_{i2} - \hat{z}_{i2}$, and $\varepsilon_{i3} = \Psi_i(\cdot) - \hat{z}_{i3}$, and subtract (7.3.8) from (7.3.7), the estimation error system of the flux SPO_1 are:

$$\begin{bmatrix} \dot{\varepsilon}_{11} \\ \dot{\varepsilon}_{12} \\ \dot{\varepsilon}_{13} \end{bmatrix} = \begin{bmatrix} -l_{11}\ 1\ 0 \\ -l_{12}\ 0\ 1 \\ -l_{13}\ 0\ 0 \end{bmatrix} \begin{bmatrix} \varepsilon_{11} \\ \varepsilon_{12} \\ \varepsilon_{13} \end{bmatrix} + \begin{bmatrix} 0 \\ 0 \\ \dot{\Psi}_1(\cdot) \end{bmatrix} \tag{7.4.1}$$

As the speed SPO_2 is designed together with the MRAS speed observer, the error equations are obtained with the flux error defined in (7.3.14). The differential equation of (7.3.14) is calculated from the rotor circuit equations (7.3.10) - (7.3.13) as

$$\dot{\epsilon} = a_1\epsilon + a_2(\omega_{\rm m} - \hat{\omega}_{\rm m}) + a_3 \tag{7.4.2}$$

where

$$\begin{aligned} a_1 &= -\frac{2}{\tau_{\rm r}} \\ a_2 &= P(\psi_{r\alpha}\hat{\psi}_{\rm r\alpha} + \psi_{\rm r\beta}\hat{\psi}_{\rm r\beta}) \\ a_3 &= \frac{L_{\rm m}}{\tau_{\rm r}}(\psi_{\rm r\beta} - \hat{\psi}_{\rm r\beta})i_{\rm s\alpha} - \frac{L_{\rm m}}{\tau_{\rm r}}(\psi_{\rm r\alpha} - \hat{\psi}_{\rm r\alpha})i_{\rm s\beta} \end{aligned}$$

Then use the same method in (7.4.1) to obtain the estimation error system of SPO_2 as

$$\begin{bmatrix} \dot{\epsilon} \\ \dot{\varepsilon}_{21} \\ \dot{\varepsilon}_{22} \\ \dot{\varepsilon}_{23} \end{bmatrix} = \begin{bmatrix} a_1 - l_{20}a_2 & a_2 & 0 & 0 \\ -l_{21} & 0 & 1 & 0 \\ -l_{22} & 0 & 0 & 1 \\ -l_{23} & 0 & 0 & 0 \end{bmatrix} \begin{bmatrix} \epsilon \\ \varepsilon_{21} \\ \varepsilon_{22} \\ \varepsilon_{23} \end{bmatrix} + \begin{bmatrix} a_3 \\ 0 \\ 0 \\ \dot{\Psi}_2(\cdot) \end{bmatrix} \tag{7.4.3}$$

Secondly, define the system tracking error as $e_{i1} = y_i^* - z_{i1}$ and $e_{i2} = \dot{y}_i^* - z_{i2}$. Then the linear control algorithm in (7.3.18) can be presented as:

$$\begin{aligned} v_i &= k_{i1}(y_i^* - z_{i1} + z_{i1} - \hat{z}_{i1}) + k_{i2}(\dot{y}_i^* - z_{i2} + z_{i2} - \hat{z}_{i2}) \\ &= k_{i1}(e_{i1} + \varepsilon_{i1}) + k_{i2}(e_{i2} + \varepsilon_{i2}) \end{aligned} \tag{7.4.4}$$

From (7.3.6) and (7.4.4), the tracking error system is obtained as

$$\begin{bmatrix} \dot{e}_{i1} \\ \dot{e}_{i2} \end{bmatrix} = \begin{bmatrix} 0 & 1 \\ -k_{i1} & -k_{i2} \end{bmatrix} \begin{bmatrix} e_{i1} \\ e_{i2} \end{bmatrix} + \begin{bmatrix} 0 \\ -\xi_i \end{bmatrix} \tag{7.4.5}$$

where $\xi_i = k_{i1}\varepsilon_{i1} + k_{i2}\varepsilon_{i2} + \varepsilon_{i3}$ $(i = 1, 2)$, which is the estimation error in the closed-loop system.

Based on [126], it can prove that the estimation error system (7.4.1) and (7.4.3), and the tracking error system (7.4.5) are GUUB. The internal dynamic of the IM system can also be analysed using a zero dynamic technique.

Table 7.1: System parameters of IM

R_{s}	R_{r}	L_{s}	L_{r}
0.1607 Ω	0.1690 Ω	6.017 mH	5.403 mH
L_{m}	J	P	
5.325 mH	0.000145 kg·m^2	2	

Table 7.2: Controller parameters of SSNAC

Flux SPO	$l_{11} = 9 \times 10^3$	$l_{12} = 2.7 \times 10^7$
	$l_{13} = 2.7 \times 10^9$	
Speed SPO	$l_{20} = 2 \times 10^3$	$l_{21} = 6 \times 10^3$
	$l_{22} = 1.2 \times 10^7$	$l_{23} = 8 \times 10^9$
Flux Controller	$k_{11} = 1.5 \times 10^4$	$k_{12} = 2.5 \times 10^2$
Speed Controller	$k_{21} = 1 \times 10^4$	$k_{22} = 2 \times 10^2$

7.5 Simulation Results

The simulation validations are carried out at different speed profiles of vehicles, such as the forward and reverse motoring on a slope, and constant speed cruise on an unsmooth surface condition. IM parameters used for the simulation and experimental purpose are given in Table 7.1. The parameters of the SSNAC and SPOs are listed in Table 7.2.

7.5.1 Comparison of the separated speed SPO and combined SPO based Speed Sensorless Control

Comparison of simulation results of the separated speed SPO and the combined SPO is shown in Figure 7.4, which demonstrates that the estimation performance are similar. The speed estimation performance and the speed tracking performance of both the separated SPO and combined SPO are almost the same when the speed is

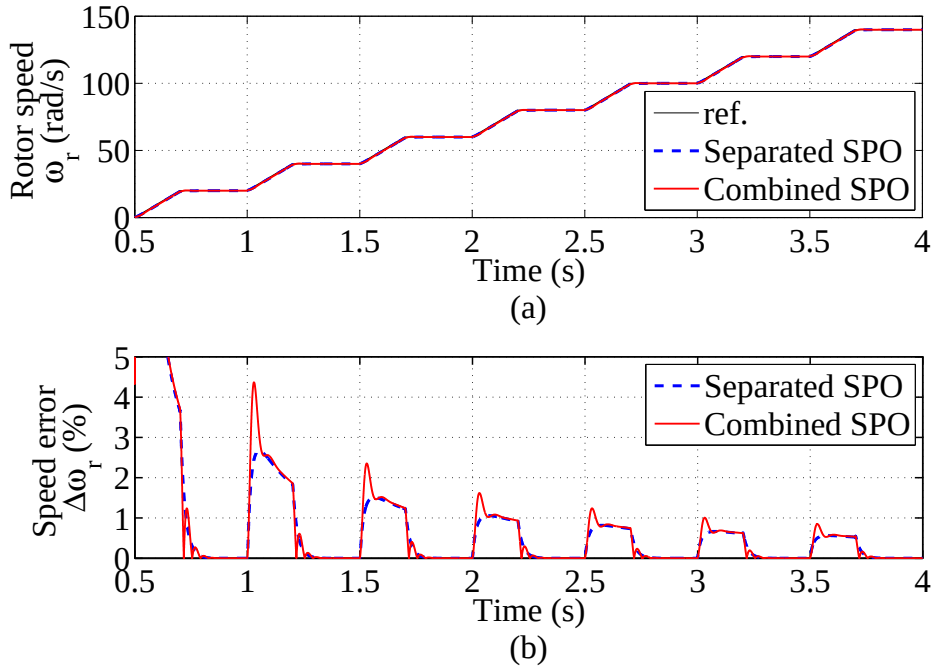

Figure 7.4: Comparison of the control performance with using the separate speed SPO and combined SPO.

increasing from 0 to 150 rad/s. Therefore, only the result of the combined SPO based SSNAC have been presented in all other case studies of simulation and experiment validation.

7.5.2 Forward and Reverse Motoring on a Sloped Surface

The first case is the forward and reverse motoring operation of an EV driving on a sloped surface. When an EV is driven facing to the slope as shown in Figure 7.5(a), assuming the road surface is smooth, the load is a constant positive torque due to its weight and the angle of the slope. When the EV is facing down on the same slope, the load is a negative torque to the motor.

From t=1.0s to t=2.0s, the induction motor speeds up from 0 rad/s to 80 rad/s and then maintain the speed after t=2.0s. At t=4.0s, the EV is driven above the peak point of the slope, which applies a negative load disturbance on the IM. At t=6.0s, the speed reference is reduced to 0 and then reversed to -80 rad/s and repeat the operation in the opposite direction. Load torque is shown in Figure 7.6(a). The rotor flux tracking performance and error of both controllers are compared in Figure

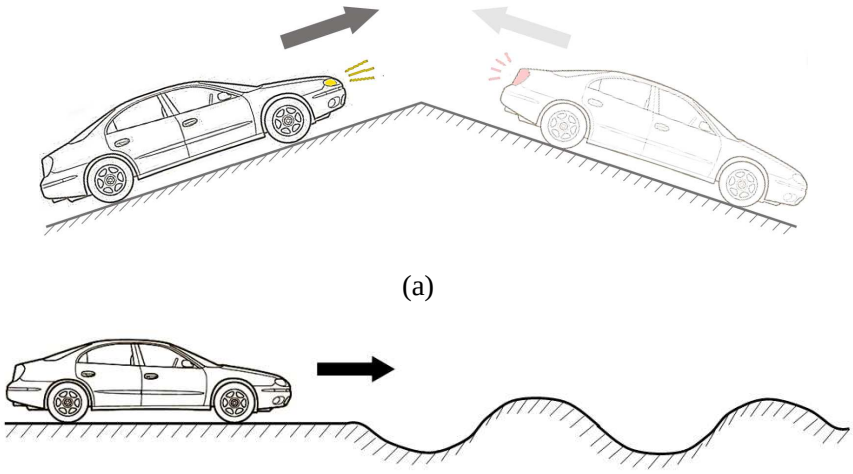

(a)

(b)

Figure 7.5: (a) EV operation case of forward and reverse motoring on a sloped surface; (b) EV operation case of constant speed cruise on an unsmooth surface.

7.6(b) and 7.6(c), together with the actual mechanical speed and the tracking error in Figure 7.6(d) and 7.6(e). It can be found that the SSNAC can provide better flux and speed tracking performance than the VC in both positive and negative speed. Moreover, to further identify the improvement of SSNAC numerically, Table 7.3 summarises the comparison of the two controllers: the maximum and the integral-absolute-error (IAE) of the flux and speed regulation error. From the summarising table, the SSNAC has 98% and 81% less maximum regulation error, and has 99% and 81% less IAE in the flux and speed tracking than the conventional VC with MRAS speed observer.

The two lumped perturbation terms and their estimation errors are shown in Figure 7.7. The results show that the estimated perturbation terms from both SPOs track the real ones under speed and load changes. The maximum estimation errors of perturbation are less than 3% in both perturbation terms.

7.5.3 Constant Speed Cruise on an Unsmooth Surface

In the second case, the vehicle speed keeps constant under a time-varying load disturbance. As shown in Figure 7.5(b), when an EV is cruising on an unsmooth

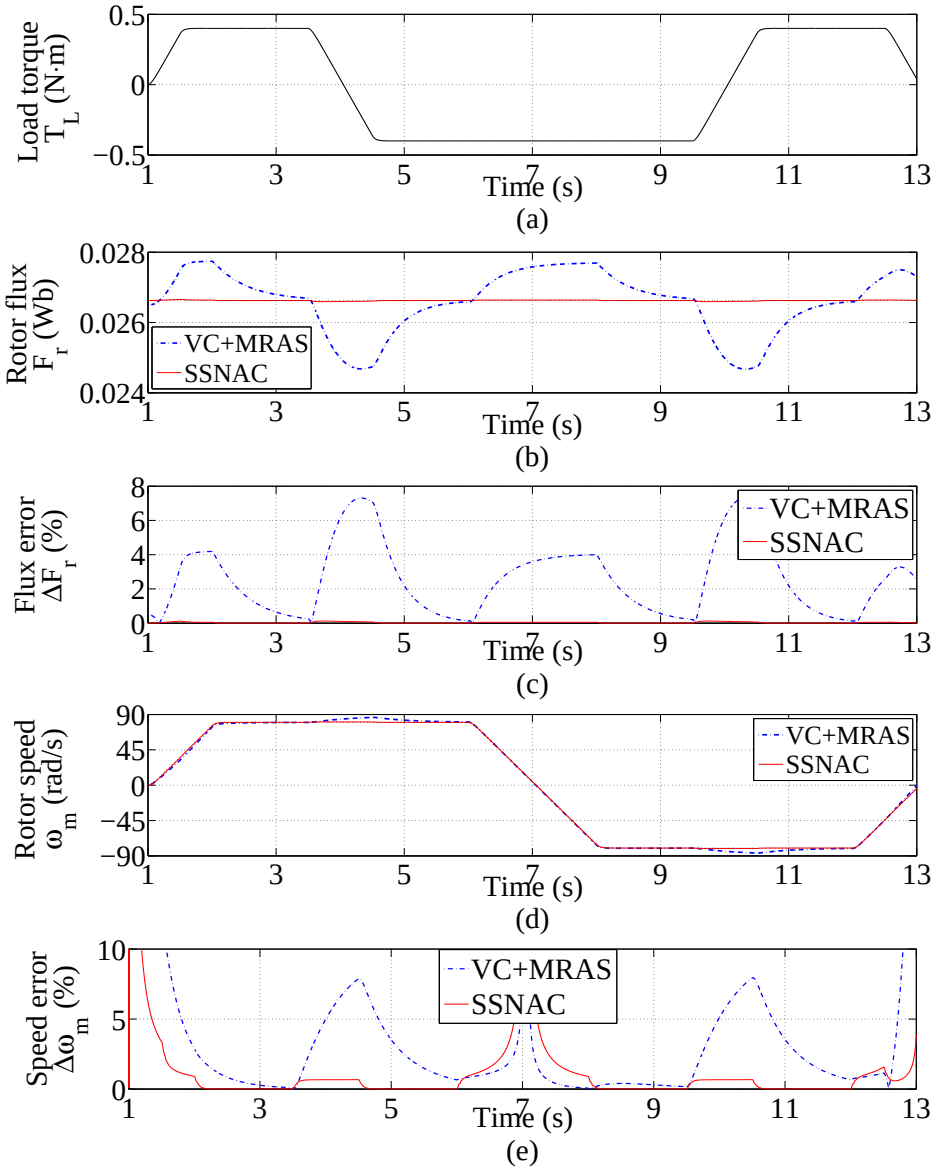

Figure 7.6: Simulation results of IM forward and reverse motoring on a sloped surface. (a) Load disturbance, (b) rotor flux, (c) flux tracking error, (d) speed response, and (e) speed tracking error.

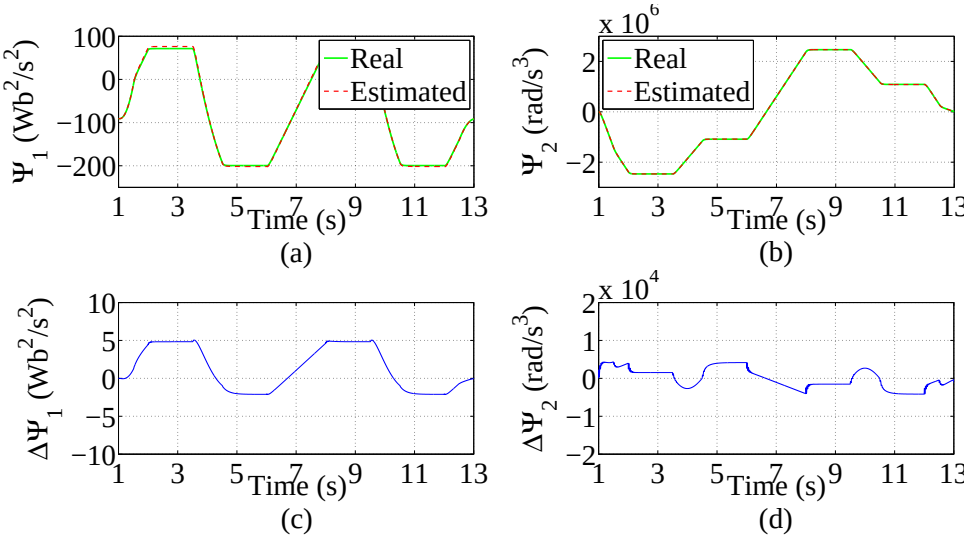

Figure 7.7: Perturbation term estimation Ψ_1 and Ψ_2, their estimation error $\Delta\Psi_1$ and $\Delta\Psi_2$ of IM forward and reverse motoring on a sloped surface.

road surface, the load disturbance is variable while the speed reference is fixed. The unloaded IM reaches the speed of 100 rad/s and rotor flux is kept at a fixed value of 0.0266 Wb. From t=4.0s to t=9.0s, a time-varying load torque, as shown in Figure 7.8(a), is applied on the IM. The flux and speed tracking performance of both controllers is compared in Figure 7.8(b) and 7.8(d), while their tracking errors are given as shown in Figure 7.8(c) and 7.8(e). Due to the perturbation terms are estimated by SPOs and compensated in the controller, the speed performance of SSNAC has obvious predictive compensation and less regulation error than the VC. The summarised performance indices are given in Table 7.3, in which it shows that the SSNAC is 99% and 87% less in maximum regulation error, and 99% and 88% less in IAE in the flux and speed tracking, respectively.

The SPOs estimate the two lumped perturbation terms defined in the previous section and their estimation errors as shown in Figure 7.9. In the simulation, due to that, all the conditions are known, the real perturbation can be calculated and compared with the estimated ones. The results show that the SPOs perform well to estimate the perturbation with the estimation error less than 3%, which is used to compensate the real perturbation and fully linearize the coupled states in the nonlinear system.

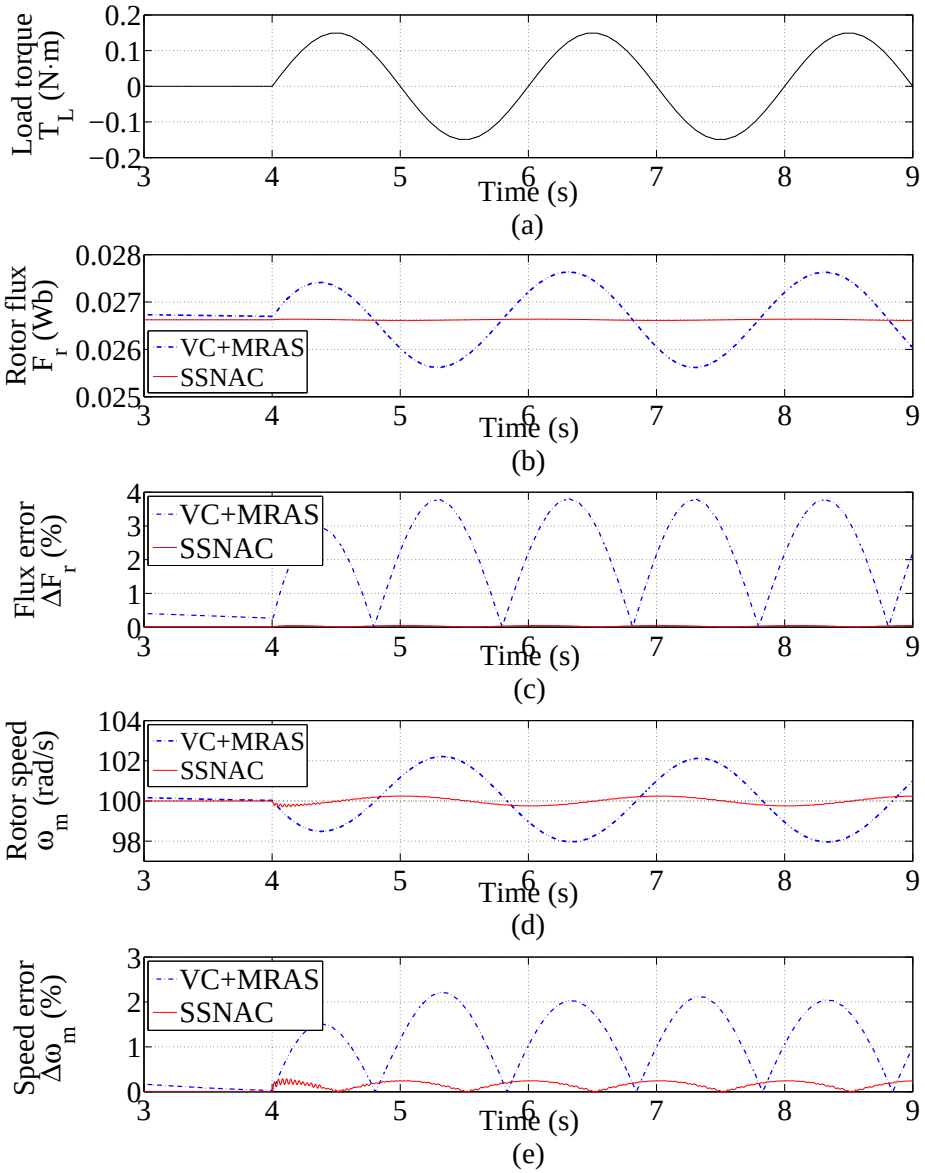

Figure 7.8: Simulation results of IM constant speed cruising on an unsmooth surface. (a) Load disturbance, (b) rotor flux, (c) flux tracking error, (d) speed response, and (e) speed tracking error.

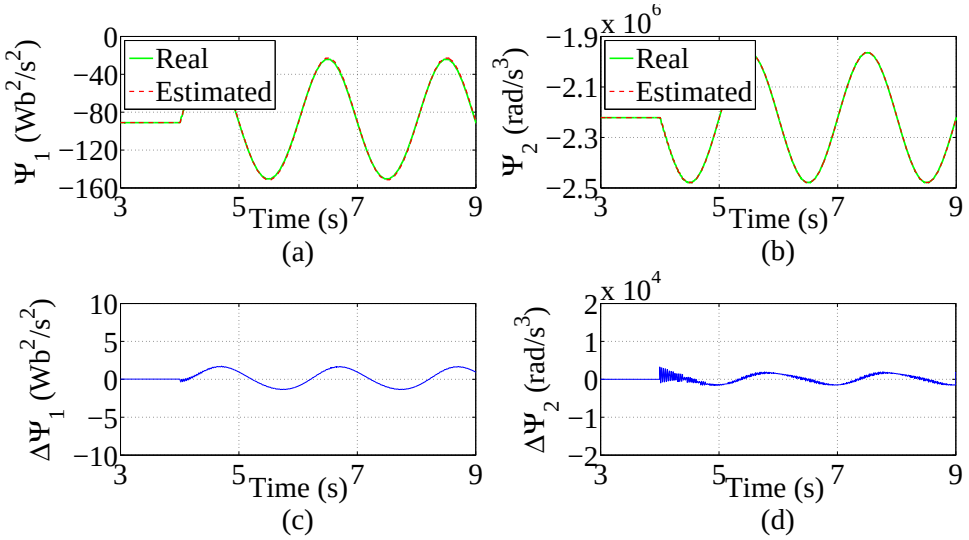

Figure 7.9: Perturbation term estimation Ψ_1 and Ψ_2, their estimation error $\Delta\Psi_1$ and $\Delta\Psi_2$ of IM constant speed cruising on an unsmooth surface.

Table 7.3: Tracking Performance Comparison of VC with MRAS and SSNAC

Indices \ Method	VC with MRAS	SSNAC	Improvements
Case: Forward and Reverse Motoring on a Sloped Surface			
Maximum Flux Error	7%	0.12%	98% less
Flux IAE ($\times 10^{-3}$Wb·s)	8.2	0.1	99% less
Maximum Speed Error	8%	1.7%	79% less
Speed IAE (rad)	20.4	3.8	81% less
Case: Constant Speed Cruise on an Unsmooth Surface			
Maximum Flux Error	3.7%	0.052%	99% less
Flux IAE ($\times 10^{-3}$Wb·s)	3.0	0.0042	99% less
Maximum Speed Error	2.2%	0.29%	87% less
Speed IAE (rad)	6.3	0.77	88% less

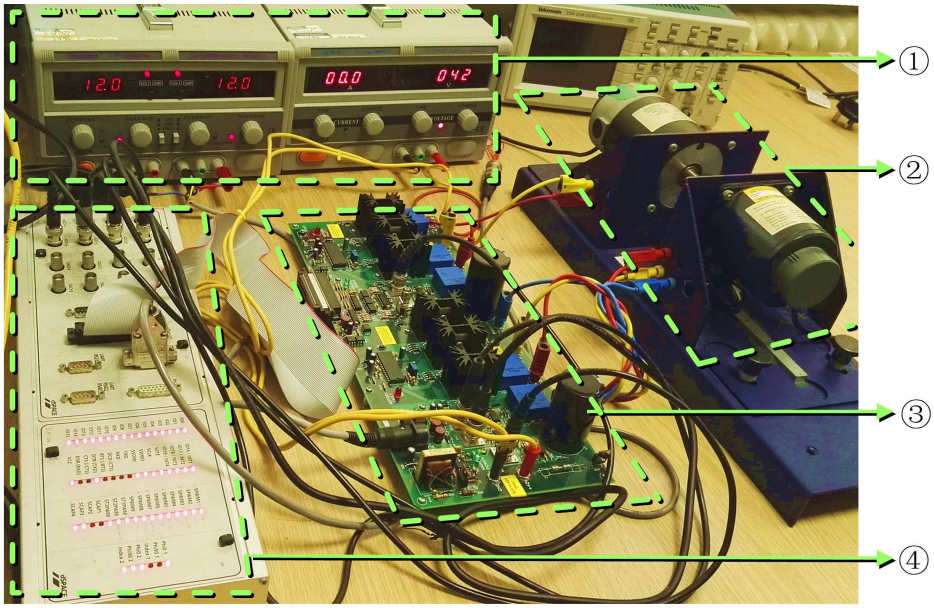

① DC power supply
② Coupled motor bench
③ MOSFET based power electronics board
④ dSPACE CLP1104 control panel

Figure 7.10: Experimental setup of IM speed sensorless control.

7.6 Experiment Results

7.6.1 Experimental Platform

The electric-drive experimental setup shown in Figure 7.10 consists of a 200W, 2 pole pairs, three phase IM from Motorsolver, a 42V power electronic converter unit, and a DS1104 controller with interface board. The motor bench has a mechanical coupling arrangement, an IM for motor driving coupled with a DC motor to produce the expected load torque.

7.6.2 Forward and Reverse Motoring on a Sloped Surface

In the experimental validation, the speed reference and load disturbance profiles are set to be the same with that in the simulation. The speed profile is forward and reverses motoring while the load torque shown in Figure 7.11(a) is produced by a coupled DC motor via control its current. The speed estimation performance and estimation error are shown in Figure 7.11(b) and 7.11(c). The results show that the

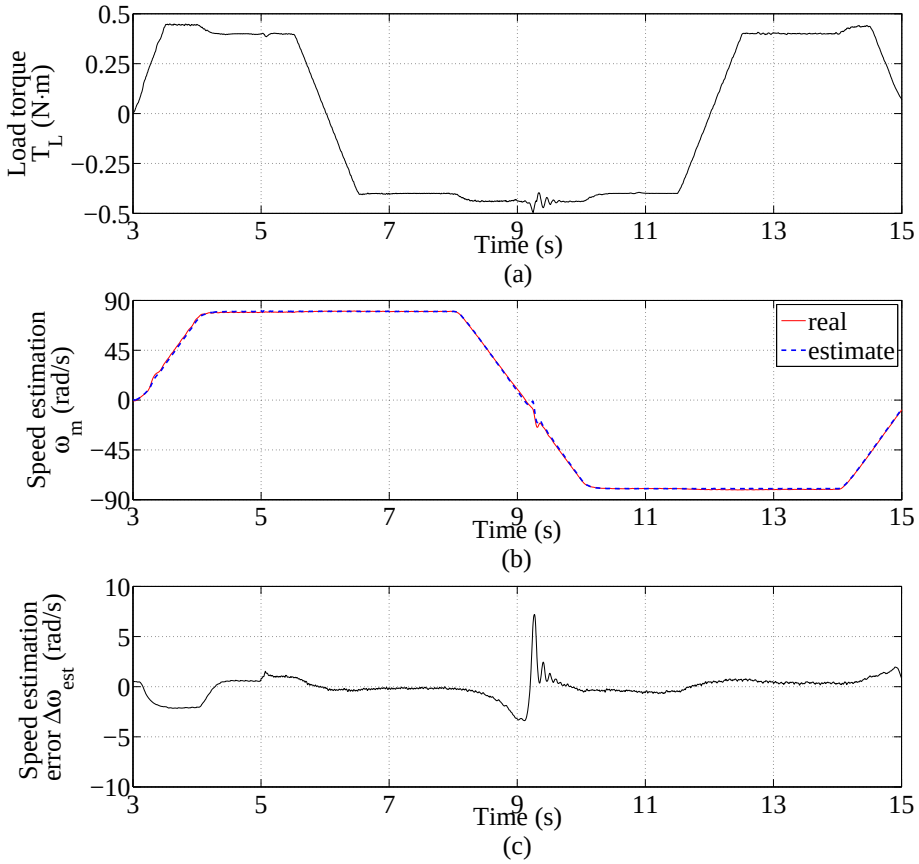

Figure 7.11: Speed estimation results of IM forward and reverse motoring on a sloped surface in experiment. (a) Load disturbance, (b) estimated speed, and (c) speed estimation error.

estimated speed tracks the real speed accurately in high speed. But there could be some obvious estimation error in low speed and zero speed, which is a traditional problem of the MRAS speed observer in IM application and it is still a popular topic in recent research studies.

Figure 7.12 shows the experimental results of the flux and speed tracking performance. The SSNAC has less regulation error and IAE than the VC with speed observer in both flux and speed tracking. The performance indices are compared in Table 7.4, in which the maximum flux and speed regulation error of the SSNAC are 29% and 13% less than that in the conventional VC method. If neglecting the estimation error of speed when it crosses zero, the flux and speed tracking performance of SSNAC is more evident better than the VC. The IAE of flux and speed tracking in the SSNAC are 77% and 75% less than that in VC. It can be observed

that the experimental tests don't demonstrate the same level of improvement of the reduction of tracking error as the simulation tests. One of the main reason is the parameter uncertainties of the IM in experimental tests has degraded the performance of the speed MRAS as it requires the accurate IM parameters which are assumed be available in the simulation test.

7.6.3 Constant Speed Cruise on an Unsmooth Surface

In the experiment case of EV with constant speed cruise on an unsmooth surface, the IM is kept at a speed of 100 rad/s. Figure 7.13(a) shows the time-varying load torque. The flux and speed tracking performance, as well as their regulation error, are shown in Figure 7.13. The performance indices comparison between the SSNAC and the traditional VC with MRAS are given in Table 7.4. The results show that the SSNAC has 79% and 33% less maximum error, and 80% and 28% less IAE in the flux and speed regulation, respectively.

7.7 Conclusion

This chapter has presented a speed sensorless nonlinear adaptive control for the speed regulation of induction motor used in electric vehicle applications. By designing a combined speed and perturbation observer, the proposed SSNAC can adaptively compensate the fast time-varying and unknown nonlinear dynamics, and the external load disturbances, without requiring the accurate model of the IM. Moreover, the SSNAC replaces the PI regulator in the MRAS speed observer with an SPO to estimate the perturbation and speed for reducing the complexity of the controller. The operational performance is verified by the simulation study and experiment implementation with the speed and load profiles from the operation conditions of EV. Simulation and experimental results comparing SSNAC and the conventional VC with an MRAS speed observer show that the SSNAC has better dynamics of speed tracking under the time-varying load disturbances which are typical in EV applications.

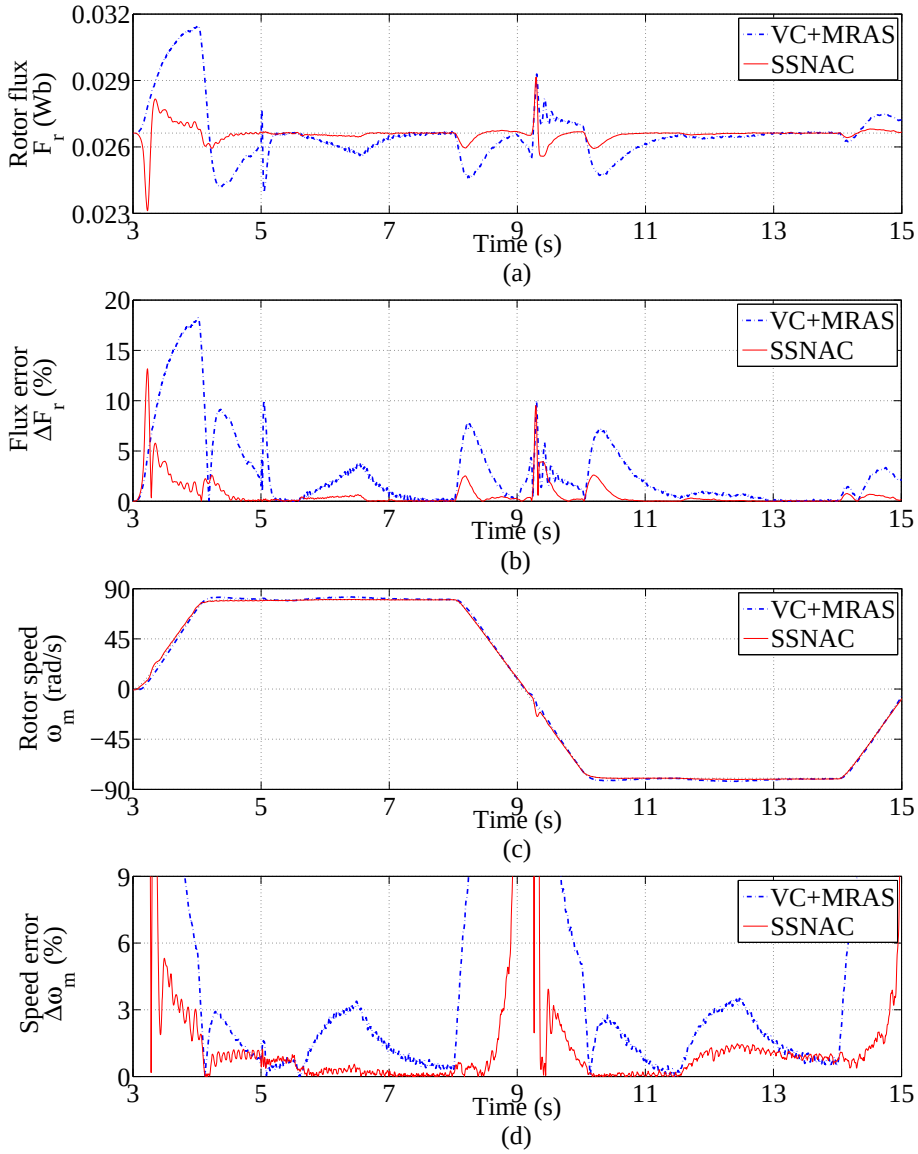

Figure 7.12: Experimental results of forward and reverse motoring of IM on a sloped surface. (a) Rotor flux, (b) flux tracking error, (c) rotor speed, and (d) speed tracking error.

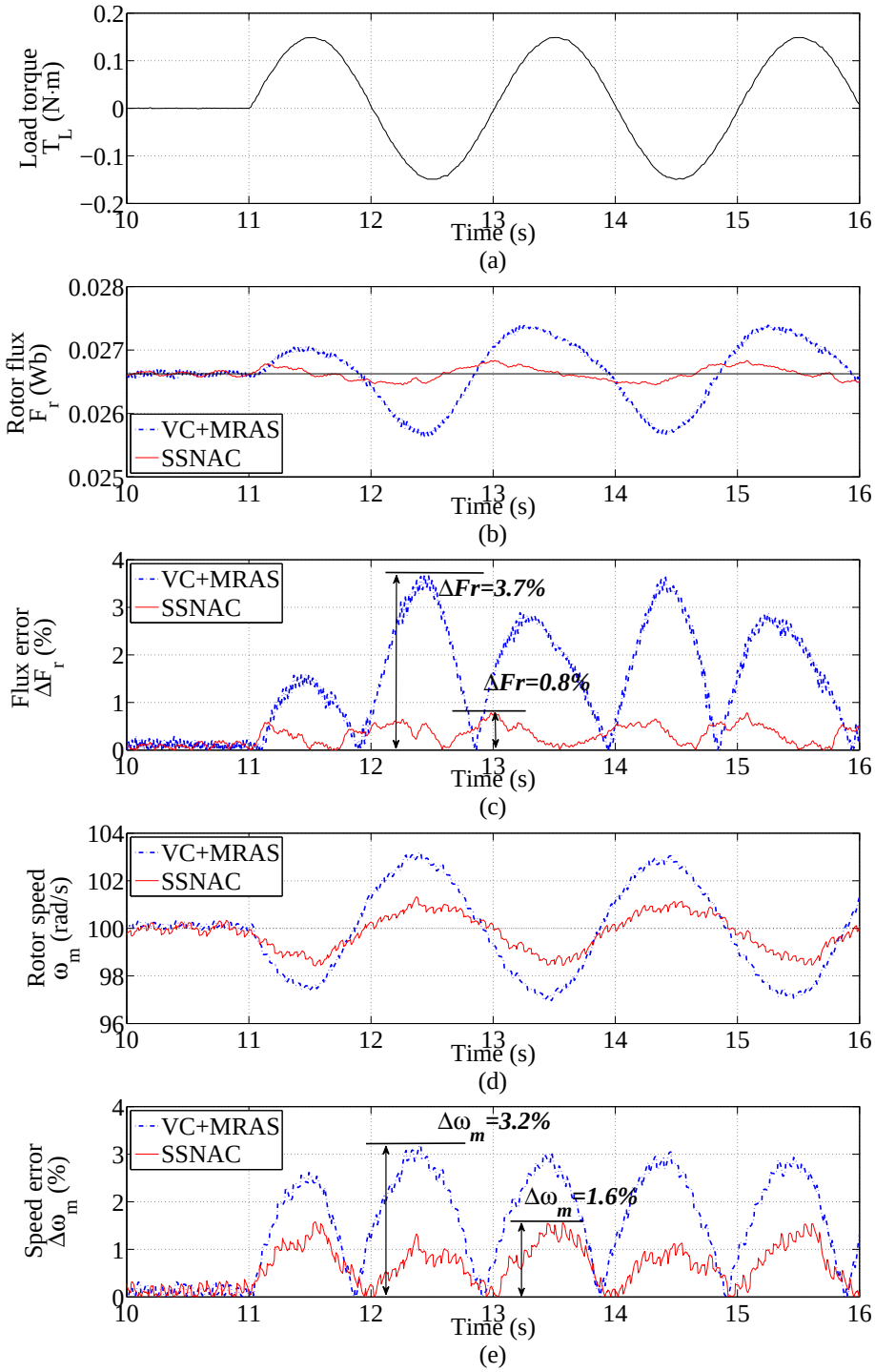

Figure 7.13: Experimental results of constant speed driving on an unsmooth surface. (a) Load disturbance, (b) rotor flux, (c) flux tracking error, (d) rotor speed, and (e) speed tracking error.

Table 7.4: Experimental performance indices of VC with MRAS and SSNAC

Indices \ Method	VC with MRAS	SSNAC	Improvements
Case: Forward and Reverse Motoring on a Sloped Surface			
Maximum Flux Error	18.3%	13%	21% less
Flux IAE ($\times 10^{-3}$Wb·s)	9.3	2.1	77% less
Maximum Speed Error	4.2%	2.8%	33% less
Speed IAE (rad)	31.0	7.7	75% less
Case: Constant Speed Cruise on an Unsmooth Surface			
Maximum Flux Error	3.7%	0.78%	79% less
Flux IAE ($\times 10^{-3}$Wb·s)	2.3	0.46	80% less
Maximum Speed Error	3.2%	1.6%	52% less
Speed IAE (rad)	8.9	6.4	28% less

Chapter 8

Conclusions and Future Work

This chapter has summarized the obtained results of this thesis and contributions. The suggestions for future investigations are also listed.

8.1 Conclusions

In this thesis, the application of perturbation estimation based nonlinear adaptive control on electric energy conversion systems for future power system has been studied and implemented. As the future power system are desired as a more power electronics enabled, more robust control system are required to improve the control performance and stability on the generation side, storage side, and consumption side of future power system.

In the power generation side, the WT is difficult to be controlled obtaining the optimal control performance on its nonlinear aerodynamic blades, which operate under random and time-varying wind speed in a wide range, using a linear controller. An N-PI controller has been investigated for the pitch angle control of a wind turbine system to capture the rated wind power to generate power to the power system. In the energy storage side, due to the low stiffness and inertia of an islanded MG, the unknown disturbance and unbalanced power demand can lead to stability problem of the MG, which requires an ESS with a robust control system to balance the power generation and demand. An NAC controller with an SPO to

estimate the unbalanced disturbance has been designed to regulate the bus voltage and frequency to improve the robustness of the islanded MG under disturbance and unbalanced load. In the consumption side, one of the most widely used industrial workhorses is the IM, which has highly coupled states and nonlinear dynamics. To cope with the problem that the conventional control method is sensitive to parameter changes and dependent on the accuracy of flux position, an NAC based speed controller has been investigated to control the IM directly under the stationary frame, which aims to reduce the dependency of flux position and improve the robustness of load disturbance and parameter uncertainty. To further reduce the dependency of speed encoder, a speed sensorless NAC controller has been designed for the IM using a combined SPO to reduce the complexity of conventional control method with an additional speed observer.

The ECS in power generation, storage and consumption side of the future power system have been studied to be controlled by the perturbation estimation based controllers. Both the N-PI and NAC use the HG-SPO for estimating the perturbation term, which includes the nonlinear interactions between states, external disturbance, parameter changes and unmodeled dynamics. The results perform that the perturbation estimation based method has improved the robustness of the ECS systems under disturbance and parameter uncertainty. However, due to the high gain of SPO used in NAC, the control methods are sensitive to noise and can amplify the sensor noise when the observer bandwidth is high. Thus, the observer and controller bandwidth can never be concluded as the higher the better, even using the high-gain SPO. It is usually to set the observer bandwidth greater than the controller bandwidth and lower than the sensor noise bandwidth. In the thesis, the optimal observer and controller bandwidth of ECSs have been tuned using the pole placement method, and their stability has been proved in Lyapunov theory.

8.2 Future Work

The possible future work are listed based on the following ideas.

- In Chapter 3, the pitch angle controller is designed for a simplified single-

input single-output wind turbine. However, as the real aero-elastic wind turbine is a multi-input multi-output (MIMO) system, both the pitch angle control and generator torque control can be used simultaneously. The wind turbine controller can be designed as a MIMO controller to coordinately control both the pitch angle and generator torque for multi control objectives: reduce the regulation error of generated power and simultaneously reduce the load stress of the drive train. In addition, as the large wind turbine always using a three-blade architecture, the blades can be individually controlled for eliminate the effect of wind turbulence from different direction and tower shadow to further reduce the load stress of drive train shaft. Thus, a MIMO NAC based individual pitch angle and generator torque controller for wind turbine will be designed and validated using FAST simulator in the future.

- In Chapter 4, the voltage controller of the voltage source converter is designed to maintain the bus voltage of a low voltage (LV) islanded microgrid under unbalanced disturbances. Thus, in the future work, the control method can be validated on a high voltage microgrid, such as a HVDC power transmission system of an offshore wind farm under single-phase fault condition. And the modular multilevel converters (MMC) are the most promising devices for the future HVDC system for offshore wind farm. It leads the requirement of designing the controller for the MMC based HVDC system for offshore wind farms.

- In Chapter 6, the speed and flux tracking is validated in both simulation and experimental studies under unknown disturbance. The main advantage of the NAC controller is it can fully decouple the interaction and dynamic between the torque and flux. In previous result, the flux is controlled to a constant at its rated value. However, in the efficiency optimization and field-weakening region control, the flux is to be changed for different control objectives. And under the time-varying load disturbance, both the torque and flux command changes quickly. The conventional method, such as vector control, cannot fully decouple the torque and flux and control them independently with perfect

performance. Thus, the NAC controller will be further validated.

In addition, as the system parameter is variable during the operation, the conventional loss-model based efficiency optimization method cannot always get the best efficiency point. The fuzzy logic method can be used to on-line optimize the flux command to search for the maximum efficiency. But the searching period is very long when using the fuzzy logic method with poor initial condition. Thus, a novel method can be presented of combining the loss-model to calculate the initial flux condition, and then use the fuzzy logic to search for the optimized efficiency. With using the loss-model method to initialize the starting condition in fuzzy logic method, the searching period will be greatly reduced. This makes the faster searching speed to find the optimized efficiency point in IM speed drive.

In the future work, the NAC controller combined with fuzzy logic searching method will be further validated in the efficiency optimization and field-weakening region to test the efficiency improvement of the IM.

- In Chapter 7, the speed sensorless control method are designed using a combined SPO in a MRAS speed observer for the IM flux and speed tracking in electrical vehicle (EV) application. In the future work, other types of speed observer can be used, such as the sliding mode observer, extended Kalman filter, and neural-network based speed observer, and combined these speed observers with the NAC based speed observer for EV tracking drive application.

- Moreover, this thesis has studied the control of wind power generation, energy storage system, and induction motor individually. In the future work, the relationship between the three energy conversion systems and their effect to the power system will be studied, such as the impact of uncertain wind power generation to the power system, the optimal sizing of energy storage system in power system for economical purpose, and the demand side control of grid-connected electrical vehicle to balance the power flow between power generation and demand, etc.

References

[1] L Fried. Global wind statistics 2015. *Global Wind Energy Council (GWEC): Brussels, Belgium*, 2016.

[2] Bin Wu, Yongqiang Lang, Navid Zargari, and Samir Kouro. *Power conversion and control of wind energy systems*. John Wiley & Sons, 2011.

[3] Fernando D Bianchi, Hernan De Battista, and Ricardo J Mantz. *Wind turbine control systems: principles, modelling and gain scheduling design*. Springer Science & Business Media, 2006.

[4] K. c. Bae, S. c. Choi, J. h. Kim, C. y. Won, and Y. c. Jung. LiFePO4 dynamic battery modeling for battery simulator. In *Industrial Technology (ICIT), 2014 IEEE International Conference on*, pages 354–358, Feb 2014.

[5] W. Li and G. Joos. A power electronic interface for a battery supercapacitor hybrid energy storage system for wind applications. In *2008 IEEE Power Electronics Specialists Conference*, pages 1762–1768, June 2008.

[6] F. Blaabjerg, Y. Yang, and K. Ma. Power electronics - key technology for renewable energy systems - status and future. In *Electric Power and Energy Conversion Systems (EPECS), 2013 3rd International Conference on*, pages 1–6, Oct 2013.

[7] F. Blaabjerg, Zhe Chen, and S. B. Kjaer. Power electronics as efficient interface in dispersed power generation systems. *IEEE Transactions on Power Electronics*, 19(5):1184–1194, Sept 2004.

[8] Thomas Ackermann et al. *Wind power in power systems*, volume 140. Wiley Online Library, 2005.

[9] Olimpo Anaya-Lara, Nick Jenkins, Janaka Ekanayake, Phill Cartwright, and Michael Hughes. *Wind energy generation: modelling and control*. John Wiley & Sons, 2011.

[10] Siegfried Heier. *Grid integration of wind energy: onshore and offshore conversion systems*. John Wiley & Sons, 2014.

[11] L. Holdsworth, X. G. Wu, J. B. Ekanayake, and N. Jenkins. Comparison of fixed speed and doubly-fed induction wind turbines during power system disturbances. *IEE Proceedings - Generation, Transmission and Distribution*, 150(3):343–352, May 2003.

[12] A. Roln, F. Crcoles Lpez, S. Bogarra, L. Monjo, and J. Pedra. Reduced-order models of squirrel-cage induction generators for fixed-speed wind turbines under unbalanced grid conditions. *IEEE Transactions on Energy Conversion*, 31(2):566–577, June 2016.

[13] S. Muller, M. Deicke, and R. W. De Doncker. Doubly fed induction generator systems for wind turbines. *IEEE Industry Applications Magazine*, 8(3):26–33, May 2002.

[14] Vladislav Akhmatov, Arne Hejde Nielsen, J Kaas Pedersen, and Ole Nymann. Variable-speed wind turbines with multi-pole synchronous permanent magnet generators. part i: Modelling in dynamic simulation tools. *Wind Engineering*, 27(6):531–548, 2003.

[15] Boubekeur Boukhezzar and Houria Siguerdidjane. Comparison between linear and nonlinear control strategies for variable speed wind turbines. *Control Engineering Practice*, 18(12):1357–1368, 2010.

[16] Lucy Y Pao and Kathryn E Johnson. Control of wind turbines. *Control Systems, IEEE*, 31(2):44–62, 2011.

[17] F. Blaabjerg and K. Ma. Future on power electronics for wind turbine systems. *IEEE Journal of Emerging and Selected Topics in Power Electronics*, 1(3):139–152, Sept 2013.

[18] D. Boroyevich, I. Cvetkovic, R. Burgos, and D. Dong. Intergrid: A future electronic energy network? *IEEE Journal of Emerging and Selected Topics in Power Electronics*, 1(3):127–138, Sept 2013.

[19] T. El-mezyani, R. Wilson, M. Sattler, S. K. Srivastava, C. S. Edrington, and D. A. Cartes. Quantification of complexity of power electronics based systems. *IET Electrical Systems in Transportation*, 2(4):211–222, December 2012.

[20] X. Wang, Y. Pang, P. C. Loh, and F. Blaabjerg. A series-lc-filtered active damper with grid disturbance rejection for ac power-electronics-based power systems. *IEEE Transactions on Power Electronics*, 30(8):4037–4041, Aug 2015.

[21] M. A. Maldonado and G. J. Korba. Power management and distribution system for a more-electric aircraft (madmel). *IEEE Aerospace and Electronic Systems Magazine*, 14(12):3–8, Dec 1999.

[22] J. A. Rosero, J. A. Ortega, E. Aldabas, and L. Romeral. Moving towards a more electric aircraft. *IEEE Aerospace and Electronic Systems Magazine*, 22(3):3–9, March 2007.

[23] P. Wheeler and S. Bozhko. The more electric aircraft: Technology and challenges. *IEEE Electrification Magazine*, 2(4):6–12, Dec 2014.

[24] R.H. Lasseter. MicroGrids. In *IEEE Power Engineering Society Winter Meeting, 2002*, volume 1, pages 305–308 vol.1, 2002.

[25] J.A. Peas Lopes, C.L. Moreira, and A.G. Madureira. Defining control strategies for microgrids islanded operation. *IEEE Transactions on Power Systems*, 21(2):916–924, May 2006.

[26] G. Diaz, C. Gonzalez-Moran, J. Gomez-Aleixandre, and A. Diez. Complex-valued state matrices for simple representation of large autonomous microgrids supplied by pq and vf generation. *IEEE Transactions on Power Systems*, 24(4):1720–1730, Nov 2009.

[27] J.M. Guerrero, J.C. Vasquez, J. Matas, L.G. de Vicua, and M. Castilla. Hierarchical control of droop-controlled ac and dc microgrids 2014;a general approach toward standardization. *IEEE Transactions on Industrial Electronics*, 58(1):158–172, Jan 2011.

[28] M. B. Camara, H. Gualous, F. Gustin, A. Berthon, and B. Dakyo. DC/DC converter design for supercapacitor and battery power management in hybrid vehicle applications - polynomial control strategy. *IEEE Transactions on Industrial Electronics*, 57(2):587–597, Feb 2010.

[29] M. B. Camara, B. Dakyo, and H. Gualous. Polynomial control method of DC/DC converters for DC-bus voltage and currents management - battery and supercapacitors. *IEEE Transactions on Power Electronics*, 27(3):1455–1467, March 2012.

[30] W. Li, G. Joos, and J. Belanger. Real-time simulation of a wind turbine generator coupled with a battery supercapacitor energy storage system. *IEEE Transactions on Industrial Electronics*, 57(4):1137–1145, April 2010.

[31] N. R. Tummuru, M. K. Mishra, and S. Srinivas. Dynamic energy management of hybrid energy storage system with high-gain PV converter. *IEEE Transactions on Energy Conversion*, 30(1):150–160, March 2015.

[32] H. Zhou, T. Bhattacharya, D. Tran, T. S. T. Siew, and A. M. Khambadkone. Composite energy storage system involving battery and ultracapacitor with dynamic energy management in microgrid applications. *IEEE Transactions on Power Electronics*, 26(3):923–930, March 2011.

[33] G. Zhang, X. Tang, and Z. Qi. Research on battery supercapacitor hybrid

storage and its application in microgrid. In *Power and Energy Engineering Conference (APPEEC), 2010 Asia-Pacific*, pages 1–4, March 2010.

[34] S. D. G. Jayasinghe, D. M. Vilathgamuwa, and U. K. Madawala. Diode-clamped three-level inverter-based battery/supercapacitor direct integration scheme for renewable energy systems. *IEEE Transactions on Power Electronics*, 26(12):3720–3729, Dec 2011.

[35] C. Zhou, K. Qian, M. Allan, and W. Zhou. Modeling of the cost of EV battery wear due to V2G application in power systems. *IEEE Transactions on Energy Conversion*, 26(4):1041–1050, Dec 2011.

[36] C. Alaoui. Solid-state thermal management for Lithium-Ion EV batteries. *IEEE Transactions on Vehicular Technology*, 62(1):98–107, Jan 2013.

[37] E. Barklund, N. Pogaku, M. Prodanovic, C. Hernandez-Aramburo, and T.C. Green. Energy management in autonomous microgrid using stability-constrained droop control of inverters. *IEEE Transactions on Power Electronics*, 23(5):2346–2352, Sept 2008.

[38] X. Yu, A. M. Khambadkone, H. Wang, and S. T. S. Terence. Control of parallel-connected power converters for low-voltage microgrid - part i: A hybrid control architecture. *IEEE Transactions on Power Electronics*, 25(12):2962–2970, Dec 2010.

[39] E. Rokrok and M. E. H. Golshan. Adaptive voltage droop scheme for voltage source converters in an islanded multibus microgrid. *IET Generation, Transmission Distribution*, 4(5):562–578, May 2010.

[40] Kyusung Kim and A. G. Parlos. Induction motor fault diagnosis based on neuropredictors and wavelet signal processing. *IEEE/ASME Transactions on Mechatronics*, 7(2):201–219, Jun 2002.

[41] Mehrdad Ehsani, Yimin Gao, and Ali Emadi. *Modern electric, hybrid electric, and fuel cell vehicles: fundamentals, theory, and design*. CRC press, 2009.

[42] Iqbal Husain. *Electric and hybrid vehicles: design fundamentals*. CRC press, 2011.

[43] M. Zeraoulia, M. E. H. Benbouzid, and D. Diallo. Electric motor drive selection issues for hev propulsion systems: A comparative study. *IEEE Transactions on Vehicular Technology*, 55(6):1756–1764, Nov 2006.

[44] C.C. Chan. The state of the art of electric, hybrid, and fuel cell vehicles. *IEEE Proceedings*, 95(4):704–718, April 2007.

[45] H. J. Van de Straete, J. De Schutter, and R. Belmans. An efficient procedure for checking performance limits in servo drive selection and optimization. *IEEE/ASME Transactions on Mechatronics*, 4(4):378–386, Dec 1999.

[46] J.W. Finch and D. Giaouris. Controlled AC electrical drives. *IEEE Transactions on Industrial Electronics,*, 55(2):481–491, Feb 2008.

[47] H. Rehman and Longya Xu. Alternative energy vehicles drive system: Control, flux and torque estimation, and efficiency optimization. *IEEE Transactions on Vehicular Technology,*, 60(8):3625–3634, Oct 2011.

[48] Y. Liu, J. Zhao, R. Wang, and C. Huang. Performance improvement of induction motor current controllers in field-weakening region for electric vehicles. *IEEE Transactions on Power Electronics*, 28(5):2468–2482, May 2013.

[49] Ken Dutton, Steve Thompson, and Bill Barraclough. *The Art of Control Engineering*. Addison-Wesley, 1997.

[50] P. Apkarian and P. Gahinet. A convex characterization of gain-scheduled h infin; controllers. *IEEE Transactions on Automatic Control*, 40(5):853–864, May 1995.

[51] Wilson J Rugh and Jeff S Shamma. Research on gain scheduling. *Automatica*, 36(10):1401–1425, 2000.

[52] Morten H Hansen, Anca Daniela Hansen, Torben J Larsen, Stig Øye, Poul Sørensen, and Peter Fuglsang. *Control design for a pitch-regulated, variable speed wind turbine*. 2005.

[53] J.M. Guerrero, L. Garcia De Vicuna, J. Matas, M. Castilla, and J. Miret. A wireless controller to enhance dynamic performance of parallel inverters in distributed generation systems. *IEEE Transactions on Power Electronics*, 19(5):1205–1213, Sept 2004.

[54] L. Amezquita-Brooks, J. Liceaga-Castro, and E. Liceaga-Castro. Speed and position controllers using indirect field-oriented control: A classical control approach. *IEEE Transactions on Industrial Electronics*, 61(4):1928–1943, April 2014.

[55] Felix Blaschke. The principle of field orientation as applied to the new transvektor closed-loop control system for rotating field machines. 1972.

[56] Rong-Jong Wai and Kuo-Min Lin. Robust decoupled control of direct field-oriented induction motor drive. *IEEE Transactions on Industrial Electronics*, 52(3):837–854, June 2005.

[57] Brice Beltran, Tarek Ahmed-Ali, and Mohamed El Hachemi Benbouzid. Sliding mode power control of variable-speed wind energy conversion systems. *Energy Conversion, IEEE Transactions on*, 23(2):551–558, 2008.

[58] A Kumar and K Stol. Simulating feedback linearization control of wind turbines using high-order models. *Wind Energy*, 13(5):419–432, 2010.

[59] P. Apkarian and R. J. Adams. Advanced gain-scheduling techniques for uncertain systems. *IEEE Transactions on Control Systems Technology*, 6(1):21–32, Jan 1998.

[60] Douglas A Lawrence and Wilson J Rugh. Gain scheduling dynamic linear controllers for a nonlinear plant. *Automatica*, 31(3):381–390, 1995.

[61] DJ Leith and WE Leithead. Implementation of wind turbine controllers. *International Journal of Control*, 66(3):349–380, 1997.

[62] A. Bidram, A. Davoudi, F.L. Lewis, and J.M. Guerrero. Distributed cooperative secondary control of microgrids using feedback linearization. *IEEE Transactions on Power Systems*, 28(3):3462–3470, Aug 2013.

[63] Riccardo Marino, Sergei Peresada, and Paolo Valigi. Adaptive input-output linearizing control of induction motors. *Automatic Control, IEEE Transactions on*, 38(2):208–221, 1993.

[64] T. K. Boukas and T. G. Habetler. High-performance induction motor speed control using exact feedback linearization with state and state derivative feedback. *IEEE Transactions on Power Electronics*, 19(4):1022–1028, July 2004.

[65] C. Lascu, S. Jafarzadeh, M. S. Fadali, and F. Blaabjerg. Direct torque control with feedback linearization for induction motor drives. *IEEE Transactions on Power Electronics*, 32(3):2072–2080, March 2017.

[66] F. Alonge, M. Cirrincione, M. Pucci, and A. Sferlazza. Input-output feedback linearization control with on-line mras-based inductor resistance estimation of linear induction motors including the dynamic end effects. *IEEE Transactions on Industry Applications*, 52(1):254–266, Jan 2016.

[67] A. Accetta, F. Alonge, M. Cirrincione, M. Pucci, and A. Sferlazza. Feedback linearizing control of induction motor considering magnetic saturation effects. *IEEE Transactions on Industry Applications*, 52(6):4843–4854, Nov 2016.

[68] S. S. Sastry and A. Isidori. Adaptive control of linearizable systems. *IEEE Transactions on Automatic Control*, 34(11):1123–1131, Nov 1989.

[69] Wen-Jieh Wang and Chun-Chieh Wang. Speed and efficiency control of an induction motor with input-output linearization. *IEEE Transactions on Energy Conversion*, 14(3):373–378, Sep 1999.

[70] H. Abootorabi Zarchi, J. Soltani, and G. Arab Markadeh. Adaptive input-output feedback-linearization-based torque control of synchronous reluctance motor without mechanical sensor. *IEEE Transactions on Industrial Electronics*, 57(1):375–384, Jan 2010.

[71] S. Shojaeian, J. Soltani, and G. Arab Markadeh. Damping of low frequency oscillations of multi-machine multi-upfc power systems, based on adaptive input-output feedback linearization control. *IEEE Transactions on Power Systems*, 27(4):1831–1840, Nov 2012.

[72] Wen-Hua Chen, Jun Yang, Lei Guo, and Shihua Li. Disturbance-observer-based control and related methodsłan overview. *IEEE Transactions on Industrial Electronics*, 63(2):1083–1095, 2016.

[73] SangJoo Kwon and Wan Kyun Chung. A discrete-time design and analysis of perturbation observer for motion control applications. *IEEE Transactions on control systems technology*, 11(3):399–407, 2003.

[74] Jingqing Han. From PID to active disturbance rejection control. *Industrial Electronics, IEEE transactions on*, 56(3):900–906, 2009.

[75] Qing-Chang Zhong and David Rees. Control of uncertain LTI systems based on an uncertainty and disturbance estimator. *Journal of dynamic systems, measurement, and control*, 126(4):905–910, 2004.

[76] Qing-Chang Zhong, Alon Kuperman, and RK Stobart. Design of ude-based controllers from their two-degree-of-freedom nature. *International Journal of Robust and Nonlinear Control*, 21(17):1994–2008, 2011.

[77] Jin-Hua She, Xin Xin, and Yaodong Pan. Equivalent-input-disturbance approachłanalysis and application to disturbance rejection in dual-stage feed drive control system. *IEEE/ASME Transactions on Mechatronics*, 16(2):330–340, 2011.

[78]

[79] Hebertt Sira-Ramirez and Marco Antonio Oliver-Salazar. On the robust control of buck-converter dc-motor combinations. *IEEE Transactions on Power Electronics*, 28(8):3912–3922, 2013.

[80] Euntai Kim. A fuzzy disturbance observer and its application to control. *Fuzzy Systems, IEEE Transactions on*, 10(1):77–84, 2002.

[81] Jong-Sun Ko and Byung-Moon Han. Precision position control of PMSM using neural network disturbance observer on forced nominal plant. In *Mechatronics, 2006 IEEE International Conference on*, pages 316–320. IEEE, 2006.

[82] Y. Lu, K. W. E. Cheng, and S. L. Ho. Auto-disturbance-rejection control for phase-shifted resonant converter. *IEE Proceedings - Electric Power Applications*, 153(5):711–718, September 2006.

[83] R. Xu, Y. Yu, R. Yang, G. Wang, D. Xu, B. Li, and S. Sui. A novel control method for transformerless h-bridge cascaded statcom with star configuration. *IEEE Transactions on Power Electronics*, 30(3):1189–1202, March 2015.

[84] Dixitbhai Patel and Lin Zhao. Active disturbance rejection control of doubly-fed induction generator during voltage dip. In *Proc. ESA Annual Meeting on Electrostatics*, page 2, 2010.

[85] X. Anjun, L. Xu, H. Shuju, L. Nianhong, and X. Honghua. A new pitch control method for large scale wind turbine based on ADRC. In *Materials for Renewable Energy and Environment (ICMREE), 2013 International Conference on*, volume 1, pages 373–376, Aug 2013.

[86] Wankun Zhou, Sally Shao, and Zhiqiang Gao. A stability study of the active disturbance rejection control problem by a singular perturbation approach. *Applied Mathematical Sciences*, 3(10):491–508, 2009.

[87] Xinkai Chen, Satoshi Komada, and Toshio Fukuda. Design of a nonlinear disturbance observer. *Industrial Electronics, IEEE Transactions on*, 47(2):429–437, 2000.

[88] J. Chen, L. Jiang, Wei Yao, and Q.H. Wu. Perturbation estimation based nonlinear adaptive control of a full-rated converter wind turbine for fault ride-through capability enhancement. *IEEE Transactions on Power Systems*, 29(6):2733–2743, Nov 2014.

[89] Y. Liu, Q. H. Wu, X. X. Zhou, and L. Jiang. Perturbation observer based multiloop control for the dfig-wt in multimachine power system. *IEEE Transactions on Power Systems*, 29(6):2905–2915, Nov 2014.

[90] Lin Jiang, Qing Hua Wu, Guoping Liu, and D. Rees. Robust adaptive control of induction motor based on perturbation estimation. In *IEEE International Electric Machines Drives Conference, IEMDC 2007.*, volume 1, pages 101–106, May 2007.

[91] Shihua Li, Jun Yang, Wen-Hua Chen, and Xisong Chen. Generalized extended state observer based control for systems with mismatched uncertainties. *Industrial Electronics, IEEE Transactions on*, 59(12):4792–4802, 2012.

[92] S. Zhenxing, L. Shihua, and Z. Xinghua. Direct torque control of induction machine using finite-time control and disturbance compensation. In *IECON 2014 - 40th Annual Conference of the IEEE Industrial Electronics Society*, pages 528–534, Oct 2014.

[93] Guang Feng, Yan-Fei Liu, and Lipei Huang. A new robust algorithm to improve the dynamic performance on the speed control of induction motor drive. *Power Electronics, IEEE Transactions on*, 19(6):1614–1627, 2004.

[94] Zhiqiang Gao. Active disturbance rejection control: a paradigm shift in feedback control system design. In *American Control Conference, 2006*, pages 7–pp. IEEE, 2006.

[95] Jie Li, Hai-Peng Ren, and Yan ru Zhong. Robust speed control of induction motor drives using first-order auto-disturbance rejection controllers. *IEEE Transactions on Industry Applications*, 51(1):712–720, Jan 2015.

[96] Haritza Camblong. Digital robust control of a variable speed pitch regulated wind turbine for above rated wind speeds. *Control Engineering Practice*, 16(8):946–958, 2008.

[97] Ahmet Serdar Yilmaz and Zafer Özer. Pitch angle control in wind turbines above the rated wind speed by multi-layer perceptron and radial basis function neural networks. *Expert Systems with Applications*, 36(6):9767–9775, 2009.

[98] David Schlipf, Dominik Johannes Schlipf, and Martin Kühn. Nonlinear model predictive control of wind turbines using LIDAR. *Wind Energy*, 16(7):1107–1129, 2013.

[99] Y.A.-R.I. Mohamed and E.F. El-Saadany. Robust high bandwidth discrete-time predictive current control with predictive internal model - a unified approach for voltage-source PWM converters. *IEEE Transactions on Power Electronics*, 23(1):126–136, Jan 2008.

[100] Y.A.-R.I. Mohamed and E.F. El Saadany. Hybrid variable-structure control with evolutionary optimum-tuning algorithm for fast grid-voltage regulation using inverter-based distributed generation. *IEEE Transactions on Power Electronics*, 23(3):1334–1341, May 2008.

[101] Q. Liu, Y. Tao, X. Liu, Y. Deng, and X. He. Voltage unbalance and harmonics compensation for islanded microgrid inverters. *IET Power Electronics*, 7(5):1055–1063, May 2014.

[102] L. Meng, X. Zhao, F. Tang, M. Savaghebi, T. Dragicevic, J. C. Vasquez, and J. M. Guerrero. Distributed voltage unbalance compensation in islanded microgrids by using a dynamic consensus algorithm. *IEEE Transactions on Power Electronics*, 31(1):827–838, Jan 2016.

[103] M. Hamzeh, S. Emamian, H. Karimi, and J. Mahseredjian. Robust control of an islanded microgrid under unbalanced and nonlinear load conditions. *IEEE*

Journal of Emerging and Selected Topics in Power Electronics, 4(2):512–520, June 2016.

[104] M. S. Golsorkhi and D. D. C. Lu. A decentralized control method for islanded microgrids under unbalanced conditions. *IEEE Transactions on Power Delivery*, 31(3):1112–1121, June 2016.

[105] A.V. Ravi Teja, C. Chakraborty, S. Maiti, and Y. Hori. A new model reference adaptive controller for four quadrant vector controlled induction motor drives. *IEEE Transactions on Industrial Electronics,*, 59(10):3757–3767, Oct 2012.

[106] A.B. Proca and A. Keyhani. Sliding-mode flux observer with online rotor parameter estimation for induction motors. *IEEE Transactions on Industrial Electronics,*, 54(2):716–723, April 2007.

[107] Hsin-Jang Shieh and Kuo-Kai Shyu. Nonlinear sliding-mode torque control with adaptive backstepping approach for induction motor drive. *Industrial Electronics, IEEE Transactions on*, 46(2):380–389, 1999.

[108] F. J. Lin, C. K. Chang, and P. K. Huang. FPGA-based adaptive backstepping sliding-mode control for linear induction motor drive. *IEEE Transactions on Power Electronics*, 22(4):1222–1231, July 2007.

[109] M. Suetake, I.N. da Silva, and A. Goedtel. Embedded DSP-based compact fuzzy system and its application for induction-motor V/f speed control. *Industrial Electronics, IEEE Transactions on*, 58(3):750–760, March 2011.

[110] P.Z. Grabowski, M.P. Kazmierkowski, B.K. Bose, and F. Blaabjerg. A simple direct-torque neuro-fuzzy control of PWM-inverter-fed induction motor drive. *IEEE Transactions on Industrial Electronics,*, 47(4):863–870, Aug 2000.

[111] Chich-Yi Huang, Tien-Chi Chen, and Ching-Lien Huang. Robust control of induction motor with a neural-network load torque estimator and a neural-network identification. *IEEE Transactions on Industrial Electronics*, 46(5):990–998, Oct 1999.

[112] Tien-Chi Chen and Tsong-Terng Sheu. Model reference neural network controller for induction motor speed control. *IEEE Transactions on Energy Conversion*, 17(2):157–163, Jun 2002.

[113] L Jiang, QH Wu, J Wang, C Zhang, and XX Zhou. Robust observer-based nonlinear control of multimachine power systems. In *Generation, Transmission and Distribution, IEE Proceedings-*, volume 148, pages 623–631. IET, 2001.

[114] L. Jiang, Q.H. Wu, and J.Y. Wen. Decentralized nonlinear adaptive control for multimachine power systems via high-gain perturbation observer. *IEEE Transactions on Circuits and Systems I: Regular Papers,*, 51(10):2052–2059, Oct 2004.

[115] J-JE Slotine, JK Hedrick, and EA Misawa. On sliding observers for nonlinear systems. *Journal of Dynamic Systems, Measurement, and Control*, 109(3):245–252, 1987.

[116] Yi Xiong and M. Saif. Sliding mode observer for nonlinear uncertain systems. *Automatic Control, IEEE Transactions on*, 46(12):2012–2017, 2001.

[117] R Sanchis and H Nijmeijer. Sliding controller-sliding observer design for non-linear systems. *European journal of control*, 4(3):208–234, 1998.

[118] BL Walcott, MJ Corless, and SH Żak. Comparative study of non-linear state-observation techniques. *International Journal of Control*, 45(6):2109–2132, 1987.

[119] Christopher Edwards and Sarah K Spurgeon. On the development of discontinuous observers. *International Journal of control*, 59(5):1211–1229, 1994.

[120] Jairo Terra Moura, Hakan Elmali, and Nejat Olgac. Sliding mode control with sliding perturbation observer. *Journal of Dynamic Systems, Measurement, and Control*, 119(4):657–665, 1997.

[121] Christopher Edwards and Sarah Spurgeon. *Sliding mode control: theory and applications*. CRC Press, 1998.

[122] Kyung-Soo Kim and Keun-Ho Rew. Reduced order disturbance observer for discrete-time linear systems. *Automatica*, 49(4):968–975, 2013.

[123] Arie Levant. Higher-order sliding modes, differentiation and output-feedback control. *International journal of Control*, 76(9-10):924–941, 2003.

[124] Kyeong-Hwa Kim and Myung-Joong Youn. A nonlinear speed control for a PM synchronous motor using a simple disturbance estimation technique. *Industrial Electronics, IEEE Transactions on*, 49(3):524–535, 2002.

[125] Shihua Li and Zhigang Liu. Adaptive speed control for permanent-magnet synchronous motor system with variations of load inertia. *Industrial Electronics, IEEE Transactions on*, 56(8):3050–3059, 2009.

[126] L Jiang and QH Wu. Nonlinear adaptive control via sliding-mode state and perturbation observer. *IEE Proceedings-Control Theory and Applications*, 149(4):269–277, 2002.

[127] Wen-Hua Chen, Donald J Ballance, Peter J Gawthrop, Jeremy J Gribble, and John O Reilly. A nonlinear disturbance observer for two link robotic manipulators. In *Decision and Control, 1999. Proceedings of the 38th IEEE Conference on*, volume 4, pages 3410–3415. IEEE, 1999.

[128] Jason M Jonkman and Marshall L Buhl Jr. FAST user's guide. *National Renewable Energy Laboratory, Golden, CO, Technical Report No. NREL/EL-500-38230*, 2005.

[129] Sven Creutz Thomsen. *Nonlinear control of a wind turbine*. PhD thesis, Technical University of Denmark, DTU, DK-2800 Kgs. Lyngby, Denmark, 2006.

[130] Wael M Korani, Hassen Taher Dorrah, and Hassan M Emara. Bacterial foraging oriented by particle swarm optimization strategy for PID tuning. In

Computational Intelligence in Robotics and Automation (CIRA), 2009 IEEE International Symposium on, pages 445–450. IEEE, 2009.

[131] Mahmud Iwan Solihin, Lee Fook Tack, and Moey Leap Kean. Tuning of PID controller using particle swarm optimization (PSO). *International Journal on Advanced Science, Engineering and Information Technology*, 1(4):458–461, 2011.

[132] Endusa Billy Muhando, Tomonobu Senjyu, Naomitsu Urasaki, Atsushi Yona, Hiroshi Kinjo, and Toshihisa Funabashi. Gain scheduling control of variable speed WTG under widely varying turbulence loading. *Renewable Energy*, 32(14):2407–2423, 2007.

[133] Endusa Billy Muhando, Tomonobu Senjyu, Aki Uehara, and Toshihisa Funabashi. Gain-scheduled control for wecs via LMI techniques and parametrically dependent feedback part ii: controller design and implementation. *Industrial Electronics, IEEE Transactions on*, 58(1):57–65, 2011.

[134] Tan Luong Van, Thanh Hai Nguyen, and Dong-Choon Lee. Advanced pitch angle control based on fuzzy logic for variable-speed wind turbine systems. *Energy Conversion, IEEE Transactions on*, 30(2):578–587, June 2015.

[135] Bonnie J Jonkman. *TurbSim user's guide: version 1.50*. National Renewable Energy Laboratory Golden, CO, USA, 2009.

[136] Mohammed G Khalfallah and Aboelyazied M Koliub. Effect of dust on the performance of wind turbines. *Desalination*, 209(1):209–220, 2007.

[137] Lasse Makkonen, Timo Laakso, Mauri Marjaniemi, and Karen Finstad. Modelling and prevention of ice accretion on wind turbines. *Wind Engineering*, 25(1):3–21, 2001.

[138] SA Saleh, R Ahshan, and CR Moloney. Wavelet-based signal processing method for detecting ice accretion on wind turbines. *Sustainable Energy, IEEE Transactions on*, 3(3):585–597, 2012.

[139] D. Graovac, V. Katic, and A. Rufer. Power quality problems compensation with universal power quality conditioning system. *IEEE Transactions on Power Delivery*, 22(2):968–976, April 2007.

[140] Hong-Seok Song and Kwanghee Nam. Dual current control scheme for PWM converter under unbalanced input voltage conditions. *IEEE Transactions on Industrial Electronics,*, 46(5):953–959, Oct 1999.

[141] Po-Tai Cheng, Chien-An Chen, Tzung-Lin Lee, and Shen-Yuan Kuo. A cooperative imbalance compensation method for distributed-generation interface converters. *IEEE Transactions on Industry Applications,*, 45(2):805–815, March 2009.

[142] M. Savaghebi, A. Jalilian, J.C. Vasquez, and J.M. Guerrero. Autonomous voltage unbalance compensation in an islanded droop-controlled microgrid. *IEEE Transactions on Industrial Electronics*, 60(4):1390–1402, April 2013.

[143] Y.A.-R.I. Mohamed and E.F. El-Saadany. Adaptive decentralized droop controller to preserve power sharing stability of paralleled inverters in distributed generation microgrids. *Power Electronics, IEEE Transactions on*, 23(6):2806–2816, Nov 2008.

[144] M.A. Mahmud, H.R. Pota, and M.J. Hossain. Dynamic stability of three-phase grid-connected photovoltaic system using zero dynamic design approach. *IEEE Journal of Photovoltaics*, 2(4):564–571, Oct 2012.

[145] Quan Li and P. Wolfs. A review of the single phase photovoltaic module integrated converter topologies with three different dc link configurations. *IEEE Transactions on Power Electronics,*, 23(3):1320–1333, May 2008.

[146] L. Jiang, Q.H. Wu, J. Wang, C. Zhang, and X.X. Zhou. Robust observer-based nonlinear control of multimachine power systems. *IEE Proceedings-Generation, Transmission and Distribution*, 148(6):623–631, Nov 2001.

[147] Remus Teodorescu, Marco Liserre, and Pedro Rodriguez. *Grid converters for photovoltaic and wind power systems*, volume 29. John Wiley & Sons, 2011.

[148] Roger C Dugan, Mark F McGranaghan, and H Wayne Beaty. Electrical power systems quality. *New York, NY: McGraw-Hill,— c1996*, 1, 1996.

[149] P. Rodriguez, R. Teodorescu, I. Candela, A.V. Timbus, M. Liserre, and F. Blaabjerg. New positive-sequence voltage detector for grid synchronization of power converters under faulty grid conditions. In *37th IEEE Power Electronics Specialists Conference, PESC 2006*, pages 1–7, June 2006.

[150] W. Li and G. Joos. A power electronic interface for a battery supercapacitor hybrid energy storage system for wind applications. In *Power Electronics Specialists Conference, 2008. PESC 2008. IEEE*, pages 1762–1768, June 2008.

[151] J. D. Dogger, B. Roossien, and F. D. J. Nieuwenhout. Characterization of Li-Ion batteries for intelligent management of distributed grid-connected storage. *IEEE Transactions on Energy Conversion*, 26(1):256–263, March 2011.

[152] M. B. Camara, H. Gualous, F. Gustin, and A. Berthon. Design and new control of DC/DC converters to share energy between supercapacitors and batteries in hybrid vehicles. *IEEE Transactions on Vehicular Technology*, 57(5):2721–2735, Sept 2008.

[153] P. Thounthong, S. Rael, and B. Davat. Control strategy of fuel cell and supercapacitors association for a distributed generation system. *IEEE Transactions on Industrial Electronics*, 54(6):3225–3233, Dec 2007.

[154] M. Mao, Y. Liu, P. Jin, H. Huang, and L. Chang. Energy coordinated control of hybrid battery-supercapacitor storage system in a microgrid. In *2013 4th IEEE International Symposium on Power Electronics for Distributed Generation Systems (PEDG)*, pages 1–6, July 2013.

[155] Yixin Zhu, Fang Zhuo, and Feng Wang. Coordination control of lithium battery-supercapacitor hybrid energy storage system in a microgrid under unbalanced load condition. In *Power Electronics and Applications (EPE'14-ECCE Europe), 2014 16th European Conference on*, pages 1–10, Aug 2014.

[156] X. Hu, S. Lin, S. Stanton, and W. Lian. A foster network thermal model for HEV/EV battery modeling. *IEEE Transactions on Industry Applications*, 47(4):1692–1699, July 2011.

[157] O. Tremblay, L. A. Dessaint, and A. I. Dekkiche. A generic battery model for the dynamic simulation of hybrid electric vehicles. In *Vehicle Power and Propulsion Conference, 2007. VPPC 2007. IEEE*, pages 284–289, Sept 2007.

[158] C. Abbey and G. Joos. Supercapacitor energy storage for wind energy applications. *IEEE Transactions on Industry Applications*, 43(3):769–776, May 2007.

[159] Remus Teodorescu, Marco Liserre, et al. *Grid converters for photovoltaic and wind power systems*, volume 29. John Wiley & Sons, 2011.

[160] A. Boglietti, A. Cavagnino, and M. Lazzari. Computational algorithms for induction-motor equivalent circuit parameter determination part I: Resistances and leakage reactances. *IEEE Transactions on Industrial Electronics*, 58(9):3723–3733, Sept 2011.

[161] W. M. Lin, T. J. Su, and R. C. Wu. Parameter identification of induction machine with a starting no-load low-voltage test. *IEEE Transactions on Industrial Electronics*, 59(1):352–360, Jan 2012.

[162] J. Guzinski and H. Abu-Rub. Speed sensorless induction motor drive with predictive current controller. *IEEE Transactions on Industrial Electronics*, 60(2):699–709, Feb 2013.

[163] C. Chakraborty and Y. Hori. Fast efficiency optimization techniques for the indirect vector-controlled induction motor drives. *IEEE Transactions on Industry Applications*, 39(4):1070–1076, July 2003.

[164] R. Ni, D. Xu, G. Wang, X. Gui, G. Zhang, H. Zhan, and C. Li. Efficiency enhancement of general AC drive system by remanufacturing induction motor with interior permanent-magnet rotor. *IEEE Transactions on Industrial Electronics*, 63(2):808–820, Feb 2016.

[165] Hamid Toliyat, Emil Levi, Mona Raina, et al. A review of RFO induction motor parameter estimation techniques. *Energy conversion, IEEE Transactions on*, 18(2):271–283, 2003.

[166] M. Hinkkanen, L. Harnefors, and J. Luomi. Reduced-order flux observers with stator-resistance adaptation for speed-sensorless induction motor drives. *IEEE Transactions on Power Electronics*, 25(5):1173–1183, May 2010.

[167] B. Karanayil, M. F. Rahman, and C. Grantham. Online stator and rotor resistance estimation scheme using artificial neural networks for vector controlled speed sensorless induction motor drive. *IEEE Transactions on Industrial Electronics*, 54(1):167–176, Feb 2007.

[168] L. Zhao, J. Huang, H. Liu, B. Li, and W. Kong. Second-order sliding-mode observer with online parameter identification for sensorless induction motor drives. *IEEE Transactions on Industrial Electronics*, 61(10):5280–5289, Oct 2014.

[169] Luis Amezquita-Brooks, Eduardo Liceaga-Castro, Jesús Liceaga-Castro, and Carlos E Ugalde-Loo. Flux-torque cross-coupling analysis of foc schemes: Novel perturbation rejection characteristics. *ISA transactions*, 58:446–461, 2015.

[170] Jingqing Han. From PID to active disturbance rejection control. *IEEE Transactions on Industrial Electronics,*, 56(3):900–906, March 2009.

[171] M. Habibullah and D. D. C. Lu. A speed-sensorless FS-PTC of induction motors using extended kalman filters. *IEEE Transactions on Industrial Electronics*, 62(11):6765–6778, Nov 2015.

[172] Shafiq Ahmed Odhano, Radu Bojoi, Aldo Boglietti, Stefan George Rosu, and Giovanni Griva. Maximum efficiency per torque direct flux vector control of induction motor drives. *Industry Applications, IEEE Transactions on*, 51(6):4415–4424, 2015.

[173] Camila P Salomon, Wilson C Sant'Ana, Luiz E Borges da Silva, Germano Lambert-Torres, Erik L Bonaldi, Levy EL de Oliveira, and Jonas G Borges da Silva. Induction motor efficiency evaluation using a new concept of stator resistance. *Instrumentation and Measurement, IEEE Transactions on*, 64(11):2908–2917, 2015.

[174] M Nasir Uddin and Sang Woo Nam. New online loss-minimization-based control of an induction motor drive. *Power Electronics, IEEE Transactions on*, 23(2):926–933, 2008.

[175] Cao-Minh Ta and Yoichi Hori. Convergence improvement of efficiency-optimization control of induction motor drives. *Industry Applications, IEEE Transactions on*, 37(6):1746–1753, 2001.

[176] Ned Mohan. Dsp based electric drives laboratory–user manual. *Department of Electrical and Computer Engineering, University of Minnesota*, 2007.

[177] Y. Hu, X. Song, W. Cao, and B. Ji. New SR drive with integrated charging capacity for plug-in hybrid electric vehicles (PHEVs). *IEEE Transactions on Industrial Electronics*, 61(10):5722–5731, Oct 2014.

[178] J. Holtz. Sensorless control of induction machines- with or without signal injection? *IEEE Transactions on Industrial Electronics,*, 53(1):7–30, Feb 2005.

[179] A. Emadi, Young Joo Lee, and K. Rajashekara. Power electronics and motor drives in electric, hybrid electric, and plug-in hybrid electric vehicles. *IEEE Transactions on Industrial Electronics,*, 55(6):2237–2245, June 2008.

[180] A. C. Lima-Filho, R. D. Gomes, M. O. Adissi, T. A. B. da Silva, F. A. Belo, and M. A. Spohn. Embedded system integrated into a wireless sensor

network for online dynamic torque and efficiency monitoring in induction motors. *IEEE/ASME Transactions on Mechatronics*, 17(3):404–414, June 2012.

[181] K. Rajashekara. Present status and future trends in electric vehicle propulsion technologies. *IEEE Journal of Emerging and Selected Topics in Power Electronics,*, 1(1):3–10, March 2013.

[182] C. Schauder. Adaptive speed identification for vector control of induction motors without rotational transducers. *IEEE Transactions on Industry Applications*, 28(5):1054–1061, Sep 1992.

[183] K. Ohyama, G.M. Asher, and M. Sumner. Comparative analysis of experimental performance and stability of sensorless induction motor drives. *IEEE Transactions on Industrial Electronics*, 53(1):178–186, Feb 2005.

[184] S.M. Gadoue, D. Giaouris, and J.W. Finch. MRAS sensorless vector control of an induction motor using new sliding-mode and fuzzy-logic adaptation mechanisms. *IEEE Transactions on Energy Conversion,*, 25(2):394–402, June 2010.

[185] Xi Zhang. Sensorless induction motor drive using indirect vector controller and sliding-mode observer for electric vehicles. *IEEE Transactions on Vehicular Technology*, 62(7):3010–3018, Sept 2013.

[186] A. Ersak B. Akin, U. Orguner and M. Ehsani. Simple derivative-free nonlinear state observer for sensorless ac drives. *IEEE/ASME Transactions on Mechatronics*, 11(5):634–643, Oct 2006.

[187] Z. Yang X. Sun, L. Chen and H. Zhu. Speed-sensorless vector control of a bearingless induction motor with artificial neural network inverse speed observer. *IEEE/ASME Transactions on Mechatronics*, 18(4):1357–1366, Aug 2013.

[188] L. Wu, W. X. Zheng, and H. Gao. Dissipativity-based sliding mode control of switched stochastic systems. *IEEE Transactions on Automatic Control*, 58(3):785–791, March 2013.

[189] Jianxing Liu, Salah Laghrouche, Mohamed Harmouche, and Maxime Wack. Adaptive-gain second-order sliding mode observer design for switching power converters. *Control Engineering Practice*, 30:124–131, 2014.

[190] Jianxing Liu, Salah Laghrouche, and Maxime Wack. Observer-based higher order sliding mode control of power factor in three-phase ac/dc converter for hybrid electric vehicle applications. *International Journal of Control*, 87(6):1117–1130, 2014.

[191] J. Liu, W. Luo, X. Yang, and L. Wu. Robust model-based fault diagnosis for pem fuel cell air-feed system. *IEEE Transactions on Industrial Electronics*, 63(5):3261–3270, May 2016.

[192] A. Haddoun, M.E.H. Benbouzid, D. Diallo, R. Abdessemed, J. Ghouili, and K. Srairi. Modeling, analysis, and neural network control of an EV electrical differential. *IEEE Transactions on Industrial Electronics*, 55(6):2286–2294, June 2008.

[193] Mehrdad Ehsani, Yimin Gao, and Ali Emadi. *Modern electric, hybrid electric, and fuel cell vehicles: fundamentals, theory, and design*. CRC press, 2009.

[194] K Bimal. Bose. *Modern power electronics and AC drives*, 2002.

[195] D Yoo, SS-T Yau, and Z Gao. Optimal fast tracking observer bandwidth of the linear extended state observer. *International Journal of Control*, 80(1):102–111, 2007.

[196] George Ellis. *Observers in Control Systems*. Academic Press, 2002.